PURE AND APPLIED GEOPHYSICS

(PAGEOPH)

Continuation of *Geofisica pura e applicata*

Birkhäuser Verlag, Basel and Stuttgart

Pageoph Vol. 64 pp. 1–256 (1966/II)

Printed by W. Rösch & Co., Bern

PURE AND APPLIED GEOPHYSICS

Vol. 64 1966/II

CONTENTS

PURE AND APPLIED GEOPHYSICS

Vol. 64 1966/II

On the Propagation of Love Waves in a Heterogeneous Layer Lying on a Homogeneous Medium

By ARABINDA BISWAS[1])

Summary – The present note is devoted to find out the possibility of propagation of love waves in a heterogeneous layer of finite depth lying on a homogeneous semi-infinite elastic medium, the rigidity and density in the upper layer varying as $(1 - \sin \alpha z)$, where α is a constant and z is the vertical distance from the interface. The numerical results for the phase velocity for some special Earth models are given.

1. Introduction

Propagation of Love waves in heterogeneous media with either varying both rigidity and density, or varying one of them in such a way that the wave velocity inside the layer either remains constant or becomes a function of the vertical distance only, has been studied by several authors [3][2]).

In this paper the propagation of Love waves is considered in the presence of heterogeneous crust lying on a homogeneous semi-infinite elastic medium. The rigidity and density for the upper layer are taken as

$$\mu_1 = \mu_0(1 - \operatorname{sun} \alpha z) , \quad \varrho_1 = \varrho_0(1 - \sin \alpha z) , \tag{1}$$

where μ_0 and ϱ_0 are the constant rigidity and density giving the values of μ_1 and ϱ_1 at the interface and z is the vertical height from the common surface.

2. Solution of the problem

In the absence of body forces the equation of motion [3] for the upper layer is

$$\nabla^2 v_1 + \frac{1}{\mu_1} \frac{d\mu_1}{dz} \frac{\partial v_1}{\partial z} = \frac{\varrho_1}{\mu_1} \frac{\partial^2 v_1}{\partial t^2} , \tag{2}$$

where

$$\nabla^2 \equiv \frac{\partial^2}{\partial x^2} + \frac{\partial^2}{\partial z^2} ,$$

and $v_1(x, z, t)$ is the transverse displacement component in the upper layer of thickness H, x-axis being taken in the direction of wave propagation, z-axis vertically upwards and the origin at the surface of separation of the two media.

[1]) Department of Mathematics, Indian Institute of Technology, Kharagpur, India, W-Bengal.

[2]) Numbers in brackets refer to References, page 8.

The displacement v_1 is assumed as

$$v_1 = V_1(z) \exp\{i\, k(x - c\, t)\}\,, \tag{3}$$

where k is the wave number and c is the phase velocity. This assumption transforms (2) in the form

$$\frac{d^2V_1}{dz^2} + \frac{1}{\mu_1}\frac{d\mu_1}{dz}\frac{dV_1}{dz} + k^2\left(\frac{\varrho_1}{\mu_1}\, c^2 - 1\right) V_1 = 0\,. \tag{4}$$

The substitution $V_1 = V'\,\mu^{-1/2}$ changes (4) as

$$\frac{d^2V'}{dz^2} + \left[\frac{1}{4\,\mu_1^2}\left(\frac{d\mu_1}{dz}\right)^2 - \frac{1}{2\,\mu_1}\frac{d^2\mu_1}{dz^2} + k^2\left(\frac{\varrho_1}{\mu_1}\, c^2 - 1\right)\right] V' = 0\,. \tag{5}$$

It is not possible to find out the general solution of (5) due to the presence of the expression in the square bracket. So μ_1 should be chosen in such a way that the equation can be solved.

Applying (1) in (5) we get

$$\frac{d^2V'}{dz^2} + \xi^2\, V' = 0\,, \tag{6}$$

where

$$\xi^2 = \frac{\alpha^2}{4} + k^2\left(\frac{c^2}{\beta_1^2} - 1\right),$$

$$\beta_1^2 = \frac{\mu_1}{\varrho_1} = \frac{\mu_0}{\varrho_0} = \text{constant}\,.$$

The solution of (6) is

$$V' = A_1 \cos\xi\, z + A_2 \sin\xi\, z\,, \tag{7}$$

A_1, A_2 are constants.
Therefore,

$$V_1 = \frac{1}{(1 - \sin\alpha\, z)^{1/2}}\left[B_1 \cos\xi\, z + B_2 \sin\xi\, z\right], \tag{8}$$

where $B_1 = \mu_0^{-1/2}\, A_1$, $B_2 = \mu_0^{-1/2}\, A_2$ are constants.

The equation of motion for the lower medium being homogeneous is

$$\nabla^2 v_2 = \frac{1}{\beta_2^2}\frac{\partial^2 v_2}{\partial t^2}\,, \tag{9}$$

where $\beta_2^2 = \mu_2/\varrho_2$, μ_2, ϱ_2 are the constant rigidity and density of the lower medium and $v_2(x, z, t)$ is the displacement component.

We take

$$v_2 = V_2(z) \exp\{i\, k(x - c\, t)\}\,, \tag{10}$$

and then (9) becomes

$$\frac{d^2V_2}{dz^2} - s^2\, V_2 = 0\,,$$

whence

$$V_2 = D\, e^{sz}\,,$$

since

$$V_2 \to 0 \quad \text{as} \quad z \to -\infty$$

and

$$s = k\left(1 - \frac{c^2}{\beta_2^2}\right)^{1/2}.$$

The boundary conditions, which are that (i) the displacement at, and (ii) the stress across the boundary surface between the two media shall be continuous at all times and places and (iii) the stress-free condition at the free surface, are

$$\left.\begin{aligned} &\text{(i)} \quad V_1 = V_2 \\ &\text{(ii)} \quad \mu_1 \frac{dV_1}{dz} = \mu_2 \frac{dV_2}{dz} \end{aligned}\right\} \quad \text{at} \quad z = 0\,,$$

$$\text{(iii)} \quad \mu_1 \frac{dV_1}{dz} = 0 \qquad \text{at} \quad z = H\,.$$

Applying these boundary conditions and eliminating the unknown constants B_1, B_2 and D from the resulting three equations we get the frequency equation in the form

$$\frac{\xi\left[\xi \tan \xi H - \frac{\alpha}{2}\frac{\cos\alpha H}{1-\sin\alpha H}\right]}{\xi + \frac{\alpha}{2}\tan \xi H \frac{\cos\alpha H}{1-\sin\alpha H}} + \frac{\alpha}{2} - \frac{\mu_2 s}{\mu_0} = 0$$

or,

$$f(c) = \left.\begin{aligned} &\frac{\left\{\frac{\alpha^2}{4} + k^2\left(\frac{c^2}{\beta_1^2} - 1\right)\right\}^{1/2}\left[\left\{\frac{\alpha^2}{4} + k^2\left(\frac{c^2}{\beta_1^2} - 1\right)\right\}^{1/2} \tan\left[\left\{\frac{\alpha^2}{4} + k^2\left(\frac{c^2}{\beta_1^2} - 1\right)\right\}^{1/2} H\right] - \frac{\alpha}{2}\frac{\cos\alpha H}{1-\sin\alpha H}\right]}{\left\{\frac{\alpha^2}{4} + k^2\left(\frac{c^2}{\beta_1^2} - 1\right)\right\}^{1/2} + \frac{\alpha}{2}\tan\left[\left\{\frac{\alpha^2}{4} + k^2\left(\frac{c^2}{\beta_1^2} - 1\right)\right\}^{1/2} H\right]\frac{\cos\alpha H}{1-\sin\alpha H}} \\ &\qquad + \frac{\alpha}{2} - \frac{\mu_2}{\mu_0} k\left(1 - \frac{c^2}{\beta_2^2}\right)^{1/2} = 0\,. \end{aligned}\right\} \tag{11}$$

3. Numerical solution of the frequency equation

To find out the roots of the frequency equation numerically the values of elastic constants for different media are taken as those assumed by NEWLANDS [2] except the density at the surface which is almost the same as taken by BULLEN [1].

μ (at the surface) $= 2.31 \times 10^{11}$ dynes/cm^2,
μ_0 (at the interface) $= 4.53 \times 10^{11}$ dynes/cm^2,
μ_2 (in the basic layer) $= 6.47 \times 10^{11}$ dynes/cm^2,
ϱ (at the surface) $= 1.75$ gm/cm^3,
ϱ_0 (at the interface) $= 3.4317$ gm/cm^3,
ϱ_2 (at the basic layer) $= 3.40$ gm/cm^3,
$\alpha = 0.0136$,
$H = 37.5$ km,

$$\beta_1 = \left(\frac{\mu_0}{\varrho_0}\right)^{1/2} = 3.6332 \text{ km/s}\,,$$

$$\beta_2 = \left(\frac{\mu_2}{\varrho_2}\right)^{1/2} = 4.362 \text{ km/s}\,.$$

For $k = 0.2$ along with the above values, and from (11)

$$f(3.69) = -0.0838,$$
$$f(3.70) = -0.05057,$$
$$f(3.71) = +0.00624.$$

For $k = 0.1$

$$f(3.85) = -0.00167,$$
$$f(3.86) = +0.00549.$$

The roots of (11) lies between 3.70 and 3.71 for $k = 0.2$ and for $k = 0.1$ it is in between 3.85 and 3.86.

The above discussion verifies that Love waves may be propagated under the assumed condition $\beta_1 < c < \beta_2$.

The author wishes to thank Prof. B. R. Seth for constant encouragement and Dr. S. B. Sinha for supervising the work. The author is also grateful to Council of Scientific and Industrial Research, New Delhi, for financial grant.

References

[1] K. E. Bullen, *An introduction to the theory of Seismology*, (1963), 226.
[2] M. Newlands, *Rayleigh waves in a two-layer heterogeneous medium*, MNRAS, Geophys. Suppl. *6* (1950), 13.
[3] W. M. Ewing, W. S. Jardetzky and F. Press, *Elastic waves in layered media* (1957), 341.

(Received 9th May 1966)

Effect of Density Stratification on Love Waves

By Subhas Dutta[1])

Summary – The effect on the propagation of love waves in a density stratified crust of finite thickness lying on a homogeneous half space is studied in this paper. Variations of phase and group velocities with wave number are obtained and the result is compared with that of Wilson.

Introduction

Propagation of Love waves in a medium where rigidity, density and velocity are functions of depth have been studied by several authors. Wilson [1][2]) considered a half space in which he took $\mu = \mu' e^{\nu z}$, $\beta = \beta' e^{\delta z}$. Dasgupta [2] had chosen a heterogeneous half space overlain by a homogeneous sub-stratum in which variations are $\mu = \mu' e^{\delta z}$, $\varrho = \varrho' e^{\delta z}$.

Mitra [3], Paul [4] and Dutta [5] also investigated the propagation of Love waves for similar laws of variation of rigidity and density, subject to the condition that the shear wave velocity remains constant.

In a recent paper Tolstoy [6] has considered a problem of propagation of sound waves in a density stratified layer lying on a homogeneous half space.

In this present paper we have studied the propagation of Love waves in a similar model. It is supposed that the density and the shear wave velocity of the crustal layer vary according to the law $\varrho = \varrho' e^{2nz}$ and $\beta = \beta' e^{-nz}$, z being the depth below the free surface and the rigidity $\mu = \mu_1$ is taken constant. It is believed that such type of variation have not yet been considered by any author.

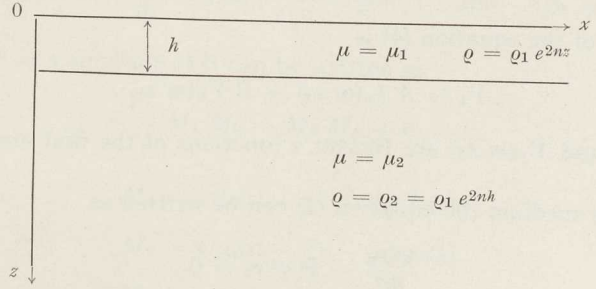

Figure 1
Shows the model considered

[1]) Department of Mathematics, Bangabasi College, 19 Scott Lane, Calcutta, India.
[2]) Numbers in brackets refer to References, page 13.

The solution is obtained in terms of Bessel's functions. The variations of group and phase velocities with wave number are shown in graphs and the result thus obtained is compared with those of WILSON, where μ and β are functions of depth. For the numerical calculation we have used the 'Table of Function' by JAHNKE and EMDE [8].

With the origin at the free surface we choose x-axis in the direction of propagation of waves and z-axis vertically downward.

The components of displacement (u, v, w) in a plane wave travelling in the direction of x increasing, in any medium may be assumed to be real part of $(0, V, 0)\, e^{i(kx-\omega t)}$, where V is a function of z only.

The equation of motion is (EWING, JARDETZKY and PRESS [7])

$$\mu \frac{\partial^2 v}{\partial x^2} + \mu \frac{\partial^2 v}{\partial z^2} = \varrho \frac{\partial^2 v}{\partial t^2} . \tag{1}$$

Let $v = V e^{i(kx-\omega t)}$, where k is the wave number and ω is the frequency. The equation (1) can be written as

$$\frac{d^2 V}{\partial z^2} - k^2 \left(1 - \frac{\varrho}{\mu} c^2\right) V = 0 . \tag{2}$$

For the upper layer we take $\mu = \mu_1$, and $\varrho = \varrho_1 e^{2nz}$. Then equation (2) takes the form

$$\frac{d^2 V_1}{\partial z^2} - k^2 \left(1 - \frac{c^2}{\beta_1^2} e^{2nz}\right) V_1 = 0 , \tag{3}$$

where

$$\beta_1 = \sqrt{\frac{\mu_1}{\varrho_1}}$$

and $V = V_1$ for the upper layer.

We now put $e^{nz} = x_1$ and the equation (3) thereby reduces to

$$\frac{d^2 V_1}{dx_1^2} + \frac{1}{x_1} \frac{dV_1}{dx_1} + \left(m^2 - \frac{p^2}{x_1^2}\right) V_1 = 0 , \tag{4}$$

where

$$m = \frac{k c}{\beta_1 n} \quad \text{and} \quad p = \frac{k}{n} .$$

The solution of the equation (4) is

$$V_1 = A J_p(m x_1) + B Y_p(m x_1) , \tag{5}$$

where $J_p(m x_1)$ and $Y_p(m x_1)$ are BESSEL's functions of the first and second kind of order p.

For the lower medium the equation (2) can be written as

$$\frac{d^2 V_2}{dz^2} - k^2 q^2 v_2 = 0 , \tag{6}$$

where

$$q = \left(1 - \frac{c^2}{\beta_2^2}\right)^{1/2} , \quad \beta_2 = \left(\frac{\mu_2}{\varrho_2}\right)^{1/2}$$

and $V = V_2$ for the lower medium.

The solution of the equation (6) suitable for the problem is easily obtained as

$$V_2 = D\, e^{-kqz}\,. \tag{7}$$

The boundary conditions are

$$\left.\begin{aligned} \frac{dV_1}{dZ} &= 0\,, && \text{at} \quad Z = 0\,, \\ V_1 &= V_2\,, && \text{at} \quad Z = h\,, \\ \mu_1 \frac{dV_1}{dz} &= \mu_2 \frac{dV_2}{dz}\,, && \text{at} \quad Z = h\,. \end{aligned}\right\} \tag{8}$$

and

From the above boundary conditions we get

$$A\{m\, J_{p-1}(m) - p\, J_p(m)\} + B\{m\, y_{p-1}(m) - p\, y_p(m)\} = 0\,, \tag{9}$$

$$A\, J_p(m\, e^{nh}) + B\, Y_p(m\, e^{nh}) = D\, e^{-kqh}\,, \tag{10}$$

$$\left.\begin{aligned} A\{m\, e^{nh} J_{p-1}(m\, e^{nh}) - p\, J_p(m\, e^{nh})\} + B\{m\, e^{nh}\, y_{p-1}(m\, e^{nh}) - p\, y_p(m\, e^{nh})\} \\ = -\frac{k\,q}{n} \frac{\mu_2}{\mu_1} D\, e^{-kqh}\,. \end{aligned}\right\} \tag{11}$$

Eliminating A, B and D between (9), (10) and (11) we get the frequency equation

$$\left.\begin{aligned} &\frac{m\, e^{nh} J_{p-1}(m\, e^{nh}) - p\left(1 - q\frac{\mu_2}{\mu_1}\right) J_p(m\, e^{nh})}{m\, J_{p-1}(m) - p\, J_p(m)} \\ &\qquad = \frac{m\, e^{nh}\, y_{p-1}(m\, e^{nh}) - p\left(1 - q\frac{\mu_2}{\mu_1}\right) y_p(m\, e^{nh})}{m\, y_{p-1}(m) - p\, y_p(m)}\,. \end{aligned}\right\} \tag{12}$$

For the numerical evaluation we take

$$\frac{\mu_2}{\mu_1} = 1.50\,, \quad \frac{\beta_2}{\beta_1} = 1.30\,, \quad \frac{k}{n} = p = 1 \quad \text{and} \quad n\,\beta_1 = 2\,. \tag{13}$$

Putting $m\, e^{kh} = s$ equation (12) can be written as

$$M_1\, M_3 - M_2\, M_4 = 0\,, \tag{14}$$

where

$$\begin{aligned} M_1 &= s\, J_0(s) - (1 - q_1)\, J_1(s)\,, \\ M_2 &= s\, y_0(s) - (1 - q_1)\, y_1(s)\,, \\ M_3 &= m\, y_0(m) - y_1(m)\,, \\ M_4 &= m\, J_0(m) - J_1(m)\,, \\ q_1 &= \frac{\mu_2}{\mu_1}\, q\,. \end{aligned}$$

The group velocity of the waves is given by

$$\frac{C}{\beta_1} = \frac{\frac{c}{\beta_1}\left[M_4\, y_1(s) - M_3\, J_1(s) + \frac{k\,h}{2\,q_3}\,(M_4\,N_4 - M_3\,N_3)\right]}{\left[M_4\, y_1(s) - M_3\, J_1(s) + \frac{1}{q_3}\left\{M_1\,N_1 - M_2\,N_2 + \frac{1}{2}\,(M_3\,N_3 - M_4\,N_4)\right\}\right]}\,, \tag{15}$$

where

$$N_1 = \frac{1}{2}\left(\frac{1}{m} - m\right) y_1(m)\,,$$

$$N_2 = \frac{1}{2}\left(\frac{1}{m} - m\right) J_1(m)\,,$$

$$N_3 = [q_1\, J_0(s) - q_2\, J_1(s)]\, e^{kh}\,,$$

$$N_4 = [q_1\, y_0(s) - q_2\, y_1(s)]\, e^{kh}\,,$$

$$q_2 = s + \frac{1}{s}\,(q_1 - 1)\,,$$

$$q_3 = \frac{\mu_2}{\mu_1}\,\frac{c}{\beta_2^2\, k\, q}\,.$$

The values of C/β_1 and c/β_1 are given with corresponding values of $k\,h$ in table 1.

Table 1

$k\,h$	0	0.10	0.20	0.30	0.40	0.50	0.60	0.70	0.80	0.90	1.00	1.30	1.50
c/β_1	1.30	1.28	1.26	1.24	1.20	1.13	1.06	1.00	0.93	0.85	0.77	0.60	0.52
C/β_1	1.30	1.20	1.05	0.77	0.43	0.13	−0.10	−0.27	−0.37	−0.45	−0.50		

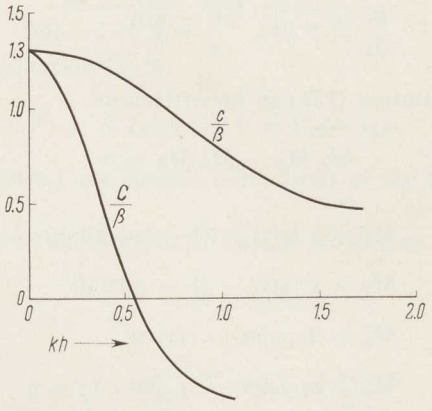

Figure 2
Variation of phase and group velocity with wave number obtained from equation (15)

Table 2

$\alpha/\beta = 3$			$\alpha/\beta = 2$		
K/β	c/b_0	C/b_0	K/β	c/b_0	C/b_0
2.60	1.84	0.93	2.83	1.63	1.025
2.83	—	—	—	—	—
3.71	1.58	0.99	4.90	1.38	1.05
5.81	1.37	1.01	—	—	—
6.84	1.32	1.03	6.93	1.28	1.05

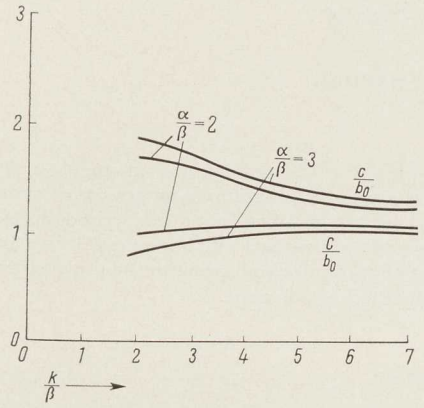

Figure 3.1
Variation of the phase and group velocity with wave number of WILSON's model

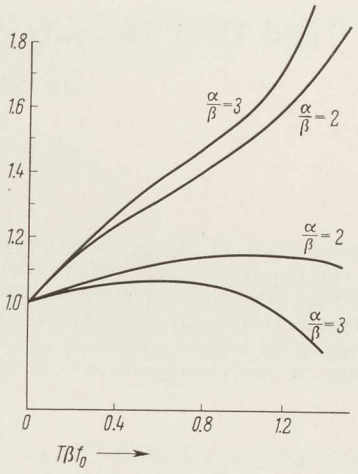

Figure 3.2
Velocity ratios as function of period of WILSON's model

Finally I express my gratitude to Dr. B. B. SEN, D. Sc., FNI, for his valuable suggestion at same stage of the work.

REFERENCES

[1] J. T. WILSON, *Surface waves in heterogeneous medium*, Bull. Seism. Soc. Amer. *32* (1942), 297.
[2] S. C. DAS GUPTA, *Note on the love waves in a homogeneous crust laid upon heterogeneous medium I*, J. App. Phys. *23* (1952).
[3] M. MITRA, *Note on a type of surface waves travelling in a semi-infinite medium*, Bull. Seism. Soc. Amer. *48* (1958).
[4] M. K. PAUL, *Note on a type of surface waves propagated in a heterogeneous medium with its lower surface rigidity fixed*, Gerlands Beitr. Geophys. *73* (1964), 3.
[5] S. DUTTA, *On the propagation of love waves in a non-homogeneous internal stratum of finite depth lying between two semi-infinite isotropic media*, Geofis. pura e appl. *55* (1963), 31.
[6] I. TOLSTOY, J. Geophys. Res. *70* (1965), 24.
[7] W. M. EWING, W. S. JARDETZKY and F. PRESS, *Elastic waves in layered media* (New York-London 1957).
[8] E. JAHNKE and F. EMDE, *Table of functions with formulae and curves* (Dover publ. 1945).

(Received 9th May 1966)

Digital Computation of Gravitational and Magnetic Anomalies and Their Derivatives for Two-dimensional Bodies of Arbitrary Shape

By P. Vallabh Sharma[1])

Summary – A simple method is presented for computing the gravity and magnetic profiles across two-dimensional bodies of arbitrary shape. The computer programme makes use of expressions for the attraction caused by an infinitely long sheet and it takes only a few seconds to compute a profile both for gravity and magnetic anomalies and their vertical and horizontal derivatives. Accuracy of the method is shown to be as good as that of graticules and owing to the use of simpler formulae, the method appears to be faster than the method of polygons.

1. Introduction

Computations of the gravity and magnetic effects of two-dimensional bodies has long been felt to be of considerable interest, because most of the common geological structures could be approximated by such distributions. Various graticules designed for evaluating the effects of two-dimensional bodies of arbitrary shape are found in the literature. While the precision attainable by graticules is quite sufficient, in practice these methods become very laborious and time consuming especially in the case of magnetic calculations.

Talwani *et al.* [3], Morgan and Grant [2] and Talwani and Heirtzler [4] have recently suggested high speed machine methods, all based on the approximation of the two-dimensional cross-section of a body by an n-sided polygon. However, these methods demand evaluation of rather lengthy expressions by the computer and in addition, these methods are not very easily extendable for calculation of higher derivatives of anomalies.

A need has therefore been felt for a simpler and more versatile method for rapid computation of gravity and magnetic effects of two-dimensional structures, which has been met by the method described in this paper. The programme of the method has been written in ALGOL for operation on the CDC–1604 computer of the Swiss Federal Institute of Technology, Zurich.

---

[1]) Department of Geophysics, Swiss Federal Institute of Technology, Zurich, Switzerland.
[2]) Numbers in brackets refer to References, page 18.

2. *Theory of the method*

We choose a right-handed system of coordinates (x_1, x_2, x_3) such that the two-dimensional body strikes from $+\infty$ to $-\infty$ in x_2 direction. The gravitational potential U at any point $P(0, 0, 0)$ due to such body of uniform density ϱ is given by

$$U = 2\,G\,\varrho \iint_S \log\left(\frac{1}{r}\right) dS\,, \tag{1}$$

where $r = \sqrt{x_1^2 + x_3^2}$, G is the gravitational constant and dS the surface element lying in the plane $x_1\,x_3$.

The components of both gravitational and magnetic attractions for a body of uniform density ϱ and uniform magnetization J are respectively given by

$$g_i = 2\,G\,\varrho\,T_i \quad (i = 1, 3)\,, \tag{2}$$

$$H_i = 2 \sum_i J_k\,T_{ik} \quad (i, k = 1, 2, 3)\,, \tag{3}$$

where

$$T_i = -\frac{\partial}{\partial x_i} \iint_S \log\left(\frac{1}{r}\right) dS\,, \tag{4}$$

and

$$T_{ik} = \frac{\partial^2}{\partial x_i\,\partial x_k} \iint_S \log\left(\frac{1}{r}\right) dS\,. \tag{5}$$

It is easy to see from equation (5) that $T_{ik} = T_{ki}$. Further, by making use of Laplace's equation and remembering that $T_{22} = 0$, we get the additional relation $T_{11} = -\,T_{33}$. Thus for evaluation of vertical and horizontal components of gravitational and magnetic effects, it should suffice to calculate only 4 quantities namely, T_3, T_1, T_{33} and T_{13}.

For an arbitrary surface S, the evaluation of T_i and T_{ik} in closed form is not possible. However, the analytical problem is considerably simplified by approximating the arbitrary cross-section by a number of thin vertical or horizontal rectangular strips. This in effect, would mean division of the two-dimensional body into a number of infinitely long sheets. The evaluated expressions for the T_i and T_{ik} components for such a vertical sheet of small thickness Δx_1 and extending from a_3 to b_3 in x_3 direction are simply given by

$$T_3 \cong \frac{1}{2}\,\Delta x_1 \left| \log\left(x_1^2 + x_3^2\right) \right|_{b_3}^{a_3}, \tag{6a}$$

$$T_1 \cong \Delta x_1 \left| \arctan\left(\frac{x_3}{x_1}\right) \right|_{b_3}^{a_3}, \tag{6b}$$

$$T_{33} \cong -\,\Delta x_1 \left| \frac{x_3}{\left(x_1^2 + x_3^2\right)} \right|_{b_3}^{a_3}, \tag{7a}$$

$$T_{13} \cong -\,x_1\,\Delta x_1 \left| \frac{1}{\left(x_1^2 + x_3^2\right)} \right|_{b_3}^{a_3}. \tag{7b}$$

Thus all the necessary components of T_i and T_{ik} being determined, gravitational and magnetic anomalies in directions x_1 and x_3 could be easily calculated by equations (2) and (3). Values of magnetization components are easily determined from the direction of the magnetization vector J, which may be either induced or remanent or mixed. For example, let us denote the inclination of the vector J by I and let the angle which the positive direction of x_1 axis makes with the horizontal projection of J, measured clockwise with respect to the later be D. Then J_1 and J_3 are given by

$$J_1 = J \cos I \cos D ,$$

$$J_3 = J \sin I .$$

If desired, the total anomaly $\Delta T \ll T$ in the direction of the earth's field could be easily calculated from the sum of projections of H_1 and H_3 along the direction of total field, i.e.,

$$\Delta T = H_1 \cos D \cos I + H_3 \sin I . \tag{8}$$

3. Derivatives of gravity and magnetic anomalies

By virtue of Poissons's relation between gravity and magnetic effects, we get

$$\frac{\partial^2 U}{\partial x_i \, \partial x_k} = -\frac{\partial g_i}{\partial x_k} = G \varrho \, T_{ik} . \tag{9}$$

The computer programme consisting of expressions for T_{ik} components (T_{33}, T_{13}), therefore enables simultaneous calculation of magnetic anomalies and derivatives of gravitational anomalies in vertical or horizontal directions. In addition, the expressions for T_{33} and T_{13} are simple enough to be differentiated further with respect to x_1 or x_3, thereby yielding derivatives of higher order. For example, the vertical derivatives of vertical, horizontal and total magnetic anomalies could be easily obtained in terms of T_{333} and T_{133} which are given by

$$T_{333} = \frac{\partial T_{33}}{\partial x_3} \cong -\Delta x_1 \left| \frac{x_1^2 - x_3^2}{(x_1^2 + x_3^2)^2} \right|_{b_3}^{a_3}, \tag{10}$$

$$T_{133} = \frac{\partial T_{13}}{\partial x_3} \cong 2 \Delta x_1 \left| \frac{x_3 \, x_1}{(x_1^2 + x_3^2)^2} \right|_{b_3}^{a_3} . \tag{11}$$

Thus the method outlined above also permits rapid calculation of higher derivatives of desired order of both gravitational and magnetic anomalies.

4. Accuracy and speed of the method

The accuracy of the method depends on how closely the thin rectangular strips fit the cross-section of the body. This is best demonstrated by applying the method to a simple model of known field anomaly and comparing the results.

For this purpose an infinitely long cylinder of diameter 2.4 km and of uniform density 1 gm/cc was chosen. A uniform magnetization of 5.34×10^{-4} CGS was assumed for the cylinder in a direction which made the values of I and D to be 60° and 30° respectively. The circular cross-section of the cylinder was approximated by 24

vertical strips of equal thickness and of varying heights. A profile of 10 points across the cylinder was computed for the vertical component of both gravity and magnetic anomalies. The top of the cylinder was assumed to be at a shallow depth of only 200 m.

As the table 1 shows, both for gravity and magnetic anomalies the computed results obtained by this method agree closely with the exactly known values for the chosen model, the maximum difference being only about 1/2%. For comparison sake, the results obtained through use of precise graticules designed by GASSMANN [1] are shown side by side, which demonstrate the accuracy of the method to be at least as good as that of graticules. It would also be interesting to compare the speed of the method with that of graticules. For 100 points, computation of gravitational anomalies (vertical and horizontal), magnetic anomalies (vertical, horizontal and total) and vertical and horizontal derivatives of both gravitational and magnetic anomalies took less than 30 seconds on a CDC–1604 computer; whereas using the graticules the time taken for calculation of only g_3, and that also for only 10 points was about 40 minutes and it took about $1^1/_2$ hours for calculation of only H_3, since in this case the graticule had to be used twice.

Table 1

Vertical components of gravitational and magnetic anomalies due to an infinitely long cylinder

x_1 (km)	g_3 (analytically) (m. gal)	g_3 (computer) (m. gal)	g_3 (graticule) (m. gal)	H_3 (analytically) (γ)	H_3 (computer) (γ)	H_3 (graticule) (γ)
0	43.11	43.12	43.5	213.48	213.88	216
0.2	42.24	42.25	42	230.13	230.48	232
0.4	39.85	39.85	40.1	219.71	220.0	218
0.6	36.42	36.41	36.2	189.68	189.43	188
0.8	32.50	32.48	32.6	151.03	150.80	152
1.0	28.54	28.53	28.2	112.70	112.48	114
1.2	24.85	24.84	25	79.63	79.48	80.1
1.4	21.55	21.55	21.7	53.37	53.31	52.5
1.6	18.69	18.69	18.5	33.59	33.60	33.8
2.0	14.18	14.18	14	8.95	9.01	9.0

5. *Discussion*

The above investigations show that the precision attainable by the method of graticules is comparable to that of the present method, but with respect to speed there is hardly any comparison possible. Even after taking into consideration the time spent in programming and in preparation of input data for CDC–1604 computer, the method described here proves to be incomparably faster than the method of graticules except when for some reason or other anomaly calculations are to be made only at a few points.

Earlier, MORGAN and GRANT [2] have shown the accuracy of the 'method of polygons' to be as good as that of graticules, which in turn should make the accuracy of the present method comparable to that of the polygon method. Though no direct comparison as to the relative speed has been made, it is felt that because of the use

of simpler formulae this method should prove to be comparatively faster than the method of polygons. The fact that the present method is very easily extendable for calculation of higher derivatives, points out yet another advantage of the method. In addition, the long uniform sheet model used in this method enables direct calculation of gravity and magnetic effects of some common two-dimensional features (e.g., thin dykes, veins) of regular shape as well. Thus a single computer programme based on this method is applicable to two-dimensional bodies of all possible shapes, whether regular or irregular.

6. Acknowledgement

I wish to thank Professor F. GASSMANN for critically reading the manuscript and for stimulating helpful discussion.

REFERENCES

[1] F. GASSMANN, *Graphical evaluation of the anomalies of gravity and of the magnetic field, caused by three-dimensional bodies*, Proc. Third World Petrol. Congress, Sec. *1* (1951), 613.

[2] N. A. MORGAN and F. S. GRANT, *High speed calculation of gravity and magnetic profiles across two-dimensional bodies having an arbitrary cross-section*, Geophysical Prospecting *11* (1963), 10.

[3] M. TALWANI, J. L. WORZEL and M. LANDISMAN, *Rapid gravity computations for two-dimensional bodies with application to the Mendocino submarine fracture zone*, J. Geophys. Res. *64* (1959), 49.

[4] M. TALWANI and J. R. HEIRTZLER, *Computation of magnetic anomalies caused by two-dimensional structures of arbitrary shape: Computers in the mineral industries*, Part 1, Stanford Univ. Publ., Geol. Sciences *9* (1964), 464.

(Received 30th May 1966)

Propagation of *Sn* and *Pn* to Teleseismic Distances

By Markus Båth[1])

Summary – *Sn* and *Pn* waves propagated to teleseismic distances are investigated by means of short-period seismograph records of the Swedish network. *Sn* is found in the distance range of 2400 to 4600 km and *Pn* in the range 3500 to 3900 km, but only provided the path is exceptionally homogeneous. Almost all paths are restricted to the Russian platform. There are probably very few areas in the world offering similar propagation paths. The velocities just under the Mohorovičić discontinuity are found to be 4.72 km/sec and 8.26 km/sec for transverse and longitudinal waves respectively. In addition, other properties of the teleseismic *Sn* and *Pn* are investigated, such as periods, dispersion, amplitudes, particle motions, propagation mechanisms, and comparisons are made with *Pa*, *Sa*, with *Li*, *Lg1*, *Lg2* and with *P*. The fact that teleseismic *Pn* occurs much more seldom than teleseismic *Sn* could be explained by different velocity profiles just under the crust.

1. Introduction

Sn and *Pn* waves are typical near-earthquake phases and found regularly in near earthquakes, i.e. up to distances of the order of 10°. *Sn* propagated to teleseismic distances was found on the Swedish records by the present writer in connection with bulletin work for the earthquake in the Caspian Sea on 27th January 1963. Exceptionally clear waves were recorded by all our short-period seismographs, and to judge from computed velocities and other properties there was no doubt that these were *Sn* waves. Later, they have been found on Swedish records in many cases, especially for earthquakes in the Caucasus and the Caspian Sea area, and were also found reported in the literature for other areas, especially for the Canadian shield (Brune and Dorman [8][2]))and in Central America (Shurbet [21]). There are obviously very few areas in the world with such a homogeneous structure as seems to be required for the propagation of *Sn* and *Pn* to teleseismic distances. The purpose of the present paper is to study these waves as far as the Swedish seismograph records permit.

Waves which like *Sn* and *Pn* propagate along an internal discontinuity surface have been subjected to several theoretical investigations in the literature (see for example Heelan [18], Sandner [20], Jeffreys [19], Donato [12], all with additional references). Such waves appear under various names as 'head waves' (German 'Kopfwellen' or 'Grenzschichtwellen'), 'Muskat waves', or 'conical waves'.

---

[1]) Seismological Institute, Uppsala, Sweden.

[2]) Numbers in brackets refer to References, page 30.

2. Observational material

The observational material is presented in the figures and tables. Table 1 lists the permanent Swedish seismograph stations and the instruments used in this research. All readings were made from short-period vertical-component (Z') records, and short-period horizontal-component (E', N') records were used only for particle motion studies in combination with Z'. The teleseismic Sn and Pn waves were not found on long-period records.

Table 1

Permanent seismograph stations in Sweden

Station	Latitude	Longitude	Instruments used in this paper
Uppsala (Up)	59° 51.5′ N	17° 37.6′ E	Benioff E' N' Z'
Kiruna (Ki)	67° 50.4′ N	20° 25.0′ E	Grenet Z'
Skalstugan (Sk)	63° 34.8′ N	12° 16.8′ E	Grenet Z'
Göteborg (Gb)	57° 41.9′ N	11° 58.7′ E	Grenet Z'
Umeå (Um)	63° 48.9′ N	20° 14.2′ E	Grenet Z' (up to 1961) Benioff E' N' Z' (from 1962)
Karlskrona (Ka)	56° 09.9′ N	15° 35.5′ E	Grenet Z'

Table 2

Data for earthquakes used in this paper

Focal parameters are determined by USCGS, ISS or BCIS, and magnitudes from Up, Ki; magnitudes in brackets are from other stations. n = normal focal depth

No.	Region	Date	Origin time GMT h m s	Latitude	Longitude	Depth km	Magnitude M_S
1	Caucasus	6 May 1958	04 15 45	43.1°N	47.8°E	n	(4½)
2	Tadzhik	31 July 1959	19 53 03	38.8°N	70.4°E	n	5.9
3	Azerbajdan	13 August 1959	00 33 08	39.8°N	48.5°E	n	5.8
4	Caucasus	25 September 1959	07 18 36	44.3°N	39.3°E	n	—
5	Hindu Kush	9 January 1960	07 24 04	36.5°N	70 °E	200	6.9
6	Hungary–Rumania	22 October 1960	19 17 47.9	45.9°N	21.2°E	25	—
7	Caspian Sea	9 June 1961	09 36 49.2	41.0°N	50.7°E	17	(6)
8	Caspian Sea	18 September 1961	11 01 04.5	41.0°N	50.2°E	55	5.8
9	Armenia	3 December 1961	18 31 56.1	40.9°N	44.1°E	44	(5)
10	Caspian Sea	1 July 1962	11 46 29.8	40.8°N	49.9°E	46	(4)
11	Caspian Sea	27 January 1963	19 35 14.3	41.2°N	49.8°E	33	6.1
12	Caspian Sea	31 January 1963	17 06 04.4	41.4°N	50.2°E	33	(5.4)
13	Black Sea	17 February 1963	08 28 24.9	42.1°N	37.2°E	33	(5)
14	Caspian Sea	26 May 1963	21 03 50.9	42.3°N	48.6°E	55	(5.3)
15	Caucasus	4 March 1964	17 33 43.3	43.3°N	46.1°E	58	(5)
16	Gibraltar	15 March 1964	22 30 26.0	36.2°N	7.6°W	27	6.7
17	Turkey	14 June 1964	12 15 31.3	38.0°N	38.5°E	8	5.8
18	Kazakh	19 July 1964	05 59 58.9	49.9°N	78.1°E	0	6.0
19	Caspian Sea	16 August 1964	21 28 49.1	39.7°N	52.6°E	33	(5½)
20	Central Russia	15 February 1965	12 34 54.8	53.6°N	81.3°E	11	5.7

Table 3

Arrival times, amplitudes and periods of Sn and Pn

Numbers (No.) refer to the list in table 2. Quality *A* = very clear case, *B* = clear case. All readings refer to the *Z'*-component

No.	Station	Distance	Arrival time		Quality	Amplitude/period μ/sec	
		km		h m s		*Sn*(*Pn*)	*P*
1	Ki	3190	*iSn*	04 27 27	*B*	0.04/1.0	0.05/1.0
	Sk	3210	*eSn*	04 27 48	*B*	0.03/1.0	0.03/1.0
2	Up	4330	*iSn*	20 08 33	*A*	0.05/1.5	0.10/0.7
3	Ki	3560	*iSn*	00 45 42	*A*	0.12/1.5	0.18/1.0
4	Sk	2740	*iSn*	07 28 44	*B*	0.03/1.0	0.09/1.0
5	Up	4510	*iSn*	07 39 58	*A*	0.3 /1.0	0.9 /0.5
	Ki	4630	*iSn*	07 40 38	*A*	0.2 /1.3	3.5 /1.3
6	Ki	2440	*iSn*	19 26 34	*B*	small	0.07/1.0
7	Ki	3500	*iSn*	09 49 21	*A*	0.3 /1.5	0.14/0.7
	Gb	3300	*iSn*	09 48 33	*A*	0.3 /1.5	0.11/1.0
	Um	3210	*iSn*	09 48 34	*A*	0.09/0.9	0.14/0.7
8	Gb	3280	*iSn*	11 12 38	*A*	0.6 /1.5	0.11/1.0
9	Up	2790	*iSn*	18 42 15	*A*	0.14/1.5	0.3 /1.0
10	Up	3080	*iSn*	11 57 23	*A*	0.04/0.7	0.01/0.5
	Ki	3500	*iSn*	11 59 08	*A*	0.08/1.5	0.05/0.9
11	Up	3030	*iSn*	19 46 01	*A*	0.3 /0.8	0.3 /0.5
	Ki	3460	*iSn*	19 47 30	*A*	1.1 /1.5	0.7 /1.0
	Sk	3480	*iSn*	19 47 31	*A*	0.5 /1.5	0.3 /1.0
	Gb	3230	*iSn*	19 46 46	*A*	1.2 /1.5	0.6 /1.3
	Um	3160	*iSn*	19 46 38	*A*	0.6 /1.0	1.0 /1.0
	Ka	2980	*iSn*	19 45 54	*A*	0.8 /1.5	2.2 /1.0
12	Up	3030	*iSn*	17 16 57	*A*	0.07/1.0	0.04/0.5
	Ki	3440	*iSn*	17 18 28	*A*	0.11/1.3	0.15/0.8
	Um	3160	*iSn*	17 17 27	*A*	0.07/1.0	0.2 /0.7
13	Ki	3030	*iSn*	08 39 24	*B*	small	small
	Um	2660	*iSn*	08 38 13	*A*	0.03/1.0	0.12/0.7
14	Up	2880	*iSn*	21 14 06	*B*	0.02/0.7	0.02/0.5
15	Um	2810	*iSn*	17 44 09	*B*	0.04/1.0	0.10/0.8
16	Up	3190	*iSn*	22 42 04	*A*	0.2 /1.0	1.0 /1.0
	Gb	2800	*iSn*	22 40 30	*A*	0.4 /1.4	4.2 /1.3
	Um	3600	*iSn*	22 43 24	*A*	0.2 /1.3	3.2 /1.5
	Ka	2820	*iSn*	22 40 43	*A*	0.4 /1.3	2.8 /1.5
17	Um	3120	*iSn*	12 26 49	*A*	0.7 /2.0	0.6 /1.2
18	Up	3890	*iPn*	06 07 59	*A*	0.03/0.5	0.06/0.5
	Ki	3690	*iPn*	06 07 31	*A*	0.02/0.8	0.2 /0.6
			iSn	06 13 38	*A*	0.03/1.2	
	Um	3700	*iPn*	06 07 37	*A*	0.04/0.7	0.15/0.7
19	Up	3310	*iSn*	21 40 29	*A*	0.02/1.0	0.04/0.5
	Ki	3690	*iPn*	21 36 24	*A*	0.04/1.0	0.05/1.0
			eSn	21 42 12	*A*	0.04/1.2	
	Um	3420	*iSn*	21 41 16	*A*	0.08/1.2	0.09/0.8
20	Up	3810	*iSn*	12 48 42	*A*	0.04/0.7	0.2 /1.0
	Ki	3500	*iPn*	12 42 03	*A*	0.05/1.0	0.12/1.0
			iSn	12 47 36	*A*	0.08/1.0	
	Um	3560	*iSn*	12 47 35	*A*	0.09/1.2	0.16/1.0

Table 2 lists the earthquakes used and table 3 readings of arrival times, periods and amplitudes. The records for the interval from January 1958 to July 1965 were searched and only those cases included which were clear and reliable, excluding all less clear cases. This gives at the same time an idea about the frequency of occurrence of teleseismic *Sn* and *Pn* at our stations.

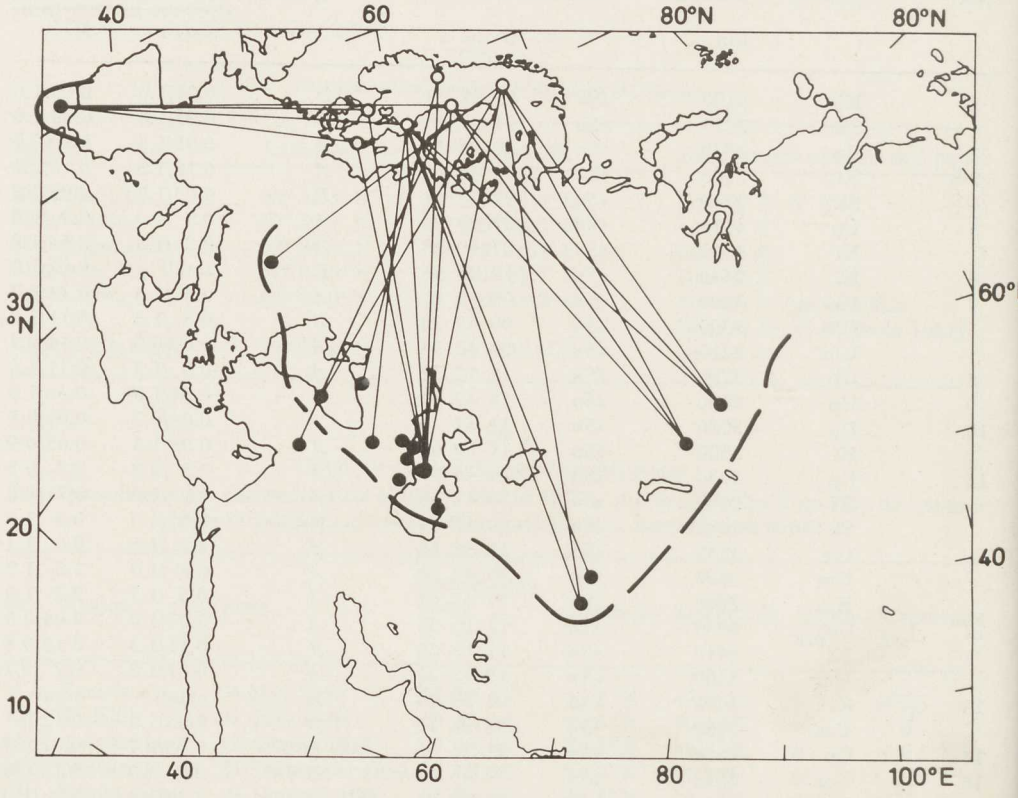

Figure 1
Earthquake epicenters (filled circles) and stations (open circles). To avoid confusion, paths have not been drawn from all epicenters in the Caucasus region, but records of *Sn* have been obtained at all our stations from earthquakes in this region. The dashed line limits the area within which teleseismic *Sn* and *Pn* propagation is possible

The epicenters, stations and the paths are depicted in figure 1. The area covered by most of the paths coincides remarkably well with the Russian platform. This has certainly a very uniform structure and practically constant thickness of the crust, which seems to be a very essential requirement for the propagation of *Sn* and *Pn* to great distances. The crustal structure of the Russian platform has been reported in numerous papers by Russian seismologists (see e.g. a summary by GODIN and EGORKIN [15]; see also BÅTH [4]). Some typical records are shown in figure 2, and figure 3 shows the travel times plotted versus epicentral distance.

The identification of the waves as *Sn* or *Pn* was essentially made by means of their calculated velocities. Special care has naturally to be taken in case where other phases may be expected to arrive at nearly the same time. Some cases where confusion with other phases (such as *PcS* etc.) could arise have been excluded. On the whole, *Sn* is easy to distinguish from other body waves, because it initiates a monotonous

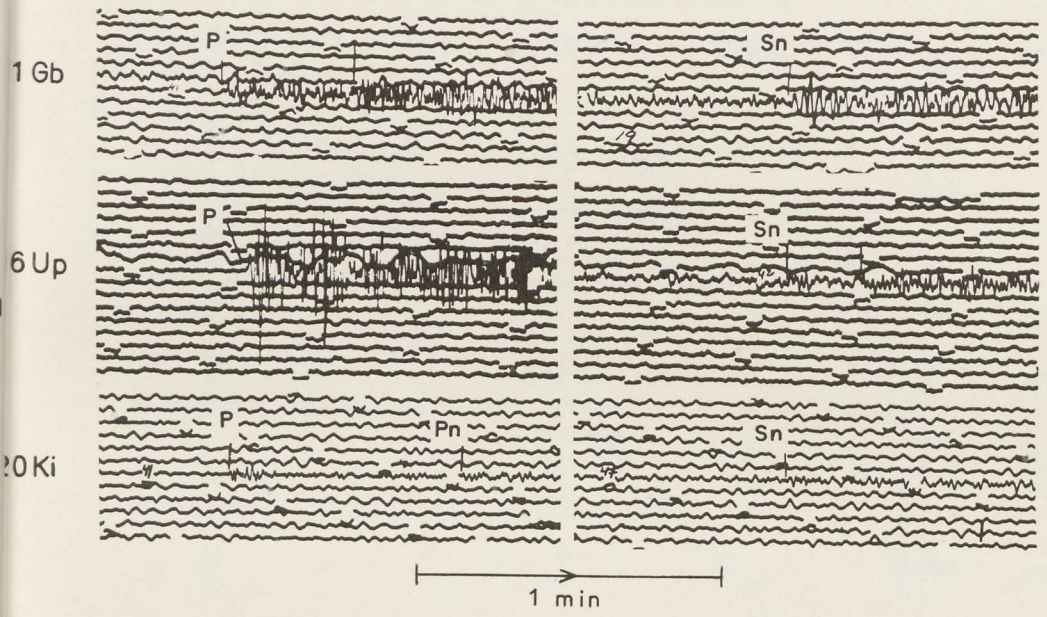

Figure 2
Some typical records of *Sn* and *Pn*. A few minutes have been left out in the middle of each of the three records. For further explanations, see tables 2 and 3

wave train which generally lasts several minutes (often 4 to 5 min), which is not the case for any body wave which could arrive about the same time. There were no complications from the ordinary *S* in readings of *Sn*, partly because *Sn* arrives much later than *S* for the distances concerned, partly because *S* was not recorded on Z' for the earthquakes investigated.

The optimum magnitude range for the existence of *Sn* and *Pn* at our stations is 4 to 7, especially between 5 and 6. Larger magnitudes mean too much preceding motion for reliable discovery of *Sn* and *Pn*, and lower magnitudes mean too weak records.

With one exception, the focal depth is less than 60 km. This would mean that the foci are close to the Mohorovičić discontinuity, which is favourable in feeding much energy into *Sn* and *Pn* waves.

Some remarks will be made on the particular cases:

No. 5. This is the deepest shock in the list (focal depth = 200 km). Seismic rays from such a deep shock could be brought into grazing incidence below Moho because of the reversed curvature of the rays produced by the low-velocity layer in the upper mantle.

No. 16. This is the only case with a path which does not traverse the Russian platform. It should be noticed that clear *Sn* waves are observed at the eastern stations (Up, Gb, Um, Ka) but there is no trace of them along more westerly paths (to Sk and Ki). The latter may be too much disturbed for the *Sn*-propagation, possibly due to the Biscay Bay and Scandinavian mountain range. The wave trains last only about 2 to 3 min in this case, against 4 to 5 min in most other cases.

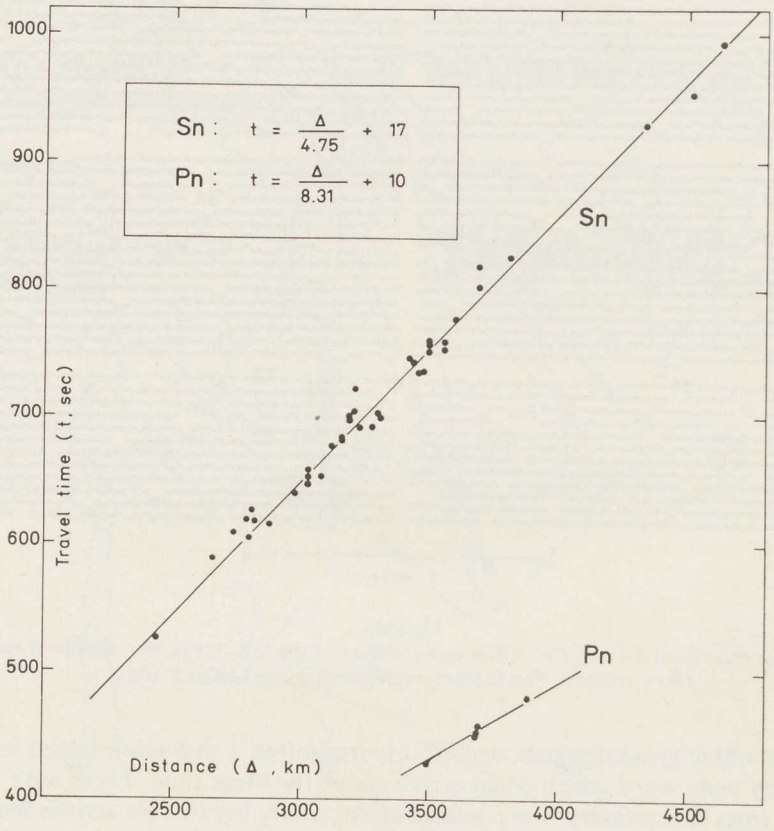

Figure 3
Travel times of *Sn* and *Pn* plotted versus epicentral distance and least-square solutions according to equation (2) = the straight lines

No. 17. The records are less convincing in this case, which is probably due to the more disturbed portion of the path through northern Turkey.

No. 18. This is an underground explosion. A series of about 15 explosions in the Semipalatinsk area has been recorded at the Swedish stations for about two years since March 1964. Examining all these records we find that Up has generally recorded clear *Pn*-phases, whereas they have been less clear at Ki and Um.

Sometimes, notable exceptions occur, such as for an earthquake on 20th May 1959 (41.8°N, 41.9°E, Caucasus, normal focal depth, origin time = 19 49 13, magnitude = 5.7). Clear *Lg2* but no *Sn* are recorded at the Swedish stations. There is no imme-

diately obvious explanation for this exceptional behaviour, even if focal mechanism and wave radiation pattern may be thought to be responsible.

Finally, it should be remarked that *Pn* has only been observed in cases 18 (Kazakh), 19 (Caspian Sea) and 20 (Central Russia), that is *Pn* is found much less often than *Sn*.

3. Properties of teleseismic Sn and Pn

Velocities. Table 4 summarizes the least-square calculations of velocities. With the following notation:

t = travel time, sec,
Δ = epicentral distance (along the earth's surface), km,
v = group velocity, km/sec,
Δ_r = epicentral distance (along arc of radius r), km,
v_r = group velocity (along arc of radius r), km/sec,

we have made the calculations in three different ways:

a) neglecting the time-term:

$$t = \frac{\Delta}{v}\,, \tag{1}$$

b) including a time-term t_0:

$$t = \frac{\Delta}{v} + t_0\,, \tag{2}$$

c) reducing the velocities to some specified level r:

$$t = \frac{\Delta_r}{v_r} + t_0\,. \tag{3}$$

Table 4

Group velocities corresponding to the onset of the wave train

N = number of observations. For *Sn* and *Pn* only observations of quality *A* (table 3) were used. All errors are standard deviations of single observations

	Equation (1)		Equation (2)			Equation (3)			
Wave	N	v km/sec	N	v km/sec	t_0 sec	N	r km	v_r km/sec	t_0 sec
Pn	5	8.13 ± 0.04	5	8.31 ± 0.05	10 ± 2	5	6335 (Moho)	8.26 ± 0.05	10 ± 2
Pa (continental)	59	8.35 ± 0.08	20	8.62 ± 0.13	23 ± 14	20	6270 (100 km deep)	8.48 ± 0.13	23 ± 14
Sn	33	4.64 ± 0.06	33	4.75 ± 0.06	17 ± 9	33	6335 (Moho)	4.72 ± 0.06	17 ± 9
Sa (continental)	88	4.56 ± 0.03	21	4.59 ± 0.07	11 ± 21	21	6220 (150 km deep)	4.48 ± 0.07	11 ± 21
Li	83	3.79 ± 0.07	39	3.76 ± 0.06	−9 ± 19				
Lg1	82	3.54 ± 0.06	65	3.55 ± 0.05	2 ± 16				
Lg2	76	3.37 ± 0.04	52	3.36 ± 0.03	0 ± 11				

Assuming that propagation takes place along some layer or surface in the earth's interior, the velocities calculated from (1) and (2) are only apparent velocities, as pointed out by CALOI [9]. In that case (3) will give real velocities, provided we know which layer we shall reduce to.

For comparison purposes earlier results on *Li* (BÅTH [3]), *Lg1* and *Lg2* (BÅTH [1]), *Pa* and *Sa* (BÅTH and LOPEZ ARROYO [6]), which were originally computed only according to equation (1), have been recalculated according to (2), and for *Pa* , *Sa* also according to (3). In these recalculations only the most reliable observations from the quoted papers were used. Reduction according to (3) was made for *Pa* to $r = 6270$ km (depth = 100 km), for *Sa* to $r = 6220$ km (depth = 150 km) and for *Pn* and *Sn* to Moho ($r = 6335$ km).

The sub-Moho velocities found are 8.26 ± 0.05 km/sec and 4.72 ± 0.06 km/sec for longitudinal and transverse waves, respectively, the latter in very good agreement with BRUNE and DORMAN's [8] result for the Canadian shield. Combining the velocities of *Pn* and *Sn*, we find a POISSON's ratio = 0.258 just under Moho. There are probably some regional variations in these velocities, though small over the area concerned, and our material is insufficient to demonstrate any possible variations.

The time-terms show relatively large scatter and no very definite conclusions can be drawn from them. Anyhow, it is of interest to note that for *Li*, *Lg1*, *Lg2* the time-terms are practically zero, suggesting either propagation along a near-surface channel or propagation as surface waves (BÅTH and CRAMPIN [7]). In these three cases there is no significant change in the velocity values from the original calculations.

For *Pn* and especially for *Sn* (being more reliable because of more observations), there is clear indication of a positive time-term. Its numerical value is in good agreement with theoretical expectation. With H = crustal thickness, v_c = crustal velocity, v_m = sub-Moho velocity, R = the earth's radius, r_m = radius of Moho, we find theoretically that

$$t = \frac{\left(\frac{r_m}{R}\right)\Delta}{v_m} + \frac{H}{v_c\, v_m}\,(v_m^2 - v_c^2)^{1/2} \tag{4}$$

for a source at Moho, and that

$$t = \frac{\left(\frac{r_m}{R}\right)\Delta}{v_m} + \frac{2\,H}{v_c\, v_m}\,(v_m^2 - v_c^2)^{1/2} \tag{5}$$

for a surface source. Assuming $H = 40$ km and $v_c = 3.66$ km/sec, we find the time-term in (4) to be 7 sec and in (5) to be 14 sec, i.e. comparable with the calculated value of 17 sec for *Sn*. Similar arguments hold for *Pn*.

The time-terms calculated for *Pa* and *Sa* are less conclusive, the one for *Sa* being unexpectedly smaller than for *Pa*. Most likely, *Pa* and *Sa* propagate as higher-mode surface waves.

Periods and amplitudes. Table 5 summarizes information on periods and amplitudes for *Pn* and *Sn*. Comparisons have been made with *P* waves on the same records (Z'). The measurements, listed in table 3, refer to maximum amplitudes shortly after the onset. The periods of *Sn* are greater than those of *P*, whereas the periods of *Pn* and *P*

Table 5

Periods (T in sec) and amplitudes (A in microns, on Z') for Sn, Pn and P

The values are in each case averages of N observations, from table 3

$T(Sn) = 1.2$	$N = 38$
$T(Pn) = 0.8$	$N = 5$
$T(P) = 0.9$	$N = 38$
$T(Sn):T(P) = 1.40 \pm 0.37$	$N = 38$
$T(Pn):T(P) = 1.07$	$N = 5$
$A(Sn):A(P) = 1.00$	$N = 38$
$A(Pn):A(P) = 0.42$	$N = 5$

are about equal. The amplitudes of *Sn* are on the average equal to those of *P*, but there are large individual variations. This is also to be expected as there are probably numerous factors which affect the amplitudes of *Sn* in relation to *P*, such as focal mechanism and radiation towards the station, propagation properties etc. The statistical frequency distribution of $(A_{Sn}/A_P)_{Z'}$ tells us that this ratio is ≤ 1.0 in 76 percent of the cases investigated. The amplitude of *Pn* is generally smaller than of *P*. Some theoretical comparisons of the amplitude variation of *Pn* and *P* with distance were made by DE BREMAECKER [11].

As already mentioned, *Sn* consists of an impulsive onset followed by a wave train, generally 4 to 5 min in duration. This may be monotonous, with no significant variations in period or amplitude. Interpreted as an integral part of the higher-mode surface waves, the practically constant period would correspond to a very steep dispersion curve. In some cases, there may be amplitude increases along the wave train at the points where the so-called channel waves *Li*, *Lg1* and *Lg2* arrive (BÅTH and CRAMPIN [7]).

Particle motions. These have been studied from Up E' N' Z' and Um E' N' Z' records of *Sn* in the cases with the largest amplitudes, i.e. 5, 11 and 16. Accurate determinations of particle motion is hampered by the relatively small time resolution on the records for the short periods of *Sn*. The orbits can only be determined by accurately timed measurements on the three component records. For more reliable results it was also found necessary to form averages of a number of measurements, such as of the amplitude ratio of different components.

Quite generally, the beginning of the motion and the first 10 to 20 sec are dominated by longitudinal motion (*SV* or conversion into *P*), and the motion is often irregular with a mixture of several wave forms. After that, the largest amplitudes set in, on the horizontal components, and the record is dominated by *SH*-motion. However, the recorded *SH* is twice the incident *SH*, whereas the horizontal components record only about 0.3 of the incident *SV* (GUTENBERG [17]). As a consequence, there are roughly equal parts of *SH* and *SV* in the later part of the *incident Sn*-motion, whereas *SV* dominates in the early part.

4. Discussion

Sn compared to Sa. Of all known seismic waves, *Sa* has the closest relations to *Sn*. But the two are not identical, which is clear for a number of reasons enumerated

below. *Sa* and *Pa* were investigated by BÅTH and LOPEZ ARROYO [6] and more recently discussed by BÅTH [5]. The most powerful interpretation which can be made of these waves is no doubt in terms of higher modes. A comparison of *Sa* with *Sn* can be summarized in the following points:

a) *Sa* is found almost exclusively on long-period seismograms and has a dominating period around 20 sec, whereas *Sn* is found only on short-period seismograms and has a period averaging 1.2 sec only.

b) *Sa* is observed for all earthquake regions and is able to propagate along both oceanic and continental paths, whereas *Sn* has been found at Swedish stations almost exclusively for paths over the Russian platform.

c) Comparing the average velocities of *Sa* and *Sn*, we find by application of the *t*-test (FISHER [14], p. 122), that they are statistically very well separated from each other in all cases, listed in table 4.

The conclusion is that *Sn* and *Sa* propagate in different ways. Whereas *Sn* is most likely bound to the Mohorovicić discontinuity, *Sa* is probably more influenced by deeper layers.

The velocity of *Sn* is significantly *higher* than the velocity of *Sa*, irrespective whether the velocities are calculated from equation (1), (2) or (3). But the corresponding velocity of *Pn* is significantly *lower* than the velocity of *Pa*. This seems to require different velocity profiles for transverse and longitudinal waves in the upper mantle.

Table 6

Correspondence between certain teleseismic and near-earthquake phases

Teleseismic phase	Near-earthquake phase
Pn	*Pn*
π_g	P_g (or possibly P^*)
Sn	*Sn*
Li	S^*(*Sb*)
Lg1	*S* in uppermost part of granitic layer
Lg2	*Sg*

Sn compared to Li, Lg1, Lg2. These four waves, observed at teleseismic distances, have in common that they correspond to waves, with exactly the same velocities, found in near earthquakes (table 6). This perfect agreement in velocities cannot be explained as pure coincidence. There are still numerous unsolved problems in the connection between near and distant earthquakes, which can probably only be solved by having a practically continuous series of stations along a profile from close-in distances out to great distances. At Swedish stations we find repeatedly that at distances less than about 500 km, the largest amplitudes belong to *Sg*, but at greater distances they belong to *Lg1*.

A significant difference between *Sn* on one hand and *Li*, *Lg1*, *Lg2* on the other is, that the latter propagate much more easily along continental structures than the former. *Sn* in fact requires an exceptionally homogeneous structure for its propagation. Under the great oceans we have in large areas structures of similar homogeneity

and we could expect teleseismic *Sn* and *Pn* to exist also there. Compare SHURBET [21]. Deep-sea seismometers will probably give more information on this point.

Sn compared to Pn. As we have seen, teleseismic *Pn* is much less frequent than teleseismic *Sn* is. There is a similar difference between π_g on one hand and *Li*, *Lg1* *Lg2* on the other, as π_g is usually erratic in occurrence and propagates only to shorter distances. A possible explanation for the difference in propagation of *Sn* and *Pn* could be that the velocity profiles are different for transverse and longitudinal waves just under Moho. The velocity profiles across the upper mantle low-velocity layer is different for *P* and *S* waves, as pointed out already by GUTENBERG (see BÅTH [2]), and there is reason to believe that such differences may extend up to the base of the crust. In order to explain propagation by grazing or near-grazing incidence under Moho, we have to assume an energy trap with downwards increasing velocity just under Moho. The vertical extent of this trap and its velocity profile will influence its capability to transmit energy to great distances.

Propagation mechanism. In case of grazing incidence from below at the Mohorovičić discontinuity, there is total reflection for both *P*, *SV* and *SH*. No energy will then be transmitted to the surface, and it is necessary to introduce diffraction to account for waves observable on the surface. But, supposing the existence of an energy trap just under Moho, we could permit also near-grazing incidence, say e.g. angles of incidence of 80° at Moho from below. In that case, we will also get waves reaching the surface by ordinary refraction and reflection, without need to introduce diffraction. The conditions will then be different for *P*, *SV* and *SH*.

SH will always transform into *SH*, and considering the system crust + upper mantle as a whole, there will be no energy loss from this system. This will be an effective wave guide for *SH*, for angles of incidence at Moho not smaller than a certain value, depending on the velocity profile in the trap. Conditions for constructive interference between waves reflected at Moho from below and those reflected from the surface and re-entering the mantle can easily be formulated. They will involve the thickness of the crust, and too large or too rapid variations in this thickness can destroy the constructive interference.

For *SV* the same system will in our conditions also be an almost perfect wave guide. There is almost total reflection into *SV* at the free surface, and there is no *P* formed on reflection or refraction at Moho (for an angle of incidence of 80°). For *P*, on the other hand, there will be greater losses, due to partial transformation into *SV* (GUTENBERG [16]). This could possibly explain why *Pn* is observed much more seldom than *Sn* at teleseismic distances, even without assuming different velocity profiles.

Such a model, involving propagation along an internal surface and where the properties of both media are of significance, will impose greater restrictions on the propagation than in cases where a wave is propagated more wholly within one or the other medium. This is suggested as a possible explanation for the restriction of *Sn* and *Pn* to exceptionally homogeneous paths, as we have observed.

This discussion concerns the ray picture of propagation (compare for instance EWING, JARDETZKY and PRESS [13], figure 4, p. 142). The corresponding wave picture would most probably be in terms of higher-mode surface waves. Available information on higher-mode surface waves, both experimental (CRAMPIN [10]) and theoretical, generally concerns longer periods and lower initial velocities than observed here.

5. Acknowledgement

The research reported in this paper was carried out at the Seismological Institute, Uppsala, Sweden, with the sponsorship of the Cambridge Research Laboratories of the Office of Aerospace Research, United States Air Force, through its European Office, as part of the Advanced Research Projects Agency's project Vela-Uniform, under Contract AF 61(052)–702.

References

[1] M. Båth, *The elastic waves Lg and Rg along Eurasiatic paths*, Ark. f. Geofysik *2* (1954), 295
[2] M. Båth, *Some consequences of the existence of low-velocity layers*, Ann. Geofis. *9* (1956), 411–.
[3] M. Båth, *A continental channel wave, guided by the intermediate layer in the crust*, Geofis. pura e appl. *38* (1957), 19.
[4] M. Båth, *Die Conrad-Diskontinuität*, Freiberger Forschungshefte *C 101* (1961), 5.
[5] M. Båth, *Lateral inhomogeneities of the upper mantle*, Tectonophysics *2* (1965), 483.
[6] M. Båth and A. Lopez Arroyo, *Pa and Sa waves and the upper mantle*, Geofis. pura e appl. *56* (1963), 67.
[7] M. Båth and S. Crampin, *Higher modes of seismic surface waves—relations to channel waves*, Geophys. J. *9* (1965), 309.
[8] J. Brune and J. Dorman, *Seismic waves and earth structure in the Canadian shield*, Bull. Seism. Soc. Am. *53* (1963), 167.
[9] P. Caloi, *On the canalization of seismic energy*, Ann. Geofis. *17* (1964), 513.
[10] S. Crampin, *Higher modes of seismic surface waves: Preliminary observations*, Geophys. J. *9* (1964), 37.
[11] J. Cl. de Bremaecker, *Use of amplitudes, Part I: Pn from 3° to 23°*, Bull. Seism. Soc. Am. *45* (1955), 219.
[12] R. J. Donato, *Amplitude of the head wave near the critical angle*, Geophys. J. *8* (1963), 203.
[13] W. M. Ewing, W. S. Jardetzky and F. Press, *Elastic waves in layered media* (McGraw-Hill 1957), 380.
[14] R. A. Fisher, *Statistical methods for research workers* (Oliver and Boyd 1950), 354.
[15] J. A. Godin and A. V. Egorkin, *Der Bau der Erdkruste im Südosten der Russischen Plattform nach Ergebnissen regionaler seismischer Arbeiten*, Bergakademie Freiberg *13* (1961), 420.
[16] B. Gutenberg, *Energy ratio of reflected and refracted seismic waves*, Bull. Seism. Soc. Am. *34* (1944), 85.
[17] B. Gutenberg, *SV and SH*, Trans. Am. Geophys. Un. *33* (1952), 573.
[18] P. A. Heelan, *On the theory of head waves*, Geophysics *18* (1953), 871.
[19] H. Jeffreys, *Head waves and the nature of the Mohorovičić discontinuity*, Geophys. J. *7* (1963), 412.
[20] A. Sandner, *Das Problem der seismischen Grenzschichtwelle bei der Behandlung der Wellengleichung*, Freiberger Forschungshefte *C 26* (1956), 47.
[21] D. H. Shurbet, *The high-frequency S phase and structure of the upper mantle*, J. Geophys. Res. *69* (1964), 2065.

(Received 17th May 1966)

A Markov Model for Aftershock Occurence

By D. Vere-Jones[1])

Summary – A model for aftershocks is put forward in which it is supposed that successive aftershocks represent transitions of an energy system from one state to the next, the successive states being linked in a Markov chain. Expressions are derived for the aftershock frequency, the energy release, and the frequency-magnitude law.

1. – The occurrence of aftershocks and foreshocks has long been acknowledged, and their statistical properties have been the subject of numerous investigations. In view of the random appearance of the times of occurrence of the shocks within these sequences, it is natural to attempt to formulate a theory of such sequences in terms of a stochastic model. The purpose of the present paper is to put forward a model for the simplest type of aftershock sequences, in which the process is regarded as a jump-type Markov process. This model cannot claim to be a very satisfactory representation even for this simplest type of sequence. In the first place, it is not related to any specific theory of earthquake mechanism, but is based on certain general assumptions whose interpretation and justification in terms af any specific theory is left an open question. In the second place the characteristics of aftershock sequences as predicted from the model differ in some important features from the characteristics of observed aftershock sequences. The attempt to formulate such a model may nevertheless help to clarify some aspects of aftershock occurrence, in particular the relations between the time and magnitude distributions of shocks, and to suggest problems for further investigation.

2. – We shall be concerned only with the case in which a large initial shock is followed by a sequence of further shocks with, in general, diminishing magnitudes and diminishing frequency. Such sequences have been studied by many authors, from Omori [5][2]) onwards, and we refer to Utsu [8] and Mogi [4] for detailed studies of a large number of sequences of this type and for further references. We should also refer to the remarkable series of papers by Mogi[3]) on the laboratory simulation of aftershocks, which also contain many references and discussions concerning the properties of real aftershock sequences.

---

[1]) Department of Statistics, The Australian National University, Canberra, Australia.

[2]) Numbers in brackets refer to References, page 42.

[3]) Bulletin of Earthquake Research Institute, Tokyo University, Vol. 40, pages 125–174, 175–186, 815–830, 831–854, and Vol. 41, pages 595–614, 615–659.

The behaviour of such sequences is summarized by three important distributions,
1. The distribution over the time axis of the frequency of aftershock occurrence;
2. The distribution over the time axis of energy release;
3. The distribution over the energy axis of the numbers of shocks.

These are evidently marginal distributions formed from a joint distribution function giving the probability of a shock of a particular energy occurring at a given time after the initial shock. The aim of our investigation will be to describe such a joint distribution function, and to show how it can be derived from some simple basic assumptions. Although spatial distributions are also of interest, in the present article we shall restrict ourselves to considerations concerning time and energy.

A characteristic feature of the observed time distributions is a very slow rate of decay: if we write $N(t)$ for the number of aftershocks that have occurred up to time t after the initial shock, it appears that the increment in $N(t)$ follows an inverse power law. The earlier investigators suggested

$$\Delta N(t) = \frac{1}{t}\,\Delta t \tag{1}$$

but more recent studies have suggested that a more appropriate form might be

$$\Delta N(t) = \frac{1}{(c+t)^{1+\alpha}}\,\Delta t\,, \tag{2}$$

where c is a constant related to the time scale of the shock mechanism (probably of the order of one day) and α is an exponent in the range $0 < \alpha < 1$, often close to the value $\alpha = 1/4$ (UTSU [8]; VERE-JONES and DAVIES [9].)

In a similar way, it appears that the energy increment decays as a power-law of the form

$$\Delta E(t) = \frac{1}{(d+t)^{1+\beta}}\,\Delta t\,. \tag{3}$$

Finally, it is usually assumed that the frequency-magnitude law has a similar form for the shocks within an aftershock sequence as it does in general, namely

$$\log N(M) = a - b\,M\,, \tag{4}$$

where $N(M)$ is the number of shocks in the sequence having magnitude greater than M. If we refer this to energy rather than magnitude, using as a first approximation the formula (GUTENBERG and RICHTER [3])

$$\log E = 11.8 + 1.5\,M \tag{5}$$

we obtain the equivalent form

$$F(E) = A\,E^{-B}\,, \tag{6}$$

where $F(E)$ denotes the number of shocks in the sequence having energies greater than E, and the constants A, B are related to a and b by

$$A = a + \frac{11.8\,b}{1.5}\,, \qquad B = \frac{b}{1.5}\,.$$

Distributions of type (6) are well-known in economic applications, where they pass under the name of the PARETO Law (see, for example, STEINDL [7]).

In general, these three distributions are not independent, and any particular model should lead to relationships between the parameters occurring in the three equations (2), (3) and (5). Of more direct importance is that *any satisfactory model of aftershock occurrence must yield the basic features of all three relations.*

3. – Let us turn now to a discussion of the assumptions underlying our model. As mentioned above, we shall not attempt to relate these assumptions to any particular theory of earthquake mechanism. However, the three relations described in the previous section are so ubiquitous, they appear so inevitably in the discussion of earthquake records, that we might expect them to depend on such general considerations as would be common features of any reasonable model of earthquake occurrence. For example, the Poisson law for the occurrence of very large shocks on the global scale can be interpreted as a consequence of the two assumptions that very large shocks are extremely rare events in any particular region of the globe, and that different regions act independently of each other; thus the Poisson law is not dependent on any particular theory of earthquake mechanism, but is a consequence of simpler and much more general considerations. In just such a way, one might expect that the PARETO form of the frequency-energy law, and the inverse power law forms for the time decay of numbers of shocks and the energy release, could be deduced from quite general considerations which would hold in common for any reasonable theory of earthquake mechanism.

The assumptions we shall make are as follows:

(i) – The process is governed by the decay of some parameter $E(t)$; each aftershock represents a jump in the value of $E(t)$ to a lower value, and we shall interpret the difference in the two values as the amount of some physical quantity that is lost as a consequence of the aftershock. For our purposes it is not necessary to identify $E(t)$ explicitly, at least until we reach the stage of comparing our results with observations, but it is natural to suppose that $E(t)$ would be closely related to the energy in the system or perhaps to the strain. In the sequel we shall suppose that E can be represented as some power of the energy.

(ii) – The future behaviour of the process (i.e. the probabilities of the sizes and times of occurrence of further aftershocks) is determined by the present value of $E(t)$ but not on the earlier history of the process. Thus the probabilities would depend in a certain way on the *sum* of the sizes of the preceding shocks (measured in terms of E), but not on their individual sizes nor on the time intervals between them. It is this assumption which embodies the Markovian property of our model, and which is, undoubtedly, one possible source of criticism. Nevertheless it seems to the writer that such an assumption, however crude, might still be expected to preserve the general features of the process.

(iii) – There is no 'immigration' from outside the system; the function $E(t)$ remains constant between shocks and is not augmented or reduced by a flow of energy into or from the surroundings. This assumption is suggested by the particular type of aftershock sequence chosen for study, but here also we have a possible source of criticism.

With these assumptions we can interpret the system as a 'jump-type' Markov process, whose state space corresponds to the range of values over which the parameter $E(t)$ may vary. Each aftershock represents a jump in the process, where the sizes of these jumps and the probabilities of their occurrence are governed by two

basic probability functions, the jump intensity $\lambda(E)$ and the distribution function for shock size $F(H, E)$. More precisely, these functions may be defined as follows. $\lambda(E)\, dt$ represents the probability (up to terms of smaller order than dt) that a shock will occur within the small time interval $t, t + dt$ given that at time t the parameter $E(t)$ has the value E. $F(H, E)$ is the probability that, given a shock occurs at a time when the quantity $E(t)$ has value H, the new value of $E(t)$ is equal to or less than E. Thus $F(H, E)$ is a probability distribution defined over the interval $0 \leq E \leq H$. We shall assume for convenience that $\lambda(E)$ and $F(H, E)$ are continuous, differentiable functions of E, and we shall denote the derivative $\partial F(H, E)/\partial E$ by $f(H, E)$, so that for each H, $f(H, E)$ is a probability density function over $(0, H)$.

We now introduce the distribution function for the state of the process at time t, which will contain the basic information concerning the time-development of the process. We shall write

$$P(t, E) = \text{prob} \quad \{\text{at time} \quad t, E(t) \leq E\}$$

and

$$S(t, E) = 1 - P(t, E) .$$

From the assumptions that we have already made it follows (see, for example, ROSENBLATT [6], § VIb) that the basic Chapman-Kolmogorov equations for a Markov chain take the form

$$\frac{\partial S(t, E)}{\partial t} = -\int_E^1 \lambda(H)\, F(H, E)\, d_H\, S(t, H) \tag{7}$$

and that for given initial conditions, these equations have a unique, differentiable distribution-function solution $S(t, E)$.

Note that in this equation we have assumed (as we clearly can without loss of generality) that for aftershock sequences of the type in which we are interested E can only range over values 0 to 1. We also assume that the initial distribution is at least a measurable function of E. Two types of initial distribution are of particular interest: when the whole distribution is concentrated at 1 (we start observing the system before the first shock occurs): and when the initial distribution is equal to $F(1, E)$ (we start observing the system at the moment of the first shock).

It is clear from equation (7) that for each fixed E in $[0,1]$, $S(t, E)$ is a monotonic decreasing function of E. Before passing on to consider the particular solutions for given choices of the functions $\lambda(E)$ and $f(H, E)$ we can note some general corollaries which follow from the assumptions we have already made and from equation (7).

(i) – It is a consequence of the Markov property that the time spent in a given state E follows an exponential distribution

$$P\ (\text{time at } E \geq t) = e^{-\lambda(E)t} .$$

Since an exponential distribution does in fact give a reasonable fit to the time distribution between aftershocks, this affords at least partial confirmation that the Markov hypothesis may provide a reasonable approximation. However, this hypothesis implies more than an exponential distribution for the interval between aftershocks; for example, it would also imply that successive intervals (corresponding to given levels

E_1 and E_2) were uncorrelated. The question is complicated by the fact that we would expect the parameter of the distribution to change from one shock to the next, so that we should compare time intervals at equivalent points on different aftershock sequences rather than at different stages of the same sequence.

(ii) – If we suppose that $\lambda(E)$ is a monotonic increasing function of E (so that $\lambda(E)$ decreases as E decreases), and that for fixed E, the function $F(H, E)$ is a decreasing function of H (so that $F(H, E)$ increases to 1 as H decreases to E) we readily obtain from equation (7) the estimate

$$S(t, E) \leq e^{-C(E)t},$$

where $C(E) = \lambda(E)\,[1 - F(1, E)]$. It is not difficult to find an exponential bound in the opposite direction, and since it is also evident from (7) that for fixed E, $S(t, E)$ is a monotonic decreasing function of t, we have that *the individual probabilities tend monotonically to zero exponentially fast.*

(iii) – Results of a rather similar nature hold for the moments of $E(t)$ and for the instantaneous shock rate $\mu(t)$. The latter is defined as the limiting ratio of the probability of a shock occurring in the interval $(t, t + h)$, to the length of the interval, h, as h tends to zero. It is clear also that

$$\mu(t) = \int_0^1 \lambda(E)\, d_E\, P(t, E)\,. \tag{8}$$

The quantity $\mu(t)$ is the theoretical analogue of the ratio $\Delta N/\Delta t$ described in section 2.

Taking the shock rate as an example, we obtain from (7), after multiplying by $\lambda(E)$, integrating from 0 to 1, and interchanging the order of integration

$$\frac{d\mu(t)}{dt} = -\int_0^1 [\lambda(E) - \bar{\lambda}(E)]\, d_E\, P(t, E)\,, \tag{9}$$

where $\bar{\lambda}(E) = \int_0^E \lambda(H)\, d_H\, F(E, H)$. If we assume that $\lambda(E)$ and $F(H, E)$ have the same properties as under (ii), then $\bar{\lambda}(E) \leq \lambda(E)$, and it follows from (8) that $\mu(t)$ *is a monotonic decreasing function of* t. Analogous arguments can be used to prove a similar result for the moments of $E(t)$.

It is not in general true, however, that these averages decrease exponentially to zero—indeed, we should hope from the observational results described earlier that their decay was much slower than exponential. If $\lambda(E)$ is bounded away from zero, the shock rate will not even tend to zero, for if $\lambda(E) \geq \varepsilon > 0$, it follows that

$$\mu(t) = \int_0^1 \lambda(E)\, d_E\, P(t, E) \geq \varepsilon \int d_E\, P(t, E) = \varepsilon\,.$$

Thus *a necessary condition for the shock rate to decrease to zero is that* $\lambda(E)$ *tends to zero with* E (we continue to assume that $\lambda(E)$ is monotonic).

(iv) – The remarks we have made so far have all concerned the time distribution of shocks. We can also use the model to provide us with information about the distribution of the *sizes* of the shocks, that is, to provide a theoretical version of the fre-

quency-magnitude law. Since, in a given aftershock sequence, we are concerned not with a sequence of shocks having the same distribution, but with a sequence each member of which has its own distribution, the appropriate analogue to the frequency-magnitude law will be the expected number of shocks in the sequence having a magnitude greater than a given value E, as E varies from 0 to 1. We shall denote this function by $\mathscr{M}(E)$. If we also denote by $P_n(E)$ the probability that the nth aftershock has a magnitude greater than or equal to E, then

$$\mathscr{M}(E) = \sum_1^\infty P_n(E) \,. \tag{10}$$

The quantities $P_n(E)$ and $\mathscr{M}(E)$ can be determined as follows; first we introduce the distribution for the value of $E(t)$ immediately following the nth aftershock, writing

$$F_n(E) = \text{prob. } (E(t) \geq E \text{ immediately following the } n\text{th shock}) \,.$$

Thus $F_n(E)$ is the complement of the distribution function for the value of $E(t)$ immediately following the nth shock. We have $F_1(E) = 1 - F(1, E)$, and

$$F_n(E) = -\int_E^1 [1 - F(H, E)]\, dF_{n-1}(E) \quad (n = 2, 3, \ldots) \,. \tag{11}$$

From this equation, it follows that

$$| F_n(E) | \leq [1 - F(1, E)] \, | F_{n-1}(E) | \leq \cdots \leq [1 - F(1, E)]^n$$

so that the series $\sum_1^\infty F_n(E)$ is uniformly convergent in any interval $0 < \varepsilon \leq E \leq 1$. Next, putting $\theta(E) = \sum_1^\infty F_n(E)$ and summing equation (11) over n, we obtain

$$\theta(E) = -\int_E^1 [1 - F(H, E)]\, d\theta(H) + 1 - F(1, E) \,. \tag{12}$$

(12) is an integral equation of Volterra type, for which it is well-known (PETROVSKY, [10]) that the solution is unique; thus we can identify $\theta(E)$ as the unique solution to the integral equation (12). The final step is to note that

$$P_n(E) = -\int_E^1 F(H, H - E)\, dF_{n-1}(H) \quad (n = 2, 3, \ldots)$$

so that

$$\mathscr{M}(E) = -\int_E^1 F(H, H - E)\, d\theta(H) + P(1, 1 - E) \,. \tag{13}$$

These arguments establish the following rule for determining the theoretical frequency-magnitude law: solve the integral equation (12) for $\theta(E)$, and determine $\mathscr{M}(E)$ from equation (13). It should be noted that the *frequency-magnitude law depends only on the distribution function $F(H, E)$, and is independent of $\lambda(E)$.*

(v) – As a final application of these formulae we can deduce the average distribution of time intervals between successive aftershocks. As we have already mentioned, for a given value of E, this time interval is exponentially distributed with parameter $\lambda(E)$. To obtain the average distribution it is therefore necessary to average this exponential distribution over the different values of E. In particular, we can find in this way $\Psi_n(\tau)$, the probability distribution for the time interval following the nth aftershock. Using the notation of the preceding paragraph, we have

$$\Psi_n(\tau) = \int_0^1 [1 - e^{-\lambda(E)\tau}] \, dF_n(E) \, .$$

Consequently the expected number of intervals in the whole sequence having length less than τ is

$$\Psi(\tau) = \sum_0^\infty \Psi_n(\tau) = \int_0^1 [1 - e^{-\lambda(E)\tau}] \, d\theta(E) \, . \tag{14}$$

Since our assumptions allow for an indefinitely prolonged sequence of shocks, it is possible that this integral may diverge. In general, however, we are interested in the case in which the average time intervals between shocks grow longer and longer, and then the expected number of such intervals with *less* than a given length will usually be finite.

4. – In this and the following section we shall consider the solution of equations (7) and (12) for some special choices of the functions $\lambda(E)$ and $F(H, E)$. In particular, we shall be concerned with the cases $\lambda(E) = k E^\alpha$ and $F(H, E) = (E/H)^\beta$, which might seem wide enough to include most possibilities that could reasonably be obtained as a first approximation to the real process. UTSU [8], Appendix), for example, gives some grounds for supposing $\lambda(E) \propto E^2$, when E is the energy. The solution of equation (7) for these cases has been given by FILIPOV [2] , in a quite different context arising from the study of particle showers, and we shall briefly recapitulate his results, making use of Laplace transforms.

For the sake of concreteness, let us suppose that we start observing the system before the first shock has occurred, so that initially all the probability is concentrated at the point $E = 1$. It is then plausible to suppose (and can easily be verified once the equations have been written down) that the solution consists of a concentration at the point $E = 1$ (representing the probability that the first shock has not yet occurred) and an absolutely continuous part over the interval (0, 1), which we shall suppose to have density function $p(t, E)$. Differentiating (7) with respect to E, we find that the equation for $p(t, E)$ takes the form

$$\frac{\partial p}{\partial t} = -\lambda(E) \, p(t, E) + \int_E^1 \lambda(H) \, f(H, E) \, p(t, H) \, dH + f(1, E) \, \lambda(1) \, e^{-t\lambda(1)} \, , \tag{15}$$

where $f(H, E)$ is the density of the jump distribution $F(H, E)$, and the final term in (15) represents the inflow of probability due to the first shock occurring at time t. Our initial conditions are $p(0, E) \equiv 0$ (E in (0, 1)).

Now introducing the Laplace transform $p^*(s, E) = \int_0^\infty e^{-st} p(t, E)\, dt$, we obtain in place of (14) the integral equation

$$p^*(s, E)\,[s + \lambda(E)] = -\int_E^1 \lambda(H) f(H, E)\, p^*(s, H)\, dH + \frac{\lambda(1) f(1, E)}{s + \lambda(1)}. \tag{16}$$

For the rest of this paragraph, let us concentrate on the special case $f(H, E) = 1/H$ (uniform distribution over 0, H). In this special case the equation can be reduced to an ordinary differential equation by the simple expedient of differentiating with respect to E. We obtain

$$\frac{\partial P^*}{\partial E}\,[s + \lambda(E)] + \left[\frac{\lambda'(E) + \lambda(E)}{E}\right] p^* = 0 \tag{17}$$

with the boundary condition $p^*(s, 1) = \lambda(1)/(s + \lambda(1))^2$. Since (17) is a straightforward first-order differential equation, its solution can always be written down in terms of quadratures, and in the particular case that $\lambda(E) = k\,E^\alpha$ these quadratures can be evaluated explicitly to give

$$p^*(s, E) = k(s + k\,E^\alpha)^{-1-1/\alpha}\,(s + k)^{-1+1/\alpha}. \tag{18}$$

In this case, the transform can also be inverted explicitly by writing $s' = (s + k)/k(1 - E^\alpha)$ and making use of the transform pair $\mathscr{L}\{t^{c-1}\,\Phi(a, c; t) = s^{-c}(1 - s^{-1})^{-a}\}$ (Bateman [1], p. 270, formula (6)), where $\Phi(a, c; t)$ is the confluent hypergeometric function. In this way we obtain finally

$$p(t, E) = k\,t\,e^{-kt}\,\Phi\left(1 + \frac{1}{\alpha}, 2, k(1 - E^\alpha)\,t\right) \tag{19}$$

in conformity with Filipov's result for this special case.

Formula (19) contains all the information that we need concerning the asymptotic time behaviour of the system in this special case. For example, to obtain the shock rate, we can expand the hypergeometric function, substitute in (8), and integrate term by term, the series clearly being uniformly convergent with respect to E. This yields (taking into account also the concentration at $E = 1$)

$$\mu(t) = k\,e^{-kt} \sum_{m=0}^{\infty} \frac{(k\,t)^m}{m!\,(1 + m\,\alpha)} = k\,e^{-kt}\,\Phi\left(\frac{1}{\alpha}, 1 + \frac{1}{\alpha}, k\,t\right)$$

so that for $t \to \infty$,

$$\mu(t) \sim \frac{1}{(\alpha\,t)} \tag{20}$$

(Bateman, p. 278, formula (3)).

In a similar manner, we find for the mean value of E at time t,

$$m_1(t) = \int_0^1 E\, d_E\, P(t, E) = e^{-kt}\,\Phi\left(\frac{1}{\alpha}, \frac{2}{\alpha}; k\,t\right)$$

so that

$$m_1(t) \sim \frac{\Gamma(2/\alpha)}{\Gamma(1/\alpha)}\,(k\,t)^{-1/\alpha}. \tag{21}$$

For the mean release (corresponding to the observed quantity $\Delta E/\Delta t$) we have

$$\left.\begin{aligned} R(T) &= \int_0^1 \lambda(H)\, d_H P(t, H) \int_0^E (H - E)\, d_E F(H, E) \\ &= \frac{1}{2} \int_0^1 H\, \lambda(H)\, d_H P(t, H) \\ &= \frac{1}{2} k\, e^{-kt}\, \Phi\left(\frac{1}{\alpha}, 1 + \frac{2}{\alpha}; k\, t\right) \sim \frac{k}{\alpha} \frac{\Gamma(2/\alpha)}{\Gamma(1/\alpha)} (k\, t)^{-1-1/\alpha} . \end{aligned}\right\} \tag{22}$$

Finally, we can calculate the theoretical frequency-magnitude law and the expected distribution of interval lengths from equations (12) to (14). Substituting $F(H, E) = E/H$ in (12) and differentiating twice with respect to E, we obtain

$$\theta''(E) = - \frac{\theta'(E)}{E}$$

with initial conditions $\theta'(1) = -1$ and $\theta(1) = 0$. Thus $\theta(E) = -\log E$. Then from (13) we have also

$$\mathcal{M}(E) = -\log E \quad (0 < E \leq 1) . \tag{23}$$

and from (14)

$$d\Psi(\tau) = \frac{k}{\alpha} \frac{1 - e^{-k\tau}}{k\, \tau} d\tau . \tag{24}$$

5. – The particular choices of $\lambda(E)$, and more especially of $F(H, E)$, made in the preceding paragraph might seem severely restrictive, but in fact these results can be immediately extended to the wider class of processes where $F(H, E)$ has the form $(E/H)^\beta$ by making a change of variable. Let us write $E = g(\eta)$, and examine the forms of the equations and their solutions when they are written in terms of η rather than E. We shall suppose that $g(.)$ is a monotonic function with a continuous derivative, and write $\pi(t, \eta) = P(t, g(\eta))$, $H = g(\zeta)$. Then the basic equation takes the form

$$\frac{\partial \pi(t, \eta)}{\partial \eta} = - \int_{g(\eta)}^{g(1)} l(\zeta)\, K(\zeta, \eta)\, d_\zeta\, \pi(t, \zeta) ,$$

where $l(\zeta) = \lambda[g(\zeta)]$ and $K(\zeta, \eta) = F[g(\zeta), g(\eta)]$.

It is evident that this is precisely the equation we would obtain from a jump-type process with basic variable η, jump intensity $\lambda[g(\eta)]$ and distribution function for jump size equal to $F[g(\zeta), g(\eta)]$. From the way it has been derived, we can immediately write down the solution to equation (7) and hence obtain all the information we may need concerning the new process. Thus the fundamental solution is simply

$$\pi(t, \eta) = P(t, g(\eta)) = \int_0^{g(\eta)} p(t, E)\, dE .$$

The theoretical shock rate will have the same value as for original system, since

$$\tilde{\mu}(t) = \int_{g(0)}^{g(1)} l(\zeta)\, d_\zeta\, \pi(t, \zeta) = \int_0^1 \lambda(E)\, d_E\, P(t, E) = \mu(t)\,.$$

The new frequency-magnitude distribution can also be obtained without further calculation; we have simply

$$\tilde{\mathcal{M}}(\eta) = \mathcal{M}[g(\eta)]$$

and for the distribution of intervals

$$\tilde{\Psi}(\tau) = \Psi(\tau)\,.$$

On the other hand the expressions for $m_1(t)$ and $R(t)$ will be different, since they depend on which variable we consider to be basic. Thus for $m_1(t)$ we find

$$\tilde{m}_1(t) = \int_{g(0)}^{g(1)} \eta\, d\, \pi(t, \eta) = \int_0^1 g^{-1}(E)\, d_E\, P(t, E)$$

and

$$\tilde{R}(t) = \int_{g(0)}^{g(1)} l(\zeta)\, d_\zeta\, \pi(t, \zeta) \int_{g(0)}^{g(\zeta)} (\zeta - \eta)\, d_\eta\, K(\zeta, \eta)$$

$$= \int_0^1 \lambda(H)\, d_H\, P(t, H) \int_0^H [g^{-1}(H) - g^{-1}(E)]\, d_E\, F(H, E)\,.$$

These substitutions allow us to treat in particular the case $\lambda(E) = k\, E^\alpha$ and $F(H, E) = (H/E)^\beta$. $(\alpha, \beta > 0)$. Taking up the notation of the preceding paragraph, we are here given

$$l(\eta) = k\, \eta^\alpha\,, \qquad K(\zeta, \eta) = (\eta/\zeta)^\beta\,.$$

The problem is to find an exponent α' and a transformation $E' = g(\eta)$ that will enable us to write

$$K(\zeta, \eta) = F[g(\zeta), g(\eta)] = \frac{g(\zeta)}{g(\eta)}$$

and

$$l(\eta) = k[g(\eta)]^{\alpha'}\,.$$

Such a substitution will allow us to describe the system in terms of an associated system where $F(H, E)$ has the simple form E/H, for which explicit solutions have already been obtained.

Evidently, for this purpose we have only to take $g(\eta) = \eta^\beta$ and choose α' so that $\alpha = \alpha'\, \beta$, i.e. $\alpha' = \alpha/\beta$. Then solving for the associated system and resubstituting, we

obtain as our final solutions (for the case $\lambda(E) = k\,E^{\alpha}$ and $F(H, E) = (E/H)^{\beta}$)

$$p(t, E) = k\,t\,e^{-kt}\,\Phi\left(\frac{1+\beta}{\alpha}, 2, k(1-E^{\alpha})\,t\right)\beta\,E^{\beta-1}\,, \tag{19a}$$

$$\mathcal{M}(E) = -\log(E^{\beta}) = -\beta\log E\,, \tag{23a}$$

$$m(t) = k\,e^{-kt}\,\Phi\left(\frac{\beta}{\alpha}, \frac{1+\beta}{\alpha}; k\,t\right) \sim \frac{\beta}{\alpha\,t}\,, \tag{20a}$$

$$m_1(t) = e^{-kt}\,\Phi\left[\frac{\beta}{\alpha}, \frac{(1+\beta)}{\alpha}; k\,t\right] \sim \frac{\Gamma[(1+\beta)/\alpha]}{\Gamma(\beta/\alpha)}\,(k\,t)^{-1/\alpha}\,, \tag{21a}$$

$$R(t) = \frac{k\,e^{-kt}}{1+\beta}\,\Phi\left[\frac{\beta}{\alpha}, \frac{1+(1+\beta)}{\alpha}; k\,t\right]\frac{k\,\Gamma(1/\alpha+\beta/\alpha)}{\Gamma(\beta/\alpha)}\,(k\,t)^{-1-1/\alpha} \tag{22a}$$

$$d\Psi(\tau) = \frac{\beta\,k}{\alpha}\,\frac{1-e^{-k\tau}}{k\,\tau}\,d\tau \sim \frac{\beta}{\alpha\,\tau}\,d\tau\,. \tag{24a}$$

The transformations used above have the following physical interpretation. If we identify E with the energy, it may be that the distribution of jump size is not uniform with respect to energy but with respect to some quantity that can be represented as a function (in this case a simple power) of the energy. Consequently we transform the problem so as to work in terms of this new quantity. After solving this transformed system we make a final transformation back again to again express the solution in terms of energy.

Conclusions

In this paper we have examined a general model for one type of aftershock sequence, and described its more detailed behaviour for some particular choices of the defining functions. In particular, if $\lambda(E) = k\,E^{\alpha}$ and $F(H, E) = (E/H)^{\beta}$ $(\alpha, \beta > 0)$ these results can be summarized as follows (we identify E with the energy).

1. The predicted frequency of aftershock falls to zero as $1/t$, independently of α and β.

2. The mean release falls to zero as $(1/t)^{1+1/\alpha}$, i.e. independently of β. If we follow Utsu by taking $\alpha = 2$, we should then expect the mean energy release to fall to zero as $(1/t)^{3/2}$.

3. The frequency-magnitude law should have the form

$$\mathcal{M}(E) = -\beta\log E_0 - \beta\log E$$

or, expressed in terms of magnitude,

$$\mathcal{N}(M) = \beta[M_0 - M]\,;\ \log\mathcal{N}(M) = \log\beta + \log(M_0 - M)\,,$$

where $\mathcal{N}(M)$ represents the expected number of shocks in the sequence with magnitude greater than M, E_0 represents the total energy initially in the system, and $M_0 = \log E_0$.

4. Individual intervals between shocks are exponentially distributed, while taken over the whole sequence, the expected number of intervals with lengths between $(\tau, \tau + d\tau)$ should be of the form

$$\frac{\beta\,k}{\alpha}\,\frac{1-e^{-k\tau}}{k\,\tau}\,d\tau \sim \frac{\beta}{\alpha\,\tau}\,d\tau\,.$$

Although the model reproduces qualitatively many observed features of aftershock occurrence, there remain some points of sharp difference, In particular the theory does not reproduce the observed Pareto form for the frequency-magnitude law. It predicts a form of this law that falls off more rapidly at high magnitudes and increases less rapidly at low magnitudes than the observed law. Moreover, the observed shock rate often appears to die down more rapidly than the model suggests: at time intervals far from the origin we observe fewer shocks than are predicted. These results are the more surprising because the predicted form of the frequency-magnitude law and the exponent (-1) in the time decay of the shock are both independent of the choice of α and β in the model.

It is possible, of course, that these discrepancies could be removed by a more successful choice of the functions $\lambda(E)$ and $F(H, E)$. The main importance of the model probably lies in the fact that is allows the observed characteristics of aftershock sequences to be referred back to quantities that can be more directly expressed in terms of any particular theory of earthquake mechanism. It would be of particular interest to discover what forms for the functions $\lambda(E)$ and $F(H, E)$ might be suggested by the elastic rebound theory.

Note added in proof

Since this paper was written, Dr. FRANK EVISON has referred me to the survey paper by Dr. KEIITI AKI, 'Some Problems in Statistical seismology' [Zisin *8* (1956) 205] which, in addition to an extensive bibliography, contains a discussion of a Markov model for aftershocks where $N(t)$, the number of shocks up to time t, plays the role of $E(t)$ in our paper. This model also leads to a power law for the frequency of aftershocks, but of course it cannot be used to discuss energy relations. I should like to thank Dr. EVISON for bringing this paper to my notice, and Dr. AKI for providing me with a copy of the English translation.

REFERENCES

[1] H. BATEMAN, *Higher transcendental functions*, Vol. *1* (Ed. P. Erdelyi et al., New York, 1953).
[2] A. F. FILIPOV, *On the distribution of the sizes of particles which undergo splitting*, Teoriya Veroyatnostei *6* (1961), 275.
[3] B. GUTENBERG and C. F. RICHTER, *The seismicity of the earth* (Princeton, 1954).
[4] K. MOGI, *On the time distribution of aftershocks accompanying the recent major earthquakes in and near Japan*, Bull. Earthquake Res. Inst. Tokyo University *40* (1962), 107.
[5] F. OMORI, *On the aftershocks of earthquake*, J. Coll. Science Imp. Univ. Tokyo, Japan *7* (1894), 111.
[6] M. ROSENBLATT, *Random processes* (Oxford 1962).
[7] J. STEINDL, *Random processes and the growth of firms — a study of the Pareto Law* (London, 1965).
[8] T. UTSU, *A statistical study on the occurrence of aftershocks*, Geophys. Mag. (Tokyo) *30* (1961). 521.
[9] D. VERE-JONES and R. DAVIES, *A statistical survey of earthquakes in the main seismic region of New Zealand*, Part II: *Time series analysis* (To appear in N. Z. J. Geol. and Geophysics 1966).
[10] I. G. PETROVSKII, *Lectures on the theory of integral equations*, English ed., (Graylo Press, Rochester NY 1957).

(Received 9th May 1966)

Aftershock Sequence of Alaskan Earthquake of 28th, March 1964

By R. K. S. CHOUHAN[1])

Summary – The aftershock sequence of Alaskan earthquake has been studied following the creep theory of aftershocks by BENIOFF. In this sequence the recovery consists of two linear segments of compressional elastic creep type and the duration of activity is about 24 days. The ratio of the total elastic strain rebound increments of aftershocks to the principal shock was 0.24 and their energy ratio released as seismic waves was 0.004. Therefore 2% of the total strain energy stored in the creep elastic element was used as seismic waves and rest, lost as heat. In dual type recovery, where compression is followed by shear, shows 6 to 8% of total energy used as seismic waves. Hence major portion of seismic wave energy is due to shear type of recovery.

1. Introduction

On March 28, 1964, at 03 h 36 min 12.7 sec GMT, northwestern Alaska was rocked by an earthquake of high intensity. The epicentre of this shock was at (61.1°N, 147.6°W) at a distance of about 22 km from Anchorage and the magnitude of this shock as estimated by USCGS was 8.5. The earthquake caused tidal waves and inundation of parts of Alaskan coast.

This earthquake was one of the largest which has occurred in the North American continent during the twentieth century. It appears that because of two main factors viz the distance of the epicentre and the nature of the sub-soil (sand and gravel with underlaying clays) the short period earthquake waves were filtered out and the longer period ground motions were predominant. The result of these conditions was that most of the tall buildings in Anchroage were significantly damaged, while in general the small area rigid masonry were undamaged.

2. Aftershock sequence of Alaskan earthquake

Following creep theory of aftershocks by BENIOFF [2][2]), the aftershock sequence of Alaskan earthquake has been studied (Appendix 1). The times t of the aftershocks are measured in days from the origin time of the principal shock which is 28th March 1964 at 03 h 36 min 12.7 sec GMT. For any particular aftershock $S = \Sigma J^{1/2}$ for the shocks which occurred in the interval begining with the first aftershock and ending

[1]) School of Research and Training in Earthquake Engineering, University of Roorkee, Roorkee, UP, India.

[2]) Numbers in brackets refer to References, page 48.

with that particular shock. Here $J^{1/2}$ is the elastic strain rebound times a constant. For computation of S i.e. $\Sigma J^{1/2}$ the magnitude energy relation given by GUTENBERG and RICHTER [6] has been used according to which

$$\log J = 11.4 + 1.5\,M \quad \text{or} \quad J^{1/2} = 10^{5.7+0.75M} \tag{1}$$

where M is the magnitude of the shock.

Table 1

The aftershock sequence of Alaskan earthquake of 28th March 1964 at 03 h 36 min 12.7 sec GMT

Date	'0'-Time	t in days	M magnitude	$J^{1/2}$ in $(\text{ergs})^{1/2} \times 10^{10}$	$\Sigma J^{1/2}$ in $(\text{ergs})^{1/2} \times 10^{10}$	Ji in ergs $\times 10^{20}$
1	2	3	4	5	6	7
28 March 1964	12 h 20 min 49.8 sec	0.364	6.5	3.76	3.76	14.1
28 March 1964	14 h 47 min 37.1 sec	0.467	6.0	1.59	5.35	2.5
28 March 1964	20 h 29 min 08.6 sec	0.704	6.1	1.88	7.23	3.55
29 March 1964	06 h 04 min 46.5 sec	1.103	5.8	1.12	8.35	1.26
29 March 1964	09 h 38 min 29 sec	1.250	5.2	0.40	8.75	0.15
30 March 1964	02 h 18 min 06.3 sec	1.945	6.2	2.24	10.99	5.02
30 March 1964	07 h 09 min 34 sec	2.148	5.9	1.33	12.32	1.78
30 March 1964	16 h 09 min 28.4 sec	2.523	5.6	0.80	13.12	0.63
3 April 1964	22 h 33 min 42.2 sec	6.790	6.1	1.88	15.0	3.55
4 April 1964	04 h 54 min 01.7 sec	7.068	5.8	1.12	16.12	1.26
4 April 1964	08 h 40 min 29.8 sec	7.221	5.7	0.94	17.06	0.89
4 April 1964	17 h 46 min 08.6 sec	7.590	6.1	1.88	18.94	3.55
5 April 1964	01 h 22 min 13.3 sec	7.908	5.8	1.12	20.06	1.26
5 April 1964	19 h 28 min 18.1 sec	8.662	6.1	1.88	21.94	3.55
12 April 1964	01 h 34 min 11.2 sec	13.910	6.0	1.59	23.53	2.50
15 April 1964	15 h 30 min 47 sec	18.496	5.9	1.33	24.86	1.78
16 April 1964	19 h 26 min 57.4 sec	19.640	5.9	1.33	26.19	1.78
18 April 1964	17 h 06 min 11.5 sec	21.513	5.3	0,47	26.66	0.22
18 April 1964	20 h 16 min 16.3 sec	21.695	5.2	0.40	27.06	0.15
20 April 1964	11 h 56 min 41.6 sec	23.347	6.1	1.88	28.94	3.55
					$\Sigma J^{1/2}$ 2.9 $\times 10^{11}$	ΣJ 5.3 $\times 10^{21}$

Figure 1 represents a graph of $S = \Sigma J^{1/2}$ in the semi-log paper as a function of time in days measured from the origin time of the principal earthquake. The aftershock sequence of the Alaskan earthquake is given in table 1. The value of $J^{1/2}$ for each aftershock is represented by a circle having a diameter related to the magnitude as shown in the legend of figure 1. It will be noted that the dots fall on two linear segments. First segment begins with the first aftershock at $t = 0.364$ days and continues up to 1.945 days. This segment is calculated from the equation

$$S_1 = (8.0 + 7.7 \log t)\, 10^{10} \tag{2}$$

which represents a compressional elastic creep strain as defined by GRIGGS. According to him for compressional strains in rock samples having elastic creep characteristics the equation.

$$\xi = a + b \log t \tag{3}$$

represents the data accurately, where ξ is the creep strain a and b are constants and t is time in days.

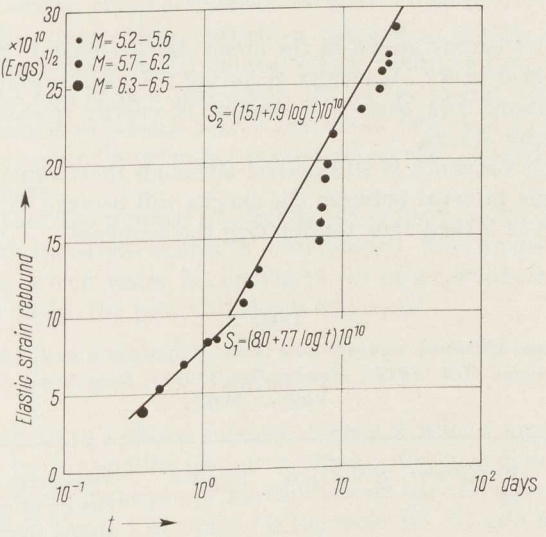

Figure 1
Accumulated elastic rebound increments (times k) of Alaskan earthquake aftershock sequence

However, the increments S have been derived from the square root of the energy, their signs are indeterminante. Thus, it is impossible from these measurements alone to distinguish between forward creep and creep strain recovery. But in this case the creep is one of recovery.

The second phase in the sequence begins at $t = 2.148$ days and continuous up to 23.347 days. The second segment can be represented by the equation:

$$S_2 = (15.1 + 7.9 \log t)\ 10^{10} \tag{4}$$

which is similar to (2) representing compressional elastic creep recovery without shear. The second phase begins with relatively large aftershock which occurred 2.148 days from the origin of the principal shock. The existence of the two segments must be associated in some manner with the mechanism of faulting. Perhaps it indicates an increase in the active area of faulting at the moment the rate changed.

3. Comparative study of energy in the elastic element and elastic creep element

The total accumulated elastic strain rebounds (times K) for the sequence up to 20th April 1964 was $2.9 \cdot 10^{11}$ (ergs)$^{1/2}$ and in the principal it was $1.2 \cdot 10^{12}$ (ergs)$^{1/2}$, the

ratio of the two being $S/J_0^{1/2} = 0.24$. Hence at the time of principal earthquake the creep elastic strain of the fault rock was at least one fourth as large as the elastic strain (see appendix). The seismic wave energy released in the aftershocks and the principal earthquake were $5.3 \cdot 10^{21}$ ergs and $1.4 \cdot 10^{24}$ ergs respectively. The ratio of the aftershock energy to the principal was 0.004. Hence the conversion efficiency of the mechanism is

$$\frac{0.004}{0.24} = 0.017 .$$

Thus of the total energy stored in the creep elastic element, 98% or $3.4 \cdot 10^{23}$ ergs was dissipated as heat in *R2* (Appendix 1) during the twenty four days of aftershock activity. This is about 0.41 times the amount of energy released by the principal earthquake as seismic waves.

Presumably this sequence is still active, although there must eventually come a time when the time interval between the shocks will become so large that the fault becomes cemented or locked thus terminating the sequence.

Table 2

Comparison of Alaskan aftershock sequence with those of BENIOFF's *study of aftershock sequences of Nevada (1932), Signal Hill (1933), Hawkes Bay (1931), Long Beach (1933) and Imperial Valley (1940)*

Principal earthquake	Magnitude M	$R = \Sigma J_i/J_0$	$S/(J_0)^{1/2}$	Percentage energy of creep elastic element released as Seismic waves	Heat	Type of recovery
1. Alaskan earthquake 28 March 1964	8.5	0.004	0.23	2	98	Solely compressional creep strain recovery with one or two linear segments
2. Nevada earthquake 20 December 1932	7.2	0.007	0.45	2	98	
3. Signal Hill earthquake 2 October 1933	5.4	0.011	0.55	2	98	
4. Hawkes Bay earthquake 3 February 1931	7.6	0.06	0.74	8	92	Compressional creep recovery followed by a shear creep recovery
5. Long Beach earthquake 10 March 1933	6.25	0.13	2.3	6	94	
6. Imperial Valley earthquake 18 May 1940	6.7	0.028	0.47	7	93	

4. Conclusion

The duration of the aftershock sequence in the present case is about 24 days and the magnitude of the principal shock is 8.5. Benioff's observations showed that earthquakes with magnitude as low as 5.4 showed aftershock activity of about one hundred days. Hence it is quite clear that there exists no relation between the magnitude of the principal shock and aftershock duration.

Considering the phases of recovery table 2 shows that in case of dual type recovery where compressional elastic creep is followed by shear creep recovery about 6 to 8% of energy stored in the creep elastic element is released as seismic waves and about 92 to 94% is dissipated as heat. But if the recovery is solely compressional creep type, though there may be two phases only about 2% of the energy stored in the creep elastic element is released as seismic waves and about 98% lost as heat. Thus shear component of recovery contributes major portion of energy released as seismic waves in an aftershock sequence.

The author feels that the number of aftershocks depend on the number of nuclei of strains about which the strain energy is accumulated, thus nuclei of strains act as hygroscopic nuclei on which water is condensed. In other words it depends on the seismicity of an area where the principal shock will occur.

5. Appendix 1

In accordance with REID's elastic rebound theory it will be assumed that earthquakes are produced by the sudden release of energy stored as elastic strain in rock masses of a fault. The earthquake producing mechanism may then be represented by a circuit diagram shown in figure 2 in which *f* is the fault. *G1*, *G2* and *R2* are the elastic and creep elements of the fault rock, *F* is the earthquake generating stress (assumed constant) and *R1* is a secular resistive element which is characteristic of the medium and which with *F* determines the rate of strain accumulation.

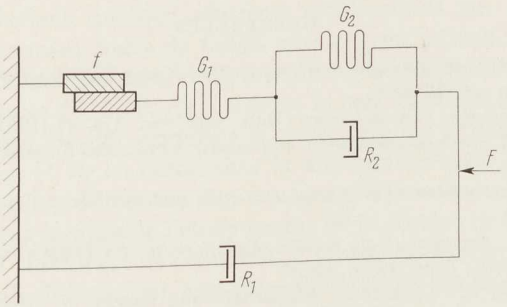

Figure 2

Starting from a released state of *G1* and *G2* the system *G1*, *G2*, *R1*, *R2* is slowly compressed at a rate determined mainly by *F*/*R1*. The elastic compression of *G1* and *G2* exerts a stress on the fault *f* which increases at a secular rate until the moment when the stress at some point along the fault exceeds the cohesive strength of the fault and thus initiates slippage at a particular point. This in turn increases the stress at neighbouring points and thus a faulting movement is propagated along the length

of the fault with a velocity less than that of compressional wave velocity. Once, movement has begun the static friction of the fault changes to much smaller value and slipping continuous until the elastic strain of *G1* is completely reduced to zero. In the short internal of fault motion which is less than 2 minutes the elements *R1* and *R2* are unable to respond appreciably, and consequently at the conclusion of the fault movement *G2* remains fully strained. The energy of the principal shock is thus derived from the quick acting element *G1*. Let us assume that immediately after the fault comes to rest the surfaces again become locked by virtue of the increased static friction, but as a results of reduced normal stress and cementing the threshold value of stress required to initiate motion is less than that which gives rise to the principal earthquake. With the release of *G1* the full stress of the compressed *G2* is effective across the frictional element *R2* and, therefore, produces a strain recovery of *R2* and *G2* with a rate which starts at maximum and decreases thereafter. As a result of high friction of *R1* its movement is too slow to be effective except over long intervals of time and consequently movement of the elements *G2* and *R2* produces a compression of *G1* which increases with time. Locking of the fault after the elastic release of *G1* during the earthquake thus provides a strain restraint. Consequently the resulting compression of *G1* symbolises the relaxation stress of the fault rock. This stress exerts a force on the fault which increases with time. When this force increases to a value such that the stress at some point on the fault exceeds the local frictional strength, the fault slips again and thus generate the first aftershock. When the slipping movement ceases, the fault locks again and relaxation process is repeated resulting in a sequence of aftershocks. Fault locking friction determines the size of an aftershock.

6. Acknowledgements

The author is greatful to Dr. V. K. Gaur for discussions from time to time and to Dr. Jai Krishna for extending the facilities to work in the School.

References

[1] M. Bath and H. Benioff, *The aftershock sequence of Kamachatka earthquake of 4 November 1952*, Bull. Seis. Soc. Am. *48* (1958) 1.

[2] H. Benioff, *Earthquakes and rock creep*, Bull. Seis. Soc. Am. *41* (1951), 31.

[3] H. Benioff, *Global strain accumulation and release as revealed by great earthquakes*, Bull. Geol. Soc. Am. *62* (1951), 331.

[4] H. Benioff, *Seismic evidence for crustal structure and tectonic activity*, Geol. Soc. Am. spec. paper *62* (1952), 61.

[5] R. K. S. Chouhan, *Regional strain release characteristics for Indian regions*, under publication in Bull. Seis. Soc. Am. June (1966), issue.

[6] B. Gutenberg and C. F. Richter, *Magnitude and energy of earthquakes*, Ann. Geofis. *9* (1956), 1.

(Received 7th April 1966)

Propagation des ondes *Li*, *Lg* et *Rg* à travers la mer Egée

Par Snejina M. Rijikova[1])

Summary – The effective propagation of *Li*, *Lg* and *Rg* waves across Aegean sea was established. It shows that the basin has the continental structure and that the orogenic area of Aegean sea doesn't influence on the continental waves transmition. There were obtained the mean *Li*, Lg_1, Lg_2 and *Rg* velocities in Aegean sea respectively 3.80, 3.57, 3.32 and 3.03 km/sec.

Pendant ces dernières années on utilise presque uniquement la manifestation des ondes séismiques *Li*, Lg_1, Lg_2 et *Rg*, pour étudier la structure de l'écorce terrestre et, en particulier, pour définir la séparation de l'écorce en structure océanique et continentale.

La propriété la plus importante de ces ondes qui les rend surtout utiles pour l'étude de la structure de la croûte terrestre consiste en ce qu'elles ne se propagent que sur une structure continentale ininterrompue.

Nous avons supposé qu'il serait intéressant d'étudier les trajectoires de *Li*, Lg_1, Lg_2 et *Rg* à travers la mer Egée afin de prouver la structure continentale de ce bassin qui se trouve à proximité immédiate du bassin à structure océanique de la Méditerranée. D'autre part, Fr. Press démontre dans [4] que quand *Lg* traversent la zone orogénique de Californie il ne résulte pas de changements dans la vitesse ou dans l'intensité des oscillations quoique plusieurs publications sur ces ondes émettent l'opinion que de puissantes zones de failles auraient pu influencer leur propagation.

En rapport avec cela il est aussi d'un intérêt considérable d'étudier les vitesses et les trajectoires des ondes *Li*, *Lg* et *Rg* à travers la mer Egée qui est une vaste zone de failles. Dans ses études [3] Pec renferme la zone Egéenne dans les trajectoires européennes des ondes Lg_1 et *Rg* en établissant la non-homogénéité dans leur manifestation. D'autre part, il n'a pas la possibilité de separer leurs vitesses, en ce qui concerne la mer Egée, seulement à cause de l'éloignement de la station de Prague.

Le but de présent travail est de comparer la vitesse de *Li*, Lg_1, Lg_2 et *Rg* à travers la mer Egée (la zone de dislocation), aux vitesses obtenues par des autres auteurs pour des trajets complètement transcontinentaux et d'établir un bon passage des ondes à travers la mer Egée.

La difficulté est due à ce que les distances foyer-station sont très petites, et qu'il y a des erreurs importantes dans la détermination de la vitesse de ces ondes à cause du manque de certitude dans les données épicentrales. Ces erreurs augmentent avec la

[1]) Institut de Geophysique, Academie des Sciences de Bulgarie, Sofia.

[2]) Les chiffres entre crochets renvoient à la bibliographie, page 51.

diminution de la longueur du trajet de la propagation. Nous avons essayé de les compenser en prenant un grand nombre de données et en cherchant les déterminations les plus exactes de paramètres épicentraux.

Nous avons utilisé les paramètres publiées dans 'International Seismological Summary' (ISS) et pour les tremblements de terre qui ont eu lieu après 1959 – ceux publiés par l'USCGS.

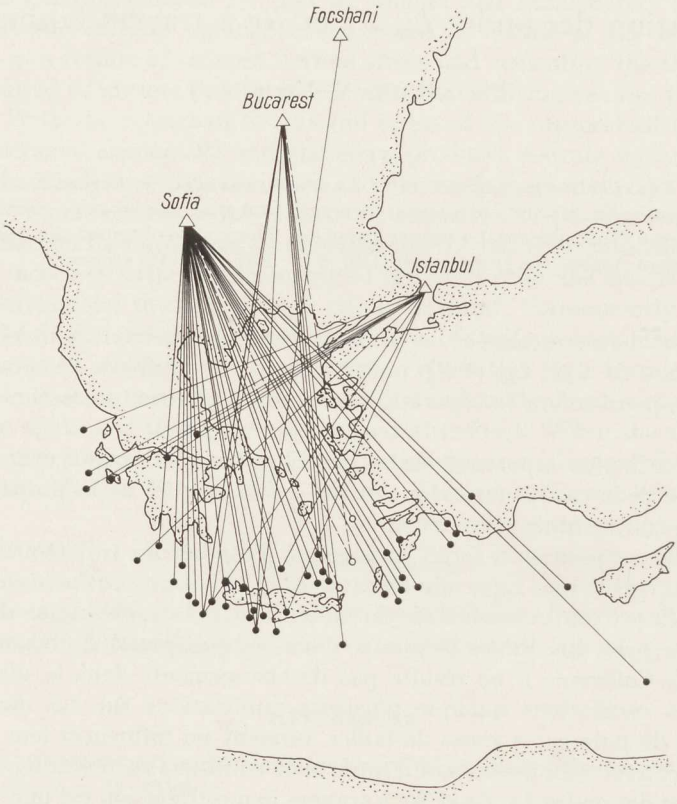

Figure 1

Notre matériel d'observation représente les enregistrements de Sofia et quelques autres de Roumanie et d'Istambul de 50 séismes de Grèce, de la Crète, de Dodécanèse et d'Asie Mineure. Les foyers des séismes sont choisis d'une manière telle que les trajets de leur propagation traversent la mer Egée dans toutes les directions (figure 1). Les enregistrements de Sofia sont effectués à l'aide du séismographe Wiechert à deux composantes horizontales d'une période de 9 sec en moyen. Les séismogrammes de Bucarest et Focshani sont obtenus par des séismographes mécaniques aux périodes moyennes 10 sec et 3.5 sec respectivement et par le séismographe Golizine de période moyenne 12 sec. Les données d'Istambul sont obtenues à l'aide des séismographes type Haguivara de courte et de longue périodes.

La figure 1 donne les phases enregistrées de *Li*, Lg_1, Lg_2 ou *Rg* presque dans tous les cas. Sur les 66 enregistrements il y a quatre cas d'absence complète de ces ondes.

Les vitesses moyennes de la propagation, déterminées pour tous les trajets qui sont démontrées sur la figure 1 sont: 3.80 ± 0.07 pour *Li*; 3.57 ± 0.06 pour Lg_1, 3.32 ± 0.07 pour Lg_2 et 3.03 ± 0.05 pour *Rg*.

Les données citées ici se distinguent par des vitesses obtenues pour l'Europe par BÅTH, PEC et SAVARENSKI-VALDNÈRE [1, 3, 5] tout au plus de trois pour-cent. Cette petite différence confirme que la structure orogénique de la mer Egée n'a pas d'influence sur les vitesses des ondes en question, mais pour les petites distances telles que les trajets examinés, la vitesse est égale à celles des distances supérieurs à 50–60°.

Les périodes observées des ondes étudiés ne différent non plus des périodes obtenues par les auteurs susmentionnés pour les trajets à travers l'Europe et l'Asie et les grandes distances épicentrales. Pour les périodes moyennes nous avons obtenu: *Li* = 6.1 sec, Lg_1 = 5.2 sec, Lg_2 = 5.0 sec et *Rg* = 6.5 sec.

Parmi les 66 enregistrements il n'y avait que quatre sans les manifestations de ces ondes. Cela probablement est dû plutôt aux singularités du foyer qu'à l'amortissement des ondes sur leur trajet. Dans tous les autres cas *Li*, *Lg* et *Rg* sont nettement enregistrées ce qui confirme la structure continentale de l'écorce terrestre au-dessous du bassin de la mer Egée.

BIBLIOGRAPHIE

[1] M. BÅTH, *The elastic waves Lg and Rg along Euroasiatic paths*, Arkiv. f. Geofys. *2* (1954), No. 13.
[2] M. BÅTH, *A continental channel wave guided by the intermediate layer in the crust*, Geof. pura e appl. *38* (1957), 19.
[3] K. PEC, *Continental waves in central Europe*, Geofysikálni Sbornik (1961), 146.
[4] F. PRESS, *Velocity of Lg waves in California*, Trans. Amer. Geophys. Union *37* (1956), 5.
[5] E. F. SAVARENSKII and N. G. VALDNER, *Volni Lg i Rg ot semletrasenii Tshernomorskogo baseina i nekotorie soobrajenia ob ich prirode*, Jsv. AN. SSSR, Seismitcheskie issledovanija (1960), 4.

(Reçu le 6 juin 1966)

On the Theory of Depositional Remanent Magnetization in Sediments

By Peter B. Nozharov[1])

Summary – A more precise solution of equation, describing process of orientation of isometric ferromagnetic particles at their deposition in liquid under influence of external homogeneous magnetic field is presented. It is shown, that this moreprecise investigation of the problem doesn't lead to qualitative new results for describing processes of particles orientation, than that given by T. Nagata.

During the last years the problem of origin and stability of remanent magnetization in sedimentary rocks has assumed great significance for paleomagnetism.

The mechanism of formation of depositional remanent magnetization (DRM) of sediments according to recent ideas is following. The small ferromagnetic particles from the destroyed rocks after their translation by the transportation agents (water, wind or ice) to the great water basins settle in them together with other amagnetic particles.

The ferromagnetic particles tend to orient their magnetic moments in the direction of earth's magnetic field acting during the sedimentational processes. The degree of this orientation depends on number of factors, as the intensity of earth's magnetic field, the size of particles's magnetic moment, their shape and size, character of bottom, the depth and hydrodynamical regime of water basin. During the dehydration and hardening of sediment, the orientation of ferromagnetic particles becomes stronger, which determines arising of the summary vector of remanent magnetization coinciding in direction with that of earth's magnetic field acting during the sedimentational process.

The first and most simple theoretical model of origin of remanent magnetization of sediments was suggested by T. Nagata [3]. Later this model was developed in [4] and [2].

We give in this paper a further precisation of Nagata's model.

Let us examine sedimentation of a spherical particle of mass m, radius r and magnetic moment M in still water basin with depth h. We suppose, that the radius of the particle is such, that its motion in the liquid is of Stockes' type. We neglect in this case the influence of Brownian motion. According [2] these conditions are satisfied by particles of radius $r > 10^{-5}$ cm.

---

[1]) Geophysical Institute, Bulgarian Academy of Science, Sofia, Bulgaria.

[2]) Numbers in brackets refer to References, page 58.

The motion of the particle in liquid is sum of its translatory motion downward under gravity and of its rotation in the vertical plane. If we direct axis z vertically down and θ is the angle formed by the direction of magnetization of the particle and that of the applied field, the equations of motion are:

$$m \frac{d^2z}{dt^2} = m g - 6 \pi \mu r \frac{dz}{dt}, \tag{1}$$

$$I \frac{d^2\theta}{dt^2} = - 8 \pi \mu r^3 \frac{d\theta}{dt} - M H \sin\theta, \tag{2}$$

where $g \equiv$ acceleration due to gravity; $\mu \equiv$ coefficient of viscosity; $H \equiv$ intensity of applied magnetic field; $I \equiv$ the moment of inertia of a particle about an axis through the center—in case of sphere $I = 2/5\, m r^2$.

We solve equations (1) and (2) under the following initial conditions:

$$\left.\begin{aligned} z(0) &= 0, \quad \theta(0) = \theta_0, \\ \left(\frac{dz}{dt}\right)_{t=0} &= 0, \quad \left(\frac{d\theta}{dt}\right)_{t=0} = 0. \end{aligned}\right\} \tag{3}$$

The solution of equation (1) under the conditions (3) is given by the expression:

$$z = \frac{m}{6 \pi \mu r} g t + \frac{m^2}{36 \pi^2 \mu^2 r^2} g \left[e^{-(6\pi\mu r/m)t} - 1\right]. \tag{4}$$

If the depth of water basin is h then from formula (4) we can determine the necessary time for the descent of the particle to the bottom:

$$t \approx \frac{6 \pi r \mu h}{m g}. \tag{5}$$

It is not possible to find the exact solution to the second equation (2), but it is possible to examine the behaviour of the solution by qualitative methods.

We change the variable

$$\frac{d\theta}{dt} = u$$

and we obtain

$$u \frac{du}{d\theta} = - \frac{8 \pi \mu r^3}{I} u - \frac{M H}{I} \sin\theta. \tag{6}$$

The equation (6) has the singular points $(0, 0)$ and $(0, \pi)$. We are interested in behaviour of the solution in the neighbourhood of the singular point $(0, 0)$ (the singular point $(0, \pi)$ is saddle point). According [5] we have the following three cases:

a) at $\left(\frac{8 \pi \mu r^3}{I}\right)^2 > 4 \frac{M H}{I}$

the singular point is a stable knot. This means, that the equation hasn't periodical solutions, when the coefficient before the second member in equation (2) is a great one. At $t \to \infty$ we have $\theta(t) \to 0$.

b) at $\left(\frac{8 \pi \mu r^3}{I}\right)^2 = 4 \frac{M H}{I}$

the singular point is also a stable knot and the solution of (2) is aperiodical.

c) $$\text{at} \quad \left(\frac{8\pi\mu r^3}{I}\right)^2 < 4\,\frac{MH}{I}$$

the singular point is a stable focus. This means that equation (2) has a solution which describes damped out oscillation process. At $t \to \infty$ we have also $\theta(t) \to 0$.

As it is shown in [2] we have nearly always case a) in sedimentation of ferromagnetic particles in liquid. That is why we will try to find a solution to the equation (2) only in this case.

The equation (2) can be given in following form:

$$\frac{d^2\theta}{dt^2} + \frac{8\pi\mu r^3}{I}\,\frac{d\theta}{dt} + \frac{MH}{I}\sin\theta = 0\,. \tag{2'}$$

We make the following change of variable

$$t = \frac{8\pi\mu r^3}{MH}\,\tau \tag{7}$$

and we denote

$$\alpha = \frac{8\pi\mu r^3}{\sqrt{MHI}}\,.$$

We obtain:

$$\frac{1}{\alpha^2}\,\frac{d^2\theta}{d\tau^2} + \frac{d\theta}{d\tau} + \sin\theta = 0\,. \tag{8}$$

If $\alpha^2 \gg 1$, then equation can be solved by methods of small parameter [1].

We put

$$\frac{1}{\alpha^2} = \lambda \ll 1\,; \quad \frac{d\theta}{d\tau} = u$$

and we obtain the system:

$$\left.\begin{aligned} \frac{d\theta}{d\tau} &= u\,, \\ \lambda\,\frac{du}{d\tau} &= -u - \sin\theta\,. \end{aligned}\right\} \tag{9}$$

The initial conditions (3) take the form

$$\theta(0) = \theta_0\,; \quad u(0) = 0\,.$$

We assume that the solution $\theta(\tau, \lambda)$ for enough small λ has the form

$$\theta(\tau, \lambda) \approx \theta(\tau, 0) + \lambda\,\frac{\partial\theta(\tau, 0)}{\partial\lambda}\,.$$

Putting $\lambda = 0$ in (9) we obtain:

$$\left.\begin{aligned} u(\tau, 0) &= -\sin\theta(\tau, 0)\,, \\ \frac{d\theta(\tau, 0)}{d\tau} &= -\sin\theta(\tau, 0)\,. \end{aligned}\right\} \tag{10}$$

We find the function $\partial\theta(\tau, 0)/\partial\lambda$ from following equations:

$$\left.\begin{aligned} \frac{d\theta_\lambda(\tau, 0)}{d\tau} &= u_\lambda(\tau, 0)\,, \\ \frac{du(\tau, 0)}{d\tau} &= -u_\lambda(\tau, 0) - \theta_\lambda(\tau, 0)\cos\theta(\tau, 0)\,, \end{aligned}\right\} \tag{11}$$

where

$$\frac{\partial u}{\partial \lambda} = u_\lambda ; \quad \frac{\partial \theta}{\partial \lambda} = \theta_\lambda .$$

The initial condition which must be satisfied by the function $\theta_\lambda(\tau, 0)$ at $\tau = 0$ is

$$[\theta_\lambda(\tau, 0)]_{\tau=0} = \int_0^{-\sin\theta(0,0)} \frac{u + \sin\theta(0, 0)}{-u - \sin\theta(0, 0)}\, du = \sin\theta_0 . \tag{12}$$

If the so found function $\theta_\lambda(\tau, 0)$ has order of magnitude 1, then the basic solution $\theta(\tau, 0)$ with error less than λ, coincides with the exact solution and can be used to describe the process.

We find from the system (10)

$$\frac{d\theta(\tau, 0)}{\sin\theta(\tau, 0)} = -\, d\tau ,$$

$$\ln \operatorname{tg} \frac{\theta(\tau, 0)}{2} = -\tau + \tau_0 ; \quad \tau_0 = \ln \operatorname{tg} \frac{\theta_0}{2}$$

and finally

$$\operatorname{tg} \frac{\theta(\tau, 0)}{2} = \operatorname{tg} \frac{\theta_0}{2}\, e^{-\tau} \tag{13}$$

i.e. we obtain the solution of T. NAGATA [3]. From the preceding it follows that we can neglect the member $I(d^2\theta/dt^2)$ in equation (2), only if the coefficient before the second member is very great or the product $M\,H\,I$ is very small.

To determine the function $\theta_\lambda(\tau, 0)$ we eliminate the function $u_\lambda(\tau, 0)$ from the system (11) and using (10) we obtain:

$$\frac{d\theta_\lambda(\tau, 0)}{d\tau} + \theta_\lambda(\tau, 0) \cos\theta(\tau, 0) = -\sin\theta(\tau, 0) \cos\theta(\tau, 0) . \tag{14}$$

From (13) we determine $\cos\theta(\tau, 0)$ and $\sin\theta(\tau, 0)$ and replace them in (14). We obtain a linear differential equation of first order with the initial condition

$$[\theta_\lambda(\tau, 0)]_{\tau=0} = \sin\theta_0 .$$

The solution if of the form

$$\theta_\lambda(\tau, 0) = \frac{2 \operatorname{tg} \frac{\theta_0}{2}\, e^{-\tau}}{1 + \operatorname{tg}^2 \frac{\theta_0}{2}\, e^{-2\tau}} \left[1 - \tau + \ln \frac{1 + \operatorname{tg}^2 \frac{\theta_0}{2}}{1 + \operatorname{tg}^2 \frac{\theta_0}{2}\, e^{-2\tau}} \right] . \tag{15}$$

To solve the equation (8) we get

$$\theta(\tau, \lambda) = 2 \operatorname{arc\,tg} \left(\operatorname{tg} \frac{\theta_0}{2}\, e^{-\tau} \right) + \lambda \frac{2 \operatorname{tg} \frac{\theta_0}{2}\, e^{-\tau}}{1 + \operatorname{tg}^2 \frac{\theta_0}{2}\, e^{-2\tau}} \left[1 - \tau + \ln \frac{1 + \operatorname{tg}^2 \frac{\theta_0}{2}}{1 + \operatorname{tg}^2 \frac{\theta_0}{2}\, e^{-2\tau}} \right] .$$

From (7) we have

$$\tau = \frac{M H}{8 \pi \mu r^3} t; \quad \lambda = \frac{M H I}{(8 \pi \mu r^3)^2}$$

and replace this in above equation. Finally:

$$\left.\begin{aligned} \theta\left[t, \frac{M H I}{(8 \pi \mu r^3)^2}\right] &= 2 \operatorname{arctg}\left[\operatorname{tg} \frac{\theta_0}{2} \exp\left(-\frac{M H}{8 \pi \mu r^3} t\right)\right] \\ &+ \frac{M H I}{64 \pi^2 \mu^2 r^6} \frac{2 \operatorname{tg} \frac{\theta_0}{2} \exp\left(-\frac{M H}{8 \pi \mu r^3} t\right)}{1 + \operatorname{tg}^2 \frac{\theta_0}{2} \exp\left(-\frac{2 M H}{8 \pi \mu r^3} t\right)} \\ &\times \left[1 - \frac{M H}{8 \pi \mu r^3} t + \ln \frac{1 + \operatorname{tg}^2 \frac{\theta_0}{2}}{1 + \operatorname{tg}^2 \frac{\theta_0}{2} \exp\left(-\frac{2 M H}{8 \pi \mu r^3} t\right)}\right]. \end{aligned}\right\} \tag{16}$$

At $t \to \infty$ the solution tends to 0. It is possible to show that the solution $\theta_\lambda(\tau, 0)$ tends to 0 faster than the solution $\theta(\tau, 0)$, which means that the solution (16) can be used for describing the process of particles' orientation at $t > 0$.

If

$$\frac{M H I}{64 \pi^2 \mu^2 r^6} \to 0 ,$$

then the solution (16) tends on the solution (13) derived by T. NAGATA [3].

The solution (16) shows, that if the time of sedimentation is great, i.e. the depth of water basin is great, then the particle orientates completely its magnetic moment in direction of applied magnetic field. Knowing parameters of a particle r, M and m and the external magnetic field H, it is possible from (16) to calculate the time necessary for orientation of the particle in the interval of errors of paleomagnetic investigation.

Let us suppose that a great number N identical spherical particles deposit having random distribution of remanent magnetization's vector at $t = 0$.

Than the general effective magnetic moment of formed on bottom sediment at $z = h$ can be obtained from the formula:

$$J_n = \frac{N M}{\pi} \int_0^\pi \cos\theta \, d\theta_0 , \tag{17}$$

$$\left.\begin{aligned} \cos\theta = \cos\Bigg\{ & 2 \operatorname{arctg}\left[\operatorname{tg} \frac{\theta_0}{2} \exp\left(-\frac{M H t}{8 \pi \mu r^3}\right)\right] \\ & + \frac{M H I}{64 \pi^2 \mu^2 r^6} \frac{2 \operatorname{tg} \frac{\theta_0}{2} \exp\left(-\frac{M H t}{8 \pi \mu r^3}\right)}{1 + \operatorname{tg}^2 \frac{\theta_0}{2} \exp\left(-\frac{2 M H t}{8 \pi \mu r^3}\right)} \\ & \times \left[1 - \frac{M H t}{8 \pi \mu r^3} + \ln \frac{1 + \operatorname{tg}^2 \frac{\theta_0}{2}}{1 + \operatorname{tg}^2 \frac{\theta_0}{2} \exp\left(-\frac{2 M H t}{8 \pi \mu r^3}\right)}\right]\Bigg\}. \end{aligned}\right\} \tag{18}$$

If we replace (16) in (17) the solution takes the form of a definite integral. If N, M, r, μ, m and h are known, then the integral can be solved numerically and numerical value of remanent magnetization of sedimentary rocks obtained.

We will investigate the two limit cases, namely when H or t respectively h are small quantities and when t is great quantity.

In the first case we have

$$\frac{M\,H\,I}{(8\,\pi\,\mu\,r^3)^2} \approx 0\,; \quad \exp\left(-\frac{M\,H\,t}{8\,\pi\,\mu\,r^3}\right) \approx 1 - \frac{M\,H\,t}{8\,\pi\,\mu\,r^3}$$

and

$$\cos\theta = \cos\left\{2\,\mathrm{arc\,tg}\left[\left(1 - \frac{M\,H\,t}{8\,\pi\,\mu\,r^3}\right)\mathrm{tg}\,\frac{\theta_0}{2}\right]\right\}.$$

We replace this value of $\cos\theta$ in (17) and we obtain

$$J_n = \frac{N\,M^2\,H\,t}{16\,\pi\,\mu\,r^3} \cdot \frac{1}{1 - \frac{M\,H\,t}{8\,\pi\,\mu\,r^3}}\,. \tag{19}$$

Using $(M\,H\,t/8\,\pi\,\mu\,r^3) \ll 1$, we take only the member of the first order in the expansion of (19) and we obtain:

$$J_n = \frac{N\,M^2\,H}{16\,\pi\,\mu\,r^3}\,t\,. \tag{20}$$

From (20) we see, that at small H or t the receiving magnetization is proportional to intensity of magnetic field and to time t. At $H = 0$ or $t = 0$ the magnetization J_n is equal to zero.

In second case we have

$$\exp\left(-\frac{M\,H\,t}{8\,\pi\,\mu\,r^3}\right) \approx 0$$

and obtain

$$\cos\theta \approx 1\,.$$

We replace in (17) and finally we have

$$J_n = \frac{N\,M}{\pi}\int_0^{\pi} d\theta_0 = N\,M\,. \tag{21}$$

It is clear from (21) that if the time of sedimentation of particles is a very great one, then the received magnetization is approximately equal to the magnetization of saturation. The above theoretical conclusions agree very well with the experimental data.

The result of the presented investigation on the problem of sedimentation of spherical ferromagnetic particles in still water confirms the basic conclusions obtained by T. NAGATA [3].

The sedimentation to the anisometric particles in still water can be examined in a similar way. The problem about the influence of a Brownian motion and of a laminar motion in a liquid on the particles's orientation will be considered in a following papers.

References

[1] U. N. Bacaev, *Pribrigennoe integrirovanie differenzialnogo uravneniia maiatnica,* Pricladnaia matematica i mehanica *XVI* (1952), 723.

[2] D. W. Collinson, *Depositional remanent magnetization in sediments,* J. Geophys. Res. *70* (1965), 4663.

[3] T. Nagata, *Rock magnetism,* Mazuren Company (Tokio 1961).

[4] P. B. Nozharov, *Über die Sedimentation ferromagnetischer Teilchen in Flüssigkeit unter dem Einfluss des erdmagnetischen Feldes,* Wissenschaftliche Tagung des Geophysikalischen Instituts (12. bis 16. Oktober 1964), Vorträge (Sofia 1966), 179.

[5] J. J. Stoker, *Nonlinear vibrations in mechanical and electrical systems* (New York 1950).

(Received 27th May 1966)

Bemerkungen zur Hypothese zweier Sturmzeitringströme[1])

Von Armin Grafe[2]) und Adolf Best[2])

Summary – For several years the theory of the main phase of geomagnetic storms takes into account the existence of two storm time ring currents which are thought to exist in different altitudes. This hypothesis is supported less by satellite data than by the analysis of recovery effects observed in the geomagnetic records, according to that the recovery phase should exist of two seperate single phases. In our opinion however the observational material seems not convincing enough, especially because material of one station only was used for the hitherto made investigations and no elimination of the *Sq*-part was executed. A critical analysis of the observational material is by all means necessary, especially for the reason that already in literature extensive inferences of the *DR2* ring current for the formation and the energy behaviour of the *DP* part were drawn. For the investigation of recovery effects it is necessary to use additionally to records of equatorial stations those of observatories in higher latitudes. The *Sq*-part has to be eliminated in the analysis. It is referred that new disturbances after the beginning of the recovery phase can feign two separated ring current effects. Some examples of the recovery phase will be discussed. They show that the observational material gives no necessity for the supposition of two separate strom time ring currents. Furthermore some theoretical considerations are opposite to this hypothesis. The charge exchange with thermical atoms of hydrogen is discussed to be a possible loss process. It is taken into account also the possibility to suppose a wide proton energy spectrum for explaining the recovery phase.

1. Einleitung

In einer Reihe von Arbeiten (Akasofu [1], Akasofu [2],Akasofu, Yakob [6] der letzten Jahre werden auf Grund der Untersuchung von Nachstörungseffekten zwei getrennte Sturmzeitringströme angenommen. Dabei stützt sich diese Annahme auf zwei erkennbare Phasen unterschiedlicher Abklingkonstanten während des Nachstörungseffektes. Diese Erscheinung soll sich in einem einwandfrei erkennbaren Knick in der Darstellung der Nachstörungsphase äussern. Die Registrierungen scheinen das zunächst zu bestätigen. Die Vorstellung, die sich Chapman und Akasofu von den beiden Ringstromanteilen gebildet haben, zeigt Figur 1. Danach wird der schneller abklingende Teil als *DR1* und der langsamer abklingende Teil als *DR2* bezeichnet. Für starke Stürme soll *DR1* stärker als *DR2* ausgebildet sein und für schwache Stürme umgekehrt. Nach der hydromagnetischen Theorie der Hauptphase von Dessler und Parker [4] soll der Sturmzeitringstrom von niederenergetischen Protonen gebildet werden, für die als Lossprozess der Ladungswechselprozess mit thermischen Wasserstoffatomen zutrifft und deren mittlere Lebensdauer der Beziehung $\tau = (1/n\,\sigma\,v)$ ge-

[1]) Mitteilung aus dem Geomagnetischen Institut Potsdam, Nr. 226.
[2]) Adolf-Schmidt-Observatorium für Erdmagnetismus in Niemegk, Kreis Belzig (DDR).
[3]) Die Ziffern in eckigen Klammern verweisen auf das Literaturverzeichnis, Seite 77.

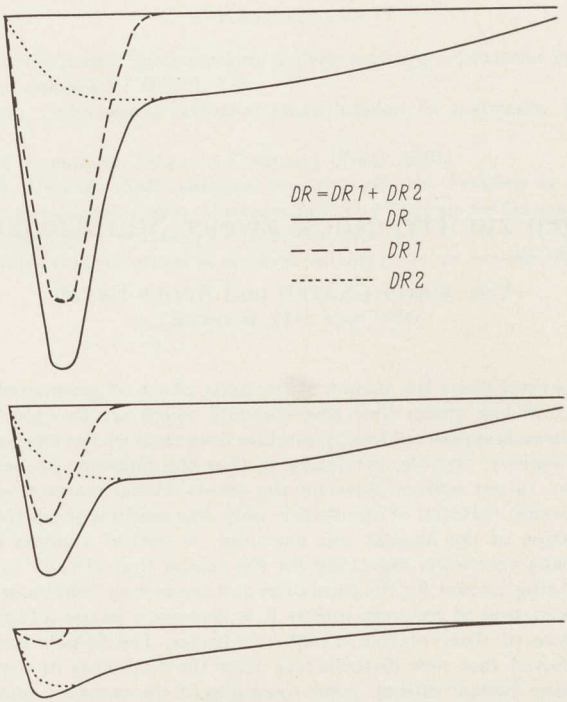

Figur 1
Schematische Darstellung der Vorstellung von zwei *DR*-Anteilen während eines Sturmes (aus AKASOFU [1])

nügt. Dabei ist n die Teilchendichte des Wasserstoffs, v die Geschwindigkeit der eingefangenen Teilchen und σ der Wirkungsquerschnitt. Nach diesem Prozess kann der *DR1*-Anteil durch einen Ringstrom erklärt werden, der erdnäher erzeugt wird als der, der den *DR2*-Anteil verursacht, da für geringere Erdentfernungen die Dichte des Wasserstoffs grösser ist und damit die Abklingzeit kürzer wird. Die Annahme eines Ladungswechselprozesses mit thermischen Wasserstoffatomen erklärt recht gut die beiden bekannten Tatsachen, dass starke Stürme schneller abklingen als schwächere und ferner, dass die Abklingzeit im Sonnenfleckenmaximum grösser ist als im Sonnenfleckenminimum. Auf die zweite Beobachtungstatsache hat besonders YAKOB [6] hingewiesen. Tatsächlich wird gegenwärtig mit einem Sturmzeitringstrom gerechnet, der aus Protonen der Energie von etwa 10 keV gebildet wird, die in einer Entfernung von 1.5 bis 2 Erdradien im erdmagnetischen Feld eingefangen sind. Für den *DR2*-Anteil wird ein Ringstrom in etwa 4 Erdradien Entfernung angenommen. Die Hypothese zweier getrennt existierender Sturmzeitringströme ist zur Grundlage weitreichender Theorien über die gesamte Hauptphase geomagnetischer Stürme geworden (AKASOFU [6]). Danach wird angenommen, dass die Energie der *DP*-Störungen von der Energie des *DR2*-Ringstromes geliefert wird.

In der folgenden Untersuchung von Nachstörungseffekten soll gezeigt werden, dass auf Grund des Beobachtungsmaterials keine Notwendigkeit besteht, zwei getrennte Sturmzeitringströme anzunehmen.

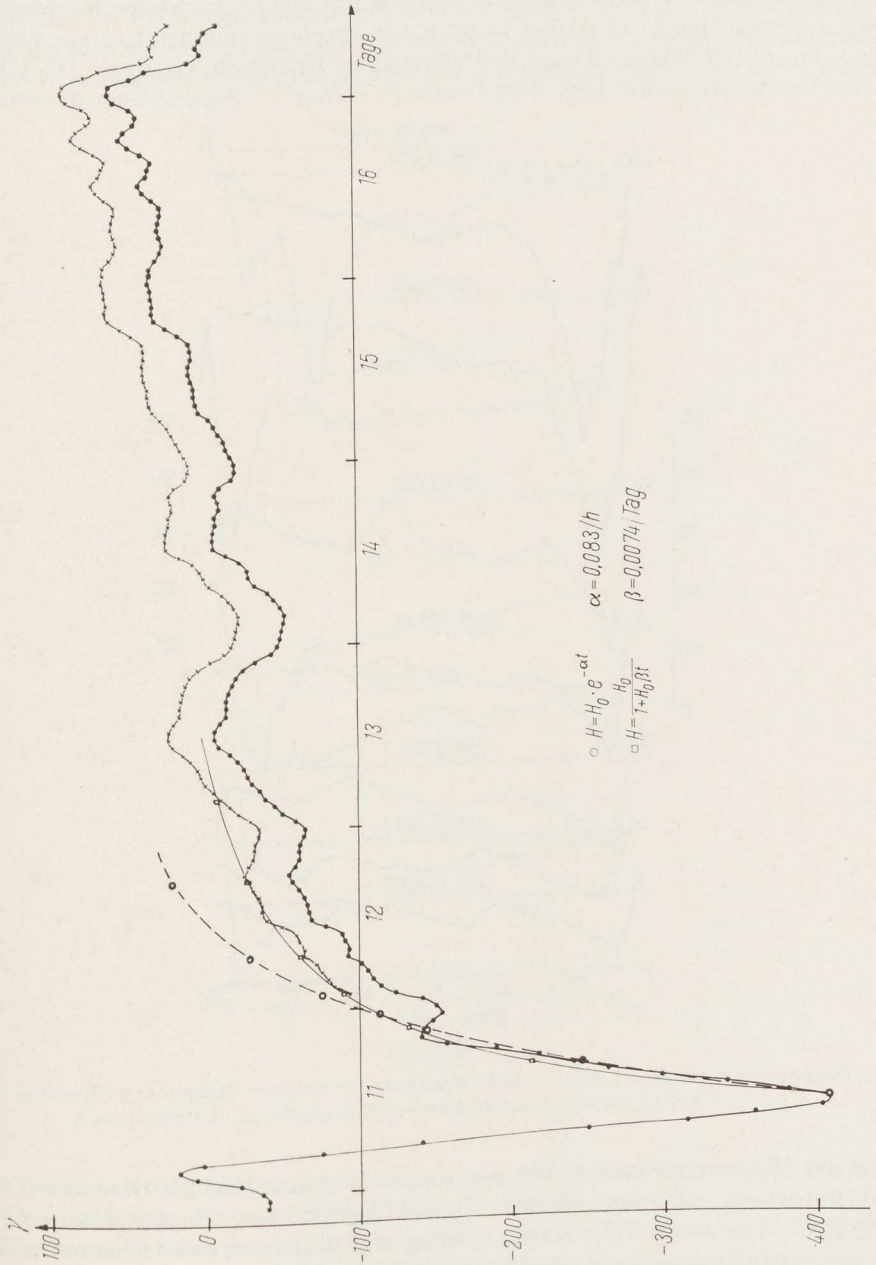

Figur 2
Stundenmittelwerte der H-Komponente von Honolulu für den Sturm vom 11. Februar 1958

2. Untersuchung von Nachstörungseffekten

Es gilt zunächst zu untersuchen, inwieweit der für Ringstrompartikel angenommene Lossprozess des Ladungsaustausches sich mit den beobachteten Nachstörungseffekten vereinbaren lässt. Dabei nehmen wir Protonen mit der Energie von etwa 10 keV an, die zwischen 1.5 bis 2 Erdradien einen Ringstrom erzeugen. Die Verminderung der Partikeldichte folgt dem Gesetz $N = N_0 e^{-n\sigma vt}$. Figur 2 zeigt die Stunden-

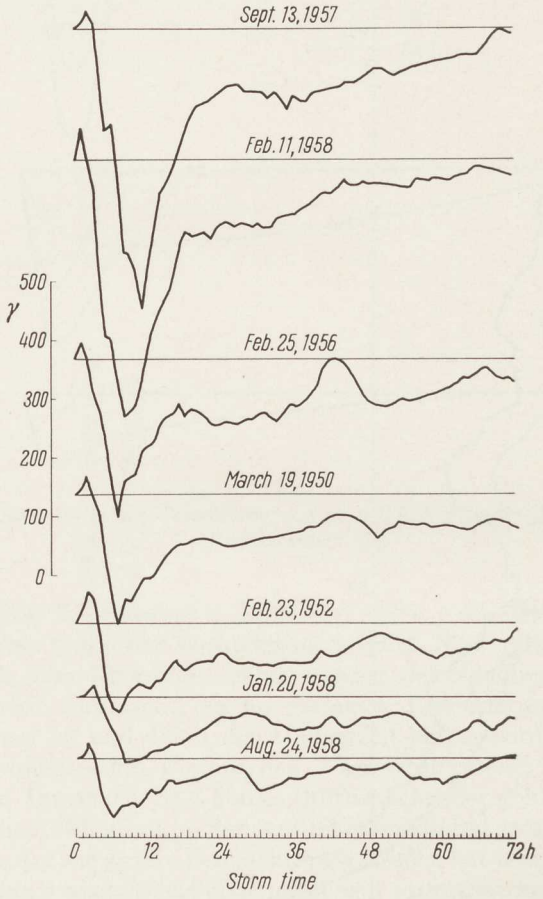

Figur 3
Stundenmittelwerte der Horizontalkomponente für mehrere Stürme von Honolulu (nach Akasofu [1])

mittel der H-Komponente des Sturmes vom 11. Februar 1958 für Honolulu. Die gestrichelte Kurve mit den offenen Kreisen genügt dem Exponentialgesetz mit $\alpha = 0.083$/h. Der e-te Teil des Maximalwertes wird nach etwa zwölf Stunden nach Beginn der Nachstörungsphase erreicht. Wie aus der Figur zu ersehen ist, genügt das Exponentialgesetz des Ladungsaustausches bei weitem nicht dem tatsächlichen Verlauf der Nachstörung. Die Rückbildung zum Anfangsniveau erfolgt wesentlich lang-

samer. Diese Diskrepanz zwischen Theorie und Beobachtung kann durch die Annahme von zwei Ringströmen in verschiedenen Entfernungen beseitigt werden. Infolge der verschiedenen Teilchendichten des Wasserstoffs sollten die Lebenszeiten der Ringstrompartikel für die beiden Ringströme unterschiedlich sein. Die Partikel des Ringstromes, der sich näher der Erde befindet, müssten nach dem Ladungswechselprozess schneller verschwinden als die, die in grösserer Entfernung einen Ringstrom bilden.

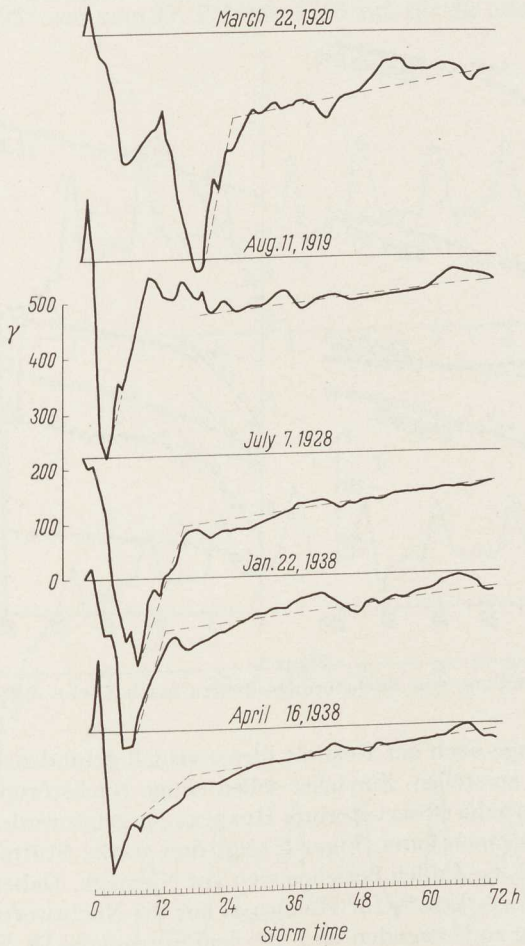

Figur 4
Zusammenstellung älterer Stürme von Honolulu (nach AKASOFU [1])

Dies muss sich in den magnetischen Registrierungen so äussern, dass die Nachstörungsphase zu Beginn ein schnelleres Abklingen als später zeigt. In den Registrierungen müsste im Verlauf der Nachstörungsphase ein Knick auftreten. Nach Untersuchungen von CHAPMAN und AKASOFU und YACOB wurde dieser Knick in der Tat gefunden. Figur 3 zeigt die Stundenmittelwerte der Horizontalkomponente für mehrere Stürme für Honolulu. Besonders gut ist dieser Knick bei dem starken Sturm vom

11. Februar 1958 zu erkennen. Figur 4 zeigt eine Zusammenstellung älterer Stürme, ebenfalls für Honolulu, bei denen der Knick nur in einigen Fällen erkennbar ist. Besonders bei dem Sturm vom 16. April 1938 kann nicht ohne weiteres auf zwei Ringströme geschlossen werden. Figur 5 gibt eine Darstellung von Nachstörungseffekten aus der Arbeit von YACOB wieder, die ebenfalls zwei Nachstörungsanteile verdeutlichen soll. In einigen Fällen könnte aber auch hier die Durchlegung der «Freihandkurve» so durchgeführt werden, dass kein «Kurvenknick» zu erkennen wäre.

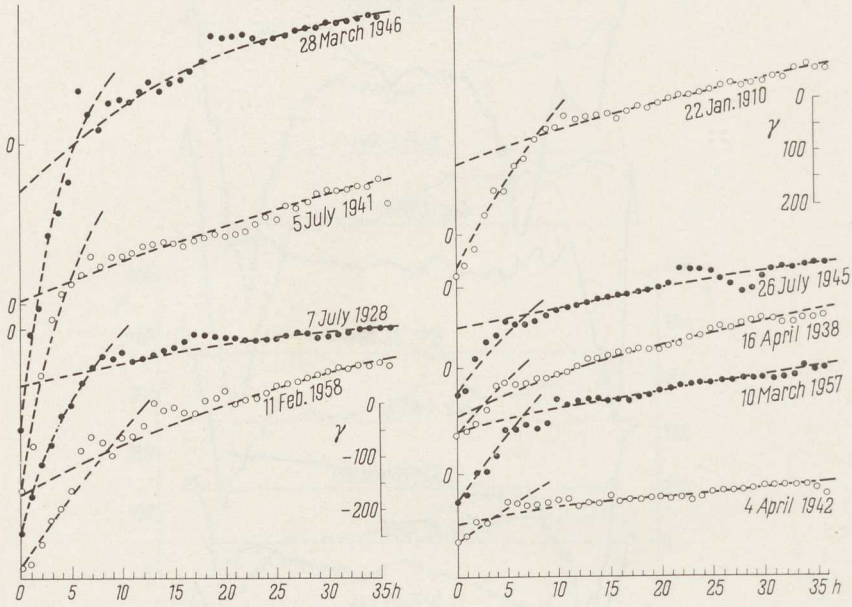

Figur 5
Darstellung von Nachstörungseffekten (nach YACOB [6])

Es gilt nun die Frage nach der Realität dieses visuell gefundenen Knicks bei den Nachstörungseffekten zu stellen. Zunächst sollen einige Nachstörungseffekte starker Stürme für das äquatornahe Observatorium Huancayo gezeigt werden, bei denen man diesen Knick nicht erkennen kann. Figur 6 zeigt drei starke Stürme aus dem Jahre 1941. Die angegebenen A_K-Zahlen beziehen sich auf Niemegk. Dabei ist zu beachten, dass infolge des enorm starken *Sq* für Huancayo nur die Nachtwerte für die Analyse der Nachstörungsphase zu verwenden sind. Bei dem Sturm vom 18. September könnte von einem Knick gesprochen werden. Aber gerade dieser Knick wird durch die *Sq*-Variation vorgetäuscht. Weitere Beispiele von Nachstörungseffekten ohne augenfälligen Knick zeigt Figur 7, für die die Stundenmittelwerte von Apia aufgezeichnet wurden. Die geomagnetische Breite für Apia beträgt $-16°$. Für diese Stürme gilt das gleiche für *Sq* gesagte wie für Huancayo. Ein deutlicher Knick wird besonders bei dem starken Sturm vom 8. Juli 1958 vorgetäuscht. Aber auch bei diesem Sturm wird der Knick eindeutig durch *Sq* erzeugt. Der Maximalwert von *Sq* fällt auf etwa 0 h 00 m GMT. Ohne weiteres als knickfreier Nachstörungseffekt ist der 25. Februar 1956 zu erkennen.

Wie die kurze Zusammenstellung zeigt, können im Gegensatz zu den von CHAPMAN und AKASOFU dargelegten Beispielen mehrere Nachstörungseffekte gefunden werden, bei denen die Wirkung zweier Ringstromeffekte in der Form eines visuell erkennbaren Knickes nicht zu finden ist. Wie steht es nun mit den von CHAPMAN, AKASOFU und YACOB angegebenen Beispielen?

Wir müssen uns der Mühe unterziehen und einige der Fälle im einzelnen diskutieren. Bei der Betrachtung der Figur 3 fallen als besonders krasse Fälle die Stürme vom 13. September 1957 und vom 11. Februar 1958 auf, für die eine nähere Untersuchung

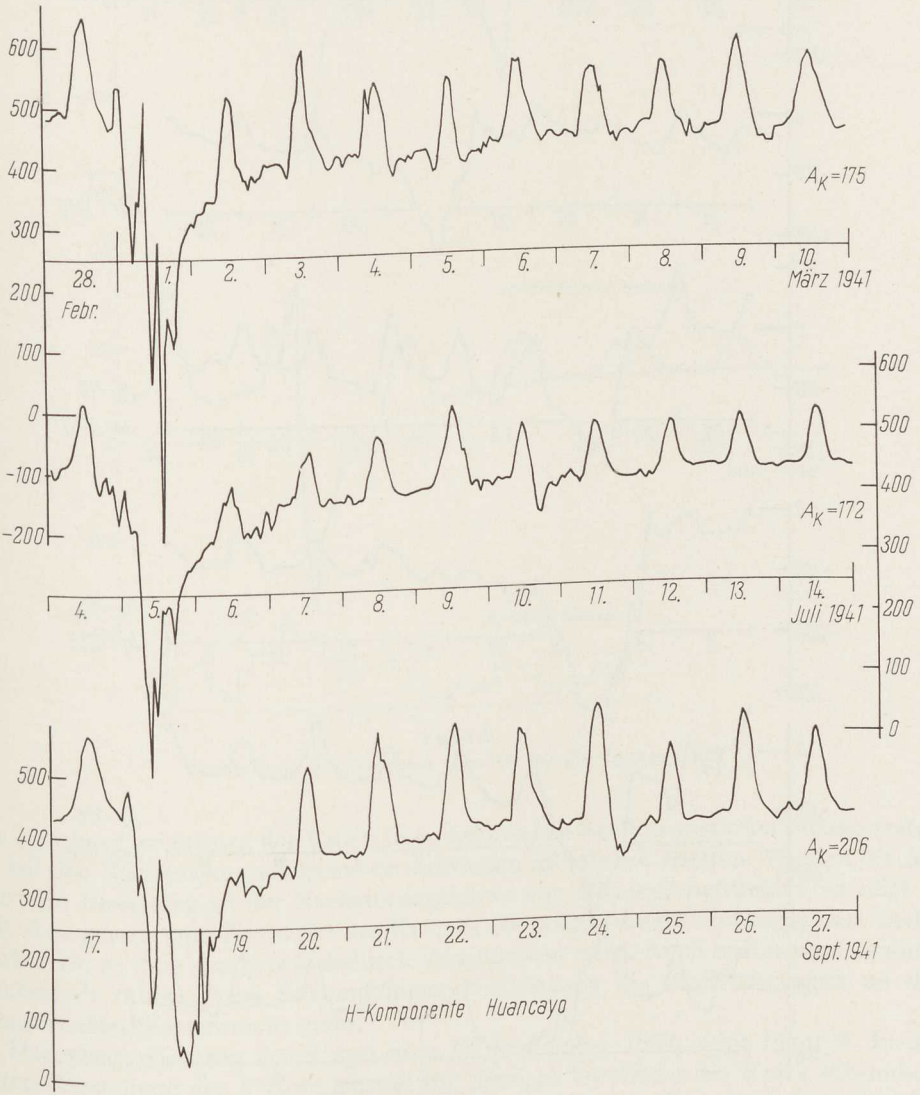

Figur 6
Darstellung von drei starken Stürmen des Jahres 1941 von Huancayo

durchgeführt werden soll. Aus den Nachstörungseffekten der Figur 4 wird der 22. Januar 1938 herausgegriffen. Figur 8 zeigt die Stundenmittelwerte in der H- bzw. X-Komponente vom 24. bis 29. Januar 1938 für Huancayo und Niemegk. Dazu wurden noch die K_1-Werte für Niemegk aufgetragen. An diesem Beispiel soll gezeigt wer-

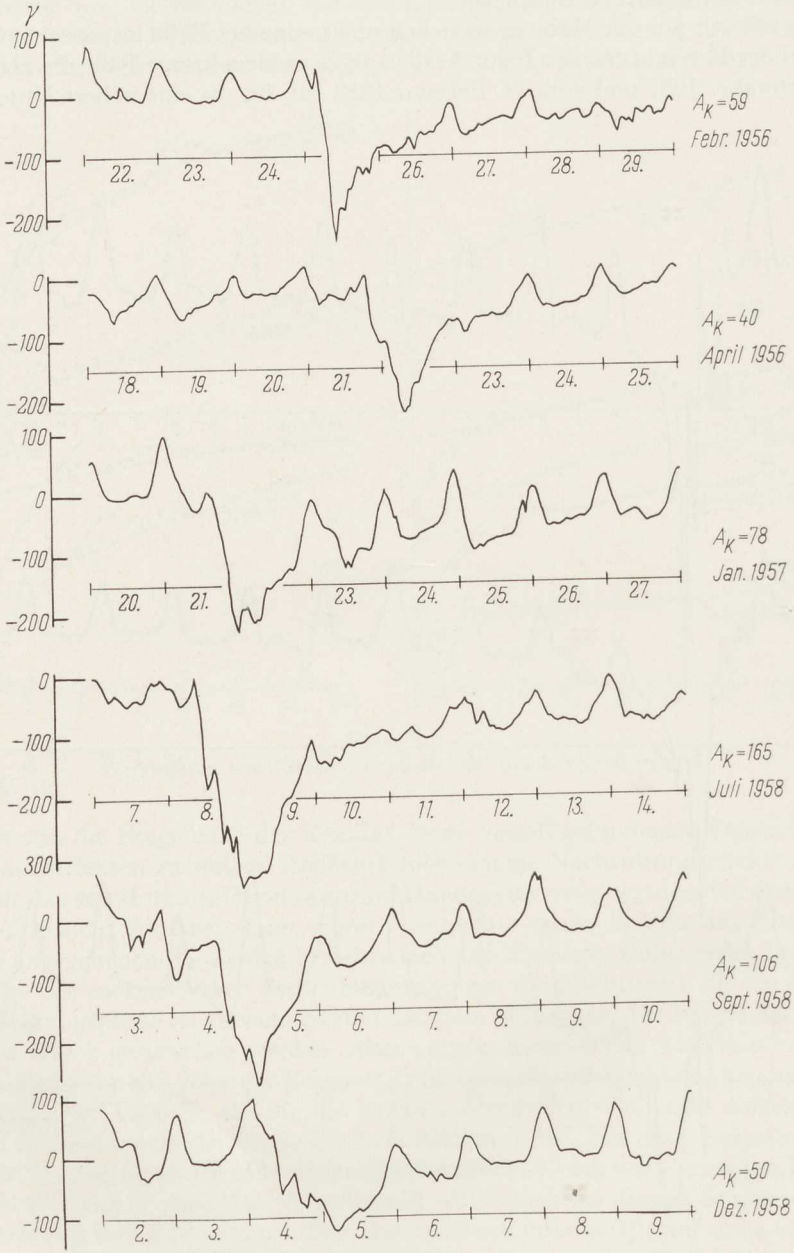

Figur 7
Darstellung von mehreren Stürmen für Apia

den, dass der Kurvenknick, der in der Darstellung für Niemegk, einer Station in mittleren Breiten, klar erkennbar ist, dagegen bei dem Nachstörungseffekt für Huancayo, einer Station in Äquatornähe, kaum wahrnehmbar ist. Der Verlauf genügt im wesentlichen dem Angenheisterschen Abklinggesetz. Wird mit zwei Ringstromeffek-

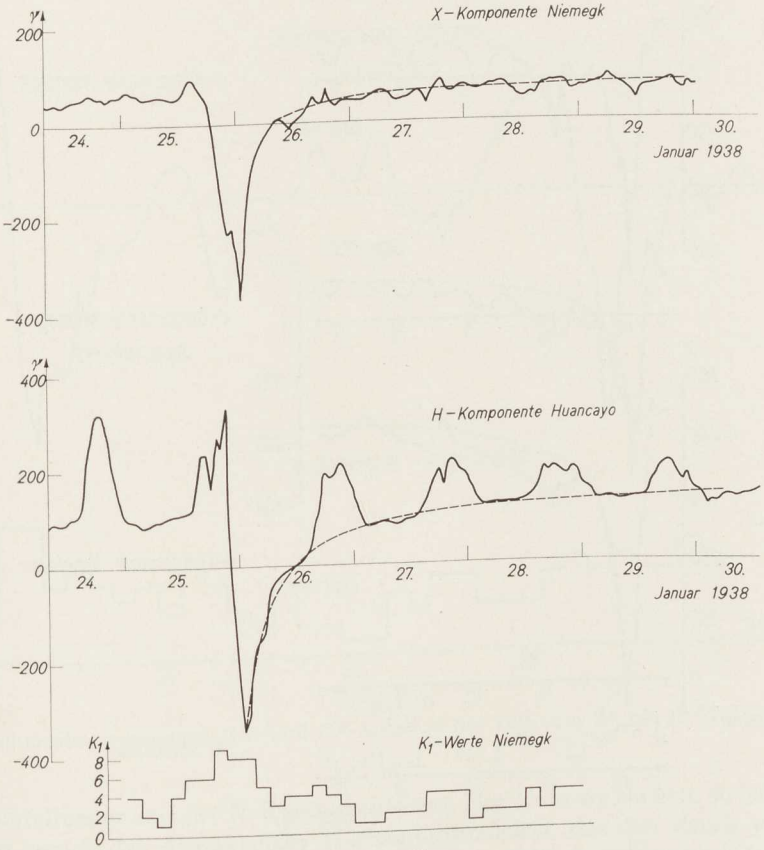

Figur 8
Darstellung des Sturmes vom 24. bis 29. Januar 1938

ten gerechnet, so müsste der Knick in äquatornahen Stationen stärker zutage treten als bei den Nachstörungseffekten von Stationen in höheren Breiten. Werden die K_1-Werte in Beziehung zu der Nachstörungskurve von Niemegk betrachtet, so zeigt es sich, dass gerade zum Zeitpunkt des Knickes der polarbedingte Störungsanteil wieder stärker ist, so dass der Knick dadurch vorgetäuscht wird. Auch später wird es nicht magnetisch ruhig. Diese Schwankungen beeinflussen die Registrierungen an der äquatornahen Station nicht mehr.

Das zweite Beispiel, der Sturm vom 13. September 1957, zeigt Figur 9. In der ersten Darstellung der X-Komponente für Niemegk ist wieder der Knick erkennbar. Wird jedoch Sq auf Grund der fünf internationalen ruhigen Tage des entsprechenden Monats eliminiert, so ist der Knick schon weniger augenscheinlich. Trotzdem genügt

der beobachtete Nachstörungseffekt nicht der eingezeichneten Abklingkurve, auch nicht für Honolulu. Wie bekannt und besonders von AKASOFU und CHAPMAN [5] besonders herausgestellt, besteht ein enger Zusammenhang zwischen der Ausbildung des Ringstromfeldes und dem *DS*-Feld. Figur 10 zeigt die *H*-Komponente von Hono-

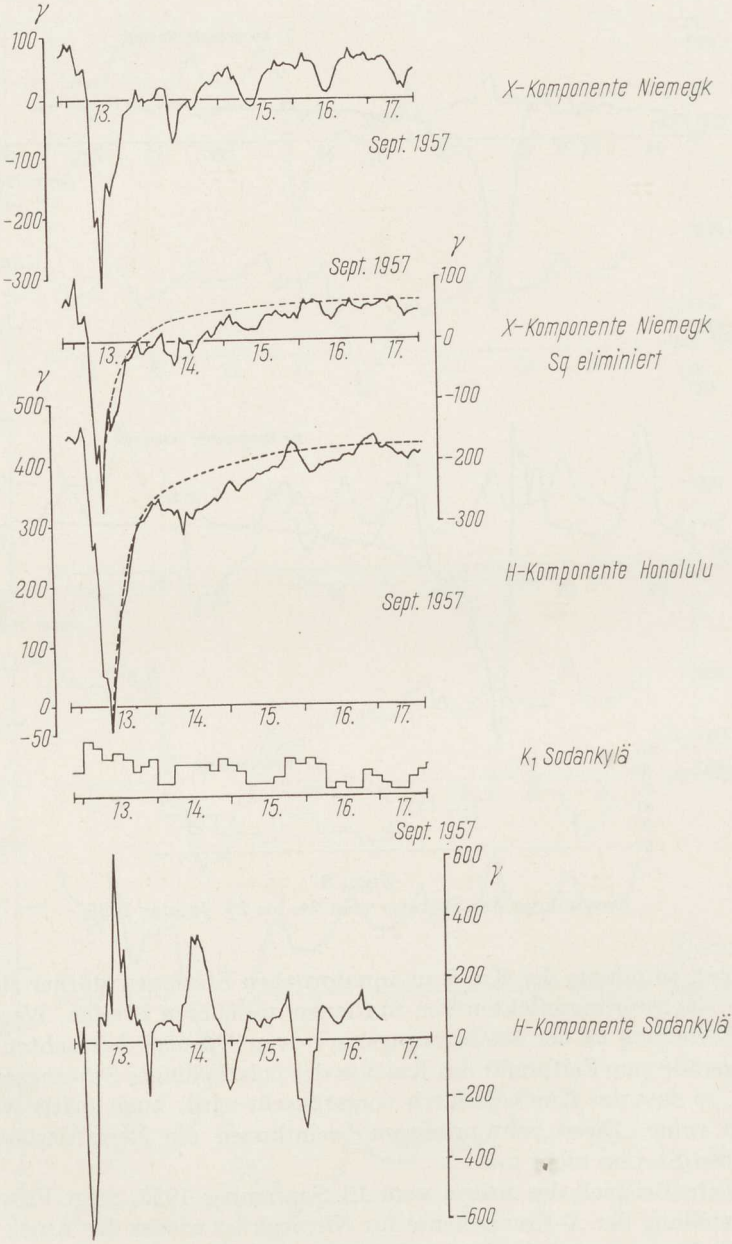

Figur 9
Darstellung des Sturmes vom 13. September 1957

lulu vom 23. bis 27. August 1958 und die K_1-Werte von Sodankylä. Es ist gut zu erkennen, dass ein wiederholtes Absinken der H-Komponente von einem Anstieg des K_1-Wertes begleitet wird. Wenden wir uns wieder der Figur 9 zu, so zeigen die beiden unteren Darstellungen die K_1-Werte und die H-Komponente für Sodankylä. Werden

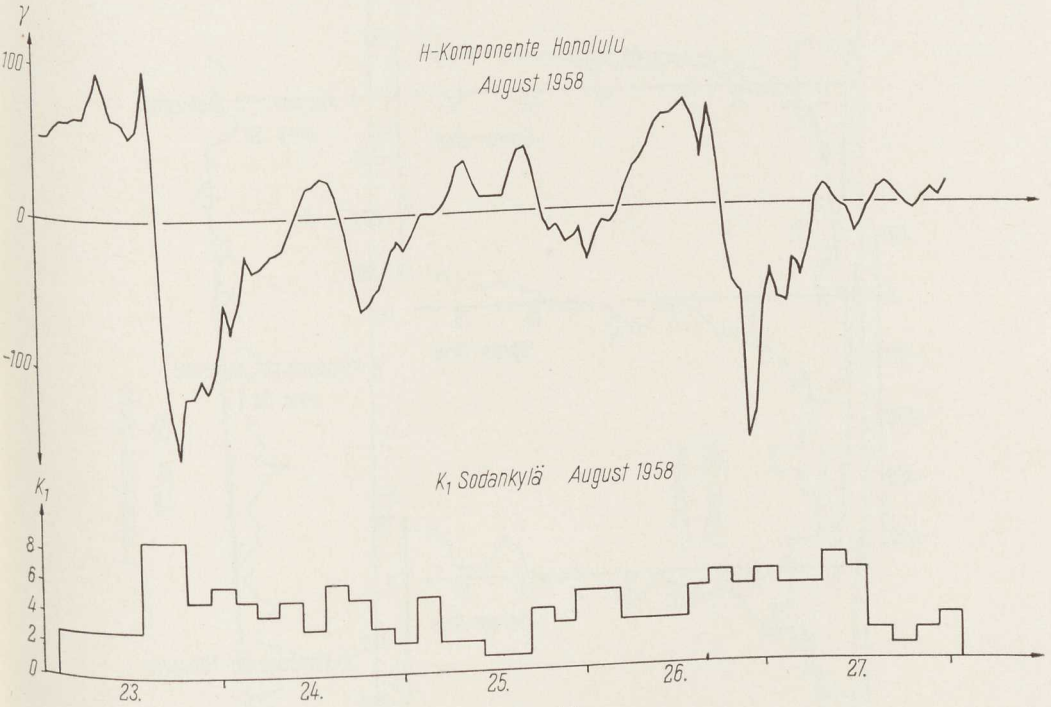

Figur 10
Zusammenhang zwischen DR- und DP-Anteil in der Zeit vom 23. bis 27. August 1958

diese Darstellungen mit der H-Komponente von Honolulu verglichen, so ist zu erkennen, dass gerade das Absinken der Horizontalintensität, das den Knick vortäuscht, mit einem Anstieg der polaren Aktivität zusammenfällt. Auch das erneute Absinken des H-Niveaus am 16. und 17. lässt sich mit der Erhöhung polarer Aktivität in Verbindung bringen. Die Vortäuschung des Knickes im Nachstörungseffekt ist demnach einzig und allein eine Folge der erneuten Verstärkung des hypothetischen Ringstromfeldes. Bei der Untersuchung von Nachstörungseffekten sollten daher nur solche Stürme verwendet werden, für die auf den Beginn des Nachstörungseffektes keine neuen Störungen folgen.

Als drittes Beispiel soll in Figur 11 der Nachstöreffekt des starken Sturmes vom 11. Februar 1958 diskutiert werden. In der Figur 3 war der Knick bei diesem Sturm am deutlichsten zu erkennen. Figur 11 zeigt diese Darstellung noch einmal, dazu die H-Komponente für Honolulu ohne Sq-Anteil. Wieder wurden zur Elimination die fünf internationalen ruhigen Tage benutzt. Auch hier ist zu erkennen, dass bereits eine Entfernung des Sq-Anteiles den vermeintlichen Knick im Nachstörungseffekt weitgehend beseitigt. Die untere Darstellung der Figur 11 zeigt wieder die H-Komponente

für Sodankylä. Danach ist zu erkennen, dass das *DS*-Störungsfeld auch noch während des Nachstörungseffektes eine aussergewöhnliche Stärke besitzt. Von diesem Gesichtspunkt aus betrachtet ist dieser Sturm zur Diskussion des Nachstörungseffektes denkbar ungeeignet. Doch untersuchen wir diesen Sturm weiter. Honolulu ist keine

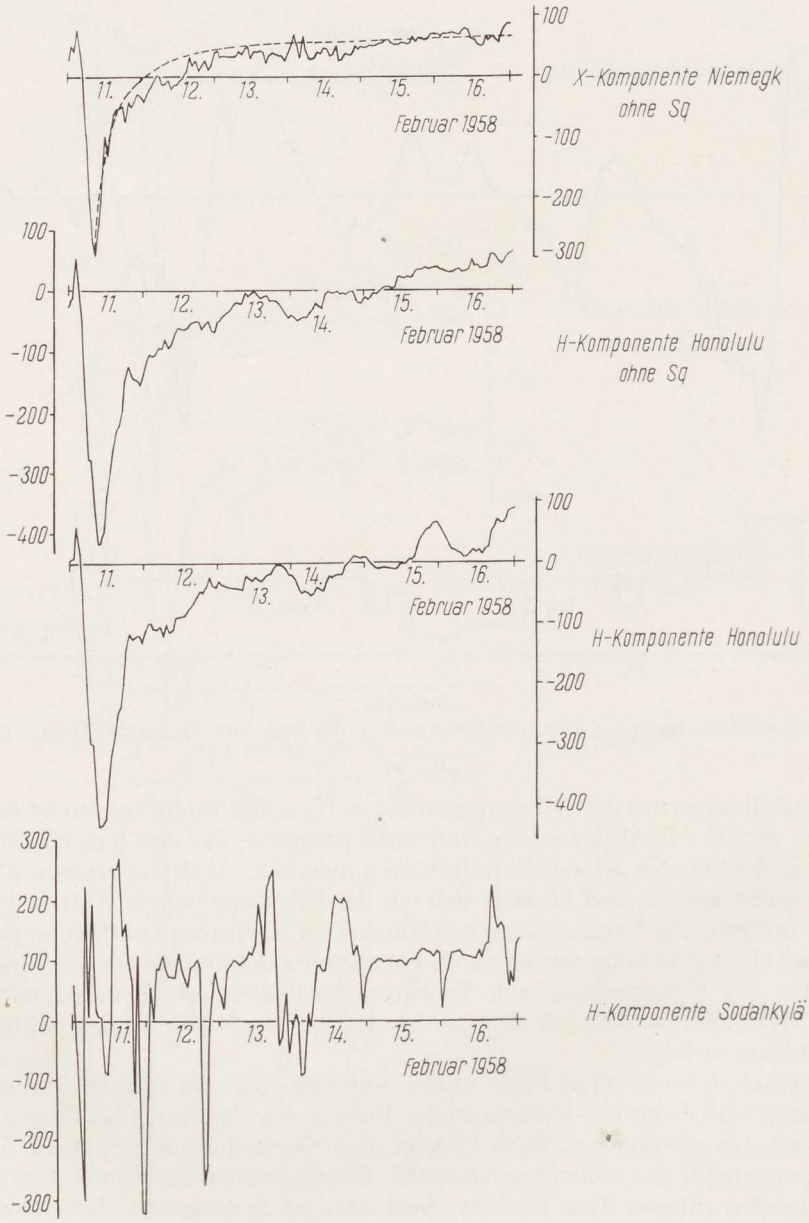

Figur 11
Darstellung des Sturmes vom 11. bis 16. Februar 1958

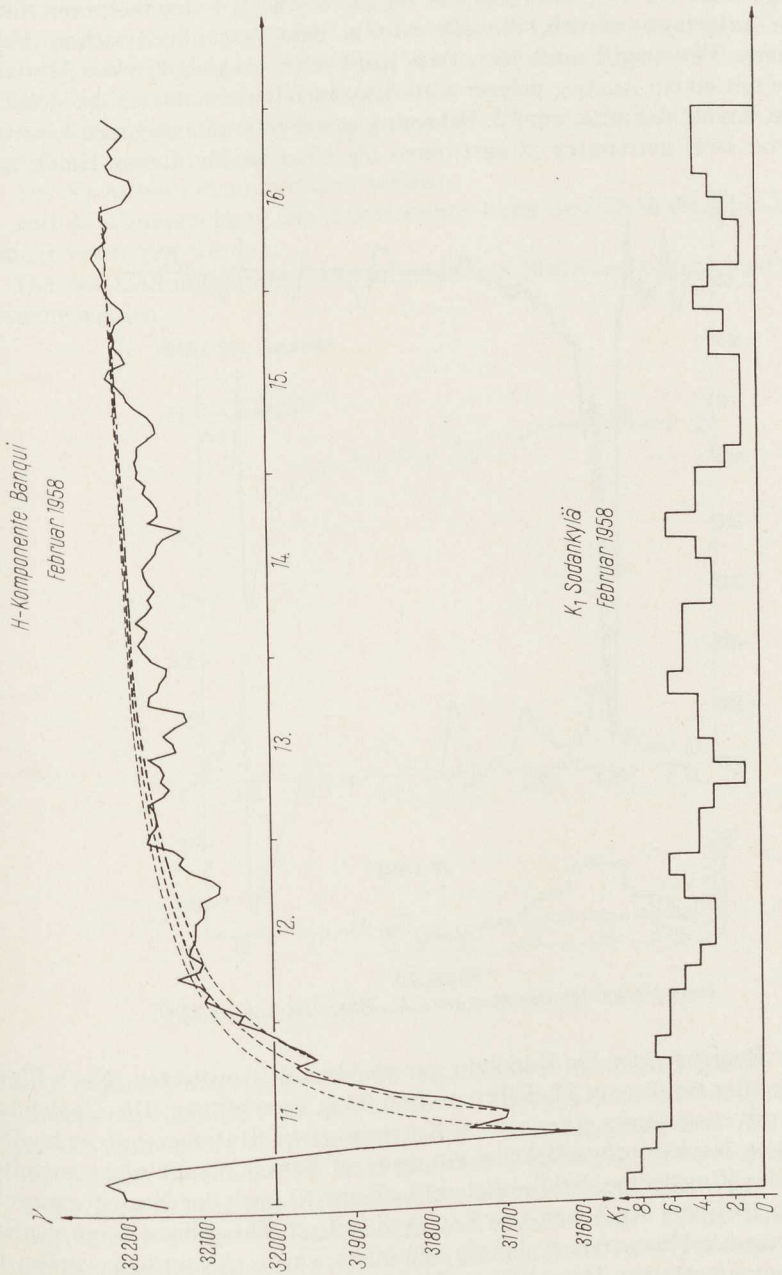

Figur 12
Stundenmittel der H-Komponente von Bangui und der K-Werte von Sodankylä für den Sturm vom 11. Februar 1958

Station in direkter Äquatornähe. Deshalb wurde in Figur 12 die H-Komponente von Bangui aufgezeichnet. Die geomagnetische Breite von Bangui beträgt $+4° 48'$. Der Nachstörungseffekt der Registrierung von Bangui kann als Folge mehrerer Nachstörungseffekte aufgefasst werden, die alle einzeln dem Angenheisterschen Abklinggesetz genügen. Ferner gilt auch hier, dass jedes erneute Absinken der Horizontalkomponente mit einem Anstieg polarer Aktivität korreliert ist. Das zeigt sich besonders bei dem Knick, den man am 12. Februar gegen 6 h 00 m annehmen könnte. Bei Annahme von zwei getrennten Ringströmen als Ursache für diesen Knick müsste

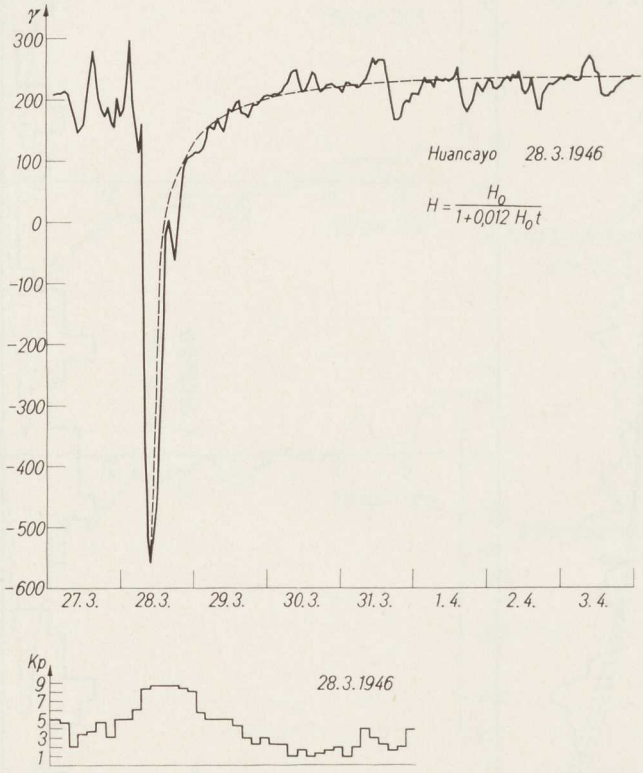

Figur 13
Darstellung des Sturmes vom 27. März bis 3. April 1946

dieser in der Registrierung für Honolulu zur gleichen Zeit auftreten. Nach Figur 11 ist der Knick aber bereits am 11. Februar, 20 h 00 m zu erkennen. Die Ungleichmässigkeit des Auftretens dieses erkennbaren Knicks an zwei Stationen unterschiedlicher Breite für einen Nachstörungseffekt ist ein weiterer Beweis für die nicht zutreffende Existenz zweier Ringströme. Schliesslich sei in Figur 13 noch der Nachstörungseffekt vom 28. März 1946 aus der Arbeit von YACOB diskutiert. Diese Figur zeigt wieder die H-Komponente für Huancayo, wobei Sq eliminiert wurde. Ausserdem wurden noch die Kp-Zahlen aufgetragen. Der Abklingeffekt genügt recht gut der Beziehung

$$H = \frac{H_0}{1 + 0.012\,H_0\,t}\,.$$

Am 28. März, 21 h 00 m GMT ereignet sich ein zusätzlicher Einsatz. Wie die Kp-zahlen zeigen, herrschen zu dieser Zeit noch stark gestörte Verhältnisse, so dass ein wiederholter Anstieg des Ringstromfeldes möglich ist.

Zusammenfassend muss gesagt werden, dass bei der Analyse von Nachstörungseffekten folgende Punkte berücksichtigt werden müssen. Eine Nichtberücksichtigung kann zur Vortäuschung eines Knickes führen.

1. Als wichtigste Voraussetzung muss die Ungestörtheit während der Wiederholungsphase genannt werden.
2. Der Sq-Anteil muss eliminiert werden.
3. Auf die Untersuchung der Registrierung einer Station in direkter Äquatornähe darf nicht verzichtet werden.
4. Der Nachstörungseffekt sollte an mehreren Stationen unterschiedlicher Breite untersucht werden.

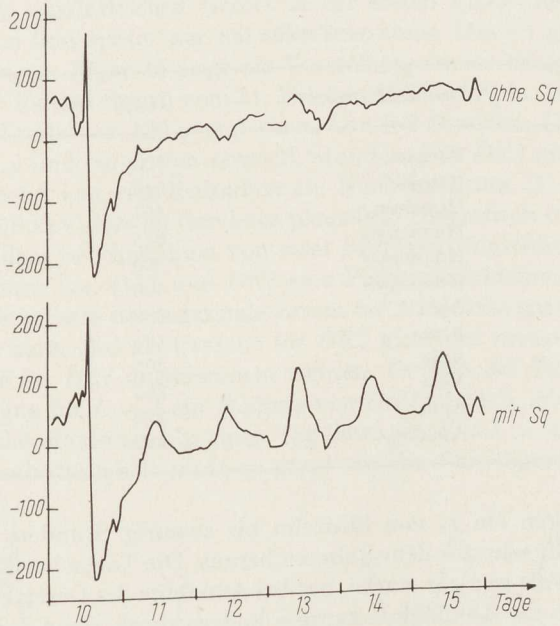

Figur 14
Darstellung des Sturmes vom 10. bis 16. März 1957

Unter Berücksichtigung der Punkte eins bis drei wurde in Figur 14 der Nachstörungseffekt vom 10. März 1957 aufgezeichnet. Dieser Sturm zeichnet sich durch sehr geringe Aktivität sofort nach Beginn der Nachstörungsphase aus. Am 10. März beträgt A_K 47, aber bereits am 11. März nur noch 8 und an den Folgetagen 8, 10 und 3. Am 14. März besitzt die internationale Charakterzahl sogar den Wert 0.0. Die Registrierung der H-Komponente von Bangui lässt demnach auch keinen Knick erkennen.

Im folgenden soll nun kurz von der Theorie her etwas zur Hypothese zweier Ringströme, die sich während der Sturmzeit verstärken sollen, gesagt werden. Dabei werden die Daten der Recovery-Zeit beobachteter Effekte zugrunde gelegt. In Figur 2 ist die Kurve, gekennzeichnet durch Kreise, eingezeichnet, die sich ergibt, wenn als

Lossprozess der Ringstrompartikel Ladungswechselprozesse angenommen werden. Diese genügt dem Gesetz $dN/dt = -dN$, wobei $\alpha = \sigma n v$ ist. Die Zeit, für die die Maximalstörung des Ringstromeffektes auf seinen e-ten Wert abgefallen ist, beträgt für diesen Fall etwa zwölf Stunden. Das entspricht nach LIEMOHN [5] bei $L = 1.5$ bis 2.0 einer Partikelenergie von ungefähr 100 keV. Bei Annahme von Protonen der Energie von 10 keV müsste die mittlere Lebensdauer wesentlich geringer, der Abfall im Nachstörungseffekt steiler sein. Wird mit einer wiederholten Verstärkung des Ringstromes am 11. Februar gegen 20 h 00 m gerechnet, wie es auch die Registrierung von Bangui zeigt, so ist die Parallelverschiebung der Störungskurve in Figur 2 zulässig. Dann genügt der Nachstörungseffekt dem Ausdruck $dN/dt = -\beta N^2$, wie durch die mit Quadraten gekennzeichnete Kurve gezeigt wird. Tabelle 1 zeigt die Recovery-Zeiten für H_0/e für verschiedene Stürme. Die ersten sechs sind starke und die letzten sechs mittlere Stürme. Für die ersteren ergibt sich ein τ_e von zehn Stunden

Tabelle 1

Datum	Beobachtungsort	$H_0(\gamma)$	$H_0/e(\gamma)$	$\tau_e(h)$
10. März 1957	Bangui	— 300	— 111	14
11. Februar 1958	Bangui	— 640	— 237	10
11. Februar 1958	Honolulu	— 467	— 173	12
28. Februar 1941	Huancayo	— 685	— 252	5
4. Juli 1941	Huancayo	— 500	— 184	10
17. September 1941	Huancayo	— 400	— 147	12
25. Februar 1956	Apia	— 230	— 85	17
21. April 1956	Apia	— 185	— 69	13
21. Januar 1957	Apia	— 205	— 76	42
8. Juli 1958	Apia	— 265	— 98	16
4. September 1958	Apia	— 270	— 100	19
4. Dezember 1958	Apia	— 120	— 44	22

und für die mittleren ein τ_e von fünfzehn bis zwanzig Stunden. Der Sturm vom 21. Januar 1957 fällt sehr aus dem Rahmen heraus. Die Tatsache, dass starke Stürme schneller abklingen als weniger starke, hat bei Annahme des Gesetzes $dN/dt = -\alpha N$ zur Folge, dass sich die Abklingkonstante α ändern muss; denn τ_e ist $1/\alpha$ und daher nicht vom Anfangswert des Nachstörungseffektes abhängig. Das liesse sich natürlich ohne weiteres durch die Annahme deuten, dass der Ringstrom für stärkere Stürme in Gebieten erhöhter Dichte des neutralen Wasserstoffs fliesst, also in geringeren Entfernungen. Wird jedoch nach AKASOFU [6] angenommen, dass die Aufheizung der Ringstrompartikel durch neutralen Wasserstoff, der sich im Sonnenplasma befindet, verursacht wird, so muss die Aufheizung um so stärker sein, je stärker der Sturm ist. Es ist wahrscheinlich, dass die Partikel energetischer werden. Das aber müsste die mittlere Lebensdauer der Teilchen von etwa 100 keV wieder vergrössern (siehe LIEMOHN). Eine quantitative Durchrechnung stösst auf Schwierigkeiten, da gerade im Gebiet von etwa 100 keV die beobachteten Veränderungen in τ_e durch geringfügige Änderungen in L und der Partikelenergie erklärt werden können.

Wird andererseits für den Nachstörungseffekt mit der Beziehung $dN/dt = -\beta N^2$ gerechnet, so erklärt auch diese Beziehung die Beobachtung, dass stärkere Stürme

eine geringere Abklingzeit besitzen, da

$$\tau_e = \frac{e-1}{N_0 \beta}$$

ist. Hierbei ist die Annahme nicht notwendig, dass sich die Abklingkonstante mit der Zeit verändert. Durch die Veränderung des Maximalwertes des Ringstromeffektes ist bereits eine Änderung von τ_e gegeben. Auf Grund der mittleren Werte für starke Stürme der Tabelle 1 von $H_0 = -500\,\gamma$ und $\tau_e = 10$ Stunden folgt $\beta = 0.34 \cdot 10^{-3}$ $h^{-1}\,\gamma^{-1}$. Das entspricht 0.0082 Tagen^{-1} γ^{-1}. Da

$$dt = -\frac{e-1}{\beta}\,\frac{1}{N_0^2}\,dN_0$$

gilt, folgt mit $dN_0 = 250\,\gamma$ als mittlerer Wert für wenig starke Stürme ein Wert von $dt = 5$ Stunden, was mit den Beobachtungen in etwa übereinstimmt. Im übrigen existiert nach dem quadratischen Gesetz in der ersten Phase der Nachstörung ein schnelles Abklingen und später nur ein sehr langsames. Das ist genau das, was die Beobachtungen zeigen. Figur 15 zeigt die Vorstellung zweier Ringströme von CHAPMAN und AKASOFU für den Sturm vom 11. Februar 1958 für Apia. *DR1* besitzt danach eine Maximalamplitude von 420 γ und ein τ_e von 9.2 Stunden, *DR2* eine Maximalamplitude von 87 γ und ein τ_e von etwa 81 Stunden. Für *DR2* nimmt AKASOFU [6] einen Äquatorabstand von vier Erdradien an. Nach LIEMOHN [5] folgen dafür Partikelenergien von 70 keV. Das ist durchaus plausibel. Theoretisch schwierig zu deuten ist die Tatsache, dass bei Annahme von zwei Sturmzeitringströmen zwischen Auftreten des Maximums von *DR1* und *DR2* eine Phasenverschiebung von etwa einem Tag auftritt. Dabei müsste der maximale Strom bei *DR2* stets später als bei *DR1* erreicht werden. Es kann also als Ursache für *DR2* nicht der neutrale Wasserstoff im Sonnenplasma wie für *DR1* angenommen werden. Gemäss der Parkerschen Theorie wäre eine Aufheizung für $L = 4$ zur Bildung von *DR2* möglich. Aber auch dann darf die Verschiebung der Maxima nicht einen Tag betragen. Für $L > 4$ ist die hydromagnetische Wellengeschwindigkeit nicht so gross wie die Phasengeschwindigkeit, aber

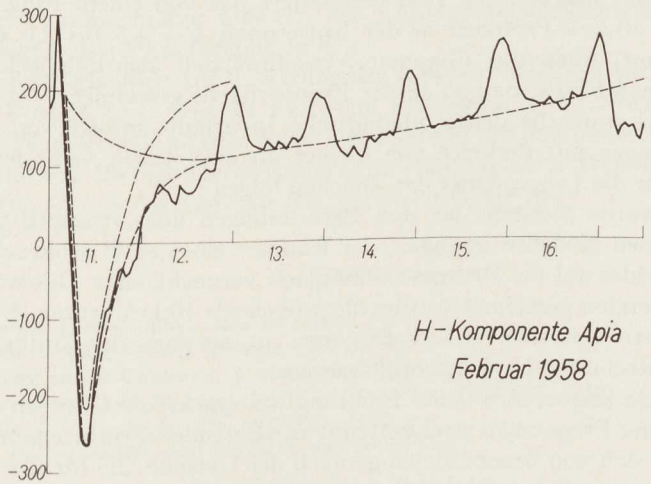

Figur 15
Trennung des Sturmes vom 11. Februar 1958 in zwei *DR*-Anteile

trotzdem ist dann nur eine Verspätung des *DR2*-Maximums von einigen Minuten möglich.

Wenden wir uns noch einmal dem *DR1*-Anteil zu und untersuchen die Gültigkeit der adiabatischen Invarianten für 10-keV-Protonen, die in der Entfernung $L = 2$ eingefangen sind. Die erste adiabatische Invariante wird auf jeden Fall konstant sein, da die Gyrationsperiode einen Wert von $0.098 \cdot 10^{-2}$ *s* besitzt. Die Oszillationsperiode beträgt ungefähr 30 sec und ist ebenfalls sehr klein gegen möglicherweise auftretende Feldänderungen. Immerhin erreichen diese Teilchen während der Oszillation keine geomagnetische Breite $> 45°$. Die Driftperiode für die 10-keV-Protonen beträgt jedoch etwa zwei Tage mit geringen Unterschieden, entsprechend dem äquatorialen Pitchwinkel. Dieser Wert ist so gross, dass mit Feldänderungen gerechnet werden muss und ein Abbruch der dritten Invarianz eintreten wird, wobei die eingefangenen Partikel verlorengehen. Ein eventuell auftretender Abbruch der dritten Invarianz würde, verbunden mit dem Ladungswechselprozess, einen anderen Ablauf der Nachstörungsphase liefern als die Beziehung $dN/dt = -\alpha N$ angibt. Was den Einfluss der Änderungen von L auf die dritte adiabatische Invariante anbetrifft, so ist wohl kaum während eines Sturmes mit Veränderungen von L für solche geringe L-Werte zu rechnen.

3. Diskussion

Die Hypothese von zwei getrennt existierenden Sturmzeitringströmen wurde aufgestellt, weil die beobachteten Nachstörungseffekte nicht mit den theoretisch geforderten übereinstimmen. Uns scheinen jedoch die Gründe, die zur Annahme zweier Ringströme führten, nicht ausreichend genug. Besonders das Beobachtungsmaterial spricht eher für einen einheitlich ablaufenden Ringstromeffekt als für zwei getrennt verlaufende. Jedoch auch die Theorie liefert – wie gezeigt – einige Gesichtspunkte, die sich nicht mit der Hypothese vereinbaren lassen.

Ausserdem bleiben noch einige Gesichtspunkte zu erörtern, für die wir eine quantitative Berechnung für notwendig halten.

1. Wie ist das magnetische Feld beschaffen, das von einem Ringstrom erzeugt wird, der von 10-keV-Protonen in der Entfernung $L = 1.5$ bis 2.0 gebildet wird. Kann überhaupt, wenn das Chapman-Akasofu-Modell zugrunde gelegt wird, mit einem homogenen Ringstromfeld an der Erdoberfläche gerechnet werden?

2. Wie stark wird die dritte adiabatische Invariante infolge von magnetischen Feldveränderungen mit Perioden von kleiner als zwei Tagen verändert? Was wird dann daraus für die Lebensdauer der Teilchen folgen?

3. Bisher wurde meistens bei den Berechnungen über «trapped particles» und besonders bei den Modellrechnungen, der Einfluss eines zu $\mathfrak{B}$ senkrecht gerichteten elektrischen Feldes auf die Driftgeschwindigkeit vernachlässigt. Das war zulässig, da mit Partikelenergien gerechnet wurde, die grösser als 10 keV waren. Nimmt man jedoch als Ringstrompartikel 10-keV-Protonen an, so muss der Einfluss elektrischer Felder in der Rechnung berücksichtigt werden.

Diese Punkte zeigen, in welcher Richtung weitergearbeitet werden muss.

Wird also die Frage nach zwei getrennt existierenden Sturmzeitringströmen verneint, so stellt sich von neuem diejenige nach der Ursache, die für das weltweite Absinken der Horizontalintensität während der Hauptphase von Stürmen verantwortlich ist. Der Sturmzeitringstrom wurde im Laufe der letzten zehn Jahre im Bereich

von 1.5 bis 10 Erdradien Entfernung überall vermutet, aber durch Satelliten nirgends entdeckt. Kann demnach die Ringstromtheorie überhaupt noch Aussicht auf Erfolg haben? Uns scheint eine Möglichkeit gegeben, wenn ein breites Spektrum niederenergetischer Protonen angenommen wird. Die Teilchendichte einer bestimmten Energie genügt der Beziehung $N = N_0\, e^{-\alpha t}$. Dabei ist α eine Funktion der Teilchenenergie. Die Beobachtung des Nachstörungseffektes genügt der Beziehung

$$N = \frac{N_0}{1 + N_0 \beta t}.$$

Es lässt sich theoretisch zeigen, dass bei bestimmter Wahl der entsprechenden Werte α die Beziehung

$$\sum_{\nu=1}^{n} e^{-\alpha_\nu t} \approx \frac{1}{1 + N_0 \beta t}$$

gilt. Werden beide Seiten in eine Reihe entwickelt, so gilt

$$1 - \sum \alpha_\nu t + \frac{\sum \alpha_\nu^2 t^2}{2!} - \frac{\sum \alpha_\nu^3 t^3}{3!} + \frac{\sum \alpha_\nu^4 t^4}{4!} \approx 1 - N_0 \beta t + N_0 \beta^2 t^2 - N_0 \beta^3 t^3 + N_0 \beta^4 t^4 .$$

Die α-Werte müssten denen des Gleichungssystems

$$\begin{aligned} 1!\, N_0 \beta &= \sum \alpha_\nu , \\ 2!\, N_0 \beta^2 &= \sum \alpha_\nu^2 , \\ 3!\, N_0 \beta^3 &= \sum \alpha_\nu^3 , \\ 4!\, N_0 \beta^4 &= \sum \alpha_\nu^4 , \end{aligned}$$

genügen. Der beobachtete Nachstörungseffekt kann demnach als Summe von n-fachen Einzeleffekten aufgefasst werden, die alle dem Ladungswechselprozess mit neutralen Wasserstoffatomen genügen. Das ist nur eine rein qualitative Überlegung. Bei einer quantitativen Durchrechnung müssten die Kopplungserscheinungen zwischen den einzelnen Effekten Berücksichtigung finden.

Eine andere Möglichkeit zur Erklärung des Ringstromeffektes besteht in der Auffassung von PIDDINGTON, dass die weltweite Erniedrigung der Horizontalintensität durch die Vorgänge erklärt werden kann, die während der Stürme den Magnetschweif der Erde verstärken. Im besonderen ist darunter ein verstärktes Wegblasen der magnetischen Kraftlinien von der Tag- zur Nachtseite zu verstehen.

LITERATUR

[1] S. J. AKASOFU, J. of Geophys. Res. *68* (1963), 3345.
[2] S. J. AKASOFU, Space Science Reviews *2* (1963), 91.
[3] S. J. AKASOFU and S. CHAPMAN, J. of Geophys. Res. *68* (1963), 3155.
[4] A. J. DESSLER and E. N. PARKER, J. of Geophys. Res. *64* (1959), 2239.
[5] H. LIEMOHN, J. of Geophys. Res. *66* (1961), 3593.
[6] A. YAKOB, Ind. J. of Met. and Geophys. *15* (1964), 578.

(Eingegangen am 6. Juni 1966)

Magnetic Anisotropy of Laboratory Materials in which Magma Flow is Simulated

By Leong Wing-Fatt[1]) and Frank D. Stacey[1])

Summary – The magnetic anisotropy of lava flows has been simulated using plaster of Paris containing about 2% of nickel filings. The ellipsoid of magnetic anisotropy was oriented with its long axis close to but tilted with respect to the flow direction and its intermediate axis in the flow plane perpendicular to the flow direction; the same alignment was obtained with four different experimental conditions. This result is at variance with observations on basalt flows in which the long axis of the magnetic ellipsoid is perpendicular to the flow direction. It appears likely that the favoured alignment of elongated grains in a fluid or semi-fluid flow is sensitive to physical parameters which have not yet been examined adequately. Reliable magnetic determinations of flow directions in lavas must await clarification of this problem.

1. Introduction

Khan [1][2]) considered the relationship between apparent flow directions and the orientations of the axes of the susceptibility ellipsoids in lava flows and concluded that for each ellipsoid the short axis was perpendicular to the flow plane, the long and intermediate axes being within the plane with the long axis across the flow direction. The fact that the short axis is normal to the flow plane is not in doubt, but the orientations of the intermediate and long axes are much more scattered both in Khan's work on lava flows and Stone's [2] observations on a phonolite ring dyke. Khan referred also to earlier theoretical and experimental work, by Jeffrey [3] and Taylor [4], on the equilibrium orientations of solid ellipsoids immersed in fluids undergoing laminar flow, in which the alignment of long axes across the flow direction was generally favoured.

That the problem may be far from simple is indicated by the observations of Rusnak [5] who considered the orientations of sand grains deposited in moving water. He concluded that when the bottom roughness was comparable with the grain size the long axes would be oriented in the direction of flow, but that if the scale of roughness of the surface on which grains were deposited was much smaller than the grains, then their long axes aligned perpendicular to the flow direction. Although this conclusion cannot be applied directly to the alignment of grains which remain immersed in a solidifying medium we might not unreasonably expect the nature of the

[1]) Physics Department, University of Queensland, Brisbane, Australia.

[2]) Numbers in brackets refer to References, page 80.

medium or grain interactions to influence the grain alignment. In particular the alignment of magnetites in a lava may be determined by the presence or absence of other, larger crystals.

2. Plaster of Paris experiments

A convenient laboratory material which can be used to simulate the viscous flow of lava is plaster of Paris. A magnetic fraction may be incorporated simply by adding powdered basalt. This gives results similar to those obtained by adding 2% of nickel filings, which we have found to be more convenient and have therefore used in most of the experiments reported here. The nickel particles were roughly prolate, averaging 0.5 mm × 0.2 mm.

We have experimented with flowing plasters in the following ways:

Flow 1. – The plaster and nickel were first mixed dry and then placed in a small compartment at one end of a wooden through, 1 m long and 12 cm wide. The mixture was then sprinkled with water and when it was completely wet the end of the trough was raised to an angle of about 40° and a partition removed to allow the plaster to flow down the slope. When the plaster was uniformly distributed down the slope the end of the trough was lowered and the plaster left to dry. Cylindrical cores were then cut from it and their magnetic anisotropy was measured using a simple high field torque meter [6] with a permanent magnet on a rotating stand.

Flow 2. – This experiment was similar to flow 1 except that the plaster was wetted in small batches to produce a succession of superimposed flows, each of which was allowed to harden before the next flowed over it. The bulk of the plaster was allowed to collect at the bottom of the slope as a series of nearly horizontal layers which were sampled for anisotropy measurements.

Flow 3. – This was a repeat of flow 1 except that 1 mm glass beads comprised the bulk of the flowing material and just enough plaster was added to make the beads stick together so that cores could be cut from the flow. Being much smaller than the beads the nickel grains settled into spaces between them, the alignment of the nickel grains being (presumably) determined by the rolling of the beads rather than the viscosity of the fluid plaster.

Flow 4. – Laminar flow of the plaster was obtained by filling with wet plaster the annular space between two concentric cylindrical tins, the outer one being fixed and the inner one rotated. The diameter of the annulus was about 17 cm and its thickness about 1.5 cm. Rotation of the inner cylinder was maintained until hardening of the plaster made this difficult.

3. Results and conclusion

In all four experiments the alignment of nickel grains indicated by the anisotropy measurements was substantially the same. The long axes were close to the flow direction but were tilted out of the flow plane by about 12° in experiments without glass beads and 22° in the experiment with beads. In the first three experiments, in which the flow plane was horizontal, the intermediate axes lay in the flow plane perpendicular to the flow direction, but in flow 4, in which the flow plane was vertical, the

intermediate axes were inclined to the flow plane at angles which averaged 25° but were quite widely scattered.

The scatter of measured axes was generally 5 to 10°. This was shown to be a statistical effect arising from the finite numbers of grains in each specimen [7], by measurements on samples of plaster from each batch which were not subjected to flow.

In view of their contradiction with our expectation the consistency of these results is quite striking. Care was taken to ensure that the plaster was finely powdered before use and that any graininess would be on a small scale compared with the nickel, but the deliberate introduction of large grains in the form of small beads did not affect the result. If the glass beads had been elongated instead of spherical their effect could have been different, but when we tried pouring a box full of cylindrical ceramic insulators down the slope, expecting them to roll down with long axes across the direction of flow, we found instead that they tended rather to slide across one another lengthwise down the slope, giving the same grain alignment as was indicated by the magnetic experiments.

The conflict between these measurements and KHAN's [1] observations on lava flows leaves the whole matter open to doubt. The only certain fact is that the minimum axes of the magnetic ellipsoids are nearly normal to the flow planes, but as these planes are almost invariably close to horizontal the minimum axes hardly provide useful information. If further work on well documented lava flows consistently confirms KHAN's conclusion, it will indicate an inadequacy of the plaster modelling. In any case, it will be necessary to produce laboratory materials in which long axes of grains align themselves perpendicular to the flow as well as materials in which they are parallel to it before we can claim to understand the problem physically. Meanwhile any conclusions about lava flow directions deduced from magnetic anisotropy measurements must be regarded as tentative.

4. Acknowledgement

In preparing this report of our experiment we have been aided by correspondence with Drs. R. F. KING, M. A. KHAN and A. I. REES.

REFERENCES

[1] M. A. KHAN, *The anisotropy of magnetic susceptibility of some igneous and metamorphic rocks*, J. Geophys. Res. *67* (1962), 2873.

[2] D. B. STONE, *Anisotropic magnetic susceptibility measurements on a phonolite and a folded metamorphic rock*, Geophys. J. Roy. Astro. Soc. *7* (1963) 375.

[3] G. B. JEFFERY, *The motion of ellipsoidal particles immersed in a viscous fluid*, Proc. Roy. Soc., London [A], *102* (1922), 161.

[4] G. I. TAYLOR, *The motion of ellipsoidal particles in a viscous fluid*, Proc. Roy. Soc., London [A], *103* (1923), 58.

[5] G. A. RUSNAK, *The orientation of sand grains under conditions of 'unidirectional' fluid flow*, J. Geol. *65* (1957), 384.

[6] F. D. STACEY, *Magnetic anisotropy of dispersed powders*, Aust. J. Phys. *13* (1960), 196.

[7] F. D. STACEY, *Magnetic anisotropy of ingenous rocks*, J. Geophys. Res. *65* (1960), 2429.

(Received 18th May 1966)

The Magnetic Anisotropy of Hematite Bearing Rocks

HARTMUT PORATH and FRANÇOIS H. CHAMALAUN[1])

Summary – The high field torque curves of hematite bearing rocks are not caused by directional differences in the energy of magnetization to saturation, but rather by the couple between the ferromagnetic moment and the applied field. An expression, derived for the high field torque curve of a single crystal of hematite, whose basal plane makes an arbitrary angle with the plane of rotation of the applied field, is found to be in excellent agreement with experiment. Furthermore it is shown that the Fourier spectrum of hematite bearing rocks should in general contain significant higher harmonics and that therefore the high field method is not particularly suitable for determining the preferred crystalline alignment of hematite bearing rocks.

1. Introduction

Magnetic anisotropy measurements on rocks have proved to be a valuable tool for studying grain orientations (see references [1 to 6][2]). The most important minerals responsible for the magnetic anisotropy are the cubic titano-magnetites and rhombohedral ilmeno-hematites. Magnetic anisotropy is measured in terms of the couple experienced by a specimen when suspended in either a relatively weak alternating magnetic field or a saturating steady field. The torque is observed as a function of the azimuth angle, θ, of the applied field relative to a reference mark on the specimen.

In the low field method the torque results from the differences of susceptibility in the plane of measurement [7, 8], and the torque curve should show essentially a $\sin 2\theta$ dependence for both the cubic and rhombohedral minerals. The physical origin of the $\sin 2\theta$ term is, however, different for the two kinds of minerals. In the case of the titano-magnetites it results from shape alignment. In hematite, on the other hand, the susceptibility depends on the crystallographic direction, because it is weakly ferromagnetic in the basal plane and paramagnetic along the trigonal axis. Shape alignment is negligible and the observed anisotropy is due to crystalline alignment only [9].

In the high field method the torque results from the dependence of the energy of magnetization to saturation on direction [10]. Shape alignment of the titano-magnetites gives rise to a $\sin 2\theta$ term, although higher harmonics could be present, if there is also a preferred alignment of crystallographic axes. In most igneous rocks, however, where the titano-magnetites are the predominant minerals, crystalline aniso-

[1]) Department of Geophysics and Geochemistry, Australian National University, Canberra, Australia.

[2]) Numbers in brackets refer to References, pages 87/88.

tropy appears to be negligible [6]. As in the low field method, hematite should give rise to a crystalline anisotropy only, because its ferromagnetic moment is too small to produce a significant shape anisotropy. STACEY [9] suggested that the crystalline anisotropy of hematite would also result in a $\sin 2\theta$ torque curve. It appears therefore that both methods should give the same result with regard to the orientation of the magnetic anisotropy ellipsoid. Since the high field method is much more rapid and convenient in operation than the low field method it seemed preferable for use as a routine method.

The purpose of this paper is to show, however, that the torque curves of hematite bearing rocks arise from a different property and must be expected to contain significant higher harmonics.

2. *Torque curves of single crystals of hematite*

In the case of magnetite the spontaneous magnetization is always parallel to a saturating applied field, but the energy of magnetization to saturation depends on direction due to the shape and crystalline anisotropies of the crystal.

In contrast the ferromagnetic moment I_s of hematite is confined to the basal plane of the crystal [11, 12]. For the purpose of calculation we assume the basal plane to be isotropic. Then a hematite crystal, whose basal plane makes an angle ϕ with the plane in which the applied field H is rotated, will experience a torque

$$\vec{T} = \vec{I_{sp}} \times \vec{H} ,$$

where I_{sp} is the component of the saturation magnetization I_s, in the plane of rotation.

The geometry is shown schematically in figure 1. Suppose that H makes an angle θ with the intersection of the two planes, then since I_s is parallel to the component of H in the basal plane, it makes an angle α with the line of intersection that is given by

$$\tan\alpha = \tan\theta \cos\phi .$$

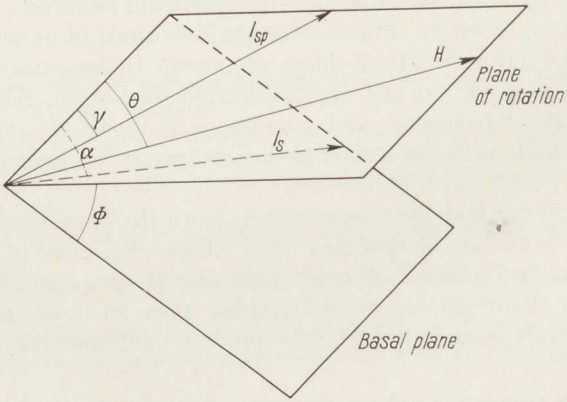

Figure 1
Angular relations between the basal plane and the plane of rotation of the applied field

The component of I_s in the plane of rotation, I_{sp}, makes an angle γ with the intersection line which is given by

$$\tan\gamma = \tan\alpha \cos\phi = \tan\theta \cos^2\phi \,.$$

Since

$$I_{sp} = I_s \sqrt{\cos^2\alpha + \sin^2\alpha \cos^2\phi}$$

we find for the torque in the plane of rotation

$$\left.\begin{aligned} T &= I_{sp} H \sin(\theta - \gamma) \\ &= I_s H \frac{\sin\theta \sin^2\phi}{\sqrt{1 + \tan^2\theta \cos^2\phi}} \,. \end{aligned}\right\} \qquad (1)$$

Equation (1) shows that the shape of the torque curve depends on the orientation of the basal plane with respect to the plane of rotation and is not a simple $\sin 2\theta$ curve. However, for small angles ϕ equation (1) can be approximated to

$$T = I_s H \frac{\delta}{2} \sin 2\theta \,, \qquad (2)$$

where $\delta = \sin^2\phi$.

On the other hand the torque in a plane containing the trigonal axis, i.e. $\phi = 90°$, is simply

$$\begin{aligned} T_{\phi=90°} &= I_s H \sin\theta \quad 0 \leq \theta \leq 90° \\ &= -I_s H \sin\theta \quad 90° \leq \theta \leq 180° \end{aligned}$$

and has a discontinuity at $\theta = 90°$. This arises from the fact that I_s reverses its direction.

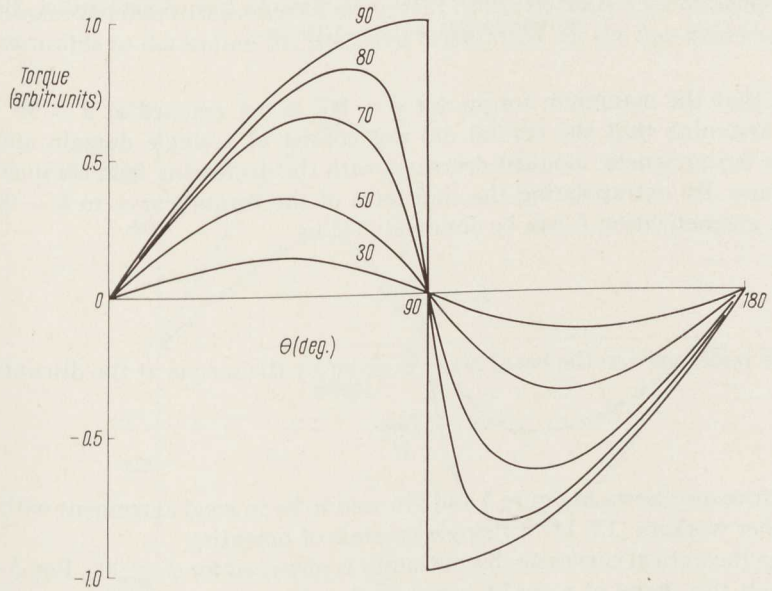

Figure 2
Torgue curves computed from equation 1 for various angles ϕ

Figure 2 shows the torque curves computed from (1) for different values of θ. No discontinuity occurs for $\phi \neq 90°$, as I_s rotates continuously in the basal plane. For $\phi < 50°$ the torque curve can be closely approximated by a $\sin 2\theta$ term.

Figure 3 shows the experimental torque curves obtained for a natural single crystal of hematite from Schabrowskoi, Ural. The agreement with figure 2 is excellent bearing in mind that the orientation of the basal plane of the crystal with respect to H was not better than 5°.

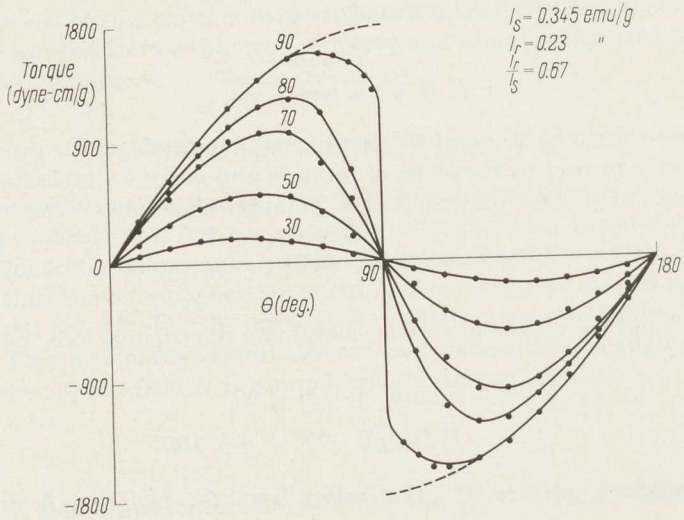

Figure 3
High field torgue curves for a natural single crystal of hematite from Schabrowskoi, Ural, for various angles ϕ; $H = 5200$ Oe

The fact that the maximum torque for $\phi = 90°$ is not reached at $\theta = 90°$ is explained by assuming that the crystal did not consist of a single domain and that therefore the ferromagnetic moment decreases with the decreasing field component in the basal plane. By extrapolating the $\sin\theta$ term of the torque curve to $\theta = 90°$ the spontaneous magnetization I_s can be obtained [14] by

$$I_s = \frac{T_{extr}}{H}.$$

Similarly the remanence in the basal plane is given by the torque at the discontinuity

$$I = \frac{T_{disc}}{H}.$$

These quantities are shown in figure 3 and are seen to be in good agreement with those found by other workers [13, 14] for single crystals of hematite.

As for the theoretical curves no discontinuity is observed for $\phi < 90°$. For $\phi < 50°$ they approach the shape of a $\sin 2\theta$ curve as is evident from the Fourier analyses presented in table 1. These also show that for $\theta > 50°$ significant higher harmonics are

Table 1

Fourier analyses of torque curves of a single crystal of hematite; torques in dyne-cm/g

	$\phi = 90°$		$\phi = 80°$		$\phi = 70°$		$\phi = 50°$		$\phi = 30°$	
	Ampl.	Phase	Ampl.	Phase	Ampl.	Phase	Ampl.	Phase	Ampl.	Phase
$\sin 2\theta$	1406	+ 14.6°	1145	+ 9.4°	969	+ 9.4°	489	+ 11.4°	186	+ 9.4°
$\sin 4\theta$	595	+ 31.1°	347	+ 18.9°	233	+ 18.9°	50	+ 4.1°	12	+ 19.4°
$\sin 6\theta$	281	+ 55.0°	62	+ 28.4°	10	+ 28.4°	39	+ 21°	9	+ 28.5°
$\sin 8\theta$	251	+ 68.1°	64	+ 37.8°	33	+ 37.8°	42	+ 7.4°	7	+ 37.1°
$\sin 10\theta$	169	− 84.2°	13	+ 47.3°	21	+ 47.3°	21	+ 69°	5	+ 46.8°
$\sin 12\theta$	169	− 74.7°	23	+ 56.8°	13	+ 56.8°	36	− 67°	2	+ 59.5°

present. The maximum torque for $\phi = 80°$ and $\phi = 70°$ is not reached at the expected value of θ, again, because of the multidomain behaviour of the crystal.

It is seen from figure 3 that the basal plane anisotropy of this particular crystal is, indeed, negligible, as assumed in the calculations. However, basal plane anisotropies and coercive forces vary substantially from crystal to crystal [13]. Furthermore they are in general not simply related to the crystallographic axes in the basal plane. It does not seem justified at present to complicate the calculations by taking their effect into account. Qualitatively one may see that a basal plane coercive force will extend the range of angle ϕ over which the discontinuous torque curve occurs.

3. Torque curves of hematite bearing rocks

In some types of iron ores, in sedimentary and metamorphic rocks the magnetic anisotropies are due to a preferred alignment of the trigonal axes of hematite and it is often desirable to determine the preferred orientation. In the low field torque method

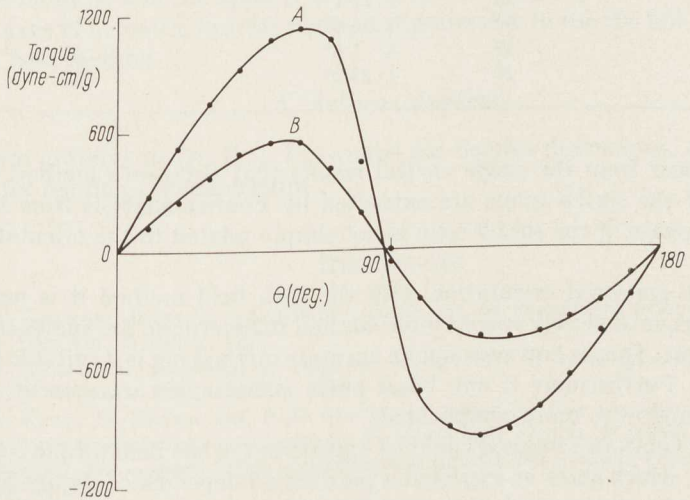

Figure 4

High field torgue curves for two specimens of hematite ore; $H = 5200$ Oe

this is done by assuming that the torque can be represented by a second rank tensor and that the torque curves are essentially of $\sin 2\theta$ dependence. The torques are measured in three mutual perpendicular planes at 45° degree intervals of θ. The computational procedure is described in some detail by GRANAR [7] and KING and REES [8].

GRANAR's method, however, cannot be used for the high field torque curves of hematite bearing rocks. From the results of single crystals of hematite it is obvious that the torque curves cannot be expected to be pure $\sin 2\theta$ curves, but that in general they must contain significant higher harmonics, especially when measured in a plane making a small angle with the preferred alignment of trigonal aces. This was confirmed by measuring the high field torque curves for two specimens of hematite ore. Specimen *A* comes from a small iron ore deposit in South Australia and is almost entirely made up of large thin flakes of specular hematite. It shows a distinct macroscopic alignment of basal planes. The torque was measured in a plane roughly perpendicular to the basal planes. Specimen *B* comes from a high-grade hematite orebody on Cockatoo Island, Western Australia [15]. It is much finer grained and shows no obvious crystalline alignment. The two torque curves are shown in figure 4 and the Fourier components are listed in table 2. In both cases higher harmonics are present. The torque curve of specimen *A* shows substantial higher harmonics indicating that the measuring plane was indeed close to the plane containing the preferred direction of the trigonal axes.

Table 2

Fourier analyses of the high field torque curves of two specimens of hematite ore: torques in dyne-cm/g

	Specimen A		Specimen B	
	Ampl.	Phase	Ampl.	Phase
$\sin 2\theta$	972	+ 11.4°	488	+ 8.9°
$\sin 4\theta$	295	+ 34.5°	109	+ 34.0°
$\sin 6\theta$	93	+ 11.1°	25	+ 4.1°
$\sin 8\theta$	82	+ 36.6°	17	+ 13.0°
$\sin 10\theta$	37	+ 1.6°	17	+ 14.3°
$\sin 12\theta$	27	+ 23.0°	11	+ 22.6°

It is also clear from the single crystal results that GRANAR's method cannot be applied even if the $\sin 2\theta$ terms are extracted by Fourier analysis from the torque curves, as the phase of the $\sin 2\theta$ term is not simply related to the orientation of the trigonal axes.

To find the preferred orientation with the high field method it is necessary to measure the torque at closely spaced intervals and to determine the angles corresponding to zero torque. This, is however, not an accurate method nor is it suitable for routine measurements. Furthermore if any basal plane anisotropies are present, the interpretation becomes even more complicated.

In contrast GRANAR's method could be applied to the low field torque curves of the two specimens, which show as expected a pure $\sin 2\theta$ dependence (figure 5).

In the case of rocks in which both hematite and magnetite contribute to the torque curves, the hematite contribution will give rise to errors when calculating the average

shape alignment of magnetite. It is, however, in principle possible to decide whether the torque is mainly due to hematite or magnetite, because the hematite torque increases linearly with field, whereas the magnetite torque should reach a saturation value.

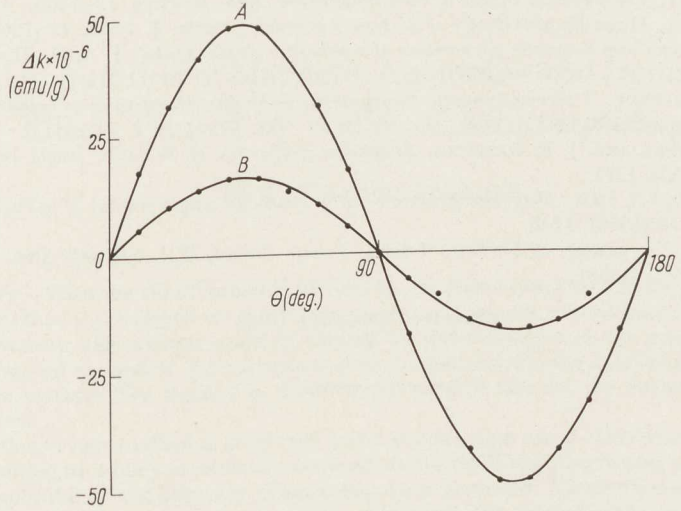

Figure 5
Low field torgue curves for two specimens of hematite ore

4. Conclusion

We conclude that the high field torque curves of hematite are not due to differences in the energy to saturation but that they result from the couple between the ferromagnetic moment and the applied field. To determine the preferred alignment of the trigonal axes of hematite bearing rocks, it is preferable to use the low field rather than the high field method.

5. Acknowledgements

We are grateful to Dr. P. J. Flanders for helpful discussions, and to Dr. F. D. Stacey for reading the manuscript.

References

[1] F. W. Graham, *Magnetic susceptibility anisotropy, an unexploited petrofabric element*, Bull. Geol. Soc. Am. *65* (1954), 1257.

[2] M. A. Khan, *The anisotropy of magnetic susceptibility of some igenous and metamorphic rocks*, J. Geophys. Res. *67* (1962), 2873.

[3] M. A. Khan, H. Brown and F. D. Stacey, *A search for flow structure in columnar basalt using magnetic anisotropy measurements*, Pure and appl. Geoph. *57* (1964), 61.

[4] R. F. King, *The magnetic fabric of granites from Galway and Donegal, Ireland*, J. of Geology *5* (1966), 43.

[5] F. D. Stacey, G. Joplin and J. Lindsay, *Magnetic anisotropy and fabric of some foliated rocks from SE Australia*, Geof. pura e appl. *47* (1960), 30.

[6] F. D. Stacey, *Magnetic anisotropy of igneous rocks*, J. Geophys. Res. *65* (1960), 2429.
[7] L. Granar, *Magnetic measurements on Swedish varved sediments*, Arkiv för Geofysik *3* (1958), 1.
[8] R. F. King and A. I. Rees, *Measurements of the anisotropy of magnetic susceptibility of rocks by the torque method*, J. Geoph. Res. *67* (1962), 1565.
[9] F. D. Stacey, *The physical theory of rock magnetism*, Adv. in Phys. *12* (1963), 45.
[10] F. D. Stacey, *Magnetic anisotropy of dispersed powders*, Austr. J. Phys. *13* (1960), 196.
[11] T. J. Lin, *Some new magnetic phenomena of a hematite single crystal*, J. Appl. Phys. Suppl. *30* (1959), 3065.
[12] I. Dzyaloshinsky, *A thermodynamic theory of the weak ferromagnetism in hematite*, J. Phys. Chem. Solids *4* (1958), 241.
[13] P. J. Flanders and J. P. Remeika, *Magnetic properties of hematite single crystals*, Phil. Mag. *11* (1965), 1271.
[14] A. Tasaki and S. Iida, *Magnetic properties of a synthetic single crystal of* α-Fe_2O_3, J. Phys. Soc. Japan *18* (1963), 1148.
[15] I. W. Reid, *The geology of Cockatoo Island, Yampi Sound, WA*, Stilwell Ann. Vol., Austr. Inst. Min. Met. (1958).

(Received 23rd May 1966)

Rapid Computation of Magnetic Anomalies and Demagnetization Effects Caused by Bodies of Arbitrary Shape[1])

By P. Vallabh Sharma[2])

Summary – With the aid of formulae derived for the field caused by a finite rectangular prism, a machine method is developed for rapid computation of magnetic anomalies due to a body of any shape. Conversely, the method could be utilised for determination of the magnetization vector from the observed anomalies. An example is given to demonstrate the applicability, accuracy and speed of the method. The method is shown to be suitable also for the evaluation of magnetic terrain effects.

In addition, a new method is presented which enables high speed calculation of demagnetization effect caused by a body of arbitrary shape where the magnetization in general may be inhomogeneous. Applicability and accuracy of the method are discussed. The method is applied to study the effect of susceptibility on inhomogeneity of the induced magnetization in a cube specimen.

For a body of any shape with low susceptibility, a new concept of average demagnetization factor is introduced. Average demagnetization factors so calculated for a cylindrical specimen are tabulated.

Zusammenfassung – Unter Anwendung der Formeln für das Feld eines Quaders wird eine Methode entwickelt um die durch einen Körper beliebiger Form erzeugten magnetischen Anomalien mit Hilfe eines Rechenautomaten zu berechnen. Umgekehrt kann die Methode verwendet werden, um aus den beobachteten Anomalien den Magnetisierungsvektor zu bestimmen. An einem Beispiel wird die Anwendbarkeit, die Genauigkeit und die Schnelligkeit der Methode erläutert. Die Methode kann auch für die Berechnung von magnetischen Terraineffekten verwendet werden.

Zudem wird eine neue Methode dargelegt, welche eine rasche Berechnung des Entmagnetisierungseffektes eines Körpers beliebiger Gestalt und inhomogener Magnetisierung ermöglicht. Anwendbarkeit und Genauigkeit der Methode werden besprochen. Die Methode wurde verwendet, um den Einfluss der Suszeptibilität auf die Inhomogenität der induzierten Magnetisierung in einem Würfel zu untersuchen.

Für Körper beliebiger Form mit kleiner Suszeptibilität wird als neuer Begriff der mittlere Entmagnetisierungsfaktor eingeführt. Mittlere Entmagnetisierungsfaktoren für eine zylindrische Probe werden tabelliert.

§ 1 *Introduction*

In the qualitative and quantitative interpretation of magnetic field data, theoretical calculation of field anomalies of various types of model sources plays an important role. The usual methods of gravity interpretation become more complicated for the magnetic case because of the additional parameter of the direction of magneti-

[1]) Part I of the dissertation 'Theoretical study of the magnetic attraction due to rock bodies and experimental investigation of the stability of rock magnetism' submitted to the Swiss Federal Institute of Technology (ETH), Zurich, for the degree of Doctor of Natural Sciences.

[2]) Department of Geophysics, Swiss Federal Institute of Technology, Zurich, Switzerland.

zation. This complication is further enhanced by the frequent presence of remanent magnetization in rocks which in association with the induced magnetization tends to orient the magnetization vector in some arbitrary direction. Thus the number of combinations of various parameters possible for a model source becomes large enough to make the calculation of theoretical profiles by conventional methods (e.g., GASSMANN [7][3]), HENDERSON and ZIETZ [10], VACQUIER *et al.* [18]) very laborious and time consuming.

Practically all the existing methods ignore the demagnetization effect of a rock body while computing its anomaly. However, for certain igneous masses and ore bodies the demagnetization effect could be quite significant so as to considerably reduce the effective magnetization induced in such bodies. Evaluation of demagnetization field inside a finite body of non-ellipsoidal geometry is an intricate problem of the potential theory. Various conventional approaches so far made in this direction ([14, 21, 3, 22]) are confined to bodies of cylindrical shape and as such are of only limited application.

The tremendous speed and high precision attainable by modern computers make it possible to attack such problems of involved nature with remarkable success. For this simple reason, at present an ever increasing use is being made of methods applicable to fast computers.

In the present paper two methods are described which have been specifically developed to enable high speed computation of magnetic anomalies and demagnetization effect caused by a finite body of arbitrary shape. Some of the mathematical and physical concepts employed in the development of the two methods are not readily available in the literature and have been, therefore, discussed elaborately later at appropriate stages.

The programme of the two methods have been developed from basic formulae for the field of a finite rectangular prism and have been written in ALGOL for operation on the CDC–1604 computer of the Swiss Federal Institute of Technology.

§ 2 *Derivation of basic formulae*

Amongst bodies of simple geometry which permit derivation of analytical expressions for their magnetic field, a rectangular prism deserves a special mention. In magnetic interpretation, various kinds of prismatic models are very often employed to approximate geological bodies like dykes, volcanic flows and sills. Formulae for magnetic anomalies of certain specific prism models exist in the literature but these are valid only for the case of induced magnetization in the earth's field. The basic formulae derived here are, however valid for an arbitrary direction of the magnetization vector.

As demonstrated later, these basic formulae enable the calculation of anomalies not only of various prismatic models but also of a body of arbitrary shape.

§ 2.1 *Expressions for the field of a rectangular prism*

We consider a right-handed system of coordinates with the axes x_1, x_2, x_3 pointing towards geographical north, east and vertically downwards respectively.

[3]) Numbers in brackets refer to References, pages 108/109.

The magnetic field at any point $P(y_1, y_2, y_3)$ due to a body of volume V and magnetization $J(x_1, x_2, x_3)$ is given by the well known formula

$$H = \text{grad}^2 \int_V J \cdot (r)^{-1} \, dV \,, \tag{1}$$

where

$$r = \sqrt{(y_1 - x_1)^2 + (y_2 - x_2)^2 + (y_3 - x_3)^2} \,.$$

Assuming J to be uniform all over the body, equation (1) could be written in terms of components as

$$H_i = \sum_{k=1}^{3} J_k \cdot T_{ik} \,, \tag{2}$$

where

$$T_{ik} = \frac{\partial^2}{\partial x_i \, \partial x_k} \int_V \left(\frac{1}{r}\right) dV \,. \tag{3}$$

With $i, k = 1, 2, 3$ the meanings of H_i and J_k are self explanatory and therefore

$$H_1 = J_1 \cdot T_{11} + J_2 \cdot T_{12} + J_3 \cdot T_{13} \,, \tag{4a}$$

$$H_2 = J_1 \cdot T_{21} + J_2 \cdot T_{22} + J_3 \cdot T_{23} \,, \tag{4b}$$

$$H_3 = J_1 \cdot T_{31} + J_2 \cdot T_{32} + J_3 \cdot T_{33} \,. \tag{4c}$$

It is easy to see from equation (3) that $T_{ik} = T_{ki}$. Further, by virtue of Laplace's equation, $T_{11} + T_{22} + T_{33} = 0$ for an external point. Thus, for evaluation of H_1, H_2, H_3 it should suffice to calculate only 5 (instead of 9) components of the orthogonal tensor namely, T_{12}, T_{13}, T_{23} and any two from T_{11}, T_{22}, T_{33}.

The calculation of the aforesaid components of T_{ik} for the case of a rectangular prism involves no considerable difficulty, since by application of the Gauss divergence theorem the volume integrals can be readily converted into a set of surface integrals which become comparatively simple to be evaluated. The final expressions obtained for the case of a prism with sides parallel to the three axes and extending from a_1 to b_1, a_2 to b_2, and a_3 to b_3 respectively are written below:

$$\left.\begin{aligned} T_{11} = {} & \arctan\left[\frac{v_2 \, w_2}{u_1 \sqrt{w_2^2 + R_2}}\right] - \arctan\left[\frac{v_1 \, w_2}{u_1 \sqrt{w_2^2 + R_1}}\right] \\ & + \arctan\left[\frac{v_1 \, w_1}{u_1 \sqrt{w_1^2 + R_1}}\right] - \arctan\left[\frac{v_2 \, w_1}{u_1 \sqrt{w_1^2 + R_2}}\right] \\ & + \arctan\left[\frac{v_1 \, w_2}{u_2 \sqrt{w_2^2 + R_3}}\right] - \arctan\left[\frac{v_2 \, w_2}{u_2 \sqrt{w_2^2 + R_4}}\right] \\ & + \arctan\left[\frac{v_2 \, w_1}{u_2 \sqrt{w_1^2 + R_4}}\right] - \arctan\left[\frac{v_1 \, w_1}{u_2 \sqrt{w_1^2 + R_3}}\right] , \end{aligned}\right\} \tag{5a}$$

$$\left.\begin{aligned} T_{12} = {} & \log\left[\frac{w_2 + \sqrt{w_2^2 + R_1}}{w_1 + \sqrt{w_1^2 + R_1}}\right] - \log\left[\frac{w_2 + \sqrt{w_2^2 + R_2}}{w_1 + \sqrt{w_1^2 + R_2}}\right] \\ & + \log\left[\frac{w_2 + \sqrt{w_2^2 + R_4}}{w_1 + \sqrt{w_1^2 + R_4}}\right] - \log\left[\frac{w_2 + \sqrt{w_2^2 + R_3}}{w_1 + \sqrt{w_1^2 + R_3}}\right] , \end{aligned}\right\} \tag{5b}$$

where $u_1, u_2, v_1, v_2, w_1, w_2$ stand for $y_1 - b_1$, $y_1 - a_1$, $y_2 - b_2$, $y_2 - a_2$, $y_3 - b_3$, $y_3 - a_3$ respectively and R_1, R_2, R_3, R_4 stand for $(u_1^2 + v_1^2)$, $(u_1^2 + v_2^2)$, $(u_2^2 + v_1^2)$, $(u_2^2 + v_2^2)$ respectively.

Expressions for the remaining components namely, T_{22}, T_{13} and T_{23} could be obtained from the above equations (5) directly by an appropriate rotation of the coordinate system for each case. Thus all the components of T_{ik} being evaluated, the field in any direction could be easily calculated from equations (4) for any arbitrary direction of the magnetization vector.

In the above treatment, three sides of a rectangular prism are assumed parallel to the axes of the coordinate system. The case of an inclined prism could be dealt with by a rotation and simultaneous translation of the axes and thereafter substituting new values of coordinates in place of y_1, y_2 and y_3.

Expressions for all possible cases of prismatic models could be directly obtained from the formulae derived above. Cases of some important models could be treated as follows:

a) For the bottomless vertical prism model, the formulae are easily obtained from the equations system (5) just by making the lower vertical dimension infinitely large.

b) The formulae for a thin horizontal slab (rectangular plate) are considerably simplified, since the thickness $\Delta h \ll y_3$ and therefore, the integration with respect to the vertical axis is not essential. The final expressions obtained in this case for the T_{ik} components are as written below:

$$T_{11} \cong \frac{u_1 \cdot \Delta h}{y_3^2 + u_1^2}\left(\frac{v_2}{\sqrt{y_3^2 + R_2}} - \frac{v_1}{\sqrt{y_3^2 + R_1}}\right) - \frac{u_2 \cdot \Delta h}{y_3^2 + u_2^2}\left(\frac{v_2}{\sqrt{y_3^2 + R_4}} - \frac{v_1}{\sqrt{y_3^2 + R_3}}\right), \tag{6a}$$

$$T_{22} \cong \frac{v_1 \cdot \Delta h}{y_3^2 + v_1^2}\left(\frac{u_2}{\sqrt{y_3^2 + R_3}} - \frac{u_1}{\sqrt{y_3^2 + R_1}}\right) - \frac{v_2 \cdot \Delta h}{y_3^2 + v_2^2}\left(\frac{u_2}{\sqrt{y_3^2 + R_4}} - \frac{u_1}{\sqrt{y_3^2 + R_2}}\right), \tag{6b}$$

$$T_{13} \cong \frac{y_3 \cdot \Delta h}{y_3^2 + u_1^2}\left(\frac{v_2}{\sqrt{y_3^2 + R_2}} - \frac{v_1}{\sqrt{y_3^2 + R_1}}\right) - \frac{y_3 \cdot \Delta h}{y_3^2 + u_2^2}\left(\frac{v_2}{\sqrt{y_3^2 + R_4}} - \frac{v_1}{\sqrt{y_3^2 + R_3}}\right), \tag{6c}$$

$$T_{23} \cong \frac{y_3 \cdot \Delta h}{y_3^2 + v_1^2}\left(\frac{u_2}{\sqrt{y_3^2 + R_3}} - \frac{u_1}{\sqrt{y_3^2 + R_1}}\right) - \frac{y_3 \cdot \Delta h}{y_3^2 + v_2^2}\left(\frac{u_2}{\sqrt{y_3^2 + R_4}} - \frac{u_1}{\sqrt{y_3^2 + R_2}}\right), \tag{6d}$$

$$T_{12} \cong \Delta h\left(\frac{1}{\sqrt{y_3^2 + R_1}} - \frac{1}{\sqrt{y_3^2 + R_2}} + \frac{1}{\sqrt{y_3^2 + R_4}} - \frac{1}{\sqrt{y_3^2 + R_3}}\right), \tag{6e}$$

$$T_{33} = -(T_{11} + T_{22}), \tag{6f}$$

the last relation being also verified through derivation of an independent expression for the T_{33} component.

As shown later, the above formulae for a thin rectangular plate could be easily programmed for a digital computer. By a suitable stacking of such plates a three-dimensional body of any shape could be approximated for evaluation of its magnetic effect.

c) For inclined sheet like bodies such as dykes, veins, the corresponding formulae could be obtained from equations (6) just by rotation of the coordinate system.

The computation of field anomalies follows from the equations (4). H_3 gives directly the vertical field anomaly ΔZ, and the horizontal anomaly ΔH could be cal-

culated from H_1 and H_2 together with the knowledge of the earth's horizontal field and declination by usual formulae given in the literature, e.g., GASSMANN and WEBER [8]. The total field anomaly $\Delta T \ll T$ is easily obtained from the following relation

$$\Delta T \cong H_1 \cos D \cos I + H_2 \sin D \cos I + H_3 \sin I \,, \tag{7}$$

where D and I are the declination and inclination of the earth's field.

§ 2.2 *Field due to a prism at an inside point*

So far we have been concerned with the computation of field due to a body at an external point. As shown later, for certain problems a knowledge of inner field is often required. From concepts of the potential theory it could be shown that the expressions derived for the T_{ik} components vide equations (5) hold good both for an external as well as an internal point. However, it should be pointed out that the expressions given by equations (5) are not valid for a point lying on the surface of the prism body. Furthermore, the relation $T_{11} + T_{22} + T_{33} = 0$, is not valid for an internal point, and has to be replaced by the POISSON's relation namely, $T_{11} + T_{22} + T_{33} = -4\pi$. As demonstrated later in § 4.2, evaluation of the T_{ik} components at points inside a body is helpful in calculation of the demagnetization effect due to the shape of the body.

§ 3 *Computation of magnetic anomalies of a body of any shape*

In evaluation of the field anomalies of a finite body of irregular shape, the fundamental problem is of triple integration. As already pointed out, for an arbitrary direction of the magnetization vector the graphical methods of integration involve colossal amount of labour and therefore, numerical methods applicable to fast computers are at present in wide use.

§ 3.1 *Review of machine methods*

Three methods have been recently suggested (VACQUIER [17], BOTT [2], TALWANI [16]) which are designed for high speed calculation of anomalies. VACQUIER and BOTT divide the body into a number of line elements and in effect perform a single analytical integration along the direction of the line element and a numerical integration over the plane defined by the other two axes. TALWANI performs a double analytical integration for a polygonal surface and a single integration numerically. The later method has the advantage of the convenience in describing the geometry of the body, but the analytical formulae required to be evaluated by the computer in this case are much more involved than those used in the former two methods.

On the other hand, the method to be described in this paper possesses both the advantages namely, of the ease in description of the geometry of the body and of using comparatively simple analytical formulae in the computation of anomalies.

§ 3.2 *Principle of the rectangular plate method*

In this method a body is first represented by contours at different elevations. Each contour representing the arbitrary cross-section of the body is then approximated by a number of rectangular blocks of varying dimensions. Thus in effect, the body is

divided into a number of horizontal rectangular plates of small thickness as shown in the figure 1. By summing the effects of the total number of plates, the magnetic effect of the whole body is evaluated.

Expressions derived in § 2.1 for the magnetic effect of a rectangular plate are in a form suitable for evaluation by a fast computer. It is easy to see from equations (4) that main bulk of calculation lies in the evaluation of T_{11}, T_{22}, T_{12}, T_{13} and T_{23} components and once these have been evaluated by the computer, calculation of anomalies for several different values of magnetization components could be done concurrently without any significant rise in the computation time.

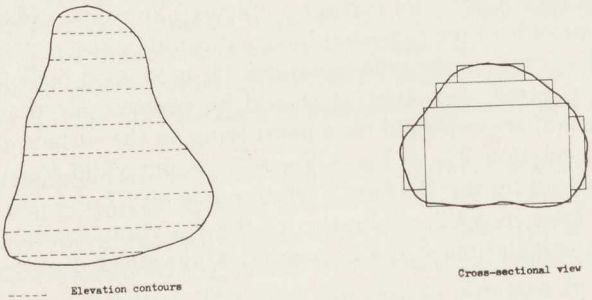

Figure 1
Approximation of a three-dimensional body by thin rectangular slabs

The main advantage of the method lies in the speed of calculations which is considerably enhanced because of using simplified formulae for a thin rectangular plate in contrast to the complicated formulae for a polygonal lamina. Besides this, reading of the positional coordinates of the rectangular sides (alternately parallel to x_1 and x_2 axes) is comparatively easier than that for the sides of a polygon.

§ 3.3 *Comprehensive programme for the digital computer*

Keeping in view the importance of prismatic models in the magnetic interpretation, a comprehensive programme for the computation of anomalies has been developed which is suitable not only for bodies of irregular shape but also for bodies of regular shape such as a finite rectangular prism.

This is accomplished by including in the main programme, expressions for the necessary five components of T_{ik} both for the case of a rectangular plate and a finite prism given by equations (6) and (5) respectively. The computer has, therefore, the option of using either of these sets of formulae depending on the geometry of the body in question. As we would see later, the formulae for the finite vertical prism could also be used for evaluating magnetic terrain effects in areas where such effects are prominent.

The input data compromises information as to the positional coordinates of the sides of the rectangular plates (or prisms), values of the magnetization components and the coordinates of the external points where the summed magnetic effect is to be obtained. For calculation of horizontal and total anomalies, data on the inclination and declination of the earth's field have also to be supplied. This information is

utilised by the main programme for calculation and summation of field intensities in a repeated way for given number of external points. The output from the computer gives the field anomaly due to a body at given number of external points.

The average time on CDC–1604 for evaluation of horizontal, vertical and total anomalies taken together is about 1/50 second per station for a plate and about 1/25 second per station for a finite prism.

§ 3.4 *Applicability and accuracy of the method*

The accuracy of the method depends primarily on how closely the rectangular blocks (see figure 1) fit the individual contour boundary, since the spacing of the contours could be made conveniently small as desired. This is best demonstrated by applying the method to a geometrical model of known field anomaly and then comparing the results.

A sphere of diameter 2.4 km was taken for this purpose and a uniform vertical magnetization was assumed due to a vertical inducing field of 41500 γ. The susceptibility contrast was taken to be of value 0.005 (CGS). This sphere was represented by 12 contours with appropriate spacings and each contour boundary was approximated by 12 rectangular blocks of varying dimensions. A profile of 7 points (in a horizontal direction) was computed for the vertical field anomaly by this method and the results are compared in table 1 with those obtained by means of the analytical expressions for the field of a sphere. The top of the sphere was assumed to be at a depth of 1.2 km from the plane containing the profile.

Table 1

Vertical field anomaly of a sphere

Station distance (km)	Calculated values from analytical expressions for field of a sphere (γ)	Computed values as summed effect of 144 plates from CDC–1604 (γ)
0	217.29	217.10
0.5	191.10	190.86
1.0	132.98	132.68
1.5	76.67	76.29
2.0	37.95	37.88
3.0	4.52	4.52
4.0	— 3.04	— 3.04

The extremely close agreement of the results computed on the basis of 144 constituent rectangular plates representing the sphere with the exactly known field values (from analytical formulae) of a sphere is a fair evidence of the accuracy and applicability of the method to a body of arbitrary shape.

§ 3.5 *Determination of magnetization vector from the observed anomalies*

Methods for determination of the direction of magnetization from observed anomalies due to some specific models have been given earlier by HALL [9] and HUT-

CHINSON [11]. For a body of an arbitrary shape, the problem becomes too involved to be dealt with by traditional methods. This problem could, however, be tackled in a convenient and rapid way with the aid of a digital computer.

For example, we assume that the vertical field anomalies as observed in a magnetic survey are caused by an anomalous body whose geometry is known in advance either from a topographical survey or from geological considerations. By the method of § 3.2 the body could be approximated by a number of rectangular plates and its vertical anomaly could be computed from the fundamental equation (4c) which could be rewritten in the following form

$$\Delta Z = J_1 \cdot \sum T_{13} + J_2 \cdot \sum T_{23} + J_3 \cdot \sum T_{33} , \tag{8}$$

where Σ denotes the summation over the number of plates used in approximation of the body.

It is easy to see from equation (8) that the observed vertical anomaly at only three points would suffice for the determination of the three unknowns J_1, J_2 and J_3, the necessary coefficients ΣT_{13}, ΣT_{23} and ΣT_{33} being evaluated by the computer for each case. However, to obtain a more representative value of the magnetization vector, the observed anomaly ΔZ at a large number of points in the magnetic survey could be used to obtain a 'least-squares solution' for J_1, J_2 and J_3. The computer programme described in § 3.3 could be slightly modified to perform least square calculations. The above method is equally applicable to the horizontal or total field anomalies for the determination of the magnetization vector.

This method could also be utilised to determine the remanent magnetization vector in case the susceptibility of the anomalous body is known precisely from measurements of rock samples. Reliability of the final results and interpretation would, of course, depend on the validity of the assumption of uniform magnetization and of the assumed geometry for the body.

§ 3.6 *Evaluation of magnetic terrain effects*

Terrain interference in magnetic surveys is not considered to be of such importance as in gravity surveys. In certain cases, however, magnetization of surrounding surface rocks may cause a significant change in the field anomaly especially in regions of igneous outcrops. At shorter distances the terrain effect is more apparent in a magnetic survey than in a gravity survey and vice versa is true for larger distances. This is because, a dipolar field decreases more rapidly with increasing distance than a polar field.

The method described here depends on dividing the region into a grid of equal squares, the average heights of which could be estimated from the topographic maps. The size of the squares and the extent of the region would in general depend on the susceptibility of surface rocks and on the irregularity of the topography. From preliminary calculations based on the assumption of induced magnetization in the earth's field, it is found that in areas where the susceptibility of rocks is of the order of 10^{-3} (CGS) and where the maximum elevation differences are of the order of some hundreds of meters, a square region of area about 64 sq. km around the station would need to be considered. This region is first divided into a number of equal squares of

size 1/2 km. For the position of measurement station as shown in the figure 2, each of the adjoining nine squares is further subdivided into four squares each of size 1/4 km. This is done because the effect of the nearmost squares would be most prominent. To save computation time, squares lying beyond a certain distance from the station could be grouped together to be treated as a single block as shown by thick lines in the figure 2. This scheme has the advantage in that, the normal square grid (1/2 km size) is independent of the position of the station and therefore, average heights of these squares need not be estimated again with the change in the position of the measurement station.

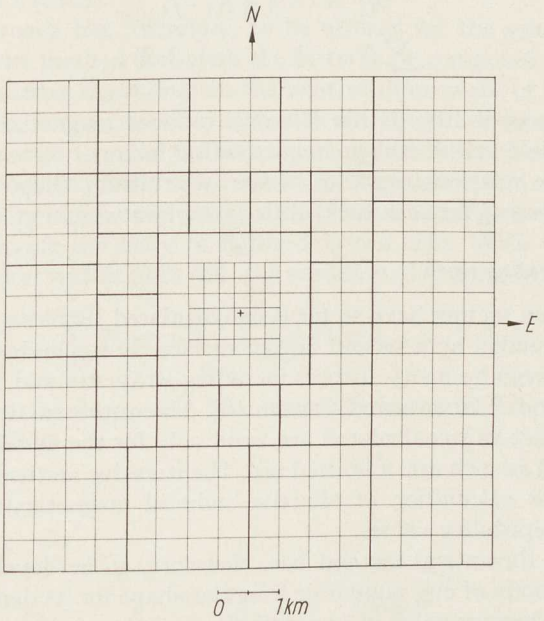

Figure 2
Division of the region into blocks for evaluation of magnetic terrain effect

In effect, each square with its average height would represent a uniformly magnetized vertical prism and the summed intensity effect of all squares for the station point could be evaluated by the computer programme described earlier in § 3.3. The same programme permits evaluation of the total intensity effect of the surrounding terrain in case the ground magnetic survey has been made by an instrument which measures the total field anomaly instead of the vertical or horizontal anomaly.

The method outlined above could also be extended to areas where the topographic irregularities are of the order of 1000 meters or more and where the susceptibility of the surface outcrops is greater than 10^{-3} (CGS). In such cases, a region of comparatively large extent may have to be considered and a still closer grid around the vicinity of the station might be necessary.

§ 4 *Demagnetization effects due to bodies of arbitrary shape*

The magnitude and direction of induced magnetization within a body of uniform susceptibility depends on the given distribution of the external inducing field and on the demagnetization effect on account of the shape of the body. For a body uniformly magnetized in the direction of the homogeneous inducing field H^0 (i.e. parallel to the vector H^0), the following three well known relations are applicable.

$$J_i = \frac{\chi H_i^0}{1 + 4\pi\chi N_i}\,, \tag{9a}$$

$$H_i^D = -4\pi N_i \cdot J_i\,, \tag{9b}$$

$$\sum_i N_i = 1 \quad (i = 1, 2, 3)\,, \tag{9c}$$

where χ is the susceptibility, J_i the effective induced magnetization, H_i^D the inner demagnetization field and N_i the demagnetization factor.

No such simple relations exist for bodies of arbitrary shape and therefore, the problem involved has so far been tackled to only a limited extent.

§ 4.1 *Review of existing work*

Demagnetization factors have so far been calculated (STONER [15], OSBORN [12]) only for bodies bounded by a second degree surface. For cylindrical bodies formulae for N have been given by many authors including STÄBLEIN and SCHLECHTWEG [14], WARMUTH [21], and BOZORTH and CHAPIN [3]. The approximate values of ballistic demagnetization factors so calculated are valid only for the middle cross-section of a cylindrical rod and as such are of limited use. The iterative method recently suggested by VOGEL [20] for calculation of effective induced magnetization is restricted to bodies of low susceptibility values.

A satisfactory theoretical method has, therefore, to be developed which should be able to treat a body of any regular or irregular shape for its demagnetization effect possibly for any arbitrary value of susceptibility and for any given distribution of the external inducing field.

§ 4.2 *Theory of the proposed method*

We consider a body of irregular shape (see figure 3), of volume V and uniform susceptibility χ, magnetized by induction due to an external homogeneous field H^0.

The effective field H at any point P inside the body would be the vectorial sum of the outer field H^0 and the inner demagnetization field H^D depending on the shape of the body.

Thus
$$H(P) = H^0 + H^D(P)\,. \tag{10}$$

Now the inner field is again given by the fundamental equation (1) of § 2.1 and therefore

$$H(P) = H^0 + \operatorname{grad}^2 \int_V J(Q)\,\frac{1}{r}\,dQ\,, \tag{11}$$

where dQ represents the volume element at Q.

The corresponding equation for the effective magnetization J is given by

$$J(P) = \chi H^0 + \chi \cdot \text{grad}^2 \int_V J(Q) \frac{1}{r} dQ \,. \tag{12}$$

As the magnetization vector $J(x_1, x_2, x_3)$ varies in magnitude and direction with the position of Q, a rigorous solution of the above integro-differential equation is difficult to be attempted. A solution based on the method of successive approximation could be attempted but on account of pretty slow convergence of the series, the method is not applicable to cases where susceptibility values are comparatively high e.g., greater than 0.1 (CGS).

A different approach has, therefore, to be utilised for the solution of the above equation. The present method considers the body to be composed of small prismatic cells (rectangular or cubic depending on the relative dimensions of the body) with the assumption of uniform magnetization within each cell. The dimensions of the cells should, however be small enough to make the above assumption fairly reasonable. The actual number of cells into which a body has to be divided would depend on the shape of the body, the susceptibility of the body material and also on the degree of accuracy desired.

Supposing we divide the body of figure 3 into n cells. With the assumption of uniform magnetization within each cell, the equation (11) accordingly becomes

$$H^m = H^0 + \sum_{s=1}^{n} J^s \cdot \text{grad}^2 \int_{V^s} \left(\frac{1}{r_{ms}}\right) dV^s \; (m, s = 1, 2, 3, \ldots, n) \tag{13}$$

the letters P and Q being dropped in favour of suffixes m and s representing the mth and sth cell respectively.

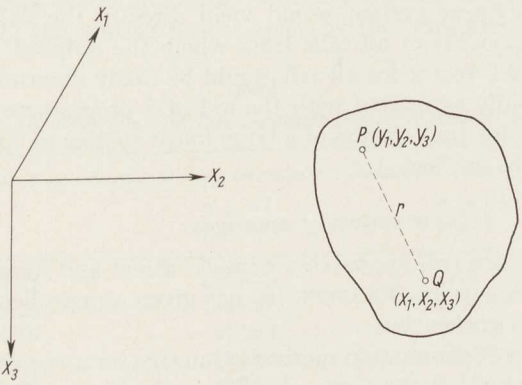

Figure 3
Coordinate system used in evaluating demagnetization field

With the analogy of equation (2) the above equation (13) could be written in terms of components as

$$H_i^m = H_i^0 + \sum_{k=1}^{3} \left[\sum_{s=1}^{n} J_k^s \cdot T_{ik}^{ms} \right], \tag{14}$$

where

$$T_{ik}^{ms} = \frac{\partial^2}{\partial x_i \cdot \partial x_k} \int_{V^s} \left(\frac{1}{r_{ms}}\right) dV^s \qquad (i, k = 1, 2, 3) \,. \tag{15}$$

The expression under the outer summation sign in equation (14) represents the demagnetization field at the centre of the mth cell due to the effect of all cells. On multiplying both sides of equation (14) by χ, we get the corresponding equation giving the effective magnetization components of the mth cell.

$$J_i^m = \chi H_i^0 + \chi \sum_{k=1}^{3} \left[\sum_{s=1}^{n} J_k^s \cdot T_{ik}^{ms} \right], \tag{16}$$

where χH_i^0 is the so called primary magnetization in absence of any demagnetization effect of the body.

For the case when the external inducing field is not homogeneous, the above equation becomes

$$J_i^m = \chi H_i^{0m} + \chi \sum_{k=1}^{3} \left[\sum_{s=1}^{n} J_k^s \cdot T_{ik}^{ms} \right], \tag{17}$$

where H_i^{0m} denotes the external field at the centre of the mth cell and is supposed to be known from the given distribution of the inducing field.

Since m, $s = 1, 2, 3 \ldots, n$ and $i, k = 1, 2, 3$ the above equation (17) in fact represents a linear system of $3\,n$ equations with $3\,n$ unknowns namely.

$$J_1^1, J_1^2, J_1^3 \ldots J_1^n$$
$$J_2^1, J_2^2, J_2^3 \ldots J_2^n$$
$$J_3^1, J_3^2, J_3^3 \ldots J_3^n$$

and $9\,n^2$ coefficients given by T_{ik}^{ms}.

Solution of this linear system would yield directly the values of the effective magnetization components of all cells from which the induced field vector and the demagnetization field vector for all cells could be easily determined. The T_{ik}^{ms} coefficients could be rapidly evaluated with the aid of a programme similar to that described in § 3.3, but for the solution of a large linear system of equations a subsidiary programme has to be devised.

§ 4.3 *Programme for a linear system of equations*

In general there are two approaches namely, direct and iterative for the solution of a linear system equations. FRÖBERG [6] has given an excellent review of methods based on these two approaches.

Amongst the direct elimination methods (suitable for a coefficient matrix without any special characteristics) the Gauss-Jordan method is usually preferred for operation on a digital computer. This is due to the fact that although Gauss' method is faster, JORDAN's modification demands less memory space for storing intermediate results. In the Gauss-Jordan elimination process only n_e^2 elements need to be stored at a time in the computer, although the total number of operations performed is of the order of $n_e^3/2$ where n_e denotes the number of linear equations.

A library programme of the Department of Applied Mathematics, SFIT permits solution of the linear equations system by the above method so long as the quantity n_e^2 is well within the available memory space of the computer (about 30000 for the CDC–1604). For a large matrix exceeding this memory space, the input data has to

be pre-recorded on a tape to be fed later into the computer according to a modified programme for treating the matrix by a general partition method. Of course, this would raise the computation time considerably and for very large value of n_e say 1000, the computation costs could be prohibitive.

Another difficulty which is inherent in the computation method is that caused by rounding-off errors. WILKINSON [23] has given a detailed analysis of such errors which grow rapidly with the increasing order of the coefficient matrix. Rounding errors could be tested and often improved by scaling the equations in a suitable way, though it requires much of trial-and-error.

§ 4.4 *Illustration of the applicability of the method*

Amongst bodies of non-ellipsoidal geometry, a cube specimen provides one of the most interesting cases for the study of inhomogeneous induced magnetization. A uniform inducing field of 20900 γ was assumed to be acting parallel to a horizontal edge of the cube of vloume 8 c.c. A rather high value of susceptibility 1 (CGS) was assumed for the material of the cube.

For lack of any precise theoretical data on bodies with inhomogenoeus magnetization, any criterion as to the number of cells (on which the accuracy depends) could not be established in advance. However, for the first trial of this new method, the cube was divided into 8 cells (small cubes) and the values of magnetization components for each cell were obtained by solving a system of 24 linear equations. A profile of 5 points lying in Gauss 1 position was computed for the horizontal attraction of the cube. Next, the cube was divided in turn into 27, 64 and 125 cells and the computations were repeated for the same profile with new values of magnetizations calculated for the respective cells. Rounding errors were found to be of insignificant magnitude within eight digits of the printed results given by the computer.

Table 2

Field intensity due to a cube specimen with inhomogeneous magnetization

Distance (cm)	Field from computed magnetization values of n cells			
	$n = 8$ (γ)	$n = 27$ (γ)	$n = 64$ (γ)	$n = 125$ (γ)
2	6524.67	6205.40	6101.46	6057.65
4	1005.26	1020.67	1030.38	1036.44
6	304.19	312.59	317.30	320.08
8	129.05	133.18	135.44	136.76
10	66.23	68.48	69.70	70.41

The computed results for the horizontal field intensity of the cube on the basis of increasing number of constituent cells are shown in table 2. As expected, the successive difference in corresponding field values decreases from one stage to another with the number of cells increasing stagewise. Considering the maximum difference which is observed at the closest distance of 2 cm, we see that it decreases stagewise from 319 γ to 104 γ and then to only 44 γ which is about 0.7% of the corresponding field value. From this trend, it could be inferred that the computed results of the fifth stage (with 216 cells) would hardly differ from those of the fourth stage by about

0.4% and of the sixth stage (with 343 cells) from those of the fifth stage by still lesser margin and so on.

The above example illustrates in a way, the relative gain in accuracy of the results with the increasing number (or decreasing size) of the cells. Depending on the degree of accuracy desired in the computation of results, an appropriate choice for the size of cells could be made accordingly. The method as such possesses two distinct advantages over the existing methods. Firstly, it is applicable to a body of any shape and for any value of susceptibility. Secondly, the order of precision and rapidity attainable by the method are higher than any of the existing methods.

§ 4.5 *Effect of susceptibility on inhomogeneity of magnetization*

Unlike the case of uniform magnetization where the effective magnetization is a known function of susceptibility vide equation (9a), there exists no such relation for the case of inhomogeneous induced magnetization. However, the method described in § 4.2 could be applied to make a quantitative study of the effect of susceptibility on inhomogeneity of the induced magnetization in a body of arbitrary shape.

For this purpose, we again consider the case of a cube divided into say, 64 cells. We start with a high value of susceptibility 10 and calculate the induced magnetization values for each of the cells due to an homogeneous external field H_1^0 of intensity say, 20900 γ acting parallel to a horizontal edge of the cube. The computation of magnetizations for the 64 cells is repeated for two other values of susceptibility 0.1 and 0.001. Table 3 shows the computed values of magnetization components for the uppermost 16 cells with their centres lying in a plane defined by $x_3 = -0.75$ a where a is half edge length of the cube. The components J_2 and J_3 for the case when the susceptibility is 0.001, are of insignificant magnitude and therefore not shown in the table.

Table 3

Effect of susceptibility on inhomogeneity of magnetization in a cube specimen

Coordinates		Computed magnetization values in γ for the uppermost 16 cells						
		$\varkappa = 10$			$\varkappa = 0.1$			$\varkappa = 0.0$
x_1	x_2	J_1	J_2	J_3	J_1	J_2	J_3	J_1
− 0.75a	− 0.75a	6389	1976	1976	1509	170.6	170.6	20.81
− 0.25a	− 0.75a	7547	386.1	386.1	1626	42.4	42.4	20.84
0.25a	− 0.75a	7547	− 386.1	− 386.1	1626	− 42.4	− 42.4	20.84
0.75a	− 0.75a	6389	− 1976	− 1976	1509	− 170.6	− 170.6	20.81
− 0.75a	− 0.25a	4913	597.1	1481	1431	49.3	187.3	20.80
− 0.25a	− 0.25a	6076	137.6	246.4	1559	15.9	44.3	20.83
0.25a	− 0.25a	6076	− 137.6	− 246.4	1559	− 15.9	− 44.3	20.83
0.75a	− 0.25a	4913	− 597.1	− 1481	1431	− 49.3	− 187.3	20.80
− 0.75a	0.25a	4913	− 597.1	1481	1431	− 49.3	187.3	20.80
− 0.25a	0.25a	6076	− 137.6	246.4	1559	− 15.9	44.3	20.83
0.25a	0.25a	6076	137.6	− 246.4	1559	15.9	− 44.3	20.83
0.75a	0.25a	4913	597.1	− 1481	1431	49.3	− 187.3	20.80
− 0.75a	0.75a	6389	− 1976	1976	1509	− 170.6	170.6	20.81
− 0.25a	0.75a	7547	− 386.1	386.1	1626	− 42.4	42.4	20.84
0.25a	0.75a	7547	386.1	− 386.1	1626	42.4	− 42.4	20.84
0.75a	0.75a	6389	1976	− 1976	1509	170.6	− 170.6	20.81

From the computed results shown in table 3, it is evident that the inhomogeneity of magnetization diminishes rapidly with the decreasing value of susceptibility. In fact for low susceptibility values of the order of 10^{-3}, inhomogeneity practically vanishes and in such cases, therefore, even a non-ellipsoidal body like a cube would behave as if it were uniformly magnetized with an average value. Evaluation of an average value of magnetization for a body of arbitrary shape is, therefore, possible only in a limiting case of low susceptibility.

§ 4.6 *Influence of natural remanent magnetization (NRM)*

So far we have considered the demagnetization effect of a body only for the case of induced magnetization, ignoring the effect of NRM that may be present in a body. Recent investigations by Books [1], Du Bois and Carey [5] to quote only a few, have shown that for certain rocks the intensity of NRM may exceed that of induced magnetization by factors ranging well over hundred. In such cases the field anomalies are mainly influenced by the remanent component of the magnetization vector, thus necessitating its determination. Furthermore, knowledge of the remanence vector is of major importance in paleomagnetic interpretation.

Rock specimens in form of a cube or cylinder are measured with the aid of an astatic magnetometer or a rock-generator [13] for determination of the remanence vector which is assumed to be uniform. As discussed earlier in § 4.5, except in cases of low susceptibility values this assumption can not be valid for such specimen shapes, although the rock body in situ may have a uniform remanent magnetization. In other cases, therefore, specimens of special shape, (e.g. sphere, long cylinder, thin disc) with known demagnetization factor should be employed for measurement of NRM. Let us assume that components of the remanence vector determined with such specific sample of a rock body are J_{r1}, J_{r2} and J_{r3}. These are however, apparent values and are less than the true values because of the demagnetization effect of the sample shape. The true values of the components would be accordingly, $J_{r1}(1 + 4\pi\varkappa N_1)$, $J_{r2}(1 + 4\pi\varkappa N_2)$ and $J_{r3}(1 + 4\pi\varkappa N_3)$. This completely determines the true remanence vector from which the fossil field direction could be established for the purpose of paleomagnetic interpretation.

§ 5 *Average demagnetization factors for rock specimens*

In general, susceptibility values for most of the rock formations are low seldom approaching the value 0.01 .In § 4.5 it was shown that for such bodies the assumption of a uniform average magnetization is fairly reasonable. Thus theoretically it should be possible to define and evaluate average demagnetization factor for a body of any shape with low susceptibility value.

§ 5.1 *Concept of average demagnetization factor*

We again consider the body of figure 3 which is subjected to a homogeneous inducing field H_i^0 in a direction i. The components of magnetization at any point P are given by the equation (16) which could be rewritten in the following form

$$J_i(P) = J_i^0(P) + \chi \sum_{k=1}^{3} \frac{\partial^2}{\partial x_i \, \partial x_k} \int_V \frac{J_k(Q)}{r} \, dQ \,, \tag{18}$$

where $i = 1, 2, 3$ and $J_i^0(P)$ is the primary magnetization in absence of any demagnetization effect of the body.

The magnetization $J_i(P)$ could be expressed by a power series in $\varkappa$ which for the case of external inducing field acting in the direction x_1 would be given by

$$J_i(P) = \delta_{i1} J_1^0 + \chi K_{i1}(P) + \chi^2 K_{i2}(P) + \chi^3 K_{i3}(P) + \cdots , \tag{19}$$

where K_{i1}, K_{i2}, K_{i3} etc., represent some unknown functions and δ the Kronecker symbol.

From equations (18) and (19), it is easy to see that

$$K_{11}(P) = J_1^0 \cdot T_{11}(P) \tag{20}$$

The magnetic moment vector of the body is given by

$$M = \int_V J(P)\, dP ,$$

where dP is the volume element at P.

Denoting the absolute value of the moment vector by M_A, we get

$$M_A = |M| = \sqrt{\sum_{i=1}^{3} M_i^2} .$$

Further

$$M^0 = V \cdot J^0$$

and

$$M_A^0 = |M^0| = V \cdot J_1^0 = M_1^0 .$$

The magnetic moment M_A could also be put in terms of a power series in χ as shown below

$$M_A = M_A^0 (1 - 4\pi \bar{N}_1 \chi) + m_2 \chi^2 + m_3 \chi^3 + \cdots , \tag{21}$$

where m_2, m_3 etc., are coefficients which could be determined with the aid of equation (19) and the quantity $\bar{N}_1$ is introduced to denote the average demagnetization factor for a body of any shape but of sufficiently small value of χ so as to make the power series given by equations (19) and (21) convergent.

As a consequence of equation (19), M_i could be expressed by the following power series

$$M_i = \int_V J_i(P)\, dP = \delta_{i1} M_1^0 + \chi \int_V K_{i1} \cdot dP + \chi^2 \int_V K_{i2} \cdot dP + \cdots . \tag{22}$$

Now M_A is given by $\sqrt{M_1^2 + M_2^2 + M_3^2}$, which on making use of equation (22) yields

$$\left.\begin{aligned} M_A &= \sqrt{(M_A^0)^2 + 2 M_A^0 \chi M_A^0 \bar{T}_{11} + \cdots \chi^2 + \cdots} \\ &= M_A^0 (1 + \chi \bar{T}_{11}) + \cdots \chi^2 + \cdots , \end{aligned}\right\} \tag{23}$$

where

$$\overline{T}_{11} = \frac{1}{V} \int_{V} T_{11}(P)\, dP \tag{24}$$

and

$$\int_{V} K_{11}\, dP = J_1^0 \cdot \overline{T}_{11} \cdot V = M_A^0\, \overline{T}_{11} \tag{25}$$

which follows from the equation (20).

Comparing equations (23) and (21), we get

$$\overline{N}_1 = -\frac{\overline{T}_{11}}{4\pi} \tag{26}$$

For the general case, when the inducing field is acting in a direction i

$$\overline{N}_i = -\frac{\overline{T}_{ii}}{4\pi} \tag{27}$$

which is an expression for the average demagnetization factor for a body with low value of susceptibility.

Evaluation of N_i to any desired degree of accuracy is then possible by finding the average of coefficients T_{ii} over a large number of points uniformly distributed over the volume of the body and dividing this average value by 4π.

§ 5.2 *Evaluation of average demagnetization factors for cylindrical specimens*

In many problems of rock magnetism e.g., study of induced and remanent magnetization, measurement of susceptibility etc., cylindrical rock specimens are often employed. For low susceptibility values their demagnetization factors could be calculated by the method proposed in § 5.1.

For example, the axial demagnetization factor $\overline{N}_3$ for a cylinder would be given by equation (27) simply as

$$\overline{N}_3 = -\frac{\overline{T}_{33}}{4\pi}\,. \tag{28}$$

The demagnetization factor $\overline{N}_3$ so evaluated on the basis of the volume average of T_{33} corresponds to the experimentally determined 'magnetometric' demagnetization factor, where as that evaluated on basis of the average of T_{33} over the middle cross-section corresponds to the experimentally determined 'ballistic' demagnetization factor and could be expressed by

$$\overline{N}_3^B = -\frac{\overline{T}_{33}^B}{4\pi}\,, \tag{29}$$

where $\overline{T}_{33}^B$ in analogy with the equation (24) is given by

$$\overline{T}_{33}^B = \frac{1}{S} \int_{S} T_{33}(P)\, dS\,, \tag{30}$$

where S represents the middle cross-section surface.

A computer programme was developed which yielded values of axial demagnetization factors averaged over about 500 points for varying dimensional ratio p (length/diameter) of a cylinder. The computed values of $\overline{N}_3$ and $\overline{N}_3^B$ for a cylinder are shown

in tables 4 and 5 respectively. For comparison sake, values of N_3 for an ellipsoid with the same dimensional ratio are shown side by side. Theoretical values of $\overline{N}_3$ and $\overline{N}_3^B$ for cylindrical rods calculated by other authors (BROWN [4], WARMUTH [21]) are also included in the tables for comparison. The agreement in the case of 'magnetometric' values (see table 4) is on the whole fairly good with BROWN's values calculated on the basis of inductance tables. For the case of 'ballistic' demagnetization factor (table 5), the computed values are in close agreement with WARMUTH's values except for low values of p. This is owing to the fact that for $p < 10$, the values of $\overline{N}_3^B$ have been obtained by WARMUTH through extrapolation of the curve for $p > 10$ to the limiting case $p = 0$ ($N = 1$) on an arbitrary basis and therefore in this range WARMUTH's values are of questionable accuracy.

An interesting observation to be made from table 4 is that for large values of p say > 5, the values of $\overline{N}_3$ for cylinder are much different than those for an ellipsoid of revolution with the same dimensional ratio. The usual assumption that for very large values of p the demagnetization factor for a cylinder is same as that for an ellipsoid with the same dimentional ratio, is not supported by these results. From the 'magnetometric' values of axial demagnetization factor, values of transverse (radial) demagnetization factor N_1 could be easily obtained from the following relation

$$\overline{N}_1 = \overline{N}_2 = \frac{1 - \overline{N}_3}{2} \tag{31}$$

which follows from the equation (9c).

Another observation of practical interest to be made from table 4 is that for value of $p = 0.9$, the demagnetization factor for a cylinder (both in axial and transverse direction) is almost same as that for a sphere. Incidentally, this dimensional ratio is same as that determined earlier by the author [19] in an investigation for representation of the field of a uniformly magnetized cylinder by that of an equivalent dipole. Thus for practical purposes, at this optimum value of p a uniform cylinder would behave like a sphere of equivalent moment with respect to both the external field and the inner demagnetization field.

Table 4

Magnetometric demagnetization factor of a circular cylinder with uniform axial magnetization

Dimensional ratio (p)	Axial demagnetization factor $\overline{N}_3$		
	Values for ellipsoid	Computed values for cylinder	Values for cylinder after BROWN
0	1.0000	1.0000	1.0000
0.2	0.7505	0.7031	0.6802
0.4	0.5882	0.5409	0.5281
0.8	0.3944	0.3660	0.3619
0.9	0.3621	0.3380	0.3349
1.0	0.3333	0.3139	0.3116
2.0	0.1736	0.1858	0.1819
4.0	0.07541	0.1004	0.09835
10.0	0.02029	0.04117	0.04119
20.0	0.006749	0.02106	0.02091
40.0	0.002116	0.01061	0.01053
100.0	0.000430	0.004263	0.004232

Table 5

Ballistic demagnetization factor of a circular cylinder with uniform axial magnetization

Dimensional ratio (p)	Axial demagnetization factor $\overline{N}_3^B$ Values for ellipsoid	Computed values for cylinder	Values for cylinder after WARMUTH
0	1.000	1.000	1.000
0.1	0.860	0.792	0.810
0.2	0.750	0.682	0.666
0.5	0.528	0.425	0.406
0.8	0.394	0.292	0.270
1.0	0.333	0.233	0.213
2.0	0.174	0.0937	0.0860
5.0	0.0559	0.0189	0.0185
8.0	0.02842	0.00764	0.00770
10.0	0.02029	0.00493	0.00500
20.0	0.006749	0.001245	0.001249
50.0	0.0014400	0.0001999	0.0001997
100.0	0.0004300	0.00004999	0.00004997

§ 6 *Conclusions*

The following statements are confined to points relating to general conclusions made from the present study and some suggestions regarding the future geophysical applications.

1. The indirect method of magnetic interpretation is made more feasible by the high speed of modern computers. The method given in the present paper should enable making up sets of characteristic curves for anomalies of any interpretation model with varying values of parameters defining the geometry, depth and magnetization.

2. A 'least-squares solution' for the magnitude and direction of the magnetization vector provides still another aid to magnetic interpretation. From the computed values of magnetization components, a back calculation of anomalies could be made and the geometry of the body characterised by a finite number of parameters could be varied to obtain a best fit with the observed anomalies.

3. By virtue of POISSON's relation between the gravity and the magnetic attraction of a uniformly magnetized body, the double derivatives of the gravitational potential U are related to the T_{ik} components (of § 2.1) as shown below

$$\frac{\partial^2 U}{\partial x_i \, \partial x_k} = G \cdot \varrho \cdot T_{ik} \, ,$$

where G is the gravitational constant and ϱ the density of the body.

Thus the method described in § 3.2 could also be utilised for rapid computation of the gravity gradients and differential curvature.

4. In hilly regions where the susceptibility of surface rocks is of the order of 10^{-3} (CGS) or more, magnetic terrain effects could be significant enough to demand a correction in the field anomalies measured from ground surveys.

5. The present study emphasizes the need for a more precise knowledge of the demagnetization effect of a rock body. For bodies with susceptibility value $\geq 10^{-2}$,

the effective induced magnetization due to the earth's field can be strongly inhomogeneous depending on the shape factor. The assumption of uniform magnetization for a cube or cylindrical specimen should, therefore, be made with great caution.

6. It is suggested that the field anomalies due to strongly magnetic igneous masses and ore bodies with inhomogeneous magnetization should be computed with the 'cell division' method of § 4.2 to obtain a better fit with the observed anomalies. The method could also be applied to evaluate the effective induced magnetization for the case when two or more bodies lie close enough to exert magnetic attraction on one another.

7. Even for the case of uniform magnetization, considerable error might be involved in values of demagnetization factors obtained on approximation of the body by an ellipsoid of same dimensional ratio. When greater accuracy is desired, an independent evaluation of demagnetization factors for the body should be made by the method of § 5.1.

Acknowledgements

I am much grateful to Prof. F. GASSMANN for suggesting this study and for his continued interest and guidance. Thanks are extended to Prof. M. WEBER for profitable discussion and for a critical appraisal of the work. I also wish to thank Prof. H. RUTISHAUSER for helpful suggestions in the development of the computer programme.

This work was done during the tenure of a Swiss Federal scholarship award made available at the Department of Geophysics, SFIT, Zürich.

REFERENCES

[1] K. G. BOOKS, *Remanent magnetism as a contributor to some magnetic anomalies*, Geophysics *27* (1962), 359.

[2] M. H. P. BOTT, *Two methods applicable to computers for evaluating magnetic anomalies due to finite three-dimensional bodies*, Geoph. Prospecting *11* (1963), 292.

[3] R. M. BOZORTH and D. M. CHAPIN, *Demagnetizing factors of rods*, J. Appl. Phys. *13* (1942), 320.

[4] W. F. BROWN JR., *Single domain particles: New uses of old theorems*, Amer. J. Phys. *28* (1960), 548.

[5] R. L. DUBOIS and W. W. CAREY, *Magnetic investigations of a ring dike, Buell Park Arizona*, Geophysics *29* (1964), 553.

[6] C. E. FRÖBERG, *Introduction to numerical analysis* (Addison Welseley Publ. Co., London 1965), 73.

[7] F. GASSMANN, *Graphical evaluation of anomalies of gravity and of the magnetic field caused by three-dimensional bodies*, Proc. Third World Petrol. Congress, Sec. 1 (1951), 613.

[8] F. GASSMANN and M. WEBER, *Einführung in die angewandte Geophysik* (Verlag Hallwag, Bern 1960), 119.

[9] D. H. HALL, *Direction of polarization determined from magnetic anomalies*, J. Geoph. Res. *64* (1959), 1945.

[10] R. G. HENDERSON and I. ZIETZ, *Graphical calculation of total-intensity anomalies of three-dimensional bodies*, Geophysics *22* (1957), 887.

[11] R. D. HUTCHINSON, *Magnetic analysis by logarithmic curves*, Geophysics *23* (1958), 749.

[12] J. A. OSBORN, *Demagnetization factors of the general ellipsoid*, Phys. Rev. *67* (1945), 351.

[13] S. K. RUNCORN, *Methods and techniques in geophysics* (Interscience Publ., New York 1960), 170.

[14] F. Stäblein and H. Schlechtweg, *Über den Entmagnetisierungsfaktor zylindrischer Stäbe*, Z. Phys. *95* (1935), 630.
[15] E. C. Stoner, *Demagnetization factors for ellipsoids*, Phil. Mag. *36* (1945), 803.
[16] M. Talwani, *Computation with the help of a digital computer of magnetic anomalies caused by bodies of arbitrary shape*, Geophysics *30* (1965), 797.
[17] V. Vacquier, *A machine method for computing the magnitude and direction of magnetization of a uniformly magnetized body from its shape and a magnetic survey*, Proc. Benedum Earth Magnetism Symposium 1962, University of Pittsburgh Press (1962), 123.
[18] V. Vacquier, N. C. Steenland, R. G. Henderson and I. Zietz, *Interpretation of aeromagnetic maps*, Memo. Geol. Soc. America *47* (1951).
[19] P. Vallabh Sharma, *On the point dipole representation of a uniformly magnetized cylinder*, Helv. Phys. Acta *38* (1965), 234.
[20] A. Vogel, *The application of electronic computers to the calculation of effective magnetization*, Geoph. Prospecting *11* (1963), 51.
[21] K. Warmuth, *Über den ballistischen Entmagnetisierungsfaktor zylindrischer Stäbe*, Archiv für Elektrotechnik *33* (1939), 747.
[22] S. Werner, *Determination of magnetic susceptibility of ores and rocks from Swedish iron ore deposits*, Sveriges Geol. Undersokning Ser. C *39* (1945), 79.
[23] J. H. Wilkinson, *Error analysis of direct methods of matrix inversion*, J. Assoc. Comput. Machines *8* (1961), 281.

Application of A. C. Demagnetization to Investigate the Stability of Rock Magnetization Caused by Lightning Currents[1])

By P. Vallabh Sharma[2])

Summary – An apparatus is described which enables progressive demagnetization of rock specimens under alternating fields in order to remove the unstable components of magnetization while retaining a measurable fraction of the stable component.

The apparatus is utilised to study the stability of magnetization created in rock specimens by artificial lightning currents. It is shown that the remanent magnetization due to strong lightning currents could be fairly stable and in certain cases peak a.c. fields of intensity as high as 1700 Oe may fail to destroy completely the effect of this hard component.

Possible means for avoiding the 'magnetic noise' effect of lightning on paleomagnetic investigations are discussed.

Zusammenfassung – Es wird eine Apparatur beschrieben die es ermöglicht, Gesteinsproben mit Hilfe von Wechselfeldern schrittweise zu Entmagnetisieren. Dabei werden die unstabilen Komponenten der Magnetisierung entfernt, während ein Teil der stabilen Magnetisierung erhalten bleibt.

Die Apparatur wurde verwendet, um die Stabilität der in den Gesteinsproben durch künstliche Beblitzung erzeugten Magnetisierung zu untersuchen. Es wird gezeigt, dass die durch starke Blitze erzeugte remanente Magnetisierung recht stabil sein kann und dass es in gewissen Fällen selbst Wechselfeldern mit Feldstärken bis zu 1700 Oe nicht gelingt, diese harte Magnetisierung zum Verschwinden zu bringen.

Möglichkeiten, um den störenden Einfluss der Blitze bei päleomagnetischen Untersuchungen zu vermeiden, werden besprochen.

§ 1 *Introduction*

In paleomagnetic research, we are usually interested in the primary stable component of natural remanent magnetization (NRM) for determining the past direction of the earth's field and therefore, it is desirable to remove the subsequently acquired secondary components namely, viscous remanent magnetization (VRM) and isothermal remanent magnetization (IRM) which are usually unstable. Various field and laboratory tests for examining whether the NRM present in a rock is the stable fossil magnetization have been described by many authors including Graham [7][3]), Brynjolfsson [2], As and Zijderveld [1], Creer [3], Everitt and Clegg [4] and Robertson [13].

---

[1]) Part II of the dissertation 'Theoretical study of the magnetic attraction due to rock bodies and experimental investigation of the stability of rock magnetism' submitted to the Swiss Federal Institute of Technology (ETH), Zurich, for the degree of Doctor of Natural Sciences.

[2]) Department of Geophysics, Swiss Federal Institute of Technology, Zurich, Switzerland.

[3]) Numbers in brackets refer to References, pages 119/120.

The laboratory tests usually involve progressive demagnetization either by alternating fields (a.c. washing) or by heating (thermal cleaning) or by a combination of both. The associated instrumental design is more complicated in the case of thermal cleaning and therefore, the a.c. method of cleaning is usually preferred.

The present paper describes an a.c. demagnetization apparatus designed and built at the Department of Geophysics, Swiss Federal Institute of Technology, Zurich. The apparatus has been used to study the stability of the IRM acquired by rock specimens subjected to artificial lightning currents. This study has shown that a.c. washing while normally successful in removing the unstable component of magnetization, may often fail to destroy completely the relatively stable IRM caused by lightning strikes.

§ 2 *Principle of a.c. washing*

The coercive force of the magnetic particles in a rock material depends on the composition and grain size of the magnetic minerals. Thus the presence of one or more magnetic minerals of varying grain size may give rise to magnetization components of different coercivities in a rock body. The magnetization of particles with relatively high coercive force and long relaxation time is not likely to be affected by the present earth's field and hence represents the stable fossil magnetization. In contrast to this, the magnetization of particles with a low coercive force is apt to be considerably influenced by the changing earth's field and also due to various surface effects of small or long duration.

During application of an a.c. field of suitable peak value, the aforesaid components of magnetization will behave differently; the soft component (with low coercive force) may be totally demagnetized while the stable component is likely to be retained in a measurable fraction. Peak a.c. fields required for this purpose may vary from less than a hundred to more than a thousand oersted for different rock materials.

A suitably designed apparatus should, therefore, permit demagnetization of a rock specimen in steps of increasing intensity of a.c. field. After each demagnetization step the specimen is measured for the remanent magnetization vector which often shrinks and changes its direction. If, after initial changes, we observe only a shrinking vector without rotation, it is assumed that this represents the direction of the stable fossil magnetization.

§ 3 *Experimental design of the demagnetization apparatus*

The essential components of the apparatus to be described are the demagnetization coil, specimen holder, the compensating coils system and the electrolytic resistance. The considerations arising in the design of each component are discussed separately.

§ 3.1 *Design of the demagnetization coil*

In the design of the coil three main considerations have to be kept in view namely, optimal shape to produce a maximum field with minimum power consumption, a fairly good homogeneity of the field at the centre of the coil and a minimum heating effect.

Elementary calculations made to give on optimum relation between the length and thickness of a coil with an internal diameter of 14 cm (fixed in view of the size

of the specimen holder) and capable of producing a peak field of 2000 Oe by about 4500 windings of copper wire of thickness 1.5 mm are shown in table 1.

The coil actually designed for use in the apparatus is 20 cm long and consists of 4684 windings in 36 layers of copper wire of thickness 1.45 mm and has internal and external diameters of 14 and 24.6 cm respectively. It has a resistance of 28 Ω and a self-inductance of 2.2 henry. A cooling jacket consisting of copper spiral tube around the coil has been used with running water from tap to minimise the heating of coil especially when working with high currents. For preserving the shape of the coil and for preventing any subsequent short circuiting of the windings, the whole coil system is sealed under vacuum in araldit.

Table 1

Power requirements by coils of varying dimensions for producing a field of 2000 Oersteds

Length (cm)	Thickness (cm)	Resistance (Ω)	Current required (amp) r.m.s.	Rise in temp.[1] °C/min	Field inhomogeneity[2] %
30	3.33	22	9.76	9	0.8
25	4	23	8.66	7	1.0
20	5	24.5	7.75	5	1.5
14	7.14	27	7.03	4.5	2.8
10	10	31	7.26	4.5	5.0

[1] without consideration of heat losses
[2] at a distance of 2 cm from the centre in axial direction

The coil is used in series resonance with a suitable condenser to minimise the power consumption by reducing the effective reactance of the LC circuit. The condenser used for tuning the coil to 50 c/s mains supply had a capacitance of 4.27 μF with provision of further addition of capacitance by 0.24 μF in 8 steps each of 0.03 μF. The condenser was designed to be capable of standing high tension of the order of 10 kilovolts (peak value) developed at optimum resonance. The coil was calibrated by passing a small known direct current and measuring the field generated at the centre of the coil by an Oerstedmeter. In terms of a.c. current, the coil is capable of producing a peak field of 300 ± 6 Oe per amp (r.m.s.). With 220 V mains supply, the tuned coil produced a field of 1700 Oe (peak value).

§ 3.2 *Specimen holder and its rotation mechanism*

Rock specimens cut in cylinders of diameter 4.2 cm and length 3.6 cm were used in demagnetization experiments. The design of specimen holder is based on two considerations: firstly, it should be non-magnetic and secondly, to avoid the disturbing effect caused by the presence of asymmetrical harmonics in the a.c. mains supply it should be capable of being rotated simultaneously on two perpendicular axes to cause a random motion of the specimen. Synthetic delrin was used for the construction of the specimen holder and the two gears. The specimen rotated about a horizontal axis with a speed of 60 revolutions per minute and about a vertical axis at 24/25 of this speed, both speeds being about 50 times slower than the frequency of the a.c. supply.

This device provides every possible direction of the rotating specimen to be demagnetized by the a.c. field, besides preventing the specimen from acquiring an IRM due to asymmetrical harmonics of the a.c. frequency. Figure 1 shows the photograph of the demagnetization coil and the specimen holder together with the compensating coils system.

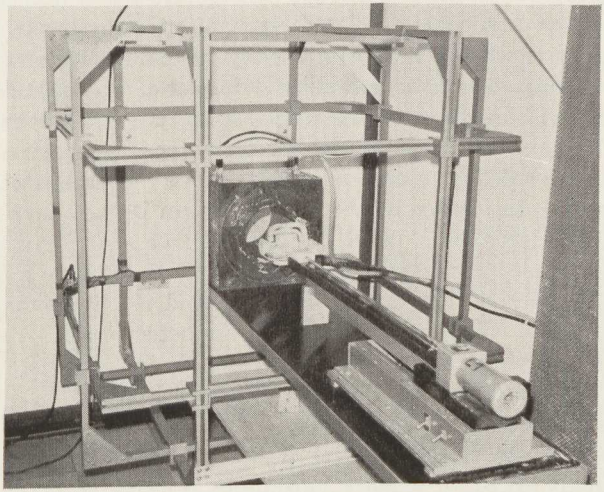

Figure 1
Photograph of demagnetization coil, specimen holder and compensating coils system

§ 3.3 *Design of the compensating coils*

In order to prevent the rock specimen from acquiring an anhysteretic magnetization due to the present earth's field, the demagnetization of the specimen has to be carried out in a field free space. For this purpose a set of 3 pairs of square shaped coils (see figure 1) are designed to annual the earth's field. Use of the three pair coil system permits the installation of the assembly in any desired horizontal direction. The horizontal pair of coils has dimensions of 94 cm each and consists of 42 windings of 0.6 mm thick copper wire, where as the two vertical pairs are of dimensions 97 cm and 100 cm and each consists of 21 windings of copper wire. The distance of separation for each pair of the coil was fixed in accordance with the FANSELAU relation [5] given below

$$a : d = 1 : 0.5445 ,$$

where a is the dimension of the coils and d the distance of separation for the pair.

The magnitude of currents required by the 3 pairs of coils to annul the earth's field were 590 mA, 610 mA and 25 mA respectively, the order of inaccuracy in compensation being about 1% of the earth's field as checked by an Oerstedmeter. As compared to the circular Helmholtz coils system, the square coils have the advantage of ease in the mechanical design and construction, although they require a slightly larger space.

§ 3.4 *Design of the electrolytic resistance*

In a.c. washing the normal procedure is to subject a rock specimen to an alternating field of chosen peak value which is slowly and smoothly reduced to zero, the rate of decrease of the field being slow compared with the speed of rotation of specimen, which in turn must be much slower than the frequency of the a.c. supply.

The smooth reduction in the coil current (to regulate a slow and steady fall of a.c. field) has been achieved by using an electrolytic potential divider which consists of a doubled walled glass tube with a built-in cooling system for running tap water. The glass tube is 1.2 m long with inner and outer diameter of 6.5 cm and 10.5 cm respectively and has two cylindrical copper electrodes at its ends which are connected to the mains supply. The third electrode of smaller diameter is supported by a thin insulated copper rod suspended by a cord vertically above the tube which has a solution of copper nitrate, the resistance of the liquid column being about 23 Ω. The cord carrying the middle electrode is directly connected to a shaft driven by an electric motor with a multi-speed gear box to regulate a slow and steady motion of the electrode in the liquid column. The middle electrode and the upper fixed electrode are connected to the tuned coil circuit through an ammeter which is calibrated to read both the current and peak field values. With this design, the field could be varied very slowly and smoothly towards zero. For a peak field of 1700 Oe to be reduced to zero, the time taken was about 12 minutes.

The advantage of the built-in cooling jacket for the electrolytic resistance tube becomes increasingly apparent when a continuous working with the apparatus for a longer time is desired. A steady cooling of the tube minimises the effects of temperature variation on the resistance of the liquid column, thereby ensuring a smooth functioning of the electrolytic potential divider even with high values of current. The only difficulty experienced with this design was the rapid oxidation of the copper electrodes which required a routine cleaning. This difficulty could, of course, be overcome by electroplating of the electrodes by a thin film of some stable metal.

§ 3.5 *Comparison of the apparatus with other existing designs*

This apparatus owes a great deal to earlier designs described by CREER [3] and by MCELHINNY and GOUGH [11]. The main difference between these designs and the present design is in the field producing capacity of the demagnetization coil. The coil described in § 3.1 is capable of producing 300 Oe per amp (r.m.s.) compared to 200 Oe and 160 Oe respectively from coils used by above authors. The cooling provision both for the coil and the electrolytic resistance is another distinguishing feature of the described apparatus. With this design, thus it is possible to demagnetize one specimen after another without any loss of time which may otherwise have to be incurred on account of the excessive heating of the coil or boiling of the electrolytic resistance.

§ 4 *Use of the apparatus for testing stability of IRM caused by lightning currents*

In paleomagnetic studies, scattered directions of magnetization are commonly found in rock specimens collected from the same site and even from the same layer. The dispersion in intensities and directions observed in some cases is abnormally large and is difficult to be explained only on grounds of the inhomogeneity of rocks or

irregular viscous effects. Such cases have been earlier reported in studies by RIMBERT [12], KHAN [10] and GRAHAM [8] and the obvious explanation given is that surface rocks ore often strongly and irregularly magnetized by lightning strikes.

An important question arises—how and to what extent the 'magnetic noise' effect of lightning on paleomagnetic observations could be removed? Another associated aspect of this question is whether this disturbing magnetization could be completely removed by a.c. washing while preserving a good deal of the useful fossil magnetization. The described apparatus was used to make a study of the stability of this disturbing component of magnetization created in rock specimens by artificial lightning currents of intensities usually occuring in nature.

§ 4.1 *Experimental procedure*

As the main aim of the present study was to investigate the behaviour of the artificial IRM (caused by lightning) under alternating magnetic fields, no due attention was given to any particular selection of site or to a sampling procedure. 19 samples from different sites (see table 2) were measured for the remanence vector before and after a.c. washing in fields of increasing intensity till the vector in each individual specimen showed a fairly consistent direction. Later the specimens were subjected to lightning currents of different intensities and were again measured for the remanence vector. Thereafter the process of a.c. washing was repeated in an attempt to destroy the artificial IRM. The method of measurement of NRM and the technique of producing IRM due to artificial lightning discharges are described in the following sections.

§ 4.11 Measurement of NRM by a Förster Oerstedmeter

Most of the investigated specimens showed a fairly strong magnetization measurable by a Förster Oerstedmeter [6]. The method of measurement of the remanence vector by this instrument has been earlier described by KIENLEY and WYSS [9]. The essential procedure is same as that for the measurement of a specimen for the three components of magnetization by an astatic magnetometer, the difference being mainly in the orientation of the specimen and in the compensation of the earth's field. To separate the remanent and induced magnetization vectors and to determine the susceptibility components along the three axes of the specimen, in all 6 measurement positions with respect to the nearer probe of the Oerstedmeter are necessary. However, to minimise the effect of inhomogeneity of the rock material, specimens were measured in 12 different positions. For a better precision in the orientation of specimen and for improving the speed of measurement operations, three non-magnetic Plexiglass holders were designed, one for the manipulation of the specimen and the other two for the two probes of the Oerstedmeter which were mounted on a stable bench. Figure 2 shows the complete design of the device. The minimum distance between the specimen and the nearer probe was kept 7 cm, since at distances closer than this the specimen could no longer be considered to act as a point dipole. [14]

The degree of accuracy in measurement of the remanence vector by this instrument is much lower than that attainable by an astatic magnetometer or by a rock-generator. However, for specimens showing a fairly strong magnetization the mean error in measurement of magnetization is about $\pm$ 5%.

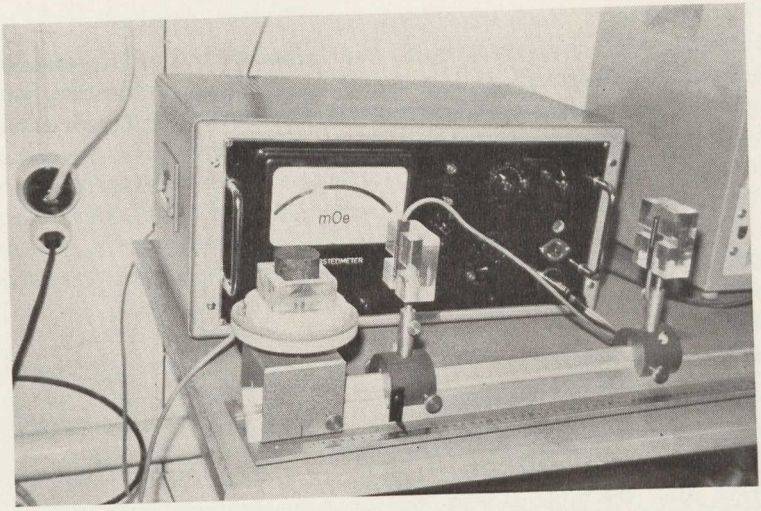

Figure 2
Orientation of the specimen with respect to the probes of the Oerstedmeter

§ 4.12 Production of artificial IRM in rock specimens

With the cooperation of Mr. H. SCHWAB of the Department of High Voltage Technology, SFIT, it was possible to create short duration pulse fields due to current intensities usually associated with lightning strikes in nature. The cylindrical specimens were placed with their axes along a horizontal circle at a known distance from a long straight conductor connected via a spark gap to a source of high tension. The pulse field arising from the lightning discharge is in the form of a circle around the conductor thereby creating an IRM along the axis of each specimen. At close distances from the conductor, the curvature and the gradient of the field could be significant enough to cause a strongly inhomogeneous magnetization in the specimens.

Six specimens lying at a distance of 5 cm from the conductor were subjected to a pulse field arising from 29000 amp (peak value) current and other 10 specimens were treated likewise with a stronger discharge current of 36000 amp (peak value) at a distance of 10 cm, the error in the current estimation being of the order of 10%. The abnormally large alterations in NRM of specimens caused by the above lightning discharges are shown in table 3.

§ 4.2 *Experimental results*

Table 2 shows the intensity of a.c. fields required for washing the soft component of magnetization for all the specimens investigated, the alternating field demagnetization curves for the 3 typical specimens being shown in figure 3. It would be seen from the curves that for the diorite sample the decrease in the intensity of NRM with an increase of a.c. field is much faster than that for the magnetite and haematite specimen, the rate of fall being slowest for the haematite specimen. This is probably on account of the high coercivity of the sediments compared to that of the igneous material. For all specimens excepting three, the directions of NRM were found to be

fairly consistent after a.c. washing which clearly demonstrates the efficacy of the a.c. demagnetization to remove the unstable components of secondary magnetization of relatively low coercivity.

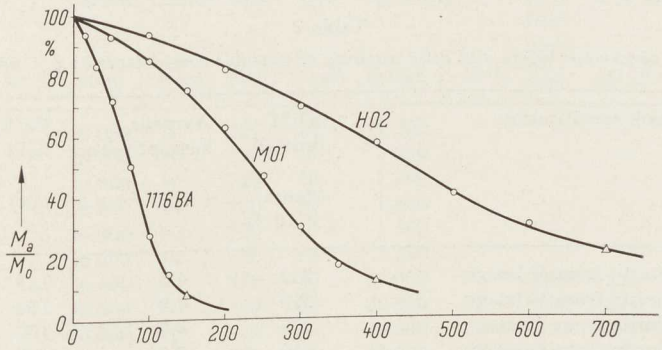

Figure 3
Alternating field demagnetization curves for the haematite (*HO 2*), magnetite (*MO 1*) and diorite (1116 *BA*) specimens.

M_a/M_0 Fraction of NRM left after a.c. washing
△ End-point where the NRM vector ceases to rotate

Table 3 shows the abnormally large values of NRM acquired by specimens after being subjected to pulse fields of lightning currents and the a.c. fields used in attempting to destroy the 'magnetic noise' effect of lightning. Normally it might be expected that a.c. fields of same intensity order as the pulse fields produced by lightning currents should be able to restore the original directions of NRM in the rock specimens. However, this did not occur and a.c. washing even on application of higher fields failed to restore the original directions of all but two haematite specimens (*HO 2* and *HO 1*). For these specimens, the direction of NRM vector became fairly stable after a.c. washing in peak fields of 900 Oe and 1400 Oe respectively, where as for the other 8 specimens rotation and shrinking of the vector contiuned without reaching an end-point. The irregularity in rotation of the NRM vector, in most cases did not seem to decrease even with peak a.c. fields exceeding 1000 Oe. Six specimens shown in the last column of table 3 were not subjected to a.c. fields and were left as such with their axes randomly oriented in the earth's field in order to examine the effect on the stability of IRM caused by lightning. On being again measured after a period of two weeks, NRM values of these specimens remained practically same within limits of experimental error.

§ 4.3 *Discussion of results and conclusions*

This study shows that lightning currents could give rise to a hard IRM of relatively high coercivity depending on the strength of the current, distance of the affected rock body and magnetic properties of the rock material. A.C. washing while usually successful in removing the soft component of magnetization of low coercivity, may

often fail to destroy completely the hard component of IRM caused by lightning. Rock specimens taken from surface outcrops which show an abnormally large and irregular NRM at a localised site should, as a rule be discarded from being used for paleomagnetic interpretation.

Table 2

NRM of rock specimens before and after washing of unstable components by a.c. demagnetization

Specimen No.	Rock specification	NRM (initial) (gauss $\times 10^{-5}$)	Average susceptibility ($\times 10^{-3}$ c.g.s.)	Peak a.c. field (Oe)	NRM after a.c. washing (gauss $\times 10^{-5}$)
1116 AA	Diorite from Brissago	295	4.6	125	30
1116 BA	Diorite from Brissago	320	4.9	150	26
1116 BB	Diorite from Brissago	370	4.8	100	25
1116 CA	Diorite from Brissago	420	5.0	100	25
1116 DA	Diorite from Brissago	375	4.8	125	26
1103 BB	Diorite from Brissago	245	2.2	100	27
1103 BA	Diorite from Brissago	185	1.8	75	26
1103 AA	Diorite from Brissago	200	1.9	100	24
1304 AA	Diorite from Brissago	25	0.1	30	..[1]
1304 BA	Diorite from Brissago	20	0.1	15	..[1]
1304 CA	Diorite from Brissago	22	0.1	15	..[1]
MO 1	Magetite ore[2]) from Ct. Wallis	2370	235	400	270
MO 2	Magetite ore[2]) from Ct. Wallis	4250	390	300	300
MS 1 A	Swedish magnetite ore[2])	7700	980	600	320
MS 1 B	Swedish magnetite ore[2])	8150	860	500	255
MS 2 A	Swedish magnetite ore[2])	11300	1070	600	290
MS 2 B	Swedish magnetite ore[2])	10500	1110	600	295
HO 1	Haematite ore[3]) from Gonzen	970	44	700	175
HO 2	Haematite ore[3]) from Gonzen	780	38	700	160

[1]) very weak and not measurable by Förster Oerstedmeter
[2]) of igneous origin
[3]) of sedimentary origin

In nature, lightning currents varying in intensity from 10 kAmp to about 200 kAmp have been observed with an average of about 50 kAmp. For altogether avoiding the disturbing effect of pulse field caused by lightning, samples may well have to be taken from depths below 15 m which at present does not seem to be an easy task. However, it should be a good practice to collect samples from mines and deep quarries where ever possible. In regions of paleomagnetic interest where mines and quarries do not exist, the next best possibility would be to get drilled cores from moderate depths such as 1 or 2 m. For samples taken from such moderate depths, a.c. washing may prove to be useful as demonstrated by findings of GRAHAM [8].

The author is not aware of any study so far made where thermal demagnetization has been employed to destroy the relatively stable IRM caused by lightning strikes. In this case, it remains doubtful to be seen whether thermal cleaning could succeed where a.c. washing has failed.

Table 3

Change in NRM *caused by artificial lightning currents and a. c. fields used in attempting to destroy lightning effects*

Specimen No.	NRM before lightning	Peak current	Distance	Pulse field	Duration	NRM after lightning	Peak a. c. field used	NRM after a. c. washing	NRM (2 weeks after lightning)
	(gauss × 10^{-5})	(amp)	(cm)	(Oe)	(μs)	(gauss × 10^{-5})	(Oe)	(gauss × 10^{-5})	(gauss × 10^{-5})
1116 AA	30	36 000	10	720	10	1 500	—	—	1400
1116 BA	26	36 000	10	720	10	1 650	—	—	1600
1116 BB	25	36 000	10	720	10	1 750	—	—	1800
1116 CA	25	36 000	10	720	10	1 600	—	—	1500
1103 AA	24	36 000	10	720	10	1 500	—	—	1500
1103 BB	27	36 000	10	720	10	1 250	—	—	1200
HO 2	160	36 000	10	720	10	13 000	900	135	—
MO 2	300	36 000	10	720	10	21 500	800	225	—
MS 1A	325	36 000	10	720	10	26 000	750	290	—
MS 2B	295	36 000	10	720	10	33 000	700	210	—
1116 DA	26	29 000	5	1160	10	4 650	1000	10	—
1103 BA	26	29 000	5	1160	10	2 800	800	14	—
HO 1	175	29 000	5	1160	10	29 500	1400	180	—
MO 1	270	29 000	5	1160	10	37 000	1200	155	—
MS 1B	255	29 000	5	1160	10	52 500	1600	70	—
MS 2A	290	29 000	5	1160	10	78 500	1700	125	—

Acknowledgements

I am indebted to Prof. F. GASSMANN and Prof. M. WEBER for their guidance and encouragement in the course of the work. Sincere thanks are due to Mr. G. BERSET for his help and suggestions in the design of the demagnetization apparatus and to Mr. W. GRABER for the mechanical out-fit and assembly of the complete set-up. I also wish to thank Dr. N. PAVONI and Mr. F. HELLER for the supply of suitable rock samples.

This work was done during the tenure of a Swiss Federal scholarship award made available at the Department of Geophysics, SFIT, Zurich.

REFERENCES

[1] J. A. AS and J. D. A. ZIJDERVELD, *Magnetic cleaning of rocks in paleomagnetic research*, Geoph. J. *1* (1958), 308.

[2] A. BRYNJOLFSSON, *Studies of remanent magnetism and viscous magnetism in the basalts of Iceland*, Advances in Physics *6* (1957), 247.

[3] K. M. CREER, *A. C. demagnetization of unstable Triassic Keuper Marls from SW England*, Geoph. J. *2* (1959), 261.

[4] C. W. F. EVERITT and J. A. CLEGG, *A field test of paleomagnetic stability*, Geoph. J. *6* (1962), 312.

[5] G. FANSELAU, *Die Erzeugung von homogenen Magnetfeldern durch Rechteckstrome*, Abhdlg. Geomagn. Inst. und Obs. *19* (Potsdam 1956).

[6] F. FÖRSTER, Zeitschrift für Metallkunde *32* (1940), 184.

[7] J. W. GRAHAM, *The stability and significance of magnetism in sedimentary rocks*, J. Geoph. Res. *54* (1949), 131.

[8] K. W. T. Graham, *The re-magnetization of a surface outcrop by lightning currents*, Geoph. J. *6* (1961), 85.
[9] J. Kienle and M. Wyss, Diplomarbeit ETH (1964), unpublished.
[10] M. A. Khan, *The remanent magnetization of basic tertiary igneous rocks of Syke*, Geoph. J. *3* (1960), 45.
[11] M. W. McElhinny and D. I. Gough, *Paleomagnetism of the great dyke of Southern Rhodesia*, Geoph. J. *7* (1963), 287.
[12] F. Rimbert, *Thesis* (University of Paris 1958).
[13] W. A. Robertson, *The paleomagnetism of some mesozoic intrusives and tuffs from eastern Australia*, J. Geoph. Res. *68* (1963), 2299.
[14] P. Vallabh Sharma, *On the point dipole representation of a uniformly magnetised cylinder*, Helv. Phys. Acta *38* (1965), 234.

Heat Flow in the Natural Gas Field of Hajduszoboszló

By T. Boldizsár[1])

Summary – The natural gas field of Hajduszoboszló in the Hungarian plain offered several virgin rock temperature measurements, further rock samples for measurement of conductivity. The Paleozoic bottom rock is covered by Mezozoic and Tertiary sediments inclusively flysch. One big and three small gas caps are found at a depth of about 1000 to 1200 in anticlyne structures. The average temperature gradient is 60 °C/km. The heat flow is between 2.2 and 2.7 μ cal/cm² sec, which is consistent to other heat flow values measured in the Hungarian basin.

1. Introduction

The natural gas field of Hajduszoboszló (21°18′E and 47°30′N) was located 10 years ago in the Eastern part of the Hungarian Plain. One big and three small gas caps were found and during the development of the field numerous borholes were put down and temperature measurements of considerable accuracy were made.

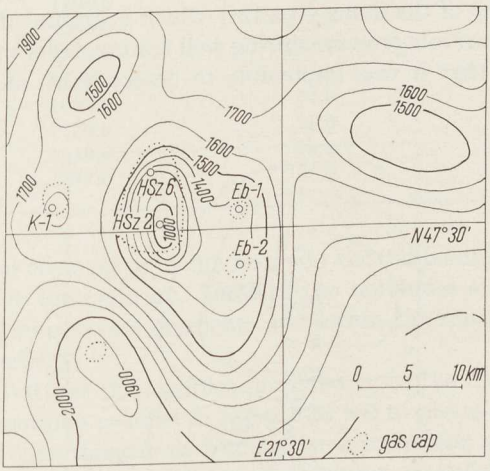

Figure 1
Gas fields of Hajduszoboszló and isobath lines of the bottom of the Tertiary basin in metres under sea level

[1]) Technical University, Miskole Hungary. – Privat-Address: Budapest I, Naphegy utca 27, Hungary.

The bottom rocks of the Hungarian basin at Hajduszoboszló are Palaeozoic crystalline schists, which are covered irregularly by Jurassic limestone, Cretaceous and/or Eocene flysch sediments. The Mesozoic sediments were tectonically strained during the Alpine orogenesis and numerous faults and small folds show the strong tectonic activity of this period. The thickness of the Mesozoic strata is between 200 and 800 m, but south of the territory the Mesozoic formations are absent showing the effect of the denudation in the Oligocene.

The Tertiary formation is represented by the upper part of the flysch which may perhaps be Paleocene, then 60 to 120 m thick Upper-Miocene (Sarmatien) lime, riolite tuff and marl follows. During the Pliocene periode litorale and lagoon sediments of 1000 to 2000 m thickness were deposited, covered by 100 to 150 m Pleistocene deposits of the same facies. The natural gas is stored in seven lithologic levels. One-one in the flysch and Miocene limestone and five in the Pliocene sands. The gas caps except, in the flysch are encirled by water contained in the pores of the sediments and an active water drive is present. The depth of the bottom of the Tertiary sediments and the gas fields are shown in figure 1 including the small Kaba and Ebes fields west respectively east of the main field of Hajduszoboszló.

2. *Measurements of temperature and conductivity*

Before starting gas production repeated temperature measurements were made at the bottom of the gas wells (table 1). The gradients of temperature are very uniform being between $5.7 \cdot 10^{-4}$ and $6.6 \cdot 10^{-4}$ deg °C/cm. Figure 2 shows the isotherms at the level of 1100 metres under the sea, which corresponds about 1200 m depth under the surface of the Hungarian plain in the main gas field of Hajduszoboszló. From figures 1 and 2 it can be seen that the maximum of temperature approximately corresponds to the top of the dome structure which is around the well Hsz-2.

The decrease of reservoir pressure during well testing, before temperature measurements was so small that it was impossible to detect it by measurement. Since no

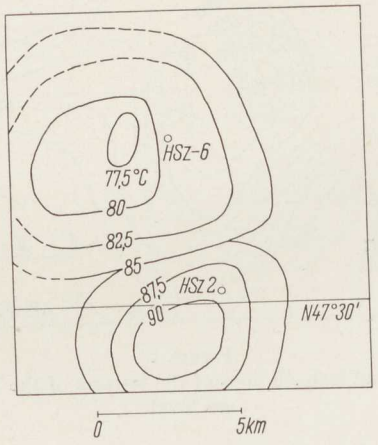

Figure 2
Isotherms of the Hajduszoboszló gas field at 1200 m depth

Table 1

Measurement of temperature

Number of borehole	Depth m	Temperature °C	Temperature gradient 10^{-4} °C/cm
Hsz–3	1215.0	87.0	6.33
Hsz–4	1200.0	79.0	5.75
Hsz–5	1190.0	80.0	5.88
Hsz–6	1270.0	85.0	5.88
Hsz–7	1175.0	84.0	6.29
Hsz–8	1160.0	85.0	6.45
Hsz–12	1039.0	73.0	6.06
Hsz–13	1316.0	83.0	5.56
Hsz–14	1240.0	89.0	6.37
Hsz–16	1062.0	74.0	6.02
Hsz–20	1040.0	73.5	6.10
Hsz–21	970.0	69.0	6.10
Hsz–23	1286.0	85.0	5.81
Hsz–26	1080.0	75.0	6.02
Hsz–29	1300.0	87.0	5.92
Hsz–30	1290.0	87.0	5.95
Hsz–31	1300.0	86.0	5.78
Hsz–32	1296.0	84.0	5.71
Hsz–33	1070.0	76.0	6.17
Hsz–37	1290.0	85.0	5.81
Hsz–53	942.0	69.0	6.25
Hsz–61	1310.0	90.0	6.10
HÁ–1	1250.0	87.0	6.17
HÁ–2	2032.0	127.0	5.78
Kaba–1	1100.0	77.0	6.10
Kaba–2	1600.0	115.0	6.58
Kaba É–1	2120.0	134.0	5.88
Ebes–2	1330.0	95.0	6.37
Ebes–5	1035.0	74.0	6.17
Ebes–6	1320.0	91.0	6.13
Ebes–7	1355.0	96.5	6.21
Ebes–10	1347.0	94.0	6,21

measurable expansion took place in the reservoir the temperatures approximate very closely the virgin rock temperature. Some of the boreholes are out of the gas field and their measured temperature gradients are within the range of the observed gas field temperature gradients.

Thermal conductivity of the samples prepared from the cores were measured in dry state. Since the samples swelled in water and fell to pieces it was not possible to measure the conductivity in saturated state. So a correction was applied to obtain the saturated conductivity, according to the method established at the heat flow measurement at Szentendre (T. Boldizsár [2][2])). The factor of correction adopted is 1.73, which is the average applied at Szentendre for 40 samples. There is no special reason why this correction factor was applied, except that it is not a high one and

[2]) Numbers in brackets refer to References, page 125.

other correction formulas give higher conductivities. Table 2 contains the lithology, average conductivity and the thickness-conductivity ratio for each stratigraphically defined sediment unit. No samples are available from the pleistocene and the value is adopted from Lakitelek, where the conductivity of similar Pleistocene deposits are available.

Table 2

Thermal conductivity of the specimens Hajduszoboszló Hsz–6 borehole

Stratum	Thickness, h m	Number of samples	Average conductivity, k cal/cm, sec, °C	$10^6\ h/k$ cm², sec, °C/cal
Pleistocene sand, sandy clay	163	–	0.006[1])	2.717
Levantinien, sand and clay	305	–	0.0037[2])	8.243
Upper Pannonien sand, sandy and limy clay	504	5	0.00430	11.721
Lower Pannonien marl, clay and sandy clay	211	2	0.00420	5.024
Upper Miocene Limestone, riolite tuff	87	5	0.00590	1.475
	$\Sigma h = 1270$			$\Sigma h/k = 29.180$

Kaba KÉ–1 borehole

Stratum	Thickness, h m	Number of samples	Average conductivity, k cal/cm, sec, °C	$10^6\ h/k$ cm², sec, °C/cal
Pleistocene sand, sandy clay	95	–	0.006[1])	1.583
Levantinien, sand and clay	419	2	0.0037	11.324
Upper Pannonien sand, sandy and limy clay	654	8	0.0038	17.211
Lower Pannonien marl, clay and sandy clay	214	–	0.0042[3])	5.095
Upper Miocene limestone	17	–	0.0059[3])	0.288
	$\Sigma h = 1399$			$\Sigma h/k = 35.501$

1) Adopted from Lakitelek.
2) Adopted from Kaba KE–1.
3) Adopted from Hsz–6.

3. Heat flow

Using data contained in tables 1 and 2, the terrestrial heat flow is calculated by the following formula:

$$q = \frac{\Delta t}{\Sigma \frac{h}{k}}$$

where Δt is the measured virgin rock temperature difference between bottom hole and surface. For annual average surface temperature $+10.0\,^{\circ}\mathrm{C}$ was adopted. Bottom hole temperatures were measured after several month of shutting down the Hsz-6 and KÉ-1 gas wells; commercial production started some 3 to 4 years after testing and temperature measurement.

In the well Hsz-6 at the Hajduszoboszló gas field, the heat flow is

$$q = \frac{75.0}{29.18 \cdot 10^{-6}} = 2.57 \cdot 10^{-6}\ \mathrm{cal/cm^2\ sec.}$$

In the KÉ-1 well at the Kaba-É gas cap the terrestrial heat flow is

$$q = \frac{82.4}{35.501 \cdot 10^{-6}} = 2.32 \cdot 10^{-6}\ \mathrm{cal/cm^2\ sec.}$$

The average heat flow of this region of the Hungarian plain may be given by

$$q = 2.45 \cdot 10^{-6}\ \mathrm{cal/cm^2\ sec.}$$

in good agreement with other data measured within the Carpathians (T. Boldizsár [1]).

The equivalent rock conductivity for Hsz-6, according to formula

$$k_e = q/\mathrm{grad}\ t$$

is 0.00437 cgs and for KÉ-1 0.00380 cgs, showing lower conductivities for KÉ-1 cores, whereas the measured temperature gradients are the same (table 1). Rocks samples represent but poorly the formation in both boreholes and it may be, that the difference in conductivity, and consequently in heat flow is not real. The difference seems to be within the error of measurement owing to the misrepresentation of the formation by the samples. In the Hsz-6 borehole the Pleistocene and Miocene formations with good conductivity are thicker (250 m) then in the KÉ-1 hole (112 m) and in Hsz-6 the upper and lower Pannonien samples show also higher conductivities.

Considering the uncertainty of the factor of correction for the in situ conductivity, further the poor representation of the formation by the 22 samples, the error in heat flow may be assumed to be about 10 per cent. Consequently the average heat flow of the territory can be considered between

$$2.2 - 2.7\ \mu\ \mathrm{cal/cm^2\ sec.}$$

References

[1] T. Boldizsár, *Heat flow in the Hungarian basin*, Nature *202* (1964), 1278.

[2] T. Boldizsár, *Heat flow in Oligocene sediments at Szentendre*, Pure and appl. Geophys. *61* (1965), 127.

(Received 7th April 1966)

The Effect of Solar Activity on the Boundary Frequencies of the E_S-Layer

By Dimitr Samardjiev[1])

Summary – On the basis of data from three temperate latitude stations (Dourbes, Juliusruh and Moscow) for the 1957 to 1964 period a study has been made of the correlation between the midday values of the boundary frequencies of the E_S-layer and the relative number of sun spots. A positive correlation with the solar cycle has been established. The decrease in the boundary frequencies of the sporadic layer from 1957 to 1964 was about 25 per cent.

The change in $f_0\,E_S$ at a constant zenith angle of the Sun ($\chi = 75°$) has been studied. A seasonal movement has been outlined with a very well expressed double wave with maximal values of $f_0\,E_S$ in the winter and the summer and minimal values during the equinoctial seasons.

The general probability or the probability for the occurrence of a layer with a fixed boundary frequency has been used in the studies made so far for the elucidation of the effect exercised by the cycle of solar activity on the E-sporadic layer, as a parameter characterising for instance the E_S-layer.

Studies on this question indicate that the probability of the occurrence of a sporadic layer (PE_S) for different geographical latidutes, does not show or has a slightly expressed positive or negative correlation with the cycle of solar activity [1, 2, 3][2]). In addition, for a given point in the annual course of PE_S, for different boundary frequencies, alternative tendencies are also established. These results show the diverse character of the causes which give rise to the formation and destruction of the sporadic layer, which, as it seems, depend on solar activity in different manners.

For this reason, it is interesting to analyse once again the problem of the effect of solar activity on the sporadic layer.

As it is known, at the altitude at which the E_S-layer is formed, both internal ionospheric processes and extra-ionospheric factors, differing in their character and degree, are active. Some of them determine the normal ionising state of the sporadic layer and others bring about some fixed temporary changes (increase and decrease) in its electronic concentration. Some or other factors manifest themselves more markedly, according to the geographical latitude. For this reason, for a given geographical region it is necessary to determine the basic ionising source conditioning the normal ionising state of the sporadic layer. For the temperate geographical latitudes, as experimental studies show [4, 5, 6, 7, 8] solar ultra-violet radiation constitutes the basic ionising source.

[1]) Geophysical Institute of the Bulgarien Academy of Sciences, Moskovska 6, Sofia, Bulgary.

[2]) Numbers in brackets refer to References, page 132.

The changes in solar activity, represented by the relative number of sun-spots, lead to changes in the degree of ionising radiation. For the normal layers (*E*, *F1*, *F2*), the changes in ionising radiation in the cycle of solar activity bring about changes in their electronic concentration and in the critical frequencies, respectively. The probability of the occurrence of a sporadic layer is such characteristics as is not directly connected with the ionising radiation and the electronic concentration of the E_S-layer. The change in the probability PE_S with the cycle of solar activity does not mean that the ionising state of the layer changes. It is rather that such a correlation reflects the changes in some other ionising or deionising factor which exercises an influence on the mechanism of the formation of the sporadic layer and which is more strongly changed by the solar cycle. For instance, if PE_S decreases in years of maximal solar activity, it should be assumed that this unknown factor sharply rises with the increase in the relative number of sun-spots and that it exercises a marked negative influence on the conditions for the formation of the sporadic layer. On the contrary, at stations where a negative correlation is observed, it may be assumed that this cause has decreased whereby the possibility for the occurrence of an E_S-layer has increased.

On account of this, the probability PE_S cannot be used as a characteristics for the changes in the ionising state of the sporadic layer which occur as a result of changes in the ionising radiation.

There are certain grounds to believe, as is also shown by rocket investigations, that the E_S-layer is a constant ionospheric formation which appears at a certain altitude in the atmosphere [9, 10]. In such case, similarly to the other ionospheric layers, it would be useful also for the sporadic layer to be defined in a normal, quiet ionising state. This will make it possible to determine certain regularities in the diurnal and seasonal course of the normal ionising state, and to establish anomalous period and their relation to certain geophysical and heliophysical phenomena and processes.

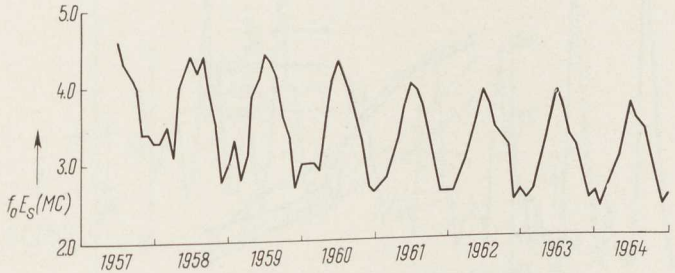

Figure 1

It is obvious that PE_S cannot be used for the determination of the undisturbed ionising state of the sporadic layer. For this purpose, the boundary frequency of the E_S-layer is a more suitable parameter, as to a certain extent it reflects the ionising state and its electron concentration.

It is known that the median values of the ionospheric characteristics of the permanent layer express the undisturbed state of the ionosphere. The boundary frequencies of the sporadic layer in a given month are not dispersed irregularly but are grouped in a narrow frequency interval. It is seen that the most probable values of

$f_0 E_S$ are slightly lower than the median values, while for the Es-layer, C type, they coincide with the median [11]. In the study [12], on the basis of a few temperate latitude stations, it has been confirmed that the boundary frequencies of the diurnal sporadic layer have no great dispersion and are grouped round the mean values. These studies permit the median value of the Es-layer to be used as a parameter characterising its undisturbed ionising state. In [12], making use of the median value of Es, a cosynus correlation with the zenith angle of the Sun, with a power indicator changing by about 0.25, has been established.

These results show that in the moderate geographical latitudes, the undisturbed ionising state of the diurnal sporadic layer, expressed through the mean values of the boundary frequencies, depends on ionising solar radiation. It should be expected in this case that the solar cycle and the changes in ionising radiation respectively would have an effect on the ionising state and the boundary frequencies of the sporadic layer.

In order to establish the correlation between the boundary frequencies of the Es-layer and the solar cycle (the relative number of the sun spots W), data from the following stations have been used: Dourbes: $\varphi = 50°06'$ N, $\lambda = 4°36'$ E; Juliusruh (Rügen): $\varphi = 54°38'$ N, $\lambda = 13°23'$ E; Moscow: $\varphi = 55°28'$ N, $\lambda = 37°19'$ E, for the period June 1957 to December 1964.

The results show that the mean values of the boundary frequencies of the Es-layer in the midday hours (11.00, 12.00 and 13.00 h) decrease with the drop in solar activity. As an example in figure 1, according to data from the Dourbes station, the monthly changes in these values are given. The figure shows a well-expressed seasonal course with maximal values during the summer months and minimal values in the autumn and winter periods. Besides, the trend towards a decrease in the boundary frequencies from 1957 to 1964, i.e. with the decrease in solar activity, is very well expressed. This reduction comprises all months, being best outlined for the summer maximal and the winter minimal values.

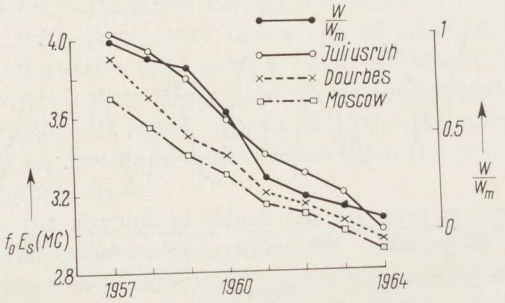

Figure 2

In order to outline this correlation still more clearly, the mean annual values of the midday values of the boundary frequencies for each station are plotted in figure 2. In the same figure 2 are also given the mean annual values of the relative number of the sun spots W (for the sake of comparison on the ordinate the relation of W to W_{max} is indicated). The diagram shows that with the decrease in W, the boundary frequencies of the sporadic layer also decrease steadily. For the Juliusruh station they went down from 4.0 megacycles in 1957 to 3 megacycles in 1964, i.e. by about 25 per cent. The

drop for Dourbes and Moscow was also about 1 megacycle, amounting to 24 and 22 per cent, respectively. This relative decrease in the midday values of the boundary frequencies is equal or greater than the corresponding decrease in the critical frequencies of the normal E-layer. Thus, for the Dourbes station the percentage drop in the critical frequencies of the E-layer from 1957 to 1964 was about 22 per cent, i.e. a little lower than that of the sporadic layer. For the Moscow and Juliusruh stations the boundary frequencies of the Es-layer shows a greater percentage in the decrease than the normal E-layer.

These results show that the ionising state of the sporadic layer expressed through its boundary frequencies has a positive correlation with the solar cycle. With the reduction in the relative number of the sun spots, the boundary frequencies and the ionising state of the Es-layer respectively also gradually decrease. This positive relationship, as well as the almost equal relative drop of the boundary frequencies of Es and the critical frequencies of the E-layer show that the quiet ionising state of the sporadic layer is determined by the same ionising factors which determine that of the normal E-layer as well.

In order to eliminate the considerable influence of the diurnal and seasonal progress of the height of the sun, and whence of that of the boundary frequencies, it is of interest to examine the behaviour of $f_0\,Es$ at a constant zenith angle. In this manner it is possible to evaluate the long-term changes of $f_0\,Es$ in the course of the year and the solar cycle.

As an example in figure 3, according to data from the Dourbes station, the course is indicated of the monthly median values for the boundary frequencies at a zenith angle of the sun $\chi = 75°$ (a: for morning values; b: for evening ones). Mean values of

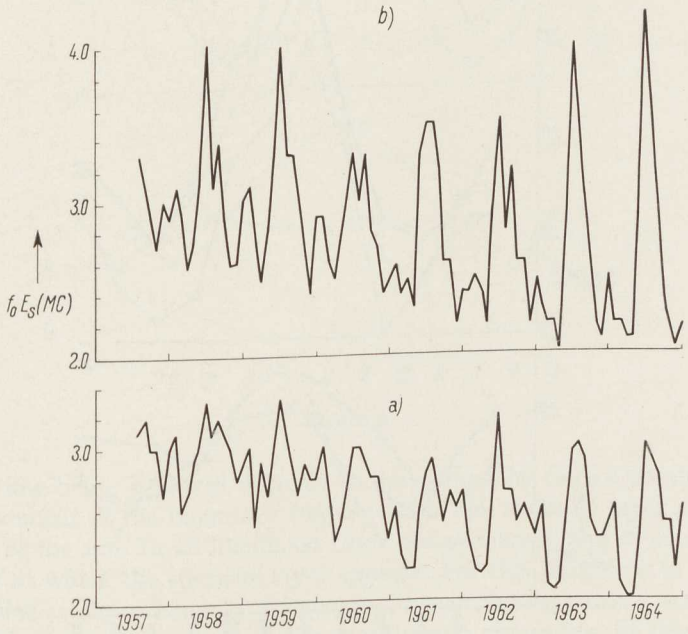

Figure 3

$f_0 E_S$ at the same zenith angle for the whole period are plotted in the next figure 4 for the three stations.

Certain peculiarities in the progress of $f_0 E_S$ may be easily discerned from the figures.

a) A well-expressed seasonal correlation exists in the boundary frequencies with a maximum in the winter (Dezember to January) and the summer (June to July) and a minimum during the spring-autumn season. In the years close to the maximum of solar activity this seasonal progress is less markedly expressed, whereas in the following period of decrease in the solar activity it becomes ever more outlined. This tendency is particularly strongly expressed in the evening values of the boundary frequencies. In years close to the minimum of solar activity, the difference increases in an especially marked way, reaching 2.3 megacycles between the maximal and minimal values of $f_0 E_S$ and conversely, in years close to the maximal solar activity this difference, especially in the morning values, decreases greatly (to 0.5 and 0.7 megacycles). In addition, a certain difference is observed in the seasonal courses in the morning and evening hours. For the morning values in all the three stations the minimum sets on in February, March and November, whereas for the evening values it shifts and is observed in March-April and in October.

b) A progressive drop in the boundary frequencies is observed with the decrease in solar activity. Both the maximal and minimal values of $f_0 E_S$ go down in the morning hours. For the evening hours the minimal values gradually decrease in years with minimal solar activity, while the opposite tendency is observed in the maximal values of $f_0 E_S$.

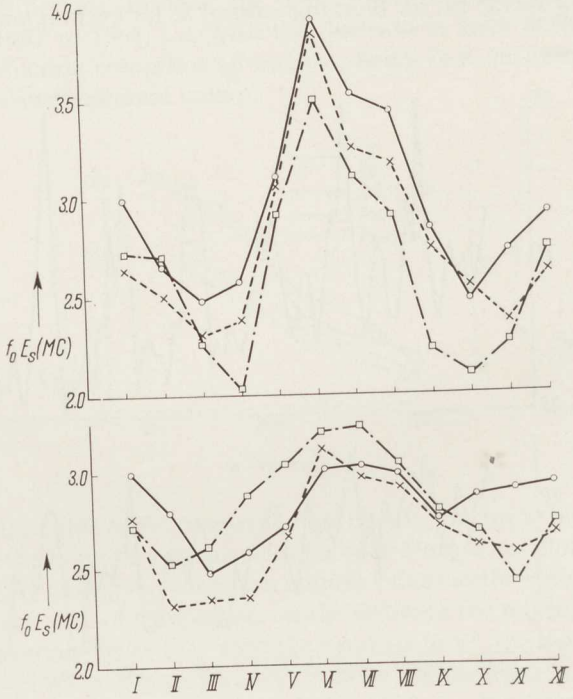

Figure 4

The obvious difference in the boundary frequencies of E at a constant zenith angle of the sun is an indication of the existence of different conditions in the morning and evening periods.

Of considerable interest is the comparison of the seasonal course of $f_0\,E_S$ with the changes in the critical frequencies of the normal E-layer at the same zenith angle. Mean data for the whole period of observation are given in figure 5 for $f_0\,E_S$ and $f_0\,E$ from Moscow station at $\chi = 75°$. It is seen from the figure that the morning hours of $f_0\,E$ show almost no seasonal correlation, whereas in the evening values a defined course with a maximum during the winter season (the well-known winter anomaly) and minimums in the summer is noticeable. A certain similarity between them is observed in the evening values in the descending (II, III, IV) and ascending, (X, XI, XII) parts of the two curves.

The comparison of the seasonal movement of the boundary frequencies with the changes in the absorption of long waves [13] at a zenith angle of $\chi = 80°$ shows a complete analogy. The data on the absorption from [13] are plotted on figure 5b. This similarity of the two curves probably speaks of the same causes conditioning these two phenomena.

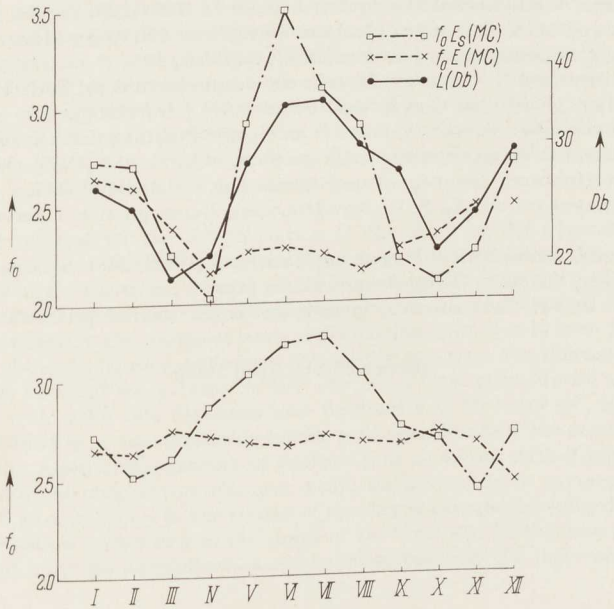

Figure 5

For the time being it is still difficult to determine the causes which lead to the seasonal movement of the boundary frequencies of the sporadic layer at a constant zenith angle of the sun. In all likelihood these are aeronomic and dynamic processes of the height at which the sporadic layer appears. For this purpose it is necessary to make a detailed study of temperature changes, atmospheric pressure, composition of the air and the seasonal changes in the atmospheric circulation in this part of the atmosphere.

Finally, the following more important conclusions can be drawn:

1. The use of the median values of the boundary frequencies has proved more practicable in establishing the effect of solar activity on the sporadic layer as an element reflecting its ionising state.

2. In the temperate geographical latitudes a decrease in the values of the boundary frequencies has been observed with the decrease in the relative number of sun spots. This reduction of $f_0 Es$ from 1957 to 1964 was about 25 per cent and was slightly greater than that of the critical frequencies of the normal E-layer.

3. A seasonal course is outlined with a very well expressed double wave in the values of the boundary frequencies of the Es-layer at a constant zenith angle ($\chi = 75°$). Maximal values of $f_0 Es$ are observed in the winter and the summer and minimal during the equinoctial seasons.

The author expresses his profound gratitude to Dr. G. Nestorov and Dr. K. Serafimov for the creative discussion of this paper.

References

[1] M. B. Ostanina, Ionospherical Researches Articles *13* (1964), 35.
[2] A. P. Seregina, Ionospherical Researches Articles *13* (1964), 29.
[3] R. K. Mitra and M. K. Dasgupta, J. Atm. Terr. Phys. *25* (1963), 415.
[4] T. S. Kerblai, Geomagnetism i aeronomia *II*, 3 (1962), 495.
[5] K. B. Serafimov and N. Gorinov, Isvestia na Geoph. institut pri BAN *VII* (1965), 73.
[6] D. Samardjiev, Isvestia na Geoph. institut pri BAN *VIII* (1966).
[7] D. Samardjiev and L. Triskova, Isvestia na Geoph. institut pri BAN *VII* (1965), 49.
[8] L. Triskova and D. Samardjiev, Studia geophys. et geod. *9*, 3 (1965), 306.
[9] G. S. Ivanov-Holodni, Geomagnetism i Aeronomia *IV*, 3 (1964), 417.
[10] T. V. Kasachevskaia and G. S. Ivanov-Holodni, Geomagnetism i Aeronomia *V*, 6 (1965), 1009.
[11] N. I. Potapova, Ionospherical Researches Articles *3* (1962), 34.
[12] D. Samardjiev, Gerlands Beitr. Geophysik (in print).
[13] G. Nestorov and B. Tafradjieva, Isvestia na Geoph. institut pri BAN *IX* (1966).

(Received 9th April 1966)

L'ordre du coefficient de récombinaison dans la couche E

Par Kyryl Borissov Serafimov[1])

Résumé – On propose une méthode de détermination de l'ordre du coefficient équivalent de récombinaison α en n'utilisant que les données ionosphériques. A cette fin on évalue l'apport de la vitesse des changements passagers $dN_m\,E/dt$ dans la densité électronique $N_m\,E$. L'évaluation se fait en présence d'une série de valeurs choisies de α, on observe laquelle des courbes définis $\delta_m(t)$ dans cette étude coïncidera de plus près avec $\delta_m(t)$ mesurée. Les changements de α montrés sur la figure 4 sont obtenus de cette manière. La valeur diurne de α varie de $(0.5 \div 1)\ 10^{-7}$ cm^3 sec^{-1}; peu après le lever et peu avant le coucher du soleil α devient $> 10^{-7}$ cm^3 sec^{-1}. Lorsque $\cos\chi > 0$, α d'après la règle décroît et devient $\alpha \leq 10^{-8}$ cm^3 sec^{-1}. Les explications des changements de α obtenus de cette manière sont données en rendant compte des changements par rapport aux ions atomiques et moléculaires, à la disparition rapide des ions positifs pendant le coucher du soleil en présence d'un coefficient de récombinaison plus grand et des changements de température eventuels. La symétrie ou l'asymétrie des fréquences critiques $f_0\,E$ quand $\cos\chi$ sont égaux permettent dans la marche diurne de juger de l'ordre de α. Toutes ces évaluations indiquent également des valeurs de α environ 10^{-7} cm^3 sec^{-1}. En précisant des mesures de $f_0\,E$ il est possible de définir non seulement l'ordre, mais aussi la valeur de α elle-même.

Summary – A method for the determination of the order of the equivalent recombination coefficient α is suggested, by using ionospheric data only. The increase in the speed of temporary changes in dN_m/dt in the electronic density $N_m\,E$ is estimated for this purpose. The estimation is done with series of selected for the sake of expediency values of α, following at the same time which curves $\delta_m(t)$, determined in the course of work, will coincide most closely with the $\delta_m(t)$ measured. The changes in α, shown in figure 4, have been obtained in this way. The diurnal value of α is in the range of (0.5 to 1) 10^{-7} cm^3 sec, α being $> 10^{-7}$ cm^3 sec a little after sunrise and a little prior to sunset. At $\cos\chi < 0$, α by rule decreases and becomes $\alpha \leq 10^{-8}$ cm^3 sec. Explanations of the changes thus obtained in α are indicated, taking into consideration the relation of atomic and molecular ions, the rapid disappearance of positive ions at sunset with a higher recombination coefficient and eventual temperature changes. From the symmetry or asymmetry of the critical frequencies of $f_0\,E$ at equal $\cos\chi$ in the course of the day it can also be judged for the order of α. All those estimates show values of α in the range of 10^{-7} cm^3 sec. In the case of precise measurements of $f_0\,E$, not only the determination of the order but also the real value of α is possible.

1. *Introduction*

Malgré les succès réalisés dans le rapprochement des valeurs du coefficient équivalent de récombinaison α, valeurs déduites suivant les données obtenues à l'aide du sondage vertical ionosphérique, des expériences de laboratoire, des mesures faites à l'aide de fusées et des calculs théoriques, nous pouvons considérer que le problème de la valeur de neutralisation et de là de l'ionisation (q) dans la couche E n'est pas

[1]) Institut Géophysique de l'Académie des Sciences de Bulgarie, Moskovska 6, Sofia, Bulgarie.

encore résolu d'une manière satisfaisante. La couche E est, relativement à la formation de la ionosphère, la plus régulière et c'est par les données ionosphériques s'y rapportant que devraient être le plus exactement déterminés les coefficients d'ionisation et de neutralisation. Mais il n'en est pas ainsi. Les données sur α obtenues au moyen du sondage vertical, par les mesures de la variation de la densité électronique maximale $N_m E$ durant des éclipses solaires, au coucher et au lever du soleil, d'après des données diurnes, ainsi que pendant les perturbations ionosphériques, fournissent des résultats inadéquats, souvent avec des ordres différents. Ainsi dans [1][2]) sont systématisées les recherches concernant α pendant l'éclipse solaire avec des valeurs pour α entre 0.5 et $4.5 \cdot 10^{-8}$ cm^3 sec^{-1}, tandis que des mesures faites dans d'autres conditions, permettent de constater que α varie entre 0.11 et $1.2 \cdot 10^{-8}$ cm^3 sec^{-1}. Dans la revue [2] on trouve des valeurs de α (obtenues à l'aide du sondage vertical) qui varient entre 10^{-9} et 10^{-6} cm^3 sec^{-1}. Dans [3] les valeurs de α obtenues pour la couche E, varient aussi de 10^{-9} à 10^{-7} cm^3 sec^{-1}. Il existe en outre une tendance déterminée vers les valeurs inférieures de α (de l'ordre de 10^{-8} et même moindre). Cette tendance est due au fait que les données ionosphériques précisées de la manière la plus simple par une équation du bilan d'ionisation-neutralisation du type α en prenant la moyenne de deux inconnues — q et α, permettent d'obtenir les valeurs de l'ordre de 10^{-8} cm^3 sec^{-1}. Mais une pareille mise au point des données ionosphériques est très primitive car elle ne prend pas en considération les changements possible dans α, les modifications de q et l'influence du transport des électrons, en admettant, en même temps, une série de défauts de méthode (voir par exemple la critique de [4] et [5]. Les résultats actuels des éclipses au cours des années 1961 à 1963 d'après les données radiophysiques et des fusées, indiquent des valeurs de α de $10^{-6} \div 0.20 \cdot 10^{-7}$ cm^3 sec^{-1} [4, 6, 7]. Si l'on fait une revue des données de laboratoire et de fusées on obtiendra une dispersion encore plus grande dans les valeurs de α de 10^{-6} à 10^{-9} (voir par exemple la revue [2]). En outre, il existe une série d'indication, montrant que α est une valeur variable ([3, 4, 5] ainsi que la discussion portant sur la partie de la couche E dans le [8]). Même sous ce rapport il existe des données et des opinions alternatives. Dans les [4] et [9] nous avons montré que α pendant la période du lever et du coucher et à l'approche de la phase de l'éclipse totale du soleil croît de $0.63 \cdot 10^{-7}$ approximativement à $3 \cdot 10^{-7}$. Dans [10] sont confirmés ces résultats en estimant que l'accroissement de α continue même durant la nuit. Dans la discussion relative aux rapports sur la couche E dans [3] et [8] des opinions contradictoires se développent: on considère d'une part que α croît pendant la transition à des conditions nocturnes, mais d'autre part, on fait remarquer qu'en présence d'un coefficient accrû de nuit α des sources supplémentaires d'ionisation pendant la nuit devraient être désignées. D'après des données de fusées dans la couche nocturne E $\alpha = 2 \cdot 10^{-8}$ cm^3 sec^{-1} [11]. D'après [12] α nocturne est environ $2 \cdot 10^{-8}$ et d'après [13] α varie de 10^{-8} à 10^{-9} cm^3 sec^{-1}. La source des opinions et des données évidemment contradictoires consiste en ce que les auteurs tâchent ordinairement d'utiliser des positions méthodiques qui conduisent vers une certaine coordination des données expérimentales et de fusées et des notions théoriques existantes. Pourtant, les données des mesures de laboratoire, ainsi que les données de fusées sont très contradictoires et admettent des interprétations alternatives. C'est pourquoi, nous tâcherons de définir et d'appliquer ici la

[2]) Les chiffres entre crochets renvoient à la bibliographie, pages 143/144.

méthode à l'aide de laquelle α est trouvé uniquement à l'aide de données du sondage vertical ionosphérique.

2. *Quelques considérations théoriques – Méthode*

Les données ionosphériques permettent la définition directe et suffisamment exacte de l'indice d'ionisation (nombre caractéristique, courbes caractéristiques) $J_E = Ch_E$ pour la couche E:

$$J_E \equiv Ch_E = \frac{q_0}{d} = (N_m E)^2 \sec \chi \,. \tag{1}$$

De là, la production électronique q_0 étant connue, on peut trouver le coefficient α. Cependant la définition de q_0 d'après des données héliophysiques et certaines notions de la section d'ionisation (σ) ainsi que la hauteur d'échelle par rapport aux composantes ionisées (H_0) est très conventionnelle et correspond au modèle choisi avec plus ou moins de liberté pour les processus aéronomiques. Le partage en deux parties de l'indice d'ionisation – q_0 et α est méthodiquement possible pendant les éclipses solaires (voir [4]). Dans les autres cas nous devons être jusqu'à un certain point de l'avis de NICOLET [14] que les solutions possibles du problème sur α et q séparés, exigent la supposition de la valeur de certains de ces paramètres, toutefois, il n'est pas clair comment on peut obtenir une interprétation correcte des processus ionosphériques des équations de base pour le bilan ionisation-neutralisation. Dans ce cas, nous proposons la méthode de la définition séparée de l'ordre q_0 et α se basant uniquement sur les données ionosphériques. A cette fin, en partant de la forme de base de l'équation de bilan pour la partie proche du maximum de la couche E [15, 16]:

$$\frac{dN_m E}{dt} = q_0 \cos^n \chi - \alpha (N_m E)^2 - \operatorname{div}(N_m E \cdot \vec{V}) \tag{2}$$

où: $\eta = 1 + \gamma - V$, γ est le gradient de la hauteur d'échelle, V est l'exposant dans la loi équivalente: $H = H_0 \cos^V \chi$ (voir [17]). $\vec{V}$ est la vitesse du transport électronique. En calculant le membre divergent, ainsi que l'influence des changements saisonniers de α, σ et H_0 pour l'indice corrigé d'ionisation $J_{E,0}$ dans [18] nous avons obtenu la formule:

$$J_{E,0} = \varphi(f_0 E, \alpha, V_z) \sec^{p'} \chi_m \cdot \sec^n \chi \,, \tag{3}$$

$$\varphi(f_0 E, \alpha, V_z) = K(f_0 E)^4 + \frac{\sqrt{K}(f_0 E)^2}{\alpha} \frac{\partial V_z}{\partial z} \,, \tag{3a}$$

$$p' = p_1 - (p_2 + p_3) \,, \tag{3b}$$

où: V_z la composante verticale de vitesse V, et p_1, p_2 et p_3 sont des exposants dans la dépendance approximative:

$$\sigma = \sigma_0 \cos^{p_1} \chi_m ; \; H_0 = H_{0m} \cos^{p_2} \chi_m \quad \text{et} \quad \alpha = \alpha_{0m} \cos^{p_3} \chi_m \,.$$

L'utilisation de (3) est rendu difficile à cause du manque de données de mesures du gradient de vitesse $\partial V_z/\partial z$. Pour l'éloignement des influences dynamiques et la négligence contrôlée de $\partial V_z/\partial z$ nous pouvons utiliser la dépendance logarithmique $\lg f_0 E (\lg \cos \chi)$. Si cette dépendance est une ligne droite, le membre divergent dans

(2) et (3) est immédiatement négligé, ainsi que les conditions quasi-stationnaires (liées à la possibilité de négliger aussi $dN_m\, E/dt$). Les écarts plus grands de ceux des fluctuations statistiques (exprimés dans la fréquence $\pm$ 0.05 MC) peuvent être rapportés aux influences dynamiques, aux relaxations et d'autres processus ionosphériques, ainsi qu'aux troubles des conditions quasi-stationnaires. Des nombreuses observations permettent la répartition de ces trois sources principales de l'écart de la ligne droite dans le champ logarithmique $\lg f_0\, E(\lg \cos \chi)$.

Sur la figure 1 a est montré le champ logarithmique pour la station ionosphérique de Sofia (septembre 1964) et sur la figure 1 b, le champ respectif avec les données mensuelles pour la station de Dourbes (juin 1964). Ces figures montrent que les trois principaux types d'écarts sont observés, notamment: a) Dans la période de l'aube et du coucher tardif; b) dans la période de midi (vers la culmination du soleil) et c) dans la période précédent de peu la culmination du soleil. Ces écarts sont observés aussi par d'autres auteurs [21, 22] etc. A plus forte raison, on trouve que les troubles essentiels de la dépendance linéaire entre $\lg f_0\, E$ et $\lg \cos \chi$ pendant la période précédent de peu et suivant le coucher du soleil et avant le déclin sont dues aux troubles des

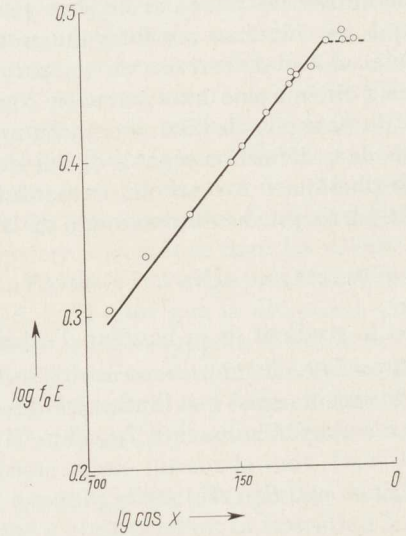

Figure 1 a

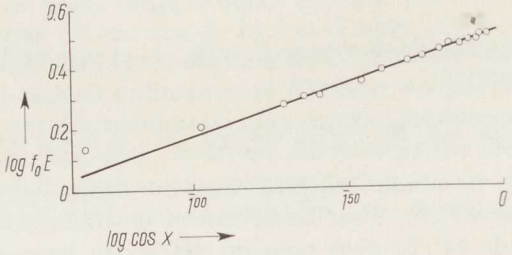

Figure 1 b

conditions quasi-équilibrées et des changements dans le coefficient α [4, 18, 19, 20]. Si pendant la période de midi on fait des sondages fréquents, alors pour $\lg f_0 E(\lg \cos\chi)$ dans cette partie de la journée on obtient de nouveau une dépendance linéaire, mais souvent avec un autre coefficient angulaire qui n'est pas égal à celui de toute la journée. Ce fait peut être bien expliqué par la dépendance spécifique saisonnière des valeurs σ, H_0 et α l'angle du soleil au zénith minimum (χ_m) [19, 20]. En outre, cette période est influencée également par la relaxation de midi qui caractérise l'inertie de l'ionosphère par rapport au modification dans la direction de changement de l'intensité de la source ionisée ($I \infty$). La baisse des fréquences critiques $f_0 E$ observée souvent avant midi où la rétention de leur accroissement sont liées étroitement à la stratification dans la structure de la couche E (voir [23, 24]), respectivement aux phénomènes dynamiques qui les engendrent. D'après [23, 24, 25] nous pouvons rapporter ces écarts d'avant midi à l'influence intensifiée de Sq système de courant électrique, qui confirme encore une fois que l'influence du transport électronique dans cette partie de la journée seulement n'est pas négligeable.

Nous pouvons conclure de ce qui précède que si nous voulons éliminer l'influence du mouvement il suffira de ne pas prendre en considération les écarts de la dépendance $\lg f_0 E(\lg \cos\chi)$ de la ligne droite un peu avant midi. Si nous éliminons aussi de l'analyse la période touchant ($+ 1 \div 3°$ après la culmination du soleil) nous aurons la partie de la journée, dans laquelle on peut négliger le membre divergent pour estimer que tous les écarts de la ligne droite dans le champ logarithmique sont dus aux conditions quasi-équilibrées non-remplies y compris également aux changements dans le coefficient α.

Par conséquent dans les secteurs de dépendance linéaire $\lg f_0 E$ de $\lg \cos\chi$ les conditions quasi-équilibrées sont observées, le membre divergent est négligeable et l'indice d'ionisation est constant. Il s'ensuit que l'équation de la ligne droite conformément à l'expression (2) et la dépendance connue $N_m E = 1.24 \cdot 10^4 \, f_0 E$ sera:

$$\lg f_0 E_g = -\frac{1}{4} \lg K + \frac{1}{4} \lg \frac{q_0}{\alpha} + \frac{n}{4} \lg \cos\chi \tag{4}$$

où: $K \approx 1.54 \cdot 10^8$, et par l'indice g nous marquons les valeurs correspondantes à la ligne droite.

En cas des conditions quasi-stationnaires non-accomplies mais de membre divergent négligeable nous obtenons aussi de (2) pour $f_0 E$:

$$\lg f_0 E = -\frac{1}{4} \lg K + \frac{n}{4} \lg \cos\chi + \frac{1}{4} \lg \left[\frac{q_0}{\alpha} - \frac{1}{\alpha \cos^n \chi} \frac{dN}{dt} \right]. \tag{5}$$

L'expression (5) indique qu'en présence d'un coefficient angulaire connu η (qui peut être obtenu de la période diurne la dépendance linéaire dans le champ logarithmique) étant observé nous pouvons définir le coefficient α et par conséquent aussi q_0. Il faut supposer pour cela que α est une valeur constante. Mais dans ce cas, nous pouvons obtenir α directement de l'expression:

$$\alpha = \frac{\frac{dN_m E}{dt}}{J_{E,0} \cos^{p'} \chi_m \cos^n \chi - N_m E^2}. \tag{6}$$

En prenant la moyenne d'une manière convenable d'après la méthode des moindres carrés des différents α obtenus aux differents moments. Un tel procédé mène à la

nécessité de prendre la moyenne des variations considérables dans les valeurs de α pour la station ionosphérique de Sofia les α obtenus changeant de 10^{-8} à 10^{-7} cm^3 sec^{-1}. Les données aéronomiques actuelles, ainsi que les résultats des recherches pendant les éclipses du soleil, indiquent que α subit probablement des changements considérables pendant la journée et surtout pendant la période du lever, du coucher et de la nuit. A cet effet et dans le but d'évaluer au moins l'ordre de α ainsi que la direction des changements de ce coefficient dans les différentes parties de la journée, nous procéderons ici de la manière suivante.

Nous utilisons la différence relative:

$$\delta_b = \frac{\lg f_0 E_b - \lg f_0 E_g}{\lg f_0 E_g} = \frac{\lg \left[\frac{q_0}{\alpha} - \frac{\sec^n \chi}{\alpha} \frac{dN_m E}{dt} \right] - \lg \frac{q_0}{\alpha_m}}{\lg f_0 E_g} \tag{7}$$

Dans (7) nous désignons par l'indice «b» les valeurs déduites des données pour $N^m E(t)$ d'après l'expression (5), en relevant des valeurs différentes du coefficient α (par exemple $\alpha' = 10^{-7}$ cm^3 sec^{-1}, $\alpha'' = 10^{-8}$ cm^3 sec^{-1} etc.; nous désignons par l'indice δ_b respective de la même manière δ_b', δ_b'' . . .). Nous marquons par α_m la valeur α précédent midi de près. Quand $\alpha = \text{const} = \alpha_m$ pour δ_b nous obtenons:

$$\delta_b = \frac{\lg \left[1 - \frac{\sec^n \chi}{q_0} \frac{dN_m E}{dt} \right]}{\lg f_0 E_g} \tag{8}$$

puisque $q = J_{E,0}\, \alpha$. On peut aussi obtenir de (8) q_0 et de même par conséquent α. Dans toute analyse ultérieure nous sommes d'avis que pour trouver $J_{E,0}$ on doit utiliser la méthode de [16], en éliminant la marche saisonnière ou bien la méthode de «coupes» developpée par nous dans [15]. Si $\alpha \neq \text{const}$ nous présentons alors par

$$\delta_b = \frac{\lg \frac{\alpha_m}{\alpha} + \lg \left(1 - \frac{\sec^n \chi}{q_0} \frac{dN_m E}{dt} \right)}{\lg f_0 E_g} . \tag{9}$$

La dépendance (9) permet de juger de la direction du changement de l'ordre de α. Pour définir l'ordre de α nous utilisons comme valeur de comparaison de l'écart relatif $\lg f_0 E$ de la ligne droite excluant, bien entendu, les secteurs aux influences négligeables des processus dynamiques et précédent de près midi:

$$\delta_m = \frac{\lg f_0 E - \lg f_0 E_g}{\lg f_0 E_g} . \tag{10}$$

Considérant que les processus ionisation-neutralisation au secteur près maximum dans la couche E se caractérisent par cette valeur du coefficient équivalent de recombinaison α_k, nous pouvons écrire:

$$\delta_b(\alpha_K) \approx \delta_m \tag{11}$$

au moment respectif examiné.

Ainsi pour obtenir l'ordre de α dans les différents moments propices à une analyse, il faut:

a) constituer les dépendances $\lg f_0 E(\lg \cos \chi)$;

b) éliminer les secteurs ou se manifeste l'influence des processus dynamiques et touchant de près midi;

c) définir d'après un procédé convenable q_0/α_m (voir [15, 16];

d) en présence de différentes constantes α il faut calculer le spectre des fonctions $\delta_b'(t)$, $\delta_b''(t)$, $\delta_b'''(t)$, . . . , en utilisant les valeurs connues de $dN_m\,E/dt$;

e) si l'une des fonctions $\delta_b^{(\kappa)}(t)$ coïncide ou est très proche de δ_m il s'ensuit que α est une valeur constante respectivement égale à α_K. Si $\delta_b^{(\kappa)}(t)$ coïncide seulement dans les périodes déterminées avec $\delta_m(t)$ il résulte que dans ces périodes nous avons $\alpha = \alpha_K$ en ce qui concerne les changements de α dans les autres périodes nous devons considérer la différence entre δ_b et δ_K en utilisant l'expression (9).

3. Résultats

Pour illustrer la méthode proposée nous utilisons les données de la station ionosphérique de Dourbes ($\varphi = 50°\,04'\,\mathrm{N}$; $\lambda = 04°\,36'\,\mathrm{E}$) pendant la période de IQSY (1964 à 1965); nous visons aussi à réduire au minimum les influences des facteurs de perturbation et des éruptions solaires chromosphériques. Nous avons fait les calculs avec trois valeurs de α (10^{-6}, 10^{-7} et 10^{-8} cm^3 sec^{-1}) et les valeurs médianes de $f_0\,E(t)$ pour chaque mois de la période indiquée. En ce qui concerne les valeurs de $\chi \geqq 75°$ nous avons utilisé au lieu de $\sec\chi$ des valeurs correspondantes de la fonction de Chapman [26] $f(R^*, \chi)$. Nous avons calculé les dérivés dN_m/dt d'après $\Delta N_m\,E/\Delta t$ accrus pour des intervalles d'une heure et de demi-heures. Il faut noter, qu'au sujet d'un grand groupe des stations de latitude moyenne (Genova, Juliusruh, Prague, Varsovie, Moscou et Sofia) les données sur $f_0\,E$ de la station de Dourbes satisfont mieux et par la moindre dispersion l'approximation linéaire de la dépendance $\lg f_0\,E(\lg\cos\chi)$. Nous avons utilisé pour les angles supérieurs à 75° et ayant $\cos\chi$ négatifs au lieu de cette dépendance, la dépendance $\lg f_0\,E\{\lg[f(R^*, \chi)]\}$.

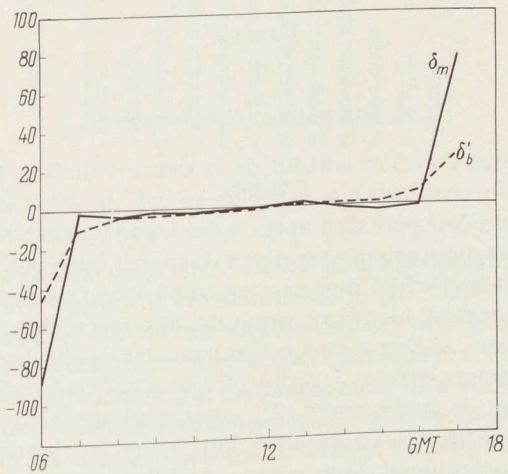

Figure 2

Les figures 2 et 3 illustrent les courbes concernant (correspondant à $\delta_b' = 10^{-7}$), δ_b'' (correspondant à 10^{-8} cm^3 sec^{-1}) et δ_m pendant le mois de mars 1964. Nous soulignons que le caractère des courbes permet de juger surtout de l'ordre de α, mais les

inexactitudes des mesures et de l'interprétation aussi que les declinations entre les courbes δ_m et δ_b empêchent de définir directement la valeur de α.

La figure 4 montre les résultats de l'évaluation de α pendant la période de recherches. Sur l'abscisse sont marqués les mois, et sur les ordonnées les valeurs d'angle du soleil au zénith χ. χ_m sert à marquer la valeur moyenne mensuelle du minimum. Les rectangles vides désignent les périodes de χ pour lesquelles $10^{-8} < \alpha \leq 10^{-7}$; le champ hachuré $\alpha > 10^{-7}$ et le champ foncé indique les valeurs de χ où $\alpha \leqq 10^{-8}$. Il faut noter que l'analyse est faite pour des valeurs horaires et que les périodes transitoires ne sont pas tracées avec précision, car on les détermine par des valeurs interpolées.

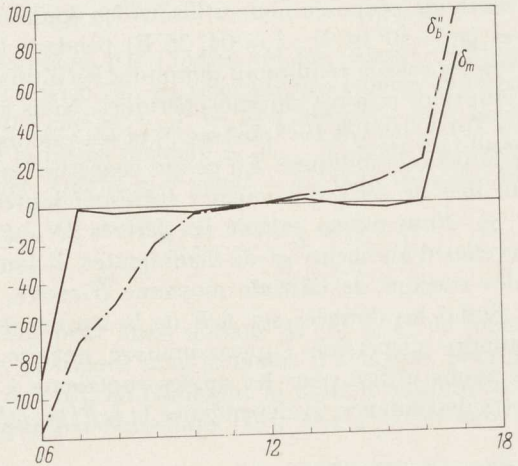

Figure 3

4. Discussions et déductions

Il ressort des figures 2 et 3 et surtout de la figure 4 dans la partie prédominante de la journée que le coefficient α est plus grand de 10^{-8} et proche ou égal à 10^{-7} cm^3 sec^{-1}. La deuxième période d'après la durée générale est de $\alpha \geqq 10^{-7}$ cm^3 sec^{-1}. Enfin il existe des secteurs temporaires d'une durée générale petite où α est $\alpha \leq 10^{-8}$ cm^3 sec^{-1}. L'ordre du coefficient moyen α est approximativement de 10^{-7} cm^3 sec^{-1}. Ces données correspondent bien aux résultats des recherches durant des éclipses solaires [4, 6, 7, 27] etc., si l'on a en vue les irradiations du disque et de la corona, ainsi que les changements dans α. L'ordre 10^{-7} est confirmé entièrement par l'interprétation des données de fusées (voir [2]), dans quelques analyses également de la marche diurne de $f_0\,E(t)$ [9]. Le résultat important en l'occurrence est celui des changements dans l'ordre de α. Nous avons montré dans [4] et [9] que de la baisse équivalente de la hauteur réduite de composantes ionisées durant la période du lever, et du déclin on peut s'attendre à un certain accroissement de α quoique pas grand. On peut obtenir s'il y a dans la couche E une concentration non négligeable d'ions négatifs pendant la période du lever, du coucher et de la nuit un plus grand accroissement de α. Les données de l'éclipse en 1961 [4] ainsi que de la marche diurne $f_0\,E(t)$ [9] indi-

quant un certain accroissement de α pendant la période du lever et du coucher. Nous pouvons constater avant tout d'après les résultats obtenus ici que le coefficient α n'est pas constant. Dans le nombre de cas prédominants pendant la période du matin, ainsi qu'avant le coucher, α dépasse 10^{-7} cm^3 sec^{-1} pour baisser ensuite aux valeurs $\leq 10^{-8}$ cm^3 sec^{-1}. Cette marche diurne caractéristique indique que pendant la nuit probablement les données ionosphériques sont interprétées comme il se doit par $\alpha \leq 10^{-8}$ cm^3 sec^{-1}. Dans 25% environ des cas observés approximativement de 10^{-7} pendant la période de midi, α augmente le matin pour baisser immédiatement au lever du soleil sur la surface terrestre et après le lever. Tel caractère de changement montre approximativement 50% de cas de la période d'après midi. Ce qui est particu-

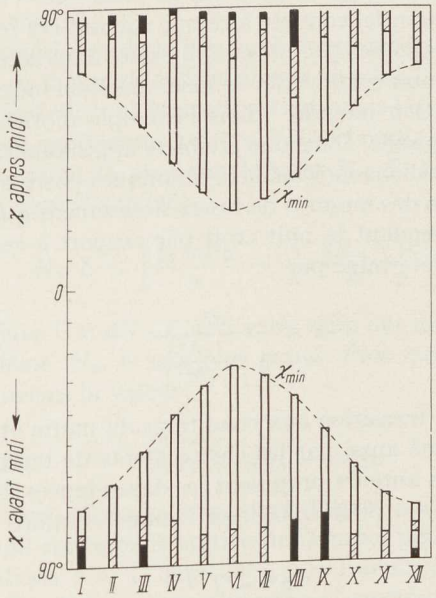

Figure 4

lièrement important et caractéristique c'est que toujours lorsque $\cos\chi < 0$ les valeurs de $f_0 E$ indiquent des valeurs décroissantes de α (10^{-8} cm^3 sec^{-1}). Dans 20% des observations la transition des hautes valeurs diurnes aux valeurs basses nocturnes de α se fait sans un accroissement intermédiaire supérieure à 10^{-7} cm^3 sec^{-1}. Environ 50% des observations n'indiquent pas un abaissement de α au lever et au coucher par rapport à ceux du jour. Malheureusement, il existe peut de données de tables sur $f_0 E$ avant le lever et après le coucher du soleil. L'analyse de ces résultats, nous permet de considérer comme vraisemblable le tableau qualificatif suivant de changements de α d'après les données de sondage ionosphérique vertical:

Pendant la période diurne α à l'ordre $(0.5 - 1) \cdot 10^{-7}$ cm^3 sec^{-1}. Tard dans l'après midi et à l'aube au debut du jour le coefficient α peut augmenter de plusieurs fois par 10^{-7} cm^3 sec^{-1} (en tout cas non moins de $4 \cdot 10^{-7}$ cm^3 sec^{-1}; épreuves isolées avec 10^{-6} et $0.5 \cdot 10^{-6}$ cm^3 sec^{-1} n'ont pas donné des résultats positifs). Lorsque $\cos\chi = 0$

et surtout quand $\cos\chi < 0$ le coefficient α diminue, ses valeurs rationnelles étant de 10^{-8} cm^3 sec^{-1}.

La transition aux valeurs décroissantes nocturnes correspondent bien aux résultats des travaux sur la couche nocturne E [11, 12, 13] etc.

La source de ces changements de α ne peut être attribué principalement au changement de température. Evidemment les changements de α indiquent des variations importantes des composantes ionisées de l'atmosphère terrestre. Grâce à des mesures masse-spéctrométriques de fusées [28, 29, 30] il a été établi que pendant le jour on trouve dans la couche E surtout deux types d'ions positifs – environ 75% NO^+ et environ 25% O_2^+. En ce qui concerne les coefficients spécifiques de récombinaison de la récombinaison de dissociation des ions moléculaires à l'aide de ces données on obtient des résultats différents. $\alpha^*_{NO^+} \leq (5 \div 13)\ 10^{-8}$ cm^3 sec^{-1} et $\alpha^*_{O_2^+}\ (1.5 \div 4) \cdot 10^{-7}$ cm^3 sec^{-1} d'après [2]. L'essentiel consiste à ce que suivant ces recherches et beaucoup d'autres encore (voir les exposées [2], [8] etc.) il existe dans la couche E deux types de base de molécules ionisés aux coefficients de neutralisation inégaux. L'un des types a une vitesse de neutralisation moindre (dans l'exemple d'orientation montré ici tel est NO^+), et l'autre plus grande. Dans une première approximation on peut considérer que la correlation entre les ions moléculaires atomiques positifs est proportionnelle à $(\cos\chi)^w$. Le résultat connu des mesures de fusées notamment que la concentration des ions moléculaires $[M^+]$ pendant la nuit croit par rapport à celle des ions atomique $[A^+]$, voir [31]. α étant déterminé par

$$\alpha = \frac{\alpha^*}{1 + \frac{[A^+]}{[M^+]}} \tag{12}$$

il s'ensuit que pendant la transition aux conditions du matin et du soir α croîtra. Cet accroissement sera souligné aussi par les changements de température qui influence α^*. Quoi que les différents auteurs proposent les dépendances de température les plus contradictoires de $\alpha^*(T)$, on peut considérer comme résultat le plus vraisemblable la proportionnalité:

$$\alpha^* \sim T^{-s} \tag{13}$$

où s est un nombre entier ou une fraction. Pendant la période du matin et du soir quand la température est plus basse, il résulte que α^* s'accroît. Ainsi, jusqu'ici nous avons argumenté qualitativement l'accroissement de α établi dans la partie précédente avec l'accroissement de χ vers le lever et le coucher. Mais il doit résulter de cet analyse que lorsque les χ sont proches de 90° ou plus grands de 90° (nuit pour la surface terrestre) α aura particulièrement de grandes valeurs ce qui est en contradiction avec le décroissement de ce coefficient établi, les $\cos\chi$ étant négatifs. Cependant l'explication de α nocturnes bas est notoire la concentration des ions positifs à récombinaison rapide qui définissent relativement élevé α de jour baisse brusquement pendant la nuit. A cet effet les ions se neutralisant relativement plus lentement prédominent pendant la nuit et conditionnent l'abaissement du coefficient équivalent de récombinaison. Ainsi, la marche diurne observée de bimaximum (avec quatre extrêmes) particulières dans la couche E est entièrement argumentée. En ce qui concerne la définition des conformités quantitatives il est nécessaire de passer de l'évaluation de l'ordre de α à des valeurs correspondantes moyennes de ce coefficient

d'après des observations plus fréquentes et convenablement précisées. C'est sur cette base seulement qu'on peut établir des relations quantitatives entre α, χ aussi que les caractéristiques de la saison et du lieu d'observation. L'essentiel consiste en ce que le tableau qualitatif montré et portant sur les modifications aux évaluations faites dans l'exposé précédent relatives à ce coefficient et il est en accord avec les notions et les données aéronomiques actuelles.

L'analyse des résultats obtenus pour δ_m nous permet de juger de l'application des conditions de l'approximation quasi stationnaire dans la couche E. Si pour la déviation relative admissible ($P = (dN/dt)/(\alpha N^2)$ nous adoptons la valeur limite $P = 5\%$, les conditions quasi stationnaires ne sont pas remplis uniquement quand $\chi \geqq 81°$, pendant la saison d'été – quand $\chi \geqq 87°$, il faut souligner que pour les χ plus grands, la déviation relative P croît brusquement, dépassant bien souvent 100%. Ces résultats confirment les recherches [18].

Les données ionosphériques de la couche E donnent la possibilité d'établir l'indice suivant le plus simple de la grande valeur diurne de α (de l'ordre 10^{-7} cm^3 sec^{-1}). Si α est de l'ordre de 10^{-8} cm^3 sec^{-1} alors systématiquement les valeurs d'après midi pour $N_m E$ (resp. $f_0 E$) seront supérieures à celles d'avant midi, les $\cos\chi$ étant égaux. C'est ce qui ressort de la relation la plus simple pour $N_m E$ [conformément à (2) en présence d'un membre divergent négligé].

$$N_m E = \left[\frac{q_0 \cos^n \chi}{\alpha} - \frac{1}{\alpha}\frac{dN_m E}{dt}\right]^{1/2}. \tag{14}$$

Etant donné que dans (14) $dN_m E/dt$ d'après midi ont un indice négatif, il s'ensuit que quand χ est le même, $N_m E$ sera plus grand. Pour caractériser cette asymétrie dans [19] nous introduisons la valeur:

$$\zeta = \frac{f_0 E_N}{f_0 E_V}\Bigg|_{\cos\chi_N = \cos\chi_V} \tag{16}$$

où par les indices N sont désignés les valeurs d'après midi et par l'indice V celles d'avant midi. En ce qui concerne la station de Dourbes pendant la période examinée dans 50% de cas analysés $\zeta \approx 1$, dans 25% $\zeta > 1$ et 25% $\zeta < 1$. Ces résultats indiquent que n'a pas de valeur systématiquement supérieure à une unité de valeur et que par conséquent α a une grande signification (c'est-à-dire $\alpha > 10^{-8}$ cm^3 sec^{-1}). Nous avons examiné dans [32] les causes de l'existence de cas $\zeta \gtrless 1$.

Pour finir notons que la méthode proposée peut considérablement augmenter la précision et par là permettre de déterminer non seulement l'ordre, mais aussi les valeurs absolues de α, si les points de mesures augmentes dans les champs logarithmiques en utilisant 15′ et 5′ de sondages et surtout si la précision de mesures et d'interprétation de la fréquence critique $f_0 E$ augmente également. La fréquence est un paramètre très bien défini (voir par exemple [23, 24])et le manque de non-précision dans sa détermination peut aboutir à $\pm$ 20 kc/s sans efforts particuliers [23]. Dans certains cas de mesures spéciales (augmentation de la fréquence) et répétition des impulsions de sondages et prolongation du temps nécessaire à faire le tour du diapason de travail [23] la déviation de fréquence $\pm$ 10 kc/s par rapport à la valeur mesurée et alors la définition de la valeur absolue de α d'après la méthode exposée devient possible. Dans l'analyse précédente, α étant égal à 10^{-7} cm^3 sec^{-1}, les déviations δ_b sont proches de celles dues à l'erreur de standard dans la détermination de $f_0 E$ (50 kc/s).

Littérature

[1] Ja. L. Al'Pert, *Rasprostranenie radiovoln i ionosfera*, Moskva (1960).
[2] A. D. Danilov et G. S. Ivanov-Holodnii, Uspehi Fisitscheskih Nauk *58*, 2 (1965), 259.
[3] *Solar Eclipse and the Ionosphere* (Pergamon Press, London NY, 1956).
[4] K. Serafimov, Pure and Appl. Geophys. *57* (1964), 133.
[5] K. Serafimov, Izwestia na Geof. Inst. pri BAN *V*, 2 (1964), 69.
[6] I. N. Odinzova et M. B. Ogir, Izwestia Krimskoi astrofis. obs. *29* (1963), 175.
[7] G. Nestorov et J. Taubenheim, J. Atm. Terr. Phys. *24* (1962), 633.
[8] *Electron Density Profiles in the Ionosphere and Exosphere*, Pergamon Press (1962).
[9] K. Serafimov et N. Gorinov, Gerlands Beitr. Geophys. *73*, 5/6 (1964), 257.
[10] G. Nestorov, Geomagnetizm i Aeronomia *5*, 6 (1966).
[11] L. G. Smith, J. Geophys. Res. *67* (1962), 1658.
[12] I. E. Titheridge, J. Atm. Terr. Phys. *17* (1959), 126.
[13] A. P. Mitra, J. Atm. Terr. Phys. *10* (1957), 140.
[14] M. Nicolet, Aeronomy (1962).
[15] K. Serafimov, Izwestia na sektiata po astronomia pri BAN *I* (1966).
[16] K. Serafimov et V. Letfus, Izwestia na Geofizitschnia Inst. pri BAN *IX* (1966).
[17] K. Serafimov, Izwestia na Geofisitschnia inst. pri BAN *VII* (1965), 61.
[18] K. Serafimov, Compt. Rend. Acad. Bulg. Sci. *18*, 10 (1965), 915.
[19] K. Serafimov, Gerlands Beitr. zur Geophys. (1966) (en presse).
[20] K. Serafimov, Compt. Rend. Acad. Bulg. Sci. *19*, 1 (1966).
[21] E. V. Appleton et A. I. Lion, J. Atm. Terr. Phys. *21* (1961), 73.
[22] C. M. Minnis et G. H. Bazzard, J. Atm. Terr. Phys. *17* (1961), 57.
[23] K. Serafimov, Izwestia na Geofisitschnia inst. pri BAN *IX* (1966).
[24] K. Serafimov, Geomagnetizm i Aeronomie (1966) (en presse).
[25] E. V. Appleton, A. I. Lyon et A. G. Pritchard, J. Atm. Terr. Phys. *7* (1955), 292.
[26] S. Chapman, Proc. Phys. Soc. *43* (1931), 483.
[27] I. H. Piddington, J. Geophys. Res. *56* (1951), 409.
[28] V. G. Istolnin, Iskustvenie sputniki Zemli *4* (1960), 171.
[29] V. G. Istolnin, Iskustvenie sputniki Zemli *7* (1961), 64.
[30] V. G. Istolnin, Iskustvenie sputniki Zemli *11* (1962), 95.
[31] G. S. Ivanov-Holodnii, Geomagnetism Aerinomia *II*, 3 (1962), 377.
[32] K. Serafimov, Compt. Rend. Acad. Bulg. Sci. *19*, 2 (1966).

(Reçu le 9 avril 1966)

Hydromagnetic Energy Balance Equations for the Solar Atmosphere

By VICTOR P. STARR[1]) and PETER A. GILMAN[1, 2])

Summary – Following the pattern established in meteorology, a system of energy balance equations for the solar atmosphere is presented. Since both hydromagnetic and thermodynamic processes are considered, the system includes kinetic, potential, thermal and magnetic forms of energy. Ionization energy is indirectly included in the treatment. The spatial distribution of the energy forms and the processes transforming them are separated into zonal means and departures from such means in order to depict turbulent eddy effects. Where available data concerning solar processes are used in order to appraise certain of the terms which arise.

1. Introduction

Since the first publication in this journal of the dynamic statistics concerning the motion of sunspots and sunspot groups by WARD [16][3]), the problem of the general circulation of the solar atmosphere has appeared in fresh light (see also WARD [17]). The nature of the new outlook on the subject, which has thus supervened, is in many crucial respects not dissimilar as regards gross features, from the description of the dynamic processes of the terrestrial atmospheric general circulation, elaborated by the first author of this paper and his associates in numerous publications during the past two decades. It is anticipated that the essentials of these publications, so prepared as to furnish a background for those interested in solar studies of the present kind, will be made available in report form shortly. It is likewise to be noted that these dynamic descriptions of the atmospheric circulation, obtained from observed data, have been duplicated with remarkable accuracy in the numerical models made for example by J. SMAGORINSKY and his coworkers [13] through the integration of the basic hydrodynamic equations.

As compared with the terrestrial problem, the solar one is rendered more complex by the fact that magnetic forces may well be comparable in size to other hydrodynamic forces. We thus must perforce deal *ab initio* with a hydromagnetic system. For this reason the new outlook owes much to the excellent and extensive measurements recently made by BUMBA and HOWARD [2, 3] of the sun's *general* magnetic field, distributed over the solar globe, as distinguished from local spot fields, etc. From both

[1]) Department of Meteorology, Massachusetts Institute of Technology, Cambridge, Massachusetts 02139, USA.

[2]) Present address: Department of Astro-Geophysics, University of Colorado, Boulder, Colorado 80302, USA.

[3]) Numbers in brackets refer to References, pages 154/155.

Ward's spot statistics (where spots are employed as tracers for large motions), and from the field measurements, it appears that in addition to the mean differential rotation there exist in the photosphere large hydromagnetic disturbances or eddies of perhaps wave numbers 6 to 10, and extending meridionally from equatorial to polar latitudes. We note here with interest that most recently PLASKETT [11] has also, on independent grounds, deduced the presence of such large photospheric disturbances.

According to STARR and GILMAN [14, 15], the large disturbances, in virtue of their shapes and orientations would feed kinetic energy into the differential rotation through the action of Reynolds stresses, in agreement with Ward's contention; while through the action of comparable eddy Maxwell stresses, kinetic energy of the mean differential rotation is converted into magnetic energy of the disturbances or, in other words, into eddy magnetic energy. This situation immediately poses the serious problem as to the source of the kinetic energy of the large disturbances. If we accept the general notion of the dynamo theory for the magnetic energy, the driving mechanism no doubt is a thermodynamic one, ultimately drawing upon the energy generated by nuclear transformations in the solar core.

Two proximate mechanisms suggest themselves to supply eddy kinetic energy for the large disturbances (STARR and GILMAN [14]).1. Convective action within and on the scale of the large disturbances. This presumably would be in response to horizontal temperature differences, and comprise what is known in meteorological parlance as baroclinic instability. 2. Convective action on a relatively small scale—say the supergranulation—accompanied by a reverse Kolmogorof cascade of kinetic energy into the large disturbances. Reverse cascades of this sort are a commonplace occurrence in meteorology. We may proceed on the basis of one or the other of these hypotheses in formulating mathematical models of the solar general circulation. The first such analytical mathematical model for investigating the possibility (1) has been published by GILMAN [6].

In order to secure a better grasp of the processes involved in such general circulation systems, it is useful to consider in some detail the energy balance equations. This has been done extensively in meteorology, in the study of model experiments and for other analogous fluid systems. In what follows, an attempt is made to formulate this set of equations for the photospheric general circulation in the sun. Actually a beginning for accomplishing this is contained in the discussions of the present writers, to which reference has already been made.

2. Energy equations

The task we wish to perform here is to set down the energy balance equations for the surface and adjacent layers of the sun in a rather general form, with as few restrictions as possible regarding the nature of the physical processes that can be represented. However, since the sun has no well defined physical boundaries, we must necessarily deal with the energetics of an open system, i.e., one in which there can be transports of energy of various kinds across the boundaries. As is well known to anyone familiar with energy formulations, this necessarily introduces a certain arbitrariness into any arrangement of the boundary transports and energy conversion terms internal to the system. Nonetheless, we feel it is worthwhile to present a formalism (albeit nonunique) which represents one possible complete accounting of the energetics. This can then

be used as a reference framework for more detailed discussion of particular aspects of the energy balance in later papers, and for fitting in place those effects which have already been discussed by the writers and others. It is hoped that the system we present may be of help both in suggesting possible terms that may be evaluated observationally, and terms which should be considered when formulating models for various solar phenomena.

For our own convenience and to focus more clearly on the physical processes, we take the liberty of writing the basic equations in a local cartesian (but rotating) coordinate system, rather than in spherical coordinates. The energy conversions and boundary terms will be basically the same as in the spherical case, except for numerous geometrical factors which would take into account the convergence of meridians. We also shall neglect the divergence of solar radii, assume gravity is constant, and take the interior to be rotating at a constant angular rate (e.g., the Greenwich convention) to which our rotating coordinates will refer.

If we had used spherical coordinates and taken our volume to be a closed spherical shell, there would have been no lateral boundaries and therefore, of course, no lateral boundary terms. To simulate this, we resort to the artifice, often used in meteorological studies, of containing the system between two vertical walls along what would be two latitude circles. If we assume those walls are rigid and perfectly electrically conducting all boundary fluxes (except by radiation and thermal conduction) will be eliminated. It is quite evident, however, that we cannot do this for the top and bottom boundaries, because transports across these boundaries are obviously important, and will have to be included.

In accordance with the above remarks, we may write the hydromagnetic equations (in cgs units) relative to a rotating coordinate system in the following form. (Here, the standard magnetohydrodynamic approximations have been made; see, e.g., SHERCLIFF [12]).

$$\frac{d\boldsymbol{v}}{dt} = -2\,\boldsymbol{\Omega} \times \boldsymbol{v} - \frac{1}{\varrho}\nabla p - g\,\boldsymbol{k} + \frac{1}{4\pi\varrho}(\nabla \times \boldsymbol{H}) \times \boldsymbol{H} + r\,, \tag{1}$$

$$\frac{d\boldsymbol{H}}{dt} = \boldsymbol{H} \cdot \nabla \boldsymbol{v} - \boldsymbol{H}\nabla \cdot \boldsymbol{v} + m\,, \tag{2}$$

$$\frac{d\varrho}{dt} = -\varrho\,\nabla \cdot \boldsymbol{v}\,, \tag{3}$$

$$\frac{dI}{dt} = -p\,\nabla \cdot \boldsymbol{v} + Q\,, \tag{4}$$

$$\nabla \cdot \boldsymbol{H} = 0\,. \tag{5}$$

In addition, there will be an equation of state appropriate to the solar constituents, their degree of ionization, etc.

Let $\boldsymbol{i}$, $\boldsymbol{j}$, $\boldsymbol{k}$, be unit vectors in the x, y, z (zonal, meridional, vertical) coordinate directions, respectively. Then in the above equations

$$\begin{aligned}
\boldsymbol{v} &= u\,\boldsymbol{i} + v\,\boldsymbol{j} + w\,\boldsymbol{k} \qquad = \text{velocity}\,,\\
\boldsymbol{H} &= H_x\,\boldsymbol{i} + H_y\,\boldsymbol{j} + H_z\,\boldsymbol{k} = \text{magnetic field}\,,\\
\boldsymbol{\Omega} &= \Omega\cos\phi\,\boldsymbol{j} + \Omega\sin\phi\,\boldsymbol{k}\,,\\
&= l/2\,\boldsymbol{j} + f/2\,\boldsymbol{k}\,.
\end{aligned}$$

Ω being the interior angular velocity of sun, where ϕ is solar latitude. The remaining notation is defined as follows:

g = acceleration of gravity,
ϱ = density,
p = pressure,
I = internal energy/unit mass, including ionization energy,
Q = rate of heat addition/unit mass, including thermal diffusion,
r = frictional force,
m = diffusion of magnetic flux.

It has been customary in studies of the energetics of the earth's atmospheric general circulation to represent the velocity fields as the sum of a zonally averaged value and the deviation from that average. In this way one can then examine, for example, the mechanisms for the maintenance of the mean zonal flow, by writing an energy balance equation for that component alone. It is useful to use the same procedure in the solar case, for the magnetic fields as well as the velocities. In this way we can focus our attention more clearly on such problems as the maintenance of the equatorial acceleration, and on the dynamics of the mean poloidal and (subsurface) toroidal magnetic fields.

Let us denote the zonal average by square brackets, and the deviation from it by a prime. Thus, for example, the zonal flow will be written as $u = [u] + u'$. The mean toroidal magnetic field will then be represented simply by $[H_x]$, while the mean poloidal field will be $[H_y]\,\boldsymbol{j} + [H_z]\,\boldsymbol{k}$. There are several ways in which one could write the energy balance, depending upon which components of the energy one wants particularly to distinguish. Here we shall split up the kinetic and magnetic energies each into three parts. Integrated over the entire volume, which we shall denote by τ, these are the mean zonal kinetic $Z\,K\,E = 1/2 \int \varrho[u]^2\, d\tau$; the mean zonal, or toroidal, magnetic $Z\,M\,E = 1/8\,\pi \int [H_x]^2\, d\tau$; the mean meridional kinetic $M\,K\,E = 1/2 \times \int \varrho([v]^2 + [w]^2)\, d\tau$; the mean meridional, or poloidal, magnetic $M\,M\,E = 1/8\,\pi \times \int ([H_y]^2 + [H_z]^2)\, d\tau$; the eddy kinetic $E\,K\,E = 1/2 \int \varrho([u'^2] + [v'^2] + [w'^2])\, d\tau$; and finally the eddy magnetic energy $E\,M\,E = 1/8\,\pi \int ([H_x'^2] + [H_y'^2] + [H_z'^2])\, d\tau$.

Finding the balance equation for any one of these energies is quite straightforward. First we assume that we can neglect density variations along a latitude circle unless they are coupled with gravity. Now suppose, for example, that we wish to find the balance equation for the mean zonal kinetic energy. We take the zonal component of the equation of motion from (1), and split all the remaining variables into their zonal averages and departures. We then take a zonal average of the equation, thereby eliminating all terms that are linear in perturbation quantities. Next we multiply the averaged equation by $[u]$, and rearrange by parts, using the mass continuity equation (3), and using (5) for the magnetic terms, to obtain an equation for $\partial/\partial t\, \varrho[u]^2/2$. This equation is then integrated over the whole volume of the system, with further rearrangements by parts. Boundary terms at the side walls are eliminated by choosing the normal components of the velocity and magnetic field to vanish there, consistent with our assumption that these walls are rigid and perfectly conducting. Boundary terms at the bottom and top are retained. In this way, we can obtain a balance

equation for the total mean zonal kinetic energy in the system, which may be written in the form

$$\begin{aligned}\frac{\partial}{\partial t}\int \frac{\varrho[u]^2}{2}\,d\tau &= \int \varrho\, f[u]\,[v]\,d\tau - \int \varrho\, l[u]\,[w]\,d\tau \\ &+ \int \varrho[u'\,v']\,\frac{\partial[u]}{\partial y}\,d\tau + \int \varrho[u'\,w']\,\frac{\partial[u]}{\partial z}\,d\tau \\ &- \int \frac{1}{4\pi}\,[H'_x\,H'_y]\,\frac{\partial[u]}{\partial y}\,d\tau - \int \frac{1}{4\pi}\,[H'_x\,H'_z]\,\frac{\partial[u]}{dz}\,d\tau \\ &- \int \frac{1}{4\pi}\,[H_x]\,[H_y]\,\frac{\partial[u]}{\partial y}\,d\tau - \int \frac{1}{4\pi}\,[H_x]\,[H_z]\,\frac{\partial[u]}{\partial z}\,d\tau \\ &+ \int \left(\frac{1}{4\pi}\,[H_x]\,[H_z] + \frac{1}{4\pi}\,[H'_x\,H'_z] - \varrho[u'\,w'] \right. \\ &\left. - \frac{\varrho}{2}\,[u]\,[w]\right)[u]\,\Big|_{z_1}^{z_2} dx\,dy - F_z\,.\end{aligned} \tag{6}$$

Here F_z is the zonal kinetic energy lost to friction, and z_2 and z_1 denote the top and bottom where the boundary terms are evaluated.

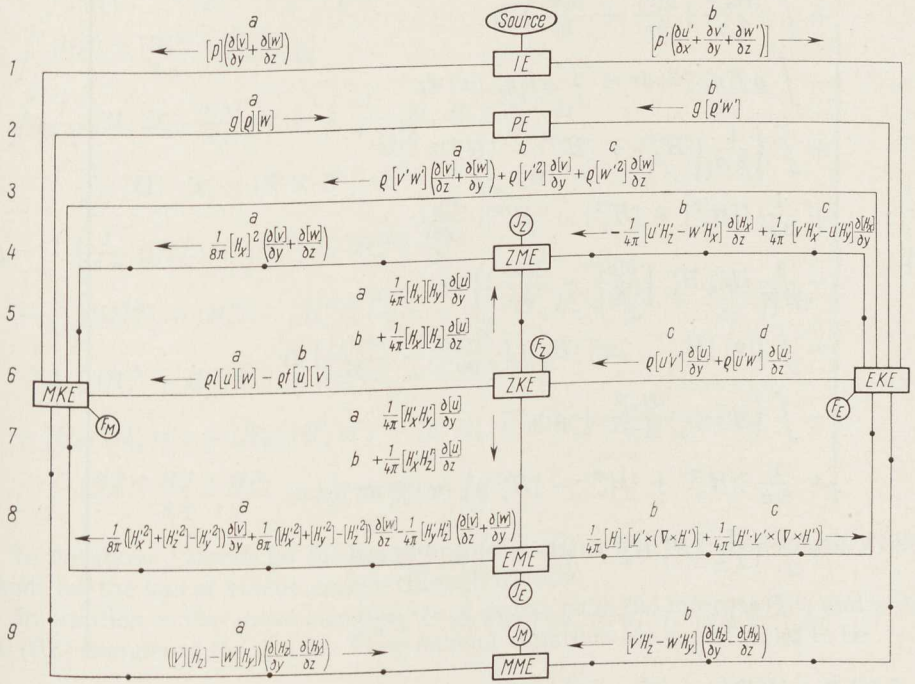

Figure 1

Energy balance diagram. The various energies appear in rectangular boxes, while dissipation terms are represented by circles. The energy conversion terms (with the volume integral signs omitted for simplicity) are written along the lines connecting the energies. The arrows indicate the direction of energy flow if the conversion term as presented is positive. The solid dots on lines distinguish the conversions between kinetic and magnetic energy. The numbers in the left margin and the small letters next to each conversion term serve as reference guides for discussion in the text.

By a similar procedure to that sketched above, we may find energy balance equations for the other types defined, as follows

$$\begin{aligned}
&\frac{\partial}{\partial t}\int \frac{[H_x]^2}{8\pi}\,d\tau = \int \frac{1}{4\pi}\,[H_x]\,[H_y]\,\frac{\partial [u]}{\partial y}\,d\tau + \int \frac{1}{4\pi}\,[H_x]\,[H_z]\,\frac{\partial [u]}{\partial z}\,d\tau \\
&- \int \frac{[H_x]^2}{8\pi}\left(\frac{\partial [v]}{\partial y} + \frac{\partial [w]}{\partial z}\right) d\tau \\
&- \int \frac{1}{4\pi}\,[u'\,H'_z - w'\,H'_x]\,\frac{\partial [H_x]}{\partial z}\,d\tau \\
&+ \int \frac{1}{4\pi}\,[v'\,H'_x - u'\,H'_y]\,\frac{\partial [H_x]}{\partial y}\,d\tau \\
&+ \int \frac{1}{4\pi}\,[u'\,H'_z - w'\,H'_x]\,[H_x]\,\Big|_{z_1}^{z_2} dx\,dy - \int \frac{1}{8\pi}\,[H_x]^2\,[w]\,\Big|_{z_1}^{z_2} dx\,dy - J_z\,.
\end{aligned} \tag{7}$$

$$\begin{aligned}
&\frac{\partial}{\partial t}\int \frac{\varrho}{2}\,([v]^2 + [w]^2)\,d\tau = \int [p]\left(\frac{\partial [v]}{\partial y} + \frac{\partial [w]}{\partial z}\right) d\tau - \int g[\varrho]\,[w]\,d\tau \\
&\quad + \int \left(\varrho[v'\,w']\left(\frac{\partial [v]}{\partial z} + \frac{\partial [w]}{\partial y}\right) + \varrho[v'^2]\,\frac{\partial [v]}{\partial y} + \varrho[w'^2]\,\frac{\partial [w]}{\partial z}\right) d\tau \\
&\quad + \int \frac{[H_x]^2}{8\pi}\left(\frac{\partial [v]}{\partial y} + \frac{\partial [w]}{\partial z}\right) d\tau \\
&\quad - \int \varrho\, f[u]\,[v]\,d\tau + \int \varrho\, l[u]\,[w]\,d\tau \\
&\quad + \int \left(\frac{1}{8\pi}\,([H'^2_x] + [H'^2_z] - [H'^2_y])\,\frac{\partial [v]}{\partial y}\right. \\
&\quad + \frac{1}{8\pi}\,([H'^2_x] + [H'^2_y] - [H'^2_z])\,\frac{\partial [w]}{\partial z} \\
&\quad \left. - \frac{1}{4\pi}\,[H'_y\,H'_z]\left(\frac{\partial [v]}{\partial z} + \frac{\partial [w]}{\partial y}\right)\right) d\tau \\
&\quad - \int ([v]\,[H_z] - [w]\,[H_y])\left(\frac{\partial [H_z]}{\partial y} - \frac{\partial [H_y]}{\partial z}\right) d\tau \\
&\quad - \int \left([p] + \frac{[H_x]^2}{8\pi} + \varrho[w'^2]\right. \\
&\quad \left. + \frac{1}{8\pi}\,([H'^2_x] + [H'^2_y] - [H'^2_z])\right)[w]\,\Big|_{z_1}^{z_2} dx\,dy \\
&\quad + \int \left(\frac{1}{4\pi}\,[H'_y\,H'_z] - \varrho[v'\,w']\right)[v]\,\Big|_{z_1}^{z_2} dx\,dy \\
&\quad - \int \frac{\varrho}{2}\,([v]^2 + [w]^2)\,[w]\,\Big|_{z_1}^{z_2} dx\,dy - F_M\,.
\end{aligned} \tag{8}$$

$$\begin{aligned}
&\frac{\partial}{\partial t}\int \frac{[H_y]^2 + [H_z]^2}{8\pi}\,d\tau = \frac{1}{4\pi}\int ([v]\,[H_z] - [w]\,[H_y])\left(\frac{\partial [H_z]}{\partial y} - \frac{\partial [H_y]}{\partial z}\right) d\tau \\
&\quad + \frac{1}{4\pi}\int [v'\,H'_z - w'\,H'_y]\left(\frac{\partial [H_z]}{\partial y} - \frac{\partial [H_y]}{\partial z}\right) d\tau \\
&\quad + \frac{1}{4\pi}\int ([v]\,[H_z] - [w]\,[H_y] + [v'\,H'_z - w'\,H'_y])\,[H_y]\,\Big|_{z_1}^{z_2} dx\,dy - J_M\,.
\end{aligned} \tag{9}$$

$$
\begin{aligned}
&\frac{\partial}{\partial t}\int \varrho\left(\frac{[u'^2]+[v'^2]+[w'^2]}{2}\right)d\tau \\
&=\int p'\left(\frac{\partial u'}{\partial x}+\frac{\partial v'}{\partial y}+\frac{\partial w'}{\partial z}\right)d\tau-\int g[\varrho'\,w']\,d\tau \\
&\quad-\int\left(\varrho[v'\,w']\left(\frac{\partial[v]}{\partial z}+\frac{\partial[w]}{\partial y}\right)+\varrho[v'^2]\,\frac{\partial[v]}{\partial y}+\varrho[w'^2]\,\frac{\partial[w]}{\partial z}\right)d\tau \\
&\quad-\int\frac{1}{4\pi}\,[v'\,H'_x-u'\,H'_y]\,\frac{\partial[H_x]}{\partial y}\,d\tau+\int\frac{1}{4\pi}\,[u'\,H'_z-w'\,H'_x]\,\frac{\partial[H_x]}{\partial z}\,d\tau \\
&\quad-\int\varrho[u'\,v']\,\frac{\partial[u]}{\partial y}\,d\tau-\int\varrho[u'\,w']\,\frac{\partial[u]}{\partial z}\,d\tau \\
&\quad+\int\frac{1}{4\pi}\,[\boldsymbol{H}]\cdot[\boldsymbol{v}'\times(\nabla\times\boldsymbol{H}')]\,d\tau+\int\frac{1}{4\pi}\,[\boldsymbol{H}'\cdot\boldsymbol{v}'\times(\nabla\times\boldsymbol{H}')]\,d\tau \\
&\quad-\int[v'\,H'_z-w'\,H'_y]\left(\frac{\partial[H_z]}{\partial y}-\frac{\partial[H_y]}{\partial z}\right)d\tau \\
&\quad-\int[p'\,w']\,\Big|_{z_1}^{z_2}dx\,dy-\int\varrho\left(\frac{[u'^2]+[v'^2]+[w'^2]}{2}\right)[w]\,\Big|_{z_1}^{z_2}dx\,dy \\
&\quad-\int\varrho\left[\left(\frac{u'^2+v'^2+w'^2}{2}\right)w'\right]\Big|_{z_1}^{z_2}dx\,dy-F_E\,.
\end{aligned}
\tag{10}
$$

$$
\begin{aligned}
&\frac{\partial}{\partial t}\int\frac{[H'^2_x]+[H'^2_y]+[H'^2_z]}{8\pi}\,d\tau \\
&=\int\frac{1}{4\pi}\,[H'_x\,H'_y]\,\frac{\partial[u]}{\partial y}\,d\tau+\int\frac{1}{4\pi}\,[H'_x\,H'_z]\,\frac{\partial[u]}{\partial z}\,d\tau \\
&\quad-\int\frac{1}{4\pi}\,[\boldsymbol{H}]\cdot[\boldsymbol{v}'\times(\nabla\times\boldsymbol{H}')]\,d\tau-\int\frac{1}{4\pi}\,[\boldsymbol{H}'\cdot\boldsymbol{v}'\times\nabla\times\boldsymbol{H}']\,d\tau \\
&\quad-\int\left(\frac{1}{8\pi}\,([H'^2_x]+[H'^2_z]-[H'^2_y])\,\frac{\partial[v]}{\partial y}\right. \\
&\quad\left.+\frac{1}{8\pi}\,([H'^2_x]+[H'^2_y]-[H'^2_z])\,\frac{\partial[w]}{\partial z}-\frac{1}{4\pi}\,[H'_y\,H'_z]\left(\frac{\partial[v]}{\partial z}+\frac{\partial[w]}{\partial y}\right)\right)d\tau \\
&\quad-\int\Big([(H'^2_x+H'^2_y)\,w']-[(u'\,H'_x+v'\,H'_y)\,H'_z] \\
&\quad+[H_x]\,[H'_x\,w']+[H_y]\,[H'_y\,w']-[u'\,H'_x+v'\,H'_y]\,[H_z]\Big)\,\Big|_{z_1}^{z_2}dx\,dy \\
&\quad-\int\frac{[H'^2_x+H'^2_y+H'^2_z]}{8\pi}\,[w]\,\Big|_{z_1}^{z_2}dx\,dy-J_E\,.
\end{aligned}
\tag{11}
$$

In the above J stands for the loss of magnetic energy due to Joule heating, while F stands for the loss of kinetic energy through friction.

In addition to the above energies, we of course have the internal (IE) and potential (PE) energies of the system. Their balance equations are easily found to be

$$
\begin{aligned}
\frac{\partial}{\partial t}\int\varrho\,I\,d\tau=&-\int[p]\left(\frac{\partial[v]}{\partial y}+\frac{\partial[w]}{\partial z}\right)d\tau-\int\left[p'\left(\frac{\partial u'}{\partial x}+\frac{\partial v'}{\partial y}+\frac{\partial w'}{\partial z}\right)\right]d\tau \\
&+\int\varrho\,Q\,d\tau-\int\varrho\,I\,w\,\Big|_{z_1}^{z_2}dx\,dy\,.
\end{aligned}
\tag{12}
$$

$$
\frac{\partial}{\partial t}\int\varrho\,g\,z\,d\tau=\int g[\varrho]\,[w]\,d\tau+\int g[\varrho'\,w']\,d\tau-\int\varrho\,g\,z\,w\,\Big|_{z_1}^{z_2}dx\,dy\,. \tag{13}
$$

To aid in visualizing the energy balance, we have also presented it in graphical form, in figure 1. Since there are so many conversion terms, we have omitted the boundary fluxes from the figure. Thus the energy diagram in figure 1 as it stands would be complete only for a system entirely enclosed by rigid, perfectly conducting walls.

3. Discussion

With regard to the energy balance equations (6) to (13) and figure 1, the following remarks are pertinent:

a) As the equations stand, they are averaged only in longitude. However, in order to evaluate any of the terms from observations, we also need to average in time, to obtain even a small degree of reliability. This time averaging may need to be different for different statistics. For example, the averaging of magnetic terms should obviously be over a time period much shorter than that of the solar cycle, while useful information about the velocity statistics can be had from much longer time averages as well (see, e.g., WARD [16, 17]).

b) The formulation as presented is nonunique in several respects. The energies could be split up in different ways. By further rearrangement by parts, the same boundary fluxes could be made to appear in different balance equations, with consequently different volume conversions. One useful further separation of the energies would be to split off the kinetic energy of the vertical component of motion. By examining the various conversion processes contained in the resulting balance equation, we could see the consequences of the hydrostatic assumption (for which all the terms except those in the hydrostatic balance would have to be omitted from the system). This could be particularly important in deciding which conversions to magnetic energy would be affected. For a discussion of energetically consistent approximations to the hydrodynamic equations in the nonmagnetic case; see LORENZ [8].

c) In section 1, we have already cited work of the writers concerning estimates of the effects of certain of the energy conversions. In particular, in STARR and GILMAN [14] the conversion

$$\int \varrho [u' v'] \frac{\partial [u]}{\partial y} d\tau$$

(6c in figure 1) between eddy kinetic and mean zonal kinetic energy was evaluated (in spherical coordinate form) from Ward's sunspot displacement data and found to be positive. That is, the eddies of super-sunspot scale were found to be feeding kinetic energy into the differential rotation. In a later paper STARR and GILMAN [15] suggested that the same large scale disturbances could concurrently take eddy magnetic energy out, through the action of horizontal Maxwell stresses. This process is represented by the conversion term

$$\int \frac{1}{4\pi} [H'_x H'_y] \frac{\partial [u]}{\partial y} d\tau$$

(7a in figure 1).

d) BUMBA and HOWARD [3] have estimated the rate at which vertical magnetic flux moves toward the poles. This process is represented by $[v' H'_z]$. Such a poleward transport of flux can obviously change the energy in the mean poloidal field. In figure 1, we can see that part of term 9b represents this conversion. BUMBA and Ho-

To aid in visualizing the energy balance, we have also presented it in graphical form, in figure 1. Since there are so many conversion terms, we have omitted the boundary fluxes from the figure. Thus the energy diagram in figure 1 as it stands would be complete only for a system entirely enclosed by rigid, perfectly conducting walls.

3. Discussion

With regard to the energy balance equations (6) to (13) and figure 1, the following remarks are pertinent:

a) As the equations stand, they are averaged only in longitude. However, in order to evaluate any of the terms from observations, we also need to average in time, to obtain even a small degree of reliability. This time averaging may need to be different for different statistics. For example, the averaging of magnetic terms should obviously be over a time period much shorter than that of the solar cycle, while useful information about the velocity statistics can be had from much longer time averages as well (see, e.g., WARD [16, 17]).

b) The formulation as presented is nonunique in several respects. The energies could be split up in different ways. By further rearrangement by parts, the same boundary fluxes could be made to appear in different balance equations, with consequently different volume conversions. One useful further separation of the energies would be to split off the kinetic energy of the vertical component of motion. By examining the various conversion processes contained in the resulting balance equation, we could see the consequences of the hydrostatic assumption (for which all the terms except those in the hydrostatic balance would have to be omitted from the system). This could be particularly important in deciding which conversions to magnetic energy would be affected. For a discussion of energetically consistent approximations to the hydrodynamic equations in the nonmagnetic case; see LORENZ [8].

c) In section 1, we have already cited work of the writers concerning estimates of the effects of certain of the energy conversions. In particular, in STARR and GILMAN [14] the conversion

$$\int \varrho [u' v'] \frac{\partial [u]}{\partial y} d\tau$$

(6c in figure 1) between eddy kinetic and mean zonal kinetic energy was evaluated (in spherical coordinate form) from Ward's sunspot displacement data and found to be positive. That is, the eddies of super-sunspot scale were found to be feeding kinetic energy into the differential rotation. In a later paper STARR and GILMAN [15]suggested that the same large scale disturbances could concurrently take eddy magnetic energy out, through the action of horizontal Maxwell stresses. This process is represented by the conversion term

$$\int \frac{1}{4\pi} [H'_x H'_y] \frac{\partial [u]}{\partial y} d\tau$$

(7a in figure 1).

d) BUMBA and HOWARD [3] have estimated the rate at which vertical magnetic flux moves toward the poles. This process is represented by $[v' H'_z]$. Such a poleward transport of flux can obviously change the energy in the mean poloidal field. In figure 1, we can see that part of term 9b represents this conversion. BUMBA and Ho-

WARD's estimate of the flux transport indicates that the mean poloidal field should be larger than is observed, implying that other processes are at work to counteract the poleward transport $[v' H_z']$. If this opposing mechanism is an eddy process, presumably it must be represented by the correlation term $[w' H_y']$ also included in term 9b, i.e., the tilting into the vertical of eddy meridional flux producing an effect of the opposite sign from the poleward advection. From equation (10), it is seen that these eddy correlations could act at the upper and lower boundaries, as well as in the interior of the region.

e) For these and other additional effects, it may be possible to make considerable further progress from a sustained observational program for the large scale solar fields such as that initiated by BUMBA and HOWARD. For example, the correlation $[u' H_z']$ which can act to convert energy between eddy kinetic and mean zonal magnetic (4b in figure 1), may be particularly susceptible to evaluation.

f) It is fairly evident that it would be useful to reexamine the hydromagnetic dynamo theories (for a review, see, e.g., ELSASSER [5]) in the context of the complete energy balance. As just one point, it is generally postulated (see, e.g., BABCOCK [1]) that the toroidal field $[H_x]$ is generated from the poloidal field $[H_y]$ through the stretching of poloidal field lines into the zonal direction by the differential rotation. Energetically, this process converts mean zonal kinetic energy into toroidal magnetic energy, as represented by the term

$$\int \frac{1}{4\pi} [H_x] [H_y] \frac{\partial [u]}{\partial y} d\tau$$

(5a in figure 1). But this is only one of several processes which can change the mean toroidal field, as we can see most clearly from figure 1.

As another point, the term

$$\int \frac{1}{4\pi} [w' H_x'] \frac{\partial [H_x]}{\partial z} d\tau$$

(from 4b in figure 1) contains the various ways by which vertical flux loops are produced from the toroidal field, this being the next step in customary dynamo schemes. But there are other eddy effects which do not appear to have been considered in dynamo theory before, which are represented by the terms

$$\int \frac{1}{4\pi} [u' H_z'] \frac{\partial [H_x]}{\partial z} d\tau$$

and

$$\int [v' H_x' - u' H_y'] \frac{\partial [H_x]}{\partial y} d\tau$$

(4b and 4c in figure 1). The first of these we have already suggested may be susceptible to evaluation from observational data, if a reasonable assumption about the sign of $\partial [H_x]/\partial z$ can be made. The second of these added terms, which represents a strictly horizontal eddy rearrangement of horizontal fields, could have strong effects on the solar cycle, if sunspots tend to form preferentially in latitudes related to particular toroidal field structure. That is, the horizontal eddy transports could build up strong toroidal fields in some latitudes, while producing weak or even oppositely directed

toroidal fields at other latitudes. In the recent theoretical work of GILMAN [6], baroclinically unstable disturbances in an uniform toroidal field do in fact, through the eddy transport $[v' H'_x - u' H'_y]$, tend to decrease the toroidal field strength in middle latitudes, and increase it in low and high latitudes. It seems evident, then, that these terms deserve more consideration in dynamo theories.

g) In studies of the energetics of the earth's atmospheric general circulation, very few attempts have been made to evaluate the conversion between eddy kinetic and meridional kinetic energy (3a, 3b, 3c in figure 1), principally because of the uncertainty in measuring the mean meridional motion. With increasing data coverage, however, it may soon be possible to evaluate these quantities more accurately. Those energy conversions which have been evaluated in atmospheric studies are reviewed by OORT [10].

h) As already stated, the construction of energy balance systems is a useful and illuminating procedure for the study of fluid systems in general, from pertinent data or from the standpoint of theoretical models. Although the details have not been worked out as yet, mention may be made of two applications, not previously touched upon, for which significant beginnings have been initiated. One is the energetics of the meanders of the Gulf Stream system investigated by WEBSTER [21, 22] and by OORT [9]. The other is the treatment of spiral galaxies by DICKINSON [4], who set down the pertinent integrals for a formulation of the present kind.

i) If the hydrostatic approximation is made, the total potential and internal energies become proportional to each other. Under these circumstances, it is useful to formulate a new energy, often called 'available' potential, energy as has been done for meteorological purposes by LORENZ [7].

4. Acknowledgement

The research reported in this paper was sponsored in part by the Air Cambridge Research Laboratories, Office of Aerospace Research, under contract AF 19(628)–5816.

REFERENCES

[1] H. W. BABCOCK, *The topology of the sun's magnetic field and the 22 year cycle*, Ap. J. *133* (1961), 572.

[2] V. BUMBA and R. HOWARD, *A study in the development of active regions on the sun*, Ap. J. *141* (1965), 1492.

[3] V. BUMBA and R. HOWARD, *Large scale distribution of solar magnetic fields*, Ap. J. *141* (1965), 1502.

[4] R. E. DICKINSON, *Hydrodynamic conservation integrals for spiral galaxies*, Pure and Appl. Geophys. *59* (1964), 142.

[5] W. M. ELSASSER, *Hydromagnetic dynamo theory*, Rev. Mod. Phys. *28* (1956), 135.

[6] P. A. GILMAN, *Hydromagnetic model for the solar general circulation*, Report No. 1, Planetary Circulations Project, Dept. of Meteor., Mass. Inst. of Tech. (1966), 214.

[7] E. N. LORENZ, *Available potential energy and the maintenance of the general circulation*, Tellus *7* (1955), 157.

[8] E. N. LORENZ, *Energy and numerical prediction*, Tellus *12* (1960), 364.

[9] A. H. OORT, *Computations of the eddy heat and density transports across the Gulf Stream*, Tellus *16* (1964), 55.

[10] A. H. OORT, *On estimates of the atmospheric energy cycle*, Mon. Wea. Rev. *92* (1964), 483.

[11] H. H. PLASKETT, *The polar rotation of the sun*, Mon. Not. R. Astr. Soc. *131* (1966), 407.

[12] J. A. SHERCLIFF, *A textbook of magnetohydrodynamics*, Commonwealth and International Library, Pergamon Press (1965), 265.
[13] J. SMAGORINSKY, S. MANABE and J. L. HOLLOWAY, JR., *Numerical results from a nine-level general circulation model of the atmosphere*, Mon. Wea. Rev. *93* (1965), 727.
[14] V. P. STARR and P. A. GILMAN, *Energetics of the solar rotation*, Ap. J. *141* (1965), 1119.
[15] V. P. STARR and P. A. GILMAN, *On the structure and energetics of large scale hydromagnetic disturbances in the solar photosphere*, Tellus *17* (1965), 334.
[16] F. WARD, *General circulation of the solar atmosphere from observational evidence*, Pure and Appl. Geophys. *58* (1964), 157.
[17] F. WARD, *The general circulation of the solar atmosphere and the maintenance of the equatorial acceleration*, Ap. J. *141* (1965), 534.
[18] F. WARD, *The effect of some systematic errors in the determination of the general circulation of the solar atmosphere*, Pure and Appl. Geophys. *60* (1965), 126.
[19] F. WARD, *The longitudinal proper motion of sunspots and the solar rotation rate*, Pure and Appl. Geophys. *63* (1966), in press.
[20] F. WARD, *Determination of the solar-rotation rate from the motion of identifiable features*, Ap. J. *145* (1966), 416.
[21] T. F. WEBSTER, *The effect of meanders on the kinetic energy balance of the Gulf Stream*, Tellus *14* (1961), 492.
[22] T. F. WEBSTER, *Measurements of eddy fluxes of momentum in the surface layer of the Gulf Stream*, Tellus *17* (1965), 239.

(Received 8th June 1966)

Numerical Integration of a Quasi-Geostrophic Atmospheric Model with an Asymmetric Zonal Current[1])

By Abraham Huss[2])

Summary – A two-level quasi-geostrophic model on a β-plane, with an initial state characterized by an asymmetric zonal current was integrated numerically for a period of 14 days. Various field variables were computed and compared with the corresponding distributions obtained in two experiments with the same model and with initial states characterized by a constant zonal flow and by a flow varying sinusoidally with latitude.

1. Introduction

Quite a number of numerical experiments have been reported in the literature, based on a two-level quasi-geostrophic model, with an initial state characterized by constant zonal flow, or by a symmetric latitudinal profile of the zonal flow. The circulation patterns obtained during the course of the integrations were seen to have a high degree of symmetry (within the limit of accuracy determined by the numerical method of solution adopted). In the experiment reported by Huss and Mintz [1][3]), for instance, a symmetrical jet developed in the central latitudes. Two regions of easterlies, identical in extent and intensity, formed at low altitudes in the north and in the south. The mean meridional circulation during the mature stages of the run consisted of a central Ferrel cell flanked by two identical Hadley cells. The poleward eddy transport of momentum was anti-symmetrical around the central latitude, and the flux-divergence was symmetrically distributed around this latitude. Other field variables also had these properties of symmetry.

To account for observed features of the general circulation of the atmosphere, it is of interest to determine the asymmetry arising from a different choice of initial conditions or from a change in the structure of the equations. In the former case we have the choice of introducing an asymmetric basic current or an asymmetric perturbation, with its maximum amplitude displaced away from the central latitude. In the numerical experiment described in the following, the initial basic flow has its maximum to the south of the central latitude. The perturbation, however, has its maximum

1) The research in this report has been sponsored wholly by the Air Force Cambridge Research Laboratories under Grant AF EOAR 63–108 through the European Office of Aerospace Research (OAR), US Air Force.

2) Department of Meteorology, Hebrew University, Jerusalem.

3) Numbers in brackets refer to References, page 168.

amplitude at the central latitude. The developing flow patterns are no longer symmetrical, and the asymmetries in the various field variables will be described in the following.

The experiment has been performed by making use of a two-level quasi-geostrophic model. The 0, 250, 500, 750 and 1000 mb level will be designated by the subscripts 0, 1, 2, 3, 4. The reference levels chosen were p_1 and p_3. The field variables at the other levels were computed by interpolation or extrapolation, assuming the lapse rate of the International Standard Atmosphere between p_1 and p_3, a constant lapse rate (in the vertical) between p_3 and p_4, and a parabolic pressure dependence of the vertical p-velocity, which has its maximum (or minimum) at p_2. This model was derived, and has been described in detail by MINTZ [4].

A theoretical investigation of the momentum transfer and the exchange of energy between the basic flow and the disturbance for somewhat similar assumption has been described by LIPPS [3]. He used the method of initial value calculations.

2. *The structure of the model*

The prediction equations, in terms of potential vorticities, were applied at the two reference levels, 250 mb and 750 mb:

$$\left.\begin{aligned} \frac{\partial q_1}{\partial t} &= -\boldsymbol{v}_1 \cdot \nabla q_1 - v_1 \beta_m \,, \\ \frac{\partial q_3}{\partial t} &= -\boldsymbol{v}_3 \cdot \nabla q_3 - v_3 \beta_m \,, \end{aligned}\right\} \tag{1}$$

with $\boldsymbol{v}$ = the non-divergent component of the horizontal velocity, quasi-geostrophically defined, with u and v its projection along x and y respectively.

β_m = the mean Rossby parameter = 1.6×10^{-11} m^{-1} sec^{-1},
q = the potential vorticity,
∇ = the horizontal del operator in an isobaric surface.

The potential vorticities at p_1 and p_3 thus carry the history of the motion. They are defined by:

$$q_1 = \zeta_1 + \lambda(\psi_1 - \psi_3) \,, \quad q_3 = \zeta_3 - \lambda(\psi_1 - \psi_3) \,, \tag{2}$$

with:

ζ = the vertical component of the relative vorticity = $\nabla^2\psi$,
ψ = the stream-function = $\frac{g}{f_m} z$,
z = the height of the reference level,
g = acceleration of gravity = 9.81 m/sec^{-2},
f_m = the mean Coriolis parameter = 10^{-4} sec^{-1},
λ = a stability parameter = -1.261×10^{-12} m^{-2}.

The quasi-geostrophic winds are defined by:

$$\boldsymbol{v} = \boldsymbol{k} \times \nabla\psi$$

with $\boldsymbol{k}$ being the unit vertical vector. The model equations were obtained under the assumption of the following distribution of the vertical p-velocity,

$$\omega = \omega_2(x, y, t)\, B(p) ,$$

with

$$B(p) = 4\, \frac{p_4\, p - p^2}{p_4^2} .$$

With this definition we obtain the required boundary conditions for ω:

$$\omega(p_0) = \omega(p_4) = 0 .$$

Between p_1 and p_3 the lapse rate was taken as equal to that of the International Standard Atmosphere. This assumption, together with the definition of $B(p)$ leads to the value of λ given above.

The set of equations was applied to a rectangular region. The space grid introduced had a fixed grid-interval in the x and y-directions, of magnitude $\Delta s = 444$ km. The grid-points were identified by the indices i, j; the first increasing in the x-direction, the second in the y-direction. Both i and j run from 1 to 15 (including boundary points).

Cyclical continuity was assumed in the x-direction. At the northern and southern boundaries the normal component of the velocity, and its zonally averaged parallel component were assumed to vanish. The lateral boundary conditions were completed by means of:

$$\left(\frac{\partial q}{\partial x}\right) \equiv 0 , \quad \left(\frac{\partial \tilde{q}}{\partial y}\right) \equiv 0$$

at the southern and northern boundaries, with the superior curved bar denoting the zonal mean.

Centered finite differences replace the time derivatives in (1), with $\Delta t = 1$ hour. Thus the solution of (1) requires values of ψ and of q at two instants of time. For the first forward step these two sets were taken to be identical.

The initial basic state was defined by the following table:

Table 1

j	1	2	3	4	5	6	7	8
$\tilde{\psi}_1$	8.204	8.204	8.085	7.887	7.570	7.253	7.016	6.817
$\tilde{\psi}_3$	0	0	− 0.027	− 0.071	− 0.142	− 0.214	− 0.267	− 0.312
$\tilde{u}_1$		13.5	36.0	58.5	72.0	63.0	49.5	40.5
$\tilde{u}_3$		3.0	8.1	13.2	16.2	14.2	11.1	9.1
$\tilde{T}_g$	298.0	298.0	295.0	290.0	282.0	274.0	268.0	263.0

j	9	10	11	12	13	14	15
$\tilde{\psi}_1$	6.659	6.500	6.421	6.382	6.342	6.302	6.302
$\tilde{\psi}_3$	− 0.348	− 0.383	− 0.401	− 0.410	− 0.419	− 0.428	− 0.428
$\tilde{u}_1$	36.0	27.0	13.5	9.0	9.0	4.5	
$\tilde{u}_3$	8.1	6.1	3.0	2.0	2.0	1.0	
$\tilde{T}_g$	259.0	255.0	253.0	252.0	251.0	250.0	250.0

$\tilde{\psi}_1$ and $\tilde{\psi}_3$ in 10^8 m^2 sec^{-1}; $\tilde{u}_1$ and $\tilde{u}_3$ in m sec^{-1}, $\tilde{T}_g$ in degrees absolute.

Thus, the center of an intense jet and the highest gradient of the surface temperature T_g are located south of the central latitude, at $j = 5$.

A sinusoidal perturbation was superimposed on this basic flow. It had a wavelength of 6216 km in the x-direction, and identical amplitudes and phases at both the 250 and 750-mb levels. At the central latitude the amplitude corresponded to 9 m in the height of the isobaric surface, and it varied sinusoidally towards north and south, vanishing at both boundaries.

The distributions resulting from the integration will occasionally be compared to those obtained in two earlier experiments. The first, described by HUSS and MINTZ [1], assumes an initial constant basic flow at each level, and the second, described by HUSS [2] assumes a sinusoidal variation of the basic initial flow, with a maximum at the central latitude. The same perturbation was assumed in all three experiments.

3. Results of the experiment

The numerical integration was carried for 14 days. Figure 1 shows the growth of the amplitude of the disturbance at both reference levels: at the central latitude $j = 8$, indicated by broken lines, and at the latitude of the initial maximum zonal velocity, $j = 5$, indicated by solid lines.

Except for slight decreases at the end of the run, we notice throughout a monotonic increase in the amplitudes, although occasionally the increase over several days was quite small. At $j = 5$ the initial amplitude was initially smaller than at $j = 8$, amounting to 6.2 m. On the other hand, the initial vertical wind-shear at $j = 5$ was significantly greater than at $j = 8$. Already within the first day of the integration, the amplitude at the upper level at $j = 5$ exceeded the corresponding amplitude at the central latitude. It remained larger during the whole run. During the middle of the second day also the amplitude at the lower level at $j = 5$ exceeded the corresponding amplitude at $j = 8$. It remained larger until the 10th day. For $j = 5$ rapid

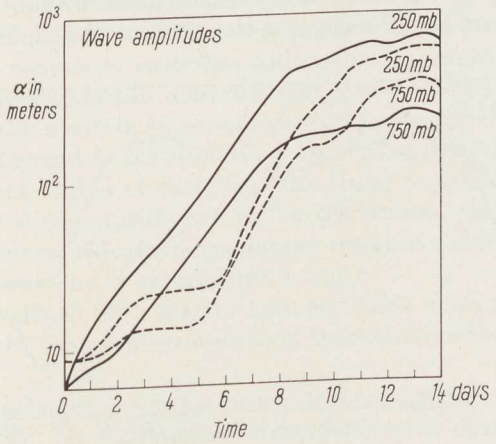

Figure 1

Wave amplitudes of contour heights for p_1 and p_3 at the initial location of the jet axis, $j = 5$ (solid lines) and at the central latitude, $j = 8$ (broken lines), as a function of time

growth (practically exponential over considerable intervals of time), was observed until the middle of the 8th day. Later on the increase was oscillatory and more gradual.

Comparing the amplitudes at corresponding levels and at latitudes with maximum zonal velocities (which were also the regions of greatest baroclinicity) in this experiment and in experiment 2, the same rate of growth was found at the upper level until the third day. The vertical shear of the zonal flow during this period was significantly greater in the present run, in which, following the 3rd day, the growth rate became much faster. In the earlier experiment growth proceeded at the upper level more or less at a constant rate until nearly the end of the integration period. In the present run the steep growth ceased at about the 8th day. Thus the maximum amplitudes were of the same order of magnitude in both experiments. In the earlier experiment a sudden drop in the amplitude was observed at the lower level on the 9th day. No sudden decrease of this nature was observed in the present experiment.

Comparing the evolution of the perturbations at the central latitudes in experiment 1 and in the present experiment, it should be noted that the differences between the zonally averaged wind velocities at the two reference levels were quite close in both cases: 31.9 m sec^{-1} and 31.4 m sec^{-1} respectively. From the point of view of baroclinic effects a similar development could possible be expected. However, the different zonal profile of the basic flow leads to different patterns of development, even during the initial stages. Compared to experiment 1, the amplitudes in the present experiment remain lower (and occasionally considerably lower) until the 8th day, and become higher following this date.

The phase lag between the perturbation at the upper and the lower reference level is shown in figure 2. The solid line refers to $j = 5$, and the broken line to $j = 8$. The former had a much smoother development than the latter. At $j = 8$ we notice a series of oscillations right from the beginning of the integration. At $j = 5$ we notice a rapid increase up to a maximum of 82° on the 3rd day. This was followed by a smooth and regular downward trend, leading to a value of 25° on the 9th day. Up to this date we have already seen that the amplitude of the perturbation rises rapidly at both levels.

During the middle of the 9th day we notice a rapid downward trend at $j = 5$. A minimum of $-12°$ occurs an the 10th day. On the 12th day the lag became positive again.

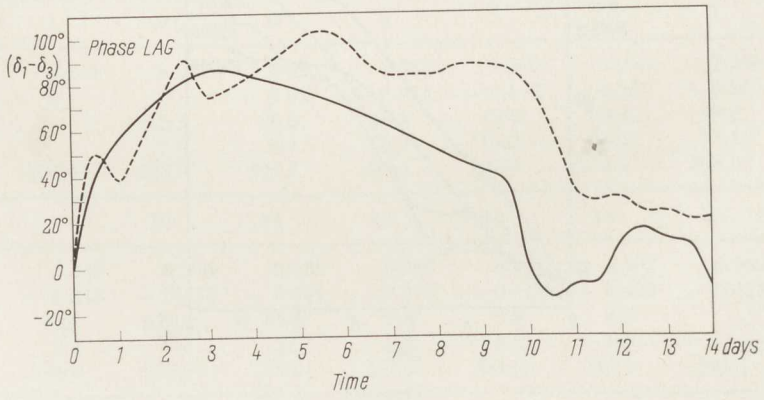

Figure 2
Phase lag at $j = 5$ (solid line) and at $j = 8$ (broken line)

The phase lag at $j = 8$ oscillated until the 4th day around the corresponding values at $j = 5$. Later on it remained consistently higher, with a peak value of 97° during the middle of the 6th day. A considerable decrease (less steep, however, than at $j = 8$) was observed around the 5th day. At the central latitude the phase lag remained positive until the end of the run.

Up to the 8th day, i.e. during the growing stages of the perturbation, the phase lag corresponds roughly in magnitude to the values obtained in experiment 2. On the other hand, no sudden increase culminating in a reversal of phase was found in the present run.

Looking at the evolution of the zonally averaged velocity distribution, it should be noted that the initial velocity at $j = 5$, at the upper reference level, was already very high: 72 m sec^{-1}. This location corresponds to the axis of a narrow jet-like formation. No further intensification took place at this point—the velocity remained practically constant until the 6th day, and decreased later on. The decrease proceeded at first quite smoothly, but later on oscillations were observed. During the middle of the 13th day, a minimum of 28 m sec^{-1} was reached. Such a range of variation, amounting to 44 m sec^{-1}, was not observed in the earlier experiments.

At the same latitude, at p_3, the velocity increased until the 10th day, with a maximum of 23 m sec^{-1} attained on the 10th day.

The distribution of the mean zonal winds with latitude and pressure for 3 selected days, the initial state, the 8th day and the 10th day, is presented in figure 3. We notice that as time went on the narrow jet at the higher altitudes broadened in extent and became less intense. Higher velocities penetrated downwards, towards the 1000 mb level. The vertical shear of the wind became less pronounced. The axis of the maximum in the mean zonal winds became slightly displaced to the north. On the 8th day easterlies are found to prevail over most of the latitudes at p_4. One region of easterlies extended from the equator to a point just beyond $j = 3$. The polar region of easterlies extended beyond the central latitude. Both regions were characterized by shallow depth and low intensity.

On the 10th day, the reduction of the velocity at high altitudes, the displacement of the axis towards the north, and the intensification at the 1000-mb level have progressed further. The regimes of easterlies had contracted horizontally. On the other hand, easterlies penetrated at this date to higher levels, beyond 750 mb. Their intensity had increased, with winds in excess of 5 m sec^{-1} appearing in the northern region.

Both on the 8th day and on the 10th day (as well as on other days not shown in the diagram) the northern region of easterlies was larger in extent than the southern region, and stronger winds prevailed in it. To this extent, the displacement of the initial wind maximum towards the south did not result in a more realistic pattern, as compared to the circulations in experiments 1 and 2.

The initially introduced very shallow Low and High at p_4 were centered on the central latitude, $j = 8$. Their centers were soon deflected into the southern half of the region.

On the 6th day the largest deviations from the mean height of the pressure surface already exceeded 75 m. No contour line corresponding to deviations of more than 25 m or less than -25 m penetrated beyond the central latitude, so that the disturbances were practically contained within the southern half of the region. The center of the low, at about $j = 6\frac{1}{2}$, was north of the center of the high, at $j = 4\frac{1}{2}$.

On the 8th day (figure 4) the disturbance had intensified further, and the deviations exceeded 200 m. The rate of intensification was greater than in experiment 2. The north-south separation of the centers had also increased, the center of the low moving northwards, and that of the high southwards. The cores of the closed configurations had an elliptical shape, and that of the Low was somewhat more elongated and of smaller size.

On the 10th day, the deviation exceeded 300 m—close to twice the corresponding values in experiment 2, and somewhat less than the deviations on the same day found

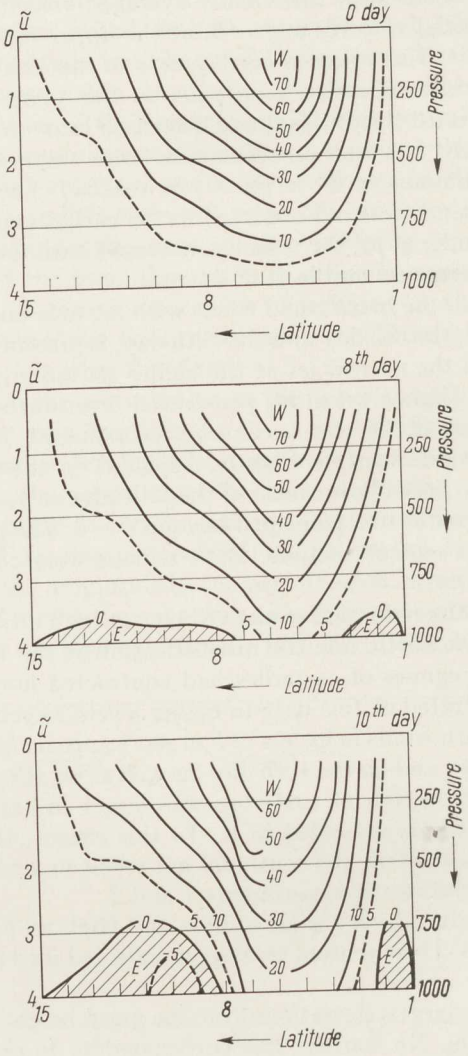

Figure 3
The zonally averaged zonal flow $\tilde{u}$ in m sec^{-1}, for the initial state, the 8th day and the 10th day. Shaded areas denote easterlies

in experiment 1. On this date the High extended well into the northern half of the region, with its center at $j = 9$.

The initial distribution of the zonally averaged temperatures has a concentration of isotherms around latitude $j = 5$, corresponding to the axis of the 'jet' located at this latitude. Inspecting the distribution at 500 mb (the isotherms were assumed to be parallel at all levels), very little change could be observed until the 10th day. Following this date the temperature difference between the southern and northern boundaries began to decrease. The cooling at low latitudes proceeded at a faster rate than the warming at high latitudes. Thus, for instance, the 26.5°N isotherm disappeared out of the region on the 7th day, while a rise in temperature at $j = 14$, corresponding in magnitude to this drop, was observed only on the 10th day. On the 14th day, the last day of the run, the total N-S temperature contrast had decreased

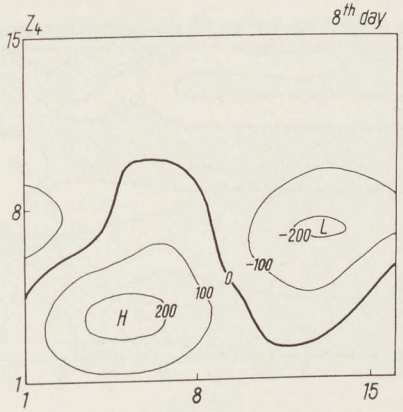

Figure 4
Contours of the 1000 mb surface, on the 8th day, as deviations from the mean height of the surface, in meters

to 22°C, indicating that the conversion of available potential energy proceeded at a faster rate than in experiment 2. The gradual reduction in the contrast was accompanied by a migration of the maximum temperature gradient towards the center.

With the initial conditions assumed, the poleward eddy transport no longer vanishes at the central latitude, and an antisymmetrical distribution around the central latitude, would not, of course, be expected. At 750 mb, momentum was transported towards latitude $j = 5$ both from the south and from the north until the 5th day, and thus a southward transport was observed at the central latitude. Between the middle of the 6th day and the 8th day northward transports prevailed at all latitudes. Beginning with the 9th day positive values were found between $j = 5$ to $j = 9$ and strong negative values at $j = 3$. At the 250 mb level southward transports were observed at the central latitude until the middle of the 10th day. Up to this time the line of separation between negative and positive transports progressed steadily towards the center. Quite high positive values were found in the southern half of the region.

The 8th day corresponds to a mature stage in the development of the circulation, but still precedes decay. On this day a narrow band with strong northward transports was observed, sloping polewards as it descended to lower levels. At the upper level a maximum of 61.9 $m^2\ sec^{-2}$ was located at $j = 5$, and at 750 mb a maximum, of the same magnitude, was ovserved more towards the north, at $j = 6$. Southward transports at the upper level, located between $j = 8$ and $j = 11$, had their highest value of $-30\ m^2\ sec^{-2}$ at $j = 9$.

This region of negative transports did not penetrate below 500 mb. The remaining part of the northern half of the region was characterized by very low values, predominantly positive. The general pattern at this date, although differing considerably from the actual distribution of the transports in the real atmosphere, is in many respects an improvement over that obtained in experiment 2.

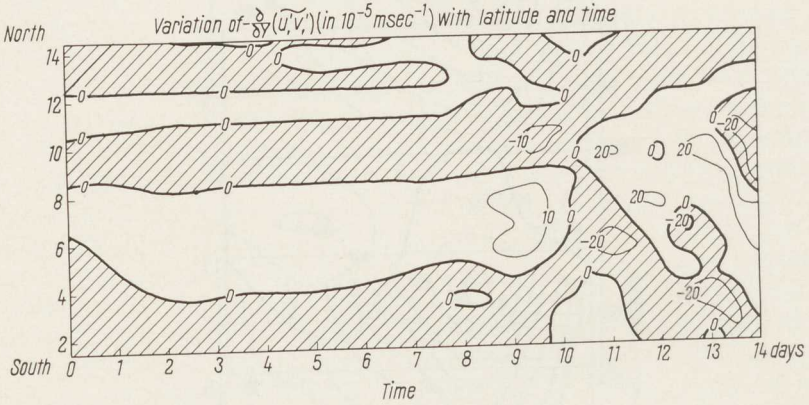

Figure 5
The meridional convergence of the poleward eddy flux of zonal momentum as a function of latitude and time, at 250 mb, in units of 10^{-5} m sec^{-2}. Shaded areas denote negative values

The distribution of convergence and divergence of flux had a quite complicated structure. The meridional convergence of the poleward eddy flux at 250 mb is shown in figure 5. Initially two bands of convergence were found at this level, a broader band in the south and a narrow band in the north. The band in the south expanded in extent during the first two days, and the highest values were found in it, exceeding 10^{-4} m sec^{-2} around the 9th day. During the 4th day another narrow region with convergence appeared in the extreme north. The two bands in the north merged around the 7th day. Following the 9th day the distribution became quite irregular, with strong convergences and divergences, and the banded structure broke down.

The corresponding pattern at 750 mb was somewhat simpler. Initially a relatively narrow band with convergence was situated somewhat south of the central latitude. with a lateral extent of less than 2 grid-intervals. On the 4th day another region with convergence made its appearence in the north, expanding with time towards the south, and merging with the former band on the 7th day. The structure became quite irregular after the 9th day. The magnitudes were considerably smaller at this level.

The mean meridional circulation can be visualized by an inspection of the zonally averaged meridional winds and vertical velocities. The distribution of the former, at p_1, with latitude and time (beginning with the 4th day) is shown in figure 6. Excluding slight contamination close to the boundaries, we notice, until the 9th day, a broad region with southward motion surrounded to the north and south by northward motion. During this period we have thus 3 cells in the vertical plane. However, the two direct cells to the north and the south were of unequal dimensions. The northern cell extended over a large region and its intensity was comparable to that of the indirect cell, The southern cell, however, was quite insignificant. On the 8th day, for instance, we find in the center of the indirect cell, at $j = 5$, values of the order of 1 m sec^{-1} or more. On the same day positive values of zonally averaged meridional velocity, $\tilde{v}_{a1}$, of about 0.5 m sec^{-1} were found in the north, around $j = 10$. Positive values in the narrow strip in the south did not exceed 10 cm sec^{-1}.

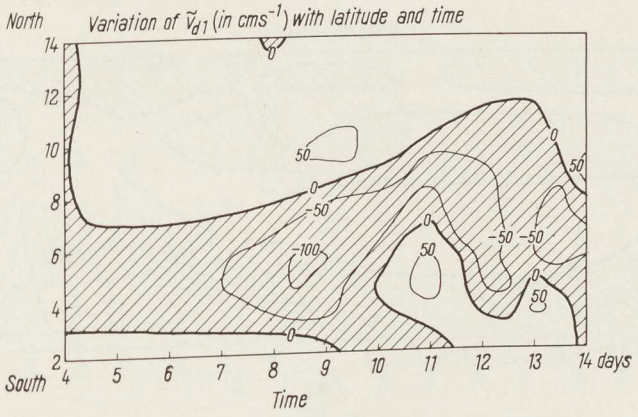

Figure 6
Zonally averaged meridional velocities as a function of latitude and time, at 250 mb, in cm sec^{-1}. Shaded areas denote southward flow

During the 9th day the direct southern cell disappeared, and for about one day only two vertical cells were in existence. With the disappearance of northward motions at $j = 5$ on the 10th day, a regime with 4 vertical cells became established, persisting for a day and a half. Following this a 3-cellular pattern was observed again. At this stage the direct cells in the north and the south had comparable intensities. Thus, during the decay stages the meridional circulation approaches somewhat more the actually observed pattern in the real atmosphere.

Turning to an inspection of the energy of the perturbations, it was observed that at 750 mb the kinetic energies were of the same magnitude as in experiment 2. During the mature stages of the run a broad region with high and almost constant values extended from $j = 8$ to $j = 3$. At the 250 mb level the maxima were located at $j = 5$, shifting gradually to the central latitude. The profiles obtained in this experiment compared much better with the observational results of PISHAROTY [5] than the patterns obtained in the earlier experiments.

The potential energy of the eddies, averaged between p_1 and p_3, had its maximum at first at $j = 5$, in the southern half of the region and shifted later on slightly to the

north. The rate at which eddy potential energy accumulated was somewhat faster in the present run, compared to the earlier runs, and higher values were observed at the end of the run.

The most conspicuous feature of the distribution of eddy kinetic energy conversion into the energy of the zonal flow, is the appearance of a broad band, in which eddy energy is transformed into zonal kinetic energy, flanked by two regions, in which the transformation proceeded in the opposite direction. The averaged values per 10 mb between 750 and 250 mb, as a function of latitude and time, are presented in figure 7.

A secondary, very narrow region with positive values of this transformation, $\{K' \cdot \tilde{K}\}$, was observed in the north, around $j = 12$. At latitude $j = 5$, in which the axis of the jet was initially located, only small amounts of kinetic energy were fed into the zonal flow, during limited time intervals. Beginning with the 8th day, the conversions became quite intense. The later stages were characterized by an irregular pattern.

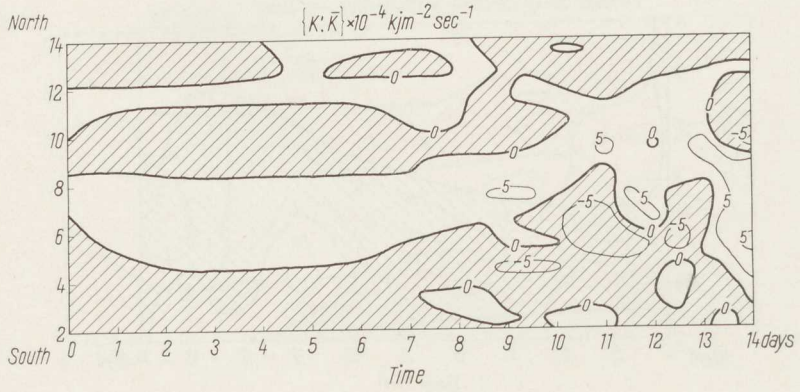

Figure 7

The conversion of eddy kinetic energy into the kinetic energy of the zonal flow, as a function of latitude and time. Averaged values per 10 mb between 750 and 250 mb, expressed in 10^{-4} kj m^{-2} sec^{-1}. Shaded areas denote conversion of zonal energy into eddy energy

As in the earlier experiments, also in the present run, eddy potential energy was transformed into eddy kinetic energy over most of the region throughout the run. Negative values, observed in the northern half of the region and penetrating southwards down to $j = 8\frac{1}{2}$ during the 6th and 7th days, where considerably smaller than the positive values in the south. Until the middle of the 9th day the most intense transformation took place at $j = 5$. The values obtained were considerably higher than those found in the earlier experiments during the corresponding period. Between the 10th and 12th day, kinetic energy was transformed into potential energy in the southern half of the region. The most intense transformation took place on the 8th day.

The distribution of the transformation of zonally averaged available potential energy into eddy potential energy, $\{\tilde{P} \cdot P'\}$, is shown in figure 8. It is very similar to the distribution of $\{P' \cdot K'\}$ discussed above, but with a tendency towards more positive values. Until the 5th day zonal potential energy was transformed into eddy potential energy at all latitudes and the most intense transformation took place at

$j = 5$. From that day on until the middle of the 8th day an extensive region with the opposite trend was found north of $j = 9$. However, the magnitude of the transformation in this region was quite small. Beginning with the 9th day negative values appeared in the southern half of the region. The most intense transformations were observed during the 8th day of the integration.

An inspection of the transformation of eddy kinetic energy into zonal kinetic energy averaged over the total region, shows that the negative and positive values at the different latitudes nearly balance. The averages until the 7th day were positive, but smaller than the corresponding values in experiment 2. The highest value during this period, obtained in the middle of the 6th day, amounted to no more than 4.4×10^{-6} kj m^{-2} sec^{-1}. On the 9th day a somewhat larger positive value was registered, 1.2×10^{-5} kj m^{-2} sec^{-1}. Negative values were found during the 10th and 11th days. (The maximum value obtained in experiment 2, before decay had set in, was 3.1×10^{-5} kj m^{-2} sec^{-1}.)

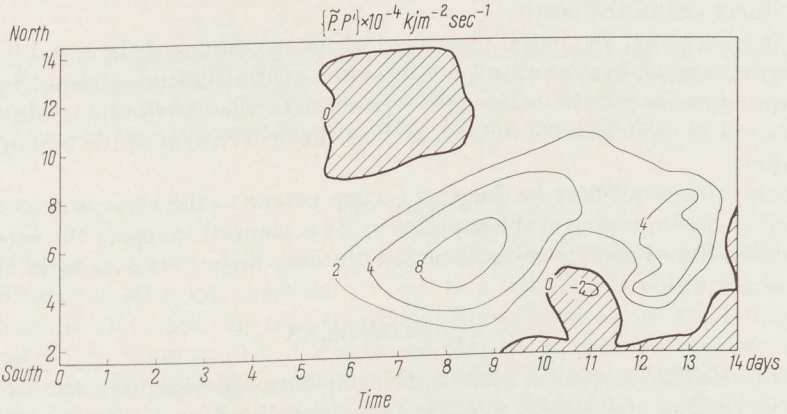

Figure 8
The conversion of zonal available potential energy into eddy available potential energy. Units as above

Up until the last day of the run, the corresponding averages of $\{P' \cdot K'\}$ remained consistently positive. The highest value was 6.6×10^{-5} kj m^{-2} sec^{-1}, observed during the middle of the 8th day. Values of a comparable magnitude were encountered in the earlier run only on the 13th day. Following the 10th day the average transformations oscillated between quite wide limits. As a rule, the order of magnitude of $\{P' \cdot K'\}$ was higher than that of $\{K' \cdot \tilde{K}\}$. The ratio of the former to the latter occasionally exceeded 30. The total average of $\{\tilde{P} \cdot P'\}$ varies with time in a similar way. At nearly the same time—only 12 hours later— the values in the present run begin to exceed the corresponding values of experiment 2. The maximum value was observed on the same date as in the case of $\{P' \cdot K'\}$, being somewhat higher: 3.3×10^{-4} kj m^{-2} sec^{-1}. In general, during the whole course of the run, the transformation proceeded in the mean at a more intensive rate than the transformation discussed before.

The values of $\{\tilde{P} \cdot \tilde{K}\}$ were relatively small, erratic and comparable in magnitude to those observed in experiment 2.

4. Concluding remarks

In the experiment described above, the initial zonal flow had a maximum to the south of the central latitude. Thus, an asymmetrical feature was enforced right from the beginning of the integration, with a concurrent evolution of asymmetries in the other field variables.

As time went on the maximum of the zonally averaged zonal wind decreased and became somewhat displaced to the north. Easterlies developed in the north and in the south. Those in the north extended over a larger region and became more intense than the corresponding winds in the south. The perturbations at 1000 mb, during the developing stages of the run, were confined mostly to the southern half of the region. Relatively strong southward eddy transports of momentum were observed at the central latitudes. During several stages of the run, the mean meridional circulation consisted of 3 vertical cells: a central Ferrel cell flanked by two Hadley cells. However, the direct cell in the southern part of the region was, as a rule, considerably less intense than the direct cell in the north.

Thus it is seen that the initial placement of the maximum of the zonal flow (and the strongest temperature gradient) south of the central latitude did not lead to a closer approximation of the other field variables to the distributions observed in nature (except in some isolated details, such as the distribution of the kinetic energy of the eddies).

However, this result may be due to a certain extent to the very pronounced 'jet' introduced at the beginning of the experiment. It is planned to repeat the experiment with modified initial conditions, and preferably with higher resolutions in the horizontal and vertical.

5. Acknowledgements

I wish to thank Professor Y. Mintz, Department of Meteorology, the University Computing Facility and Health Sciences Computing Facility, UCLA for their generosity in making available to me free computing time.

Thanks are extended to Dr. E. J. Katz for carefully reading the manuscript and for changes leading to improved clarity.

Thanks are also due to Mr. E. Doron and to Mr. A. Hecht for their help in preparing the diagrams.

References

[1] A. Huss and Y. Mintz, *Growth of a baroclinic wave and evolution of the mean zonal and mean meridional circulations*, Proc. Internat. Symposium in Numerical Weather Prediction in Tokyo (1962), 539.

[2] A. Huss, *The developing circulation patterns on a β-plane obtained in the case of an initial basic flow varying sinusoidally with latitude* (to be published Archiv. f. Meteorol., 1966).

[3] F. B. Lipps, *Momentum transfer across an asymmetric jet*, Technical Report No. 17 to the NSF, 1964, University of Chicago, Dept. of Geophysical Sciences (August 1964).

[4] Y. Mintz, *Design of some numerical general circulation experiments*, Bull. Res. Council, Israel, Geo. Sciences 7, G (1958), 67.

[5] P. A. Pisharoty, *The kinetic energy of the atmosphere*, Article XIV in Final Report, Contract AF 19(122)–48, Dept. of Meteorology, UCLA (1955).

(Received 21st May 1966)

A Remark on the Hydrostatic Approximation

By MICHAEL YANOWITCH[1])

Summary – For an autobarotropic atmosphere the exact linearized equations of motion can be solved for the pressure oscillation when $\sigma = 0$ and $\sigma = 2\,\Omega$ (σ = frequency of oscillation, Ω = angular velocity of the earth's rotation). The pressure computed in this way is shown to be in close agreement to the pressure computed by using the hydrostatic approximation.

1. Introduction

The linearized equations of motion for atmospheric oscillations (about a state of rest) on a rotating spherical earth do not lead to a separable problem unless certain approximations are made. In the 'traditional approximation' of tidal theory (see e.g. ECKART [1][2]), SIEBERT [3]), it is assumed that the horizontal component of the Coriolis force can be neglected, that the pressure and density oscillations are related by the hydrostatic law, and that in all the equations the radial coordinate, r, can be replaced by the radius of the earth, a, which is assumed to be constant. (A systematic derivation of the approximate equations can be found in PHILLIPS [2]). Since the accuracy of the approximation is unknown, and has sometimes been questioned (e.g. SOLBERG [3], THRANE [5], and the discussion in SIEBERT [3]), it is of some interest to examine problems for which both the complete and the approximate equations can be solved exactly, even if some of the assumptions are unrealistic.

Let us consider motions which are harmonic in time, like $e^{i\sigma t}$. In general, one cannot obtain directly from the exact equations a relation between the density and pressure perturbations. However, such a relation can be deduced for the case of semidiurnal oscillations ($\sigma = 2\,\Omega$, Ω = angular velocity of the earth's rotation) and for the limiting case $\sigma = 0$. Furthermore, this relation, as well as the hydrostatic equation, can be integrated if the fluid is assumed to be autobarotropic. In this way a comparison can be made between the pressures obtained from the hydrostatic approximation and from the exact equations. It is shown in this note that the two results are very close in any region which is thin compared to the earth's radius.

---

[1]) National Center for Atmospheric Research, Boulder, Colorado, USA. Permanent address: Adelphi University, Garden City, New York, USA.

[2]) Numbers in brackets refer to References, page 172.

2. *Pressure equation*

The linearized dynamical equations for oscillatory motions of an ideal fluid on a rotating earth can be written in the form

$$A(\varrho_0 V) = -F \tag{1}$$

where A is the matrix

$$A = \begin{bmatrix} i\sigma & -2\Omega\cos\theta & 0 \\ 2\Omega\cos\theta & i\sigma & 2\Omega\sin\theta \\ 0 & -2\Omega\sin\theta & i\sigma \end{bmatrix} \tag{2}$$

and

$$F = \text{grad } p - \text{body force} . \tag{3}$$

Here (θ, φ, r) represent the spherical coordinates of a point (θ = colatitude, φ = longitude), $V = (u, v, w)$ is the velocity vector, p and ϱ are the pressure and density oscillations, and ϱ_0 is the equilibrium density, which is assumed to be a function of r only. Of course, to obtain a complete system of equations one must add to (1) the continuity equation and a thermodynamic equation. Let us suppose that such a complete set of equations with appropriate boundary conditions has a unique solution. If the vector F is determined from this solution, the set of equations (1) can be regarded as a set of linear algebraic equations for u, v and w, and one can solve for these quantities provided the determinant of A does not vanish. It is easy to verify that the determinant of A vanishes if and only if $\sigma = 0$ or $\sigma = 2\Omega$, and in these two cases a solution can exist only if the right hand side, F, satisfies an appropriate compatibility condition.

For $\sigma = 0$ the compatibility condition is that F should be orthogonal to the vector $(\sin\theta, 0, -\cos\theta)$; for $\sigma = 2\Omega$, F must be orthogonal to $(\cos\theta, i, \sin\theta)$. Let us consider the case where the only body force is due to gravity, which, for simplicity, is assumed to be constant. Then the compatibility condition has the form

$$\cos\theta \frac{\partial p}{\partial r} - \sin\theta \frac{\partial p}{r\,\partial\theta} + g\varrho\cos\theta = 0 \tag{4}$$

for $\sigma = 0$, and

$$\sin\theta \frac{\partial p}{\partial r} + \cos\theta \frac{\partial p}{r\,\partial\theta} + g\varrho\sin\theta - \frac{i}{r\sin\theta}\frac{\partial p}{\partial\varphi} = 0 \tag{5}$$

for $\sigma = 2\Omega$. For these two cases, therefore, equations (4) and (5) give relations between the pressure and the density oscillations without any approximations, and it can be seen that they differ in form from the hydrostatic relation except at the poles (for $\sigma = 0$) and at the equator (for $\sigma = 2\Omega$). In general these equations must be used to replace one of the equations in (1), and one still has to solve the complete set of equations. However, if the density is known (as in the case of a homogeneous ocean), or if it is a given function of the pressure, the two equations (4) and (5) are first order partial differential equations for p, and can always be integrated if the pressure at the surface ($r = a$) is prescribed. Consequently, in these special cases the pressure field can be obtained without solving the whole set of equations, and without making the quasistatic approximation.

3. Pressure field

As an example, we will consider an isothermal atmosphere with isothermal changes of state. (The general case of an autobarotropic atmosphere can be treated in the same way, and leads to similar results.) In this case $p = R\,\varrho\,T = g\,H\,\varrho$, where $H = R\,T/g$ (T = temperature, R = gas constant). If the pressure and density oscillations satisfy the hydrostatic relation, $\partial p/\partial z + g\,\varrho = 0$ ($z = r - a$), one obtains

$$p = p_a\, e^{-z/H} \tag{6}$$

where p_a is the pressure oscillation at the ground ($z = 0$).

The case $\sigma = 2\,\Omega$. For $p \propto e^{is\varphi}$, the equation (4) becomes

$$\sin\theta\,\frac{\partial p}{\partial r} + \cos\theta\,\frac{\partial p}{r\,\partial\theta} + H^{-1}\sin\theta\,p + s(r\sin\theta)^{-1}\,p = 0\,. \tag{7}$$

Let us now take a rectangular coordinate system (α, β) in any meridional plane, with the β-axis along the earth's axis (see figure 1). The lines $\beta = \text{const}$ are characteristics of equation (7), which can be rewritten in the form

$$\frac{dp}{d\alpha} + H^{-1}\,\alpha(\alpha^2 + \beta^2)^{-1/2}\,p + s\,\alpha^{-1}\,p = 0\,, \tag{8}$$

which can be integrated to give

$$p = p_a\left[\frac{a\sin\theta_a}{r\sin\theta}\right]^s e^{-z/H} \tag{9}$$

where θ_a denotes the value of θ when $r = a$ along a given line $\beta = \text{const}$. Of course, the expression in (9) gives the pressure oscillation in the region $|\beta| < a$ only.

When $s = 0$ the expression (9) degenerates into (6). In the case of semidiurnal standing oscillations, therefore, the pressure oscillations obtained from the exact equations coincides with the one computed by using the hydrostatic relation.

When $s \neq 0$ the pressure oscillation given by (9) vanishes on the lines $\beta = a$ and $\beta = -a$. Thus, p_a has to vanish at the poles. Of course, p can be extended continuously to the region $|\beta| > a$ by setting it identically zero there. If this is done, then p vanishes identically along any radial line except for $\beta = 0$ when r is sufficiently large.

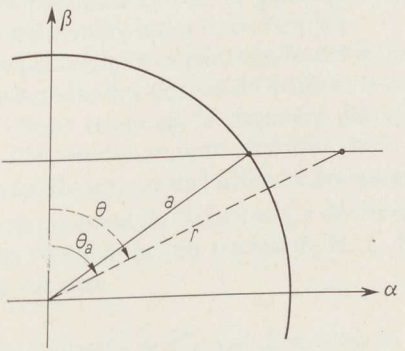

Figure 1

Although the pressure oscillation determined in this way is not identical to the one determined from the hydrostatic approximation, the two are very close in any region where (r/a) does not vary by more than a few per cent. For positive s the pressure falls somewhat than the hydrostatically determined pressure, and if the ratio of p to the equilibrium pressure is small at the ground, it remains small everywhere. The same is not true for negative s, since p increases faster with r than the hydrostatically determined pressure.

The case $\sigma = 0$. The lines $\alpha = \text{const}$ are now characteristics of (4), which can be written in the form

$$\frac{dp}{d\beta} + H^{-1}\beta(\alpha^2 + \beta^2)^{-1/2} p = 0 . \tag{10}$$

The solution for $|\alpha| < a$ is again given by (6). Thus, for any steady small perturbation about the state of rest, the pressure field is hydrostatic. The hydrostatic assumption might be expected to be accurate, therefore, for sufficiently small σ.

1. Acknowledgements

This research was supported in part by the Atmospheric Sciences Program, National Science Foundation, NSF GP–1804.

References

[1] C. Eckart, *Hydrodynamics of oceans and atmospheres*, Pergamon Press (1960), 95.
[2] N. Phillips, *The equations of motion for a shallow atmosphere and the 'traditional approximation'* (to be published).
[3] M. Siebert, *Atmospheric Tides*, in Advances in Geophysics 7, Academic Press (1961), 129.
[4] P. Thrane, *Some hydrodynamical properties of simple atmospheric oscillations*, Geof. Publ. *18* (1951).
[5] H. Solberg, *Über die freien Schwingungen einer homogenen Flüssigkeitsschicht auf der rotierenden Erde*, I, Astr. Norveg. *1* (1936), 237.

(Received 11th June 1966)

Equation de transport et de diffusion pour l'atmosphère turbulente avec des masses d'air différemment échauffées

Par MARJAN ČADEŽ[1])

Summary – Generalization of the diffusion and transport equation are given. They refer to an atmosphere in which in addition to irregular turbulent motion exists also regular motion of the heated and cooled air masses. The equations are briefly discussed.

1. Introduction

Il existe dans l'atmosphère différents phénomènes liés soit à des mouvements turbulents désordonnés, soit à des mouvements ordonnés, orientés dans des directions déterminées. Les phénomènes de cette nature sont nombreux. Ainsi, par exemple, au cours de la matinée, l'air situé au-dessus du sol s'échauffe et les masses d'air chaud s'élèvent et par là le développement du champ de la température, de l'humidité, de la pression, etc., en sont influencés. Lorsque dans le champ horizontal de la pression se trouvent des masses d'air de température différente, chaudes et froides, on peut démontrer facilement que les masses d'air froid, se déplacent en direction horizontale en sens inverse que les masses chaudes. Dans l'atmosphère, les masses d'air froid ont donc la tendance de s'assembler dans un endroit et les masses chaudes dans un autre.

Chaque apport de chaleur dans l'atmosphère est lié au transport d'énergie interne et cinétique qui, avec la vitesse du son, rayonne à partir du lieu de l'apport de chaleur. De même, il existe un transport d'énergie interne et cinétique dirigé vers la région d'émission de chaleur. Ici, il s'agit de mouvements orientés qui peuvent être effectués dans toutes les directions possibles et par là provoquer des changements dans la répartition des grandeurs météorologiques dans l'espace.

Nous avons été amenés à ces réflexions par l'étude de l'influence complexe qu'exerce sur la température de l'air la fonte des flocons de neige et la condensation de la vapeur d'eau dans l'atmosphère. Nous trouvons la première description classique de cette sorte de phénomène dans l'Hydrodynamique physique de V. BJERKNES et collaborateurs [1][2]). Analysant le refroidissement de l'atmosphère causé par la fonte des flocons de neige, ČADEŽ [2], indépendamment de BJERKNES, a décrit un phénomène semblable, mais d'un autre type. Plus récemment, un travail de H. L. KUO [3] a apporté sur ce point une contribution importante.

---

[1]) Institut de Météorologie, Université de Beograd, Dobračina 16, Beograd, Yougoslavie.

[2]) Les chiffres entre crochets renvoient à la bibliographie, page 177.

A la différence de BJERKNES et de KUO, qui se sont intéressés tout d'abord à la stabilité des systèmes nuageux-clair, nous nous sommes occupés de la dynamique de l'échauffement et du refroidissement de l'air dans ces systèmes. Nous avons observé qu'il n'est pas difficile d'établir, à cet effet, certaines équations qui sont d'une importance générale et qui peuvent s'appliquer à l'étude des phénomènes liés aux mouvements orientés de l'atmosphère mentionnés plus haut. Ici, nous allons déduire ces équations et cela à la simple condition que les valeurs moyennes des grandeurs météorologiques dans le sens horizontal ne changent pas.

2. *Généralisation des équations pour l'échange des masses d'air*

Imaginons une partie de l'atmosphère où se trouvent trois sortes de masses d'air. Les premières sont celles dont on suppose l'existence d'après la théorie de la turbulence atmosphérique et qui se mêlent entre elles et se déplacent tantôt vers le haut, tantôt vers le bas. Les deuxièmes représentent les masses d'air qui ont tendance à s'élever parce que leur température est plus grande que la température moyenne des masses d'air «neutres» à la même altitude. De même, les troisièmes représentent des masses d'air qui ont, à une altitude déterminée, une température plus faible que la température moyenne des masses d'air environnantes de la première sorte.

Cela pris en considération, nous voyons qu'à l'altitude z il existe un transport vertical dirigé vers le haut d'une grandeur spécifique s que certaines masses d'air transportent à travers la surface horizontale σ dans l'intervalle de temps Δt:

$$\phi_{s,\sigma,\Delta t} = \left[\sum m_i\, s_i(z) - \sum m_k\, s_k(z)\right] + \sum m_i^+\, s_i^+(z) - \sum m_k^-\, s_k^-(z)\,. \tag{1}$$

Ici m_i et m_k sont les masses d'air neutres de mouvement désordonné qui, dans l'intervalle de temps Δt traversent la surface σ de bas en haut ou de haut en bas. De même m_i^+ et m_k^- représentent les masses mentionnées d'air chaud respectivement d'air froid qui simultanément passent à travers la surface observée; $s_i(z)$, $s_k(z)$, $s_i^+(z)$, $s_k^-(z)$ sont les valeurs correspondantes de grandeur spécifique s à l'altitude z qui appartiennent aux masses mentionnées. Ici, nous avons supposé que la surface σ est relativement grande par rapport aux dimensions horizontales de l'air échauffé et refroidi.

Nous tenons compte tout d'abord, en accord avec la théorie élémentaire de la turbulence, qu'une particule d'air de la masse m_i est parvenue à une certaine altitude $z_i (z_i < z)$, où la valeur spécifique s, qui se rapporte à cette particule $s_i(z_i)$ a été égale à la valeur moyenne $s(z_i)$ de la grandeur s des masses d'air neutre à cette altitude. En tenant compte de ce fait et en négligeant les petites grandeurs de deuxième et de plus grand ordre nous pouvons écrire:

$$s_i(z) = s(z_i) + \frac{ds(z)}{dz}(z - z_i) = s(z) + \left[\frac{\partial s(z)}{\partial z} - \frac{ds(z)}{dz}\right](z_i - z) \tag{2}$$

[$ds(z)/dz$ changement individuel de la grandeur s qui survient durant le changement de l'altitude de la masse m_i pour une unité]. Puis nous pouvons poser:

$$\sum m_i\, s_i^+(z) = \sum m_i\, [s^+(z) - s_i^+(z) - s^+(z)] = \varrho^+\, w^+\, s^+(z)\, \sigma\, \Delta t \tag{3}$$

où ϱ^+, w^+, $s^+(z)$ représentent la valeur moyenne de la densité, la vitesse verticale respectivement de la valeur spécifique s des masses d'air chaud à l'altitude z. La valeur moyenne $s^+(z)$ est déterminée par l'équation:

$$\sum m_i \left[(s_i^+(z) - s^+(z)\right] = 0 . \tag{4}$$

Si la valeur obtenue comme la valeur semblable pour les masses qui se déplacent vers le bas sont introduites dans l'équation (1) et si nous tenons compte que:

$$\sum m_i - \sum m_k = \varrho\, w\, \sigma\, \Delta t \tag{5}$$

(ϱ densité moyenne des masses d'air neutre à l'altitude z, w vitesse moyenne verticale de ces masses d'air à cette altitude), nous obtenons le flux de la grandeur s à travers l'unité horizontale de la surface dans l'unité de temps:

$$\phi_s = K\left(\frac{ds}{dz} - \frac{\partial s}{\partial z}\right) + (\varrho\, w)\, s + (\varrho^+ w^+)\, s^+ + (\varrho^- w^-)\, s^- . \tag{6}$$

Ici on a:

$$K = \frac{1}{\sigma\, \Delta t}\left[\sum m_i(z - z_i) + \sum m_k\,(z_k - z)\right]; \quad s = s(z) . \tag{7}$$

K est le coefficient d'échange connu. La vitesse verticale w peut être positive et négative et égale à zéro. De l'autre coté est $w^- \leqq 0 \leqq w^+$.

L'équation de transport obtenue (6) représente la généralisation de l'équation connue pour l'échange des masses d'air:

$$\phi_s = - K\frac{\partial s}{\partial z} . \tag{8}$$

Cette équation est établie à la condition qu'au lieu de l'observation il n'existe pas de masses d'air échauffées et refroidies ayant leur propre régime de mouvement ($w^+ = w^- = 0$), qu'il n'y ait pas de changement individuel de la grandeur s dans le mouvement turbulent ($ds/dt = 0$) et que la vitesse verticale moyenne de l'air soit égale à zéro ($w = 0$).

De (6) il résulte immédiatement l'équation pour un changement local moyen de la grandeur s:

$$\left.\begin{aligned}\bar{\varrho}\,\frac{\partial \bar{s}}{\partial t} = \frac{\partial}{\partial z}\left[K\left(\frac{\partial s}{\partial z} - \frac{ds}{dz}\right) - \varrho\, w\, s - \varrho^+ w^+ s^+ - \varrho^- w^- s^-\right] \\ + \varrho\, w\,\frac{ds}{dz} + \varrho^+ w^+\,\frac{ds^+}{dz} + \varrho^- w^-\,\frac{ds^-}{dz}\end{aligned}\right\} \tag{9}$$

qui représente la généralisation de l'équation de diffusion ($\bar{\varrho}$ densité moyenne de l'air). Ici nous avons tenu compte du fait que le changement local $\partial\bar{s}/\partial t$ peut être conditionné aussi par le changement individuel des valeurs s, s^+ et s^- sur le lieu d'observation (trois derniers membres de l'équation). Les équations (6) et (9) pourraient être augmentées encore de deux membres, c'est-à-dire des membres qui sont conditionnés par le transport de l'eau à l'état solide et liquide sous forme de précipitations, et cela à l'occasion de l'étude de l'influence directe des précipitations sur la température et l'humidité de l'air.

Nous pouvons mentionner que l'équation (9) ne rend pas seulement compte des changements dans le champ de la grandeur s causées par le changement de position dans l'espace de certaines masses d'air, mais également des changements qui sont causées par *la trace* que certaines masses d'air, froides et chaudes, laissent derrière elles, pendant leur mouvement à travers l'atmosphère.

3. Echauffement et refroidissement de l'atmosphère causés par les changements des phases de l'eau

Dans le but d'illustrer les résultats obtenus, nous donnerons ici quelques exemples pour le cas où les mouvements s'effectuent de façon adiabatique dans le champ stationnaire de la pression. Pour s nous prenons l'enthalpie spécifique de l'air non saturée $c_p T$ (c_p chaleur spécifique de l'air à une pression constante, T température). Nous avons déjà attiré l'attention, dans un de nos travaux précédents [4], que dans ce cas nous ne devons pas séparer le changement individuel de l'enthalpie du changement simultané de l'énergie cinétique et potentielle de l'air. Si nous supposons que l'atmosphère est relativement calme, alors nous pouvons écrire, dans ce cas, avec une précision suffisante:

$$\left.\begin{aligned} & s = c_p\, T\,, \quad s^+ = c_p\, T^+\,, \quad s^- = c_p\, T^-\,, \\ & \frac{ds}{dz} = \frac{\partial s^+}{\partial z} = \frac{\partial s^-}{\partial z} = \frac{ds^+}{dz} = \frac{ds^-}{dz} = -\, c_p\, \gamma_a = -\, g \end{aligned}\right\} \tag{10}$$

où

$$T^- < T < T^+ \quad \text{et} \quad \gamma_a = \frac{g}{c_p} \quad \text{(gradient adiabatique sec de la température)}\,. \tag{11}$$

Lorsque, dans les équations (6) et (9) nous prenons cela en considération, nous obtenons pour le transport vertical de la chaleur disponible (enthalpie) à l'altitude z et pour un changement local de la température à cette altitude:

$$\phi_{c_p T} = c_p\, [K(\gamma - \gamma_a) + \varrho\, w\, T + \varrho^+ w^+ T^+ + \varrho^- w^- T^-] \tag{12}$$

$$\left.\begin{aligned} \frac{\partial \overline{T}}{\partial t} = \frac{1}{\varrho}\Big[& (\gamma_a - \gamma)\, \frac{\partial K}{\partial z} - K\, \frac{\partial \gamma}{\partial z} - (\gamma_a - \gamma)\, \varrho\, w \\ & - T\, \frac{\partial (\varrho\, w)}{\partial z} - T^+\, \frac{\partial (\varrho^+ w^+)}{\partial z} - T^-\, \frac{\partial (\varrho^- w^-)}{\partial z}\Big] \end{aligned}\right\} \tag{13}$$

où

$$\gamma = -\, \frac{\partial T}{\partial z}\,. \tag{14}$$

Il est important de remarquer que les équations obtenues sont valables, sans tenir compte si les masses d'air échauffées et refroidies se meuvent de façon adiabatique sèche ou humide.

Par l'intégration de l'équation (13), dans les conditions initiales données, nous obtiendrons une répartition de la température avec l'altitude dans l'atmosphère comme fonction de temps sous diverses conditions: dans les systèmes nuageux-clair, durant les jours où l'atmosphère s'échauffe et se refroidit à partir du sol, dans la région où fondent les flocons de neige, etc.

Ici, nous désirons brièvement expliquer les équations obtenues (12) et (13).

Le transport vertical de la chaleur dans l'atmosphère selon une direction verticale dépend dans une plus ou moins grande mesure de l'existence des masses d'air échauffées ou refroidies. Ainsi, par exemple, durant les jours clairs, quand au-dessus du sol montent des masses d'air échauffées ($w^+ \neq 0$), il est possible, en accord avec l'équation (12) et dans une atmosphère sous-adiabatique ($\gamma < \gamma_a$), qu'un transport vertical ascendant de chaleur existe. Ici, il s'agit de l'atmosphère sous-adiabatique qui est formée de masses d'air neutre ayant une température moyenne $T(z)$. La température moyenne $\overline{T}(z)$ de toutes les masses d'air présentes, qui est déterminée par l'équation (13), pendant de tels jours change certainement d'une autre manière avec l'altitude et immédiatement au-dessus du sol est possible qu'il soit $\bar{\gamma} = -\partial\overline{T}/\partial z$ selon une valeur beaucoup plus grande que γ_a. Vu que la somme des deuxième et troisième membres entre crochets de l'équation (12), dans le cas considéré, est positive, le transport vertical ascendant de la chaleur peut exister si $\bar{\gamma} < \gamma_a$, ce qui est en contradiction avec la théorie classique de la turbulence, qui n'a pu expliquer ce phénomène.

Dans une atmosphère relativement calme, où nous pouvons négliger l'influence de la turbulence ($K = 0$) et où sont invariables les composantes verticales de la vitesse moyenne des masses neutres ainsi que celles des masses échauffées et refroidies avec l'altitude, nous avons:

$$\frac{\partial\overline{T}}{\partial t} \gtrless 0 \quad \text{ci est} \quad \gamma \lesseqgtr \gamma_a \quad \text{et} \quad w \lesseqgtr 0 .$$

Donc, sans tenir compte des quantités de masses refroidies par rapport aux masses échauffées dans l'atmosphère, où le gradient de température vertical moyen γ – conditionné par la présence de masses d'air neutre – est moindre que le gradient adiabatique sec, la température $\overline{T}$ augmente (diminue) au cours du temps si la vitesse moyenne verticale des masses d'air neutre est négative (positive). Le changement local de la température moyenne est proportionné à cette vitesse.

Les trois derniers membres de l'équation (13) sont l'expression de l'arrêt (accumulation) ou du retrait (départ) des masses d'air échauffées et refroidies. Ainsi, par exemple, les masses d'air chaud s'arrêtent sous les inversions de température et les masses froides au-dessus d'elles comme au-dessus du sol.

En terminant, nous signalons encore que dans l'équation (13) n'apparaît pas le facteur θ/T (θ = température potentielle), qui devrait exister d'après la théorie classique de la turbulence.

Bibliographie

[1] V. Bjerknes, J. Bjerknes, H. Solberg et T. Bergeron, *Physikalische Hydrodynamik mit Anwendung auf die dynamische Meteorologie* (Verlag J. Springer, Berlin 1933), 693.

[2] M. Čadež, *Über den Einfluss des fallenden Schnees auf die Temperatur der trockenen Atmosphäre*, Meteor. Z. *56* (1939), 272.

[3] H. L. Kuo, *Further studies of the properties of collular convection in a conditionally unstable atmosphere*, Tellus *17* (1965), 413.

[4] M. Čadež, *Strahlstrom und der durch Turbulenz verursachte Transport der mechanischen Energie in der Atmosphäre*, Geofis. pura e appl. *46* (1960), 173.

(Reçu le 16 avril 1966)

A Vertical Interpolation Experiment

By Fedor Mesinger[1])

Summary – Vertical interpolation of the data from the constant-pressure to the constant-density surfaces is discussed, and the results of an experiment given, wherein the data are interpolated to a constant-density surface using two different sets of the constant-pressure data. Comparison of the two results gives an estimate of the order of magnitude of the errors inherent in the interpolation.

1. Introduction

It is a practice today to report the meteorological upper air data at a set of surfaces on which the pressure has a number of constant standard values. Often, however, the data at other surfaces are needed, those being mostly the surfaces where some other variable has a constant value, for instance potential temperature, density, or the quotient of the pressure and the surface pressure—vertical coordinate of the 'sigma system' [4][2]). These data normally have to be determined from the readily available constant-pressure data through vertical interpolation. There are good prospects that a constant-volume ballon observation system will in the foreseeable future substitute the existing radiosonde observations in serving as the primary medium for deriving the upper atmospheric data [5]; this is likely to make the need for such interpolations much more frequent.

Various possible methods for performing a vertical interpolation are rather straightforward. They may have a different degree of elaboration, depending upon the accuracy required. When making a decision on the degree of elaboration desired, it seems useful to have some a priori knowledge on the order of magnitude of the errors which can be expected. In scope of an earlier investigation of the author [3] an experiment was performed, giving an estimate of the magnitude of those interpolation errors. It is the purpose of this note to present the results of that experiment.

2. The interpolation method

In the mentioned investigation data had to be interpolated from the standard constant-pressure to the constant-density surfaces. This had to be done with the pur-

---

[1]) Hydrometeorological Institute of SR Serbia, Belgrade, Yugoslavia. The experiment reported here has been made while the author was visiting the National Center for Atmospheric Research, Boulder, Colorado.

[2]) Numbers in brackets refer to References, page 184.

pose of obtaining the values of the potential

$$\xi = g\,z + R\,T \tag{1}$$

at the considered constant-density surfaces, g being the acceleration of gravity, and R the gas constant. This is the potential of the pressure force in the 'ϱ-system', which is defined analogously to the commonly used p-system [3].

Natural approach to this type of vertical interpolation appears to be an assumption describing the functional form of the temperature dependence on height or pressure. In making that assumption it here seems appropriate to take into consideration data from three neighboring constant-pressure surfaces, since the considered constant-density surface can normally be chosen close to one of the constant-pressure surfaces. In this way the available data consist of three sets of corresponding values of p, T and z, p standing for the atmospheric pressure, T for temperature and z for elevation measured in units of geopotential. Taking z for the independent variable, there remains the number of six known values of dependent variables. They are not independent of one another; pressure change with height depends on temperature, assuming the hydrostatic relationship. To fit all considered data functional form of the temperature dependence on height should so have five undetermined constants.

As the logical form of that dependence it so seems that one should assume

$$T = A + B\,z + C\,z^2 + D\,z^3 + E\,z^4\,, \tag{2}$$

A, B, C, D and E being the five constants. An assumption of this type is attractive because of being capable of exactly describing the linear temperature variation with height. Applying (2) at the three levels one obtains three equations relating the five constants. Using the hydrostatic relationship the three pressure values can be combined into additional two independent equations of the form

$$\ln \frac{p_2}{p_1} = -\frac{g}{R} \int_{z_1}^{z_2} \frac{dz}{T}\,. \tag{3}$$

The system of five equations is so closed. However, it can not be solved in a straightforward way, because of the integral in (3), and some iterative procedure would have to be attempted.

An alternative procedure would be to write the reciprocal of T on the left side of (2), thereby obtaining a system which can easily be solved for the five coefficients, but loosing the capability of exactly representing the linear temperature variation with height. A simpler possibility is to abandon the desire of fitting all considered data, assuming the dependence of temperature on height of only

$$T = a + b\,z + c\,z^2\,. \tag{4}$$

The three coefficients in (4) can now be computed using the temperature and height data only. Starting from the nearest constant-pressure surface we can thereafter find the height of the considered constant-density surface with the help of (3). This, of course, enables the computation of any other function of state variables at the chosen density surface. This procedure was used to compute the values of ξ in the mentioned investigation of the author, and will be described in more detail here.

Combination of (4) and (3) leads to different formulas for $\varrho = \varrho(z)$, depending on the value of the discriminant

$$D = 4\,a\,c - b^2\,.$$

Introducing the symbol

$$\Gamma = -\,b - 2\,c\,z\,,$$

they can be written in the form

$$\left.\begin{aligned}
&\ln\frac{\varrho}{\varrho_0} = \frac{2\,g}{R\,D^{1/2}}\left(a\tan\frac{\Gamma}{D^{1/2}} - a\tan\frac{\Gamma_0}{D^{1/2}}\right) - \ln\frac{T}{T_0}\,, && \text{for}\quad D>0\,,\\
&\ln\frac{\varrho}{\varrho_0} = -\frac{g}{R(-D)^{1/2}}\ln\frac{[\Gamma+(-D)^{1/2}]\,[\Gamma_0-(-D)^{1/2}]}{[\Gamma-(-D)^{1/2}]\,[\Gamma_0+(-D)^{1/2}]} - \ln\frac{T}{T_0}\,, && \text{for}\quad D<0\,,\\
&\ln\frac{\varrho}{\varrho_0} = \frac{2\,g(\Gamma-\Gamma_0)}{R\,\Gamma\,\Gamma_0} - \ln\frac{T}{T_0}\,, && \text{for}\quad D=0\,,\quad c\neq 0\,,\\
&z = z_0 - \frac{a\,R}{g}\ln\frac{\varrho}{\varrho_0}\,, && \text{for}\quad D=0\,,\quad c=0\,.
\end{aligned}\right\} \tag{5}$$

Here the subscripts denote the values variables are having at the nearest constant-pressure surface. The equations should give the height of the chosen constant-density surface. The first three, however, can not be solved for z; therefore, except in the fourth possibility, an iterative procedure was employed. The first approximation to z was obtained using the assumption

$$T = T_0 - \Gamma_0(z - z_0)\,,$$

leading to the formulas

$$\left.\begin{aligned}
&z = z_0 + \frac{T_0}{\Gamma_0}\left[1 - \left(\frac{\varrho}{\varrho_0}\right)^{R\Gamma_0/(g-R\Gamma_0)}\right], && \text{for}\quad \Gamma_0\neq 0\,,\\
&z = z_0 - \frac{a\,R}{g}\ln\frac{\varrho}{\varrho_0}\,, && \text{for}\quad \Gamma_0 = 0\,.
\end{aligned}\right\} \tag{6}$$

Following successive approximations have been computed applying the 'regula falsi' iteration method on the function $\ln\varrho = f(z)$, until the desired degree of accuracy is obtained. The convergence rate of that process turned out to be very high, already the second approximation to z being usually exact up to about 7 digits.

3. Estimate of the errors

To obtain an estimate of the errors inherent in the interpolation method an experiment was performed. National Meteorological Center objective analysis data have been interpolated to the constant density surface of 0.801 kg m^{-3} (density corresponding to the pressure of 600 mb in the Standard Atmosphere), first using the 850, 700 and 500 mb data, and then using the 700, 500 and 300 mb ones, and the results compared. As the reference constant-pressure surface in both cases the middle one was taken, the reference data, denoted with subscripts in (5), being so different in the two computations. Data chosen for the interpolation have been those of 00 GMT 5 December 1962, what was the initial situation of the study referred to above [3]. Interpolation was performed in all 1977 points of the National Meteorological Center grid.

The two obtained fields of the heights of considered constant-density surface have been subtracted from each other, and the same was done with the corresponding fields of the potential of the pressure force ξ. Histograms of so computed differences were made and are shown in figure 1. The differences should illustrate the upper limit to the errors inherent in the interpolation method: interpolation errors have to decrease with a decrease in the distance between the constant-density and the reference constant-pressure surface.

Differences in the pressure force potential values are seen to be in absolute values generally smaller than the differences in heights, this being due to the fact that the difference in the temperature term normally counteracts a part of the difference in the height term on the right side of (1). Differences in z ranged from -142 to 136 m, and the differences in ξ from -104 to 126 gpm. Root-mean-square of the ξ differences amounted 17.8 gpm; this is somewhat more than the root-mean-square error which at that level could have been produced through the subjectivity of synoptic analysis, had a subjective analysis been made, concluding after two studies by BERGGREN ([1],

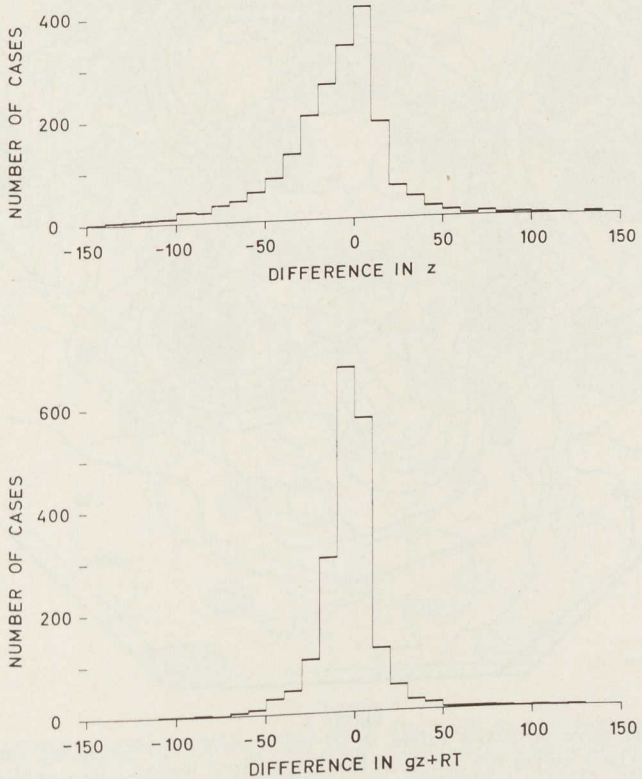

Figure 1

Histograms of differences in the height and pressure force potential values of the 0.801 kg m^{-3} isopycnic surface, 00 GMT 5 December 1962. Differences are computed by subtracting the values obtained through interpolation based on the 700, 500 and 300 mb data from those obtained by the interpolation made using the 850, 700 and 500 mb ones

[2]). Physically only the gradients of the differences in ξ are of importance, since it is only as the potential of the pressure force that ξ enters the hydrodynamic equations. About 16.6 per cent of the differences in ξ had an absolute value larger than 20 gpm; the errors in ξ of such magnitude, if distributed at random, would produce for most purposes prohibitively large errors in the gradients of ξ.

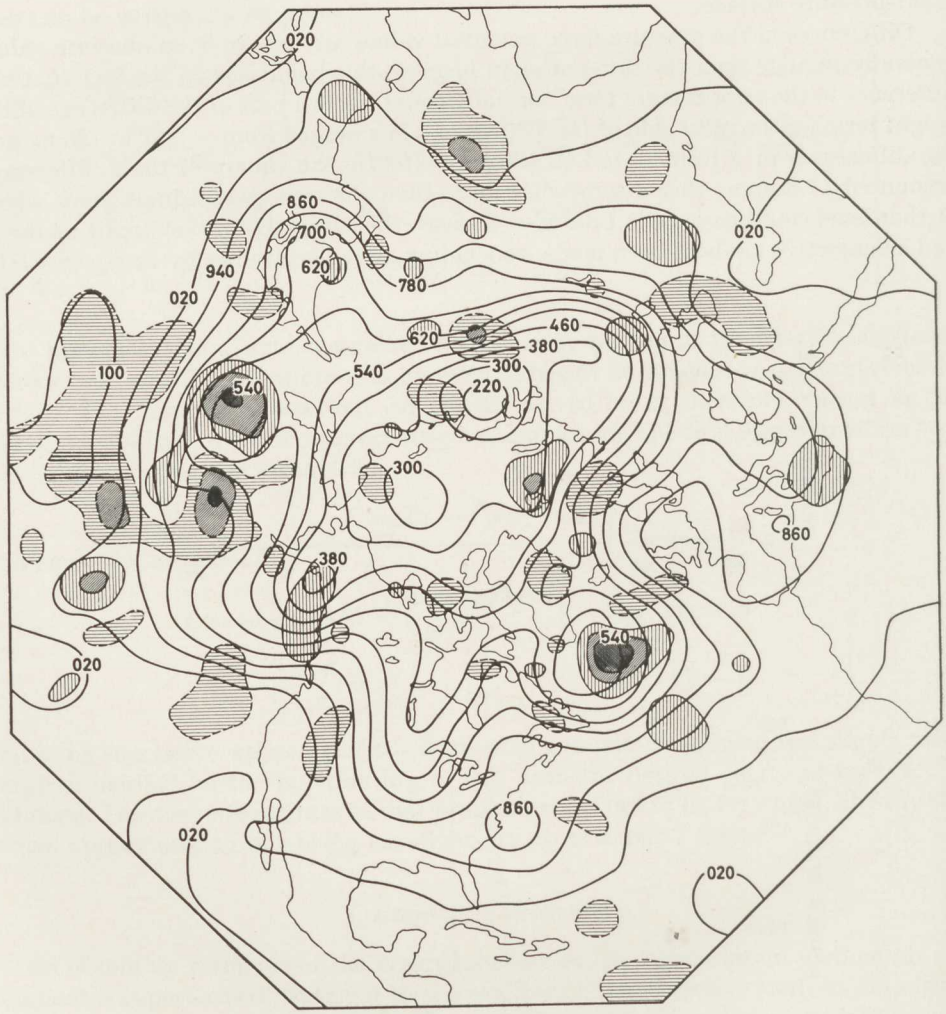

Figure 2

Map of the pressure force potential values, ξ, of the 0.801 kg m^{-3} isopycnic surface, 00 GMT 5 December 1962. The ξ values are obtained through vertical interpolation of the 700, 500 and 300 mb constant-pressure data, and are labeled in geopotential meters, with the leading digits being omitted. Non-labeled isolines have an interval of 40 gpm and show the distribution of the ξ differences, obtained by subtracting the figure 2 ξ values from the figure 3 ones. Regions where the absolute values of the ξ differences exceed 20 gpm are shaded. Dashed isolines are drawn in regions with negative ξ differences (horizontal shading between -20 and -60 gpm), and full isolines in regions with positive ξ differences (vertical shading between 20 and 60 gpm)

The space distribution of the differences in ξ has fortunately been fairly smooth, this of course being due to the smooth space distributions of the used temperature and height constant-pressure data. An estimate of the resulting differences in the gradients of ξ can be obtained by the inspection of the two ξ maps, reproduced in figures 2 and 3. The map in figure 2 is the one computed through interpolation made

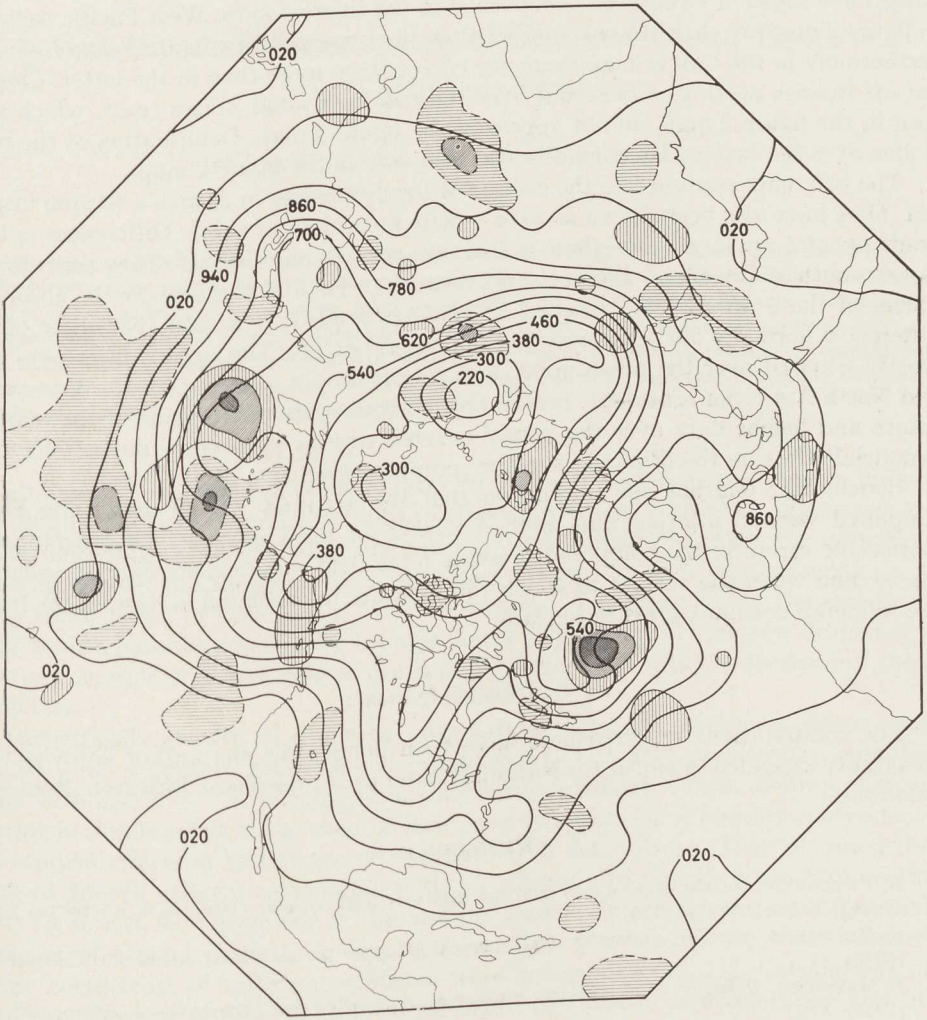

Figure 3

Map of the pressure force potential values, ξ, of the 0.801 kg m^{-3} isopycnic surface, 00 GMT 5 December 1962. The ξ values are obtained through vertical interpolation of the 850, 700 and 500 mb constant-pressure data, and are labeled in geopotential meters, with the leading digits being omitted. Non-labeled isolines have an interval of 40 gpm and show the distribution of the ξ differences, obtained by subtracting the figure 2 ξ values from the figure 3 ones. Regions where the absolute values of the ξ differences exceed 20 gpm are shaded. Dashed isolines are drawn in regions with negative ξ differences (horizontal shading between -20 and -60 gpm), and full isolines in regions with positive ξ differences (vertical shading between 20 and 60 gpm)

using the 700, 500 and 300 mb data, and the map in figure 3 that computed using the 850, 700 and 500 mb ones. When drawing the isolines some degree of smoothing is inevitably introduced; since this here has an undesired effect of partly masking the existing differences in the two ξ fields, a care was taken to draw the isolines so as to violate no grid point ξ value. Differences in the two ξ maps appear not to be serious, with only a few places where a distinct difference can visually be noticed. The cut-off low south of Greenland is deformed in the figure 3 map. West Pacific isolines in figure 2 map are closer to one another than the corresponding figure 3 map isolines, furthermore in the former map there are two of them more than in the latter. Closed cut-off isolines north of Korea and over the eastern United States coast, which are seen in the figure 2 map, do not appear in the figure 3 map. Deformation of the 620 isoline over the eastern Greenland is also seen only in the figure 2 map.

The two maps contain also the isolines of the differences in ξ, with a 40 gpm interval. They have also been drawn so as to violate no grid point value. Differences in the gradients of ξ are large when these isolines are close to one another. They seem to be closest south of Greenland and in the north-western Pacific. Areas where the absolute values of the ξ differences exceeded 20 gpm are shaded; it is seen that these large differences normally did not appear in isolated grid points. The large ξ differences are mostly situated over the ocean areas, and almost do not appear over the European and North American continent: presumably smooth space distribution of the temperature and height data over the poorly covered regions apparently did not have a beneficial effect on the differences in the computed gradients of ξ.

Concluding, one has the impression that the accuracy of the used three-level simplified vertical interpolation method should for most purposes be satisfactory. Noticeable errors in the computed pressure force field may appear only at isolated places, and when the surface to which the data are interpolated is located far from the reference constant-pressure surface.

4. Acknowledgements

The computations reported here have been done while the author enjoyed the hospitality extended to him at the National Center for Atmospheric Research, Boulder, Colorado.

References

[1] R. Berggren, *On the accuracy of 500 mb analysis with special reference to numerical forecasting*, Tellus *9* (1957), 323.

[2] R. Berggren, *Further studies on the accuracy of upper air analysis*, Arkiv för Geofysik *3* (1958), 41.

[3] F. Mesinger, *Behavior of a very large number of constant-volume trajectories*, J. Atmos. Sci. *22* (1965), 479.

[4] N. A. Phillips, *A coordinate system having some special advantages for numerical forecasting*, J. Meteor. *14* (1957), 184.

[5] R. M. White, *The world weather system—a frontier in geophysics*, Bull. Am. Meteor. Soc. *46* (1965), 623.

(Received 16th April 1966)

Gravitational Coagulation of Charged Cloud Drops in Turbulent Flow

By Lev M. Levin and Yurii S. Sedunov[1])

Summary – Gravitational coagulation of particles in turbulent flow is investigated with respect to the electrostatic forces. As turbulence mixes particle trajectories at large distances, its account reduces the consideration of drawing particles together till some definite distance. Taking into account hydrodynamical forces of interaction, series converging faster than Hocking's one and their more exact values are obtained. For electrostatic forces series with better convergence are also obtained. Equations of moment were solved numerically on electronic computer BESM–2. Results of collection efficiency computation are given.

Studying the mechanism of cloud drop formation is very important for an understanding of physical processes leading to cloud formation. Numerous investigations of this mechanism showed that at present it is very difficult to explain the formation of a wide droplet size spectrum (with diameters d from 1 to 30 $\div$ 40 μ) at a comparatively short period of time (about 20 $\div$ 30 minutes). The point is that the growth of drops by condensation must have brought to the appearance of a narrow droplet size spectrum as such a growth rate of drops rapidly decreases with the increase of their diameters.

Theoretically growth of drops by coagulation either impossible for drops with $d < 30 \div 40$ μ (purely gravitational coagulation; [1, 2, 3])[2]) or effective only for drops with $d < 5 \div 7$ μ (electrostatic coagulation at mean values of drop charges existing in clouds at the initial stage of their development: [4]). A number of investigators studied effects of turbulence on coagulation of cloud drops. They obtained the value of growth rate by coagulation with an accuracy to unknown constant coefficients [5, 6, 7, 8, 9]. Lately one at the authors made accurate calculations of mutual velocities of aerosol particles in the turbulent flow [10, 11, 12]. On these grounds precise coefficients of turbulent diffusion were determined [10, 11]. Calculations of cloud drop growth rate by the known turbulent mechanism of acceleration and by turbulent diffusion confirmed once more that velocities of cloud drop spectrum formation observed in nature could not be due only to these growth mechanism [12].

In particular, this is connected with the fact that at small distances between drops turbulent diffusion is small (it is effective at long distances) while the picture is quite

---

[1]) Hydrometeorological Service of the USSR, 12 Pavlik Morozov Street, Moscow, D–376, USSR.

[2]) Numbers in brackets refer to References, page 196.

the contrary for other coagulation mechanism—they are little effective at great distances.

In the present paper we tried to estimate the joint effect of turbulent, gravitational and electrostatic coagulation on cloud drop growth rate. This estimation was carried out for two-layer model. The space beyond the larger of coagulation drops is divided into two parts by the sphere the surface of which is away from the drop at a distance equal to turbulent free path length l_t[3]). Beyond the sphere the main mechanism of approach is turbulence. It provides fast approach of small drops with comparatively large relative velocities to this sphere. Within the sphere movement of particles relative to one another takes place under gravity, electrostatic and hydrodynamical interactions. As movement occurs within the sphere, when the distances between drop surfaces Δ are comparable with drop sizes. expressions for the given above forces must be thoroughly considered for correct formulation of the task.

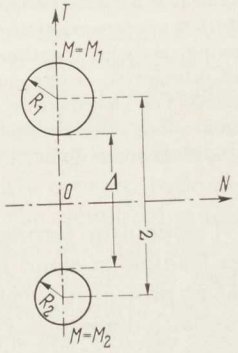

Figure 1
Bispherical coordinate system

To describe electrostatic interaction between two charged drops let us introduce bispherical co-ordinate system in which surfaces of both drops correspond to the co-ordinate values

$$\mu = \mu_1 \quad \text{and} \quad \mu = \mu_2 (\mu_1 > 0\,; \quad \mu_2 < 0)\,.$$

Then

$$2\,r\,R_1\,c\,h\,\mu_1 = r^2 + R_1^2 - R_2^2; \quad 2\,r\,R_2\,c\,h\,\mu_2 = r^2 - R_1^2 + R_2^2\,,$$

where r is the distance between drop centers ($r = R_1 + R_2 + \Delta$).

For coefficients of capacity c_{ik} connecting the drop charges q_1 and q_2 with their potentials V_1 and V_2 by the formulas

$$q_i = \sum_{k=1}^{2} C_{ik}\,V_k \quad (i = 1, 2) \tag{1}$$

---

[3]) By free path length we mean a distance at which drops must disperse in the flow lest their relative velocites in the initial and finite moments should correlate. Value $l_t \approx 1.5\,(R_1 + R_2)$ where R_1, R_2—the radius of the larger and smaller drops [12].

the following expressions take place [4]:

$$C_{ii} = R_i(1 - v_i^2) \sum_{m=0}^{\infty} (v_i^2 u^{2m+1})^m \frac{1 - v_i^2 u^{4m-1}}{(1 - v_i^2 u^{2m})(1 - u^{2m+1})} \quad (i = 1, 2), \tag{2}$$

$$C_{12} = C_{21} = -\frac{R_1 R_2}{r}(1 - u^2) \sum_{m=0}^{\infty} u^{(2m+3)m} \frac{1 - u^{4m+3}}{(1 - u^{2m+2})(1 - u^{2m+1})},$$

where

$$v_1 = e^{-\mu_1}; \quad v_2 = e^{-|\mu_2|}; \quad u = v_1 v_2 .$$

Electrostatic force of interaction of two charged spheres — F_e can be represented by an equation of the form (4):

$$F_e = \frac{q_1 q_2}{r^2} f(r, a, x), \tag{3}$$

where

$$\left.\begin{aligned} f(r, a, x) &= 1 + l_1(r, a) + x\, l_2(r, a) + \frac{1}{x} l_3(r, a) \\ &= -r^2 \frac{ds_{12}}{dr} + x \frac{r^2}{2} \frac{dS_{22}}{dr} + \frac{1}{x} \frac{r^2}{2} \frac{dS_{11}}{dr} . \end{aligned}\right\} \tag{4}$$

Here $a = R_2/R_1 \leq 1$; $x = -q_2/q_1$; S_{ik}-coefficients of induction determined by

$$v_i = \sum_{k=1}^{2} s_{ik} q_k \quad (i = 1, 2). \tag{5}$$

From the equation (1) and (5) we obtain

$$s_{11} = c_{22} \delta_c^{-1}; \quad s_{22} = c_{11} \delta_c^{-1}; \quad s_{12} = -c_{12} \delta_c^{-1} = s_{21}; \quad \delta_c = \begin{vmatrix} c_{11} & c_{12} \\ c_{21} & c_{22} \end{vmatrix}. \tag{6}$$

Computations showed that the series (2) as well as the series for dS_{ik}/dr (by these series (2) and with the help of (6) the derivatives dS_{ik}/dr entering the (4) should be expressed) converge very fast even at the distances between drop surfaces $\Delta \sim 0.01\, R_2$[4]).

This allowed us to program effectively expressions for electrostatic forces on the electronic computer BESM–2. Examples of values of functions l_i computed by the above method are given in table 1.

We consider aerodynamical forces acting on drops in the Stokes approximation because according to our task we shall deal with the drops having $R_1 < 20 \div 30\ \mu$ and at $\Delta < 2 \div 5\, R_1$[5]).

In the Stokes approximation aerodynamical forces f_1 and f_2 acting on drops are linearly related with velocities of drops moving relative to the air. We shall consider

---

[4]) For example, to compute l_i with an accuracy to 0.1% at $\Delta = 0.01\, R_2$ it is necessary to take all in all 6 to 7 terms of the series (2) and their derivatives.

[5]) The second condition is very essential because Stokes approximation is true not only when the REYNOLD's number $2 R_1 v/\nu$ is small but also when $2 r_r v/\nu$ is small [16]. Here v is the drop velocity, ν the kinematic viscosity.

Tabelle 1

Δ/a		20	10	5	2	1	0.5	0.2	0.1	0.05	0.02	0.01	0.005	0.002	0.001
$a=1$	l_1	—	0	$132\cdot10^{-6}$	$443\cdot10^{-5}$	$317\ 10^{-4}$	$130\cdot10^{-3}$	$476\cdot10^{-3}$	$998\cdot10^{-3}$	$189\cdot10^{-2}$	$408\ 10^{-2}$	$711\cdot10^{-2}$	$123\cdot10^{-1}$	$254\ 10^{-1}$	$441\cdot10^{-1}$
	$l_2=l_3$	—	$117\ 10^{-5}$	$601\cdot10^{-5}$	$346\ 10^{-4}$	$909\ 10^{-4}$	$187\cdot10^{-3}$	$400\cdot10^{-3}$	$676\cdot10^{-3}$	$113\ 10^{-3}$	$223\ 10^{-2}$	$374\ 10^{-2}$	$633\cdot10^{-2}$	$128\cdot10^{-1}$	$222\ 10^{-1}$
$a=0.9$	l_1	—	$6\cdot10^{-6}$	$223\ 10^{-6}$	$524\cdot10^{-5}$	$358\ 10^{-4}$	$142\ 10^{-3}$	$505\ 10^{-3}$	$105\cdot10^{-2}$	$197\ 10^{-2}$	$425\cdot10^{-2}$	$739\ 10^{-2}$	$128\ 10^{-1}$	$264\cdot10^{-1}$	$459\ 10^{-1}$
	l_2	—	$156\cdot10^{-5}$	$547\cdot10^{-5}$	$444\cdot10^{-4}$	$115\ 10^{-3}$	$236\cdot10^{-3}$	$505\cdot10^{-3}$	$853\cdot10^{-3}$	$142\ 10^{-2}$	$280\ 10^{-2}$	$470\ 10^{-2}$	$795\cdot10^{-2}$	$161\ 10^{-1}$	$279\cdot10^{-1}$
	l_3	—	$114\cdot10^{-5}$	$653\cdot10^{-5}$	$317\cdot10^{-4}$	$807\cdot10^{-4}$	$162\ 10^{-3}$	$342\ 10^{-3}$	$577\cdot10^{-3}$	$964\ 10^{-3}$	$190\ 10^{-2}$	$321\cdot10^{-2}$	$544\ 10^{-2}$	$110\ 10^{-1}$	$190\ 10^{-1}$
$a=0.7$	l_1	—	$11\cdot10^{-6}$	$28\cdot10^{-5}$	$751\cdot10^{-5}$	$460\ 10^{-4}$	$169\ 10^{-3}$	$564\cdot10^{-3}$	$115\cdot10^{-2}$	$314\ 10^{-2}$	$457\ 10^{-2}$	$793\cdot10^{-2}$	$137\cdot10^{-1}$	$283\ 10^{-1}$	$492\cdot10^{-1}$
	l_2	—	$310\cdot10^{-5}$	$150\cdot10^{-4}$	$797\cdot10^{-4}$	$201\ 10^{-3}$	$406\ 10^{-3}$	$865\cdot10^{-3}$	$146\cdot10^{-2}$	$242\cdot10^{-2}$	$473\ 10^{-2}$	$791\cdot10^{-2}$	$134\ 10^{-1}$	$271\ 10^{-1}$	$468\cdot10^{-1}$
	l_3	—	$105\ 10^{-5}$	$5\ 10^{-3}$	$251\cdot10^{-4}$	$591\ 10^{-4}$	$112\ 10^{-3}$	$230\cdot10^{-3}$	$386\cdot10^{-3}$	$648\cdot10^{-3}$	$129\cdot10^{-2}$	$217\ 10^{-2}$	$369\ 10^{-2}$	$753\ 10^{-2}$	$131\cdot10^{-1}$
$a=0.5$	l_1	$77\cdot10^{-7}$	$25\ 10^{-6}$	$506\cdot10^{-6}$	$111\cdot10^{-4}$	$591\ 10^{-4}$	$197\cdot10^{-3}$	$620\cdot10^{-3}$	$123\cdot10^{-2}$	$227\cdot10^{-2}$	$480\cdot10^{-2}$	$834\ 10^{-2}$	$144\ 10^{-1}$	$295\cdot10^{-1}$	$515\cdot10^{-1}$
	l_2	$133\cdot10^{-5}$	$755\ 10^{-5}$	$344\ 10^{-4}$	$168\cdot10^{-3}$	$408\ 10^{-3}$	$811\cdot10^{-3}$	$171\ 10^{-2}$	$286\ 10^{-2}$	$472\cdot10^{-2}$	$916\cdot10^{-2}$	$152\ 10^{-1}$	$257\ 10^{-1}$	$520\cdot10^{-1}$	$895\cdot10^{-1}$
	l_3	$165\cdot10^{-6}$	$917\cdot10^{-6}$	$40\ 10^{-4}$	$172\cdot10^{-4}$	$377\ 10^{-4}$	$647\ 10^{-4}$	$129\ 10^{-3}$	$216\cdot10^{-3}$	$364\ 10^{-3}$	$728\ 10^{-3}$	$123\ 10^{-2}$	$210\cdot10^{-2}$	$436\ 10^{-2}$	$742\ 10^{-2}$
$a=0.3$	l_1	$2\cdot10^{-6}$	$7\cdot10^{-5}$	$106\ 10^{-5}$	$167\ 10^{-4}$	$736\ 10^{-4}$	$220\ 10^{-3}$	$650\ 10^{-3}$	$127\ 10^{-2}$	$231\cdot10^{-2}$	$484\ 10^{-2}$	$837\ 10^{-2}$	$144\ 10^{-1}$	$296\ 10^{-1}$	$513\cdot10^{-1}$
	l_2	$529\cdot10^{-5}$	$274\cdot10^{-4}$	$112\ 10^{-3}$	$487\cdot10^{-3}$	$112\ 10^{-2}$	$219\ 10^{-2}$	$455\ 10^{-2}$	$752\cdot10^{-2}$	$123\ 10^{-1}$	$236\cdot10^{-1}$	$390\cdot10^{-1}$	$652\cdot10^{-1}$	$131\ 10^{0}$	$225\ 10^{0}$
	l_3	$139\cdot10^{-6}$	$679\ 10^{-6}$	$250\ 10^{-5}$	$831\cdot10^{-5}$	$151\cdot10^{-4}$	$247\cdot10^{-4}$	$482\ 10^{-4}$	$814\cdot10^{-4}$	$140\ 10^{-3}$	$286\cdot10^{-3}$	$483\cdot10^{-3}$	$816\ 10^{-3}$	$168\ 10^{-2}$	$228\cdot10^{-2}$

x/a		200	100	50	20	10	5	2	1	0.5	0.2	0.1	0.05	0.02	0.01
$a=0.1$	l_1	—	0	0	$21\cdot10^{-6}$	$276\ 10^{-6}$	$236\ 10^{-5}$	$218\cdot10^{-4}$	$786\cdot10^{-4}$	$215\ 10^{-3}$	$611\ 10^{-3}$	$118\ 10^{-2}$	$214\cdot10^{-2}$	$448\ 10^{-2}$	$770\cdot10^{-2}$
	l_2	—	$148\cdot10^{-5}$	$918\cdot10^{-5}$	$793\cdot10^{-4}$	$320\ 10^{-3}$	$106\ 10^{-2}$	$392\ 10^{-2}$	$868\cdot10^{-2}$	$167\ 10^{-1}$	$345\ 10^{-1}$	$565\ 10^{-1}$	$914\ 10^{-1}$	$173\ 10^{0}$	$283\ 10^{0}$
	l_3	—	$1\cdot10^{-6}$	$88\cdot10^{-7}$	$65\cdot10^{-6}$	$217\cdot10^{-6}$	$49\ 10^{-5}$	$95\cdot10^{-5}$	$138\cdot10^{-5}$	$218\cdot10^{-5}$	$464\ 10^{-5}$	$847\cdot10^{-5}$	$15\ 10^{-3}$	$314\ 10^{-4}$	$57\ 10^{-3}$
$a=0.05$	l_1	0	0	$1\ 10^{-6}$	$4\cdot10^{-5}$	$39\cdot10^{-5}$	$264\cdot10^{-5}$	$212\cdot10^{-4}$	$749\cdot10^{-4}$	$205\ 10^{-3}$	$584\ 10^{-3}$	$113\cdot10^{-2}$	$206\cdot10^{-2}$	$430\ 10^{-2}$	$729\cdot10^{-2}$
	l_2	$150\cdot10^{-5}$	$941\ 10^{-5}$	$506\cdot10^{-4}$	$352\ 10^{-3}$	$125\ 10^{-2}$	$385\ 10^{-2}$	$140\cdot10^{-1}$	$314\cdot10^{-1}$	$612\ 10^{-1}$	$127\cdot10^{0}$	$209\ 10^{0}$	$337\cdot10^{0}$	$635\ 10^{0}$	$104\cdot10^{1}$
	l_3	0	0	$55\cdot10^{-7}$	$29\ 10^{-6}$	$67\ 10^{-6}$	$114\cdot10^{-6}$	$175\cdot10^{-6}$	$238\cdot10^{-6}$	$42\cdot10^{-5}$	$10\ 10^{-4}$	$2\ 10^{-3}$	$33\cdot10^{-4}$	$7\ 10^{-3}$	$127\cdot10^{-4}$
$a=0.02$	l_1	0	0	$3\ 10^{-6}$	$6\cdot10^{-5}$	$43\cdot10^{-5}$	$255\cdot10^{-5}$	$201\cdot10^{-4}$	$714\ 10^{-4}$	$197\ 10^{-3}$	$564\ 10^{-3}$	$11\cdot10^{-1}$	$199\cdot10^{-2}$	$418\ 10^{-2}$	$718\ 10^{-2}$
	l_2	$168\cdot10^{-4}$	$866\ 10^{-4}$	$374\ 10^{-3}$	$207\cdot10^{-2}$	$680\ 10^{-2}$	$209\ 10^{-1}$	$785\ 10^{-1}$	$180\cdot10^{0}$	$357\ 10^{0}$	$747\cdot10^{0}$	$123\ 10^{1}$	$198\ 10^{1}$	$374\ 10^{1}$	$611\ 10^{1}$
	l_3	0	0	$1\cdot10^{-6}$	$56\ 10^{-7}$	$88\ 10^{-7}$	$115\ 10^{-7}$	$15\cdot10^{-6}$	$1\cdot10^{-5}$	$5\ 10^{-5}$	$112\cdot10^{-6}$	$29\ 10^{-5}$	$16\cdot10^{-5}$	$3\cdot10^{-4}$	$7\cdot10^{-4}$

drop movement on the vertical plane. Then in Cartesian coordinates connected with center line (axis 0 t-along the line of center, axis 0 n-normal to it) the relation f_i to v_i can be expressed as

$$\left.\begin{aligned} f_{in} &= (a_{i1,n}\, v_{1n} + a_{i2,n}\, v_{2n})\, 6\,\pi\,\eta\, R_i\,, \\ f_{it} &= (a_{i1,t}\, v_{1t} + a_{i2,t}\, v_{2t})\, 6\,\pi\,\eta\, R_i\,, \end{aligned}\right\} \quad (i = 1, 2)\,, \tag{7}$$

where $a_{ik,n}$ and $a_{ik,t}$-functions of r, R_1, R_2, η-viscosity of the air.

The purpose of a great number of theoretical papers and some experimental works was devoted to find $a_{ik,n}$ and $a_{ik,t}$. [13, 14, 15, 17, 20, 21]. For the case when movement takes place along the line of center ($v_{1n} = v_{2n} = 0$) the task has axial symmetry and the exact solution is obtained for it. This task was first solved for the case $v_{1t} = v_{2t}$ by STIMSON and JEFFERY [15].

For arbitrary values of v_{1t} and v_{2t} PSHENAY-SEVERIN obtained $a_{ik,t}$ [17] which can be represented in bispherical coordinates by the following way[6]):

$$\left.\begin{aligned} a_{11,t} = \frac{1}{3}\, sh\,\mu_1 \sum_{m=1}^{\infty} A_m \Big\{ & 2\,(2m-1)\,(2m+3)\,(\exp[-(2m+1)\,\mu_2] \\ & - \exp[-(2m+1)\,\mu_1]) - 2(2m+1)\,(2m+3) \\ & \times sh\Big[\Big(m+\frac{3}{2}\Big)\,(\mu_1-\mu_2)\Big] \exp\Big[-\Big(m-\frac{1}{2}\Big)\,(\mu_1+\mu_2)\Big] \\ & - 2(2m+1)\,(2m-1) \\ & \times sh\Big[\Big(m-\frac{1}{2}\Big)\,(\mu_1-\mu_2)\Big] \exp\Big[-\Big(m+\frac{3}{2}\Big)\,(\mu_1+\mu_2)\Big]\Big\}\,; \\ a_{12,t} = \frac{1}{3}\, sh\,\mu_1 \sum_{m=1}^{\infty} A_m \Big\{ & 16 \exp\Big[-\Big(m+\frac{1}{2}\Big)\,(\mu_1-\mu_2)\Big] \\ & \times sh\Big[\Big(m+\frac{1}{2}\Big)\,(\mu_1-\mu_2)\Big] + (2m+1)^2\, sh(\mu_1-\mu_2) \\ & \times [(2m+3)\exp(\mu_1-\mu_2) + (2m-1)\exp(-\mu_1+\mu_2)] \\ & + (2m+1)\,(2m+3)\,(2m-1)\,(sh\,2\,\mu_2 - sh\,2\,\mu_1)\Big\}\,, \end{aligned}\right\} \tag{8}$$

where

$$A_m = \frac{m(m+1)}{(2m+3)\,(2m-1)} \left\{4\, sh^2\Big[\Big(m+\frac{1}{2}\Big)\,(\mu_1-\mu_2)\Big] - (2m+1)^2\, sh^2(\mu_1-\mu_2)\right\}^{-1}.$$

Functions $a_{22,t}$ and $a_{21,t}$ are obtained from $a_{11,t}$ and $a_{12,t}$ respectively by substituting μ_1 for $-\mu_2$ and μ_2 for $-\mu_1$. For case when $v_{in} \neq 0$ a number of authors obtained the following series for functions $a_{ik,t}$ and $a_{ik,n}$ [3, 20]:

$$a_{ik,\frac{t}{n}} = \sum_{\mu,\nu=0}^{\infty} P_{\mu\nu}\, \frac{R_1^{\mu}\, R_2^{\nu}}{r^{(\mu+\nu)}}\,. \tag{9}$$

[6]) It's a queer thing that just the same solution of the task was published in 3 to 5 years by BRENNER [18] and MAUDE [19].

In particular, HOCKING [3] obtained expressions for $a_{ik,n}$ and $a_{ik,t}$ accurate to the terms $0(r^{-7})$ (9). We compared results by HOCKING with the exact formulas by PSHENAY-SEVERIN.

For this purpose coefficients $a_{ik,t}$ were computed from the formulas (8) and from HOCKING's series. These computations showed that at small $\Delta(\Delta < 0.5\ R_2)$. HOCKING's expressions led to essential errors in determination of $a_{ik,t}$ (figure 2 and table 2). This is connected with slow convergence of series (9). At the same time we noticed that when determining v_{in} and v_{it} from the system (7)

$$\left.\begin{aligned} v_{in} &= \left(b_{i1,n}\frac{f_{1n}}{6\pi\eta R_1} + b_{i2,n}\frac{f_{2n}}{6\pi\eta R_2}\right), \\ v_{it} &= \left(b_{i1,t}\frac{f_{1t}}{6\pi\eta R_1} + b_{i2,t}\frac{f_{2t}}{6\pi\eta R_2}\right), \end{aligned}\right\} \quad (i = 1, 2), \tag{10}$$

functions $b_{ik,n}$ and $b_{ik,t}$ can be obtained for which series of (9) type converge significantly sooner than for $a_{ik,n}$ and $a_{ik,t}$. This allowed us within the limits of the same approximation that HOCKING obtained $(0(r^{-7})$ to find expansion in series of (9) type for $b_{ik,n}$ and $b_{ik,t}$:

$$\left.\begin{aligned} -b_{11,n} &= 1 - \frac{3}{4}\frac{R_1 R_2^3}{r^4} - \frac{17}{16}\frac{R_1 R_2^5}{r^6} + 0\,(r^{-8}), \\ -b_{12,n} &= \frac{3}{4}\frac{R_2}{r} + \frac{R_2(R_1^2 + R_2^2)}{4\,r^3} + \frac{3\,R_1^3 R_2^4}{8\,r^7} + 0\,(r^{-9}), \\ -b_{11,t} &= 1 - \frac{15}{4}\frac{R_1 R_2^3}{r^4} - 2\frac{R_1 R_2^5}{r^6} + \frac{15}{2}\frac{R_1^3 R_2^3}{r^6} + 0\,(r^{-8}), \\ -b_{12,t} &= \frac{3}{2}\frac{R_2}{r} - \frac{R_2(R_1^2 + R\,)}{2\,r^3} + \frac{75}{4}\frac{R_1^3 R_2^3}{r^7} + 0\,(r^{-9}). \end{aligned}\right\} \tag{11}$$

Functions $b_{22,\frac{t}{n}}$ and $b_{21,\frac{t}{n}}$ are obtained from $b_{11,\frac{t}{n}}$ and $b_{12,\frac{t}{n}}$ respectively by transposition of R_1 and R_2.

Hence we obtained expressions for $a_{ik,t}$[7]).

$$\left.\begin{aligned} a_{11,t} &= b_{22,t}\,\delta_t^{-1}; \qquad a_{12,t} = -\,b_{12,t}\,\delta_t^{-1}; \\ a_{21,t} &= -\,b_{21,t}\,\delta_t^{-1}; \quad a_{22,t} = b_{11,t}\,\delta_t^{-1}. \end{aligned}\right\} \quad \delta_t = \begin{vmatrix} b_{11,t} & b_{12,t} \\ b_{21,t} & b_{22,t} \end{vmatrix}. \tag{12}$$

Functions $a_{ik,t}$ obtained from formulas (12) approach to the exact solution of (8) at small values of the distance Δ better than that obtained by HOCKING. This is due to the fact that in formulas (12) we compute determinants δ_t and δ_n substituting there values of $b_{ik,\frac{t}{n}}$ from (11) while HOCKING when computing these determinants limited himself to the terms $0\,(r^{-7})$. Calculations showed that the obtained approximation proved to be much better for drops of comparable sizes $(R_2/R_1 > 0.5)$. This illustrates in figures 2, table 2. The values of $\lambda = (a_{11,t} + a_{12,t})$ are given in table 2, for the case when two identical drops move along the center line at one and the same velocity v_t. The values λ characterizes the relation of the force acting on one of these drops to the

---

[7]) Functions $a_{ik,n}$ are expressed by $b_{ik,n}$ from the formulas similar to (12).

force acting on any of these drops (when it is considered isolated) moving at the same velocity. As it is seen from table 2, at $\Delta < 0.1\ R$ the force estimated from HOCKING's formulas is 1.5 to 2.5 times less than the exact value while the value obtained from (12) differs from the exact one by 4%.

Table 2

Δ/R	0	0.1	0.2	0.5	0.8	1.0
λ (exact)	0.645	0.655	0.660	0.675	0.692	0.705
λ (HOCKING)	0.257	0.440	0.525	0.636	0.675	0.695
λ (formulas (12))	0.617	0.630	0.642	0.670	0.688	0.705

As it was demanded by the task stated in the beginning of the paper we considered a system of dimensionless equations of movement for drops with electrostatic, aerodynamical forces and gravity act upon (the coordinate system is shown in figure 3):

$$I \frac{dw_1}{dt} = 1 - \frac{z\, l_1 - x\, t_1}{r} + a^3 \alpha \frac{z\, f(r)}{r^3}\,; \tag{13a}$$

$$I \frac{du_1}{dt} = - \frac{x\, l_1 + z\, t_1}{r} + a^3 \alpha \frac{x\, f(r)}{r^3}\,; \tag{13b}$$

$$I \frac{dw_2}{dt} = 1 - \frac{z\, l_2 - x\, t_2}{a^2\, r} - \alpha \frac{z\, f(r)}{r^3}\,; \tag{13c}$$

$$I \frac{du_2}{dt} = - \frac{x\, l_2 + z\, t_2}{a^2\, r} - \alpha \frac{x\, f(r)}{r^3}\,; \tag{13d}$$

$$\frac{dx}{dt} = u_2 - u_1\,; \tag{13e}$$

$$\frac{dz}{dt} = w_2 - w_1\,; \tag{13f}$$

where

$$z = z_2 - z_1; \quad x = x_2 - x_1; \quad r^2 = x^2 + z^2; \quad u_i = \frac{dx_i}{dt}; \quad w_i = \frac{dz_i}{dt}\,;$$

x_1, z_1, x_2, z_2 Cartesian coordinates of drop centers (0 z is vertical), $a = R_2/R_1 \leq 1$: $I = 4\, \varrho^2\, R_1^3\, g/81\, \eta$ is an analogue of the Stokes number[8]). $\alpha = - q_1\, q_2/6\, \pi\, \eta\, R_1^3\, a^3\, v_{1s}$ is a parameter characterising the relation of electrostatic forces to aerodynamical ones, ϱ is the drops density, g the gravity acceleration, $v_{1s} = 2\, \varrho\, R_1^2\, g/9\, \eta$ the sedimentation velocity of the larger drop.

[8]) It is easily noticed that $I = \tau_1\, v_{1s}/R_1$ where $\tau_1 = 2\, \varrho\, R_1^2/9\, \eta$ relaxation time for the larger drop. The Stokes number is $\kappa = \tau_2 (v_{1s} - v_{2s})/R_1$, where $\tau_2 = 2\, \varrho\, R_2^2/9\, \eta$-relaxation time for the smaller drop, $v_{2s} = 2\, \varrho\, R_2^2\, g/9\, \eta = v_{1s} \cdot a^2$-sedimentation velocity of the smaller drop. As $\tau_2 = a^2\, \tau_1$, Stokes number $\kappa = I\, a^2 (1 - a^2)$.

Functions

$$l_i = - u_{t_1} a_{i1,t} - u_{t_2} a_{i2,t} ; \tag{14a}$$

$$t_i = - u_{n_1} a_{i1,n} - u_{n_2} a_{i2,n} ; \tag{14b}$$

$$u_{t_i} = \frac{1}{r} (u_i x + w_i z) ; \tag{14c}$$

$$u_{n_i} = \frac{1}{r} (u_i z - w_i x) ; \quad (i = 1, 2) , \tag{14d}$$

where $a_{ik,t}$ and $a_{ik,n}$ are determined by (12) and (11).

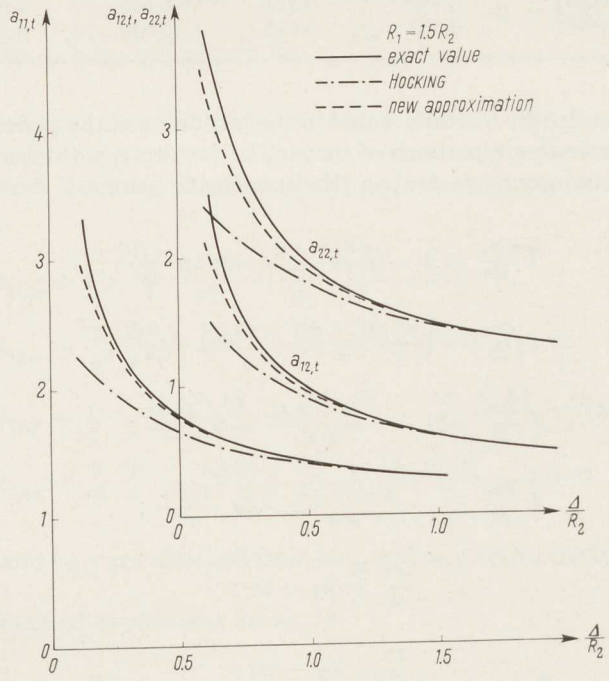

Figure 2
Dependence of coefficients $a_{ik,t}$ on the distance Δ between drop surfaces

This system of equations (13) was programmed for the electronic computer BESM–2 and was solved under the following initial conditions:

$$\text{at} \quad t = 0; \quad x = x_0; \quad z = z_0; \quad w_{10} = 1; \quad u_{10} = 0; \quad w_{20} = a^2; \quad u_{20} = 0 . \tag{15}$$

The grazing trajectory of gravity center of the smaller drop tangent the sphere 0 with its center in the larger drop center and with its radius $r = R_1 + R_2$ (in dimensionless values $r = 1 + a$) was determined for the given values of 1, a, z_0. For this purpose the trajectory of drops was determined at some arbitrary value of the initial impact parameter $x_0 = x_{0,0}$. If this trajectory of the smaller drop went past the sphere 0, the impact parameter two times decreased. If the next trajectory went past the same sphere, the impact parameter two times decreased again. And this was

repeated until the trajectory intersected the sphere. Analogous to this if the initially taken trajectory of the smaller drop intersected the sphere, the impact parameter two times increased.

If the next trajectory intersected the same sphere, the impact parameter also two times increased. This was repeated until the trajectory went past the sphere 0. After several of such trajectory computations we obtained two values of the impact parameter ($x_0 = x_{0,i}$ and $x_0 = x_{0,i-1}$).

At one of these values the trajectory intersected the sphere and at the other it went past the sphere. After it a trajectory was calculated with $x_0 = x_{0,i+1} = 1/2\,(x_{0,i-1} + x_{0,i})$. And then out of these 3 trajectories a pair was chosen one of which intersected the sphere and the other went past it. Such an operation continued until $x_{0,i+1} - x_{0,i}$ did not become less than some value given beforehand by the necessary accuracy of collection efficiency calculations.

Having found in such a way the impact parameter for the grazing trajectory $- x_{0,gr}$ we determine the collection efficiency E of smaller drops by greater ones according to the formula

$$E = x_{0,gr}^2 \,. \tag{16}$$

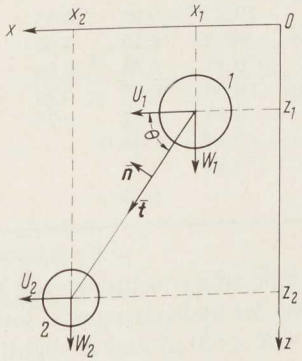

Figure 3
Geometry of the considered problem

The collection efficiency was calculated for three cases. When calculating trajectories for the first case we assumed the impact parameter z_0 of drops very high ($z_0 = 50$) and determined the collection efficiency of gravitational coagulation E_g which was calculated by a number of authors including HOCKING. To determine E_{tg} of turbulent gravitational coagulation on the base of the two-layer model described in the beginning of the paper it was assumed

$$z_0 = l_t + R_1 + R_2 = 2.5\,(R_1 + R_2) \tag{17a}$$

or in dimensionless values

$$z_0 = 2.5\,(1 + a)\,. \tag{17b}$$

On the base of the same two layer model the collection efficiency E_{teg} of turbulent electrostatic gravitational coagulation was determined. For its calculation electrostatic interaction of opposite charged drops took into account.

Calculated values of collection efficiency are listed in table 3 and figure 3. Collection efficiency values calculated by HOCKING and LANGMUIR are also given for comparison[9]).

Calculations were made at the following values of parameters: $\varrho = 1\ g \cdot cm^{-3}$; $g = 980\ cm \cdot sec^{-2}$; $\eta = 1.8 \cdot 10^{-4} P$ ($R_1 = 25$ and $20\ \mu$: $I = 23.3$ and 11.9, respectively). To calculate the mean value of the parameter $\alpha = \bar{\alpha}$, characterizing electrostatic interaction of particles the values of q_1 and q_2 charges were assumed equal to the mean value of cloud drop charges determined by [4]:

$$|q| = 10^{-4} R \quad (\text{in } CGSE) .$$

Table 3

	$R_1 = 25\ \mu$; $I = 23.3$				$R_1 = 20\ \mu$; $I = 11.9$			
a/E	E_{tg}	E_g ($z_0 = 50$)	E_g HOCKING	E_g LANGMUIR	a/E	E_{tg}	E_g ($z_0 = 50$)	E_{teg} ($\alpha = \bar{\alpha}$)
0.25	$< 10^{-3}$	$< 10^{-3}$	10^{-3}	0.05	0.45	$< 10^{-3}$	$< 10^{-4}$	0.02
0.30	0.27	0.033	0.059	0.16	0.50	0.089	$< 10^{-4}$	0.10
0.40	0.79	0.29	0.33	0.34	0.60	0.24	$\sim 10^{-4}$	0.25
0.55	1.29	0.61	0.66	0.47	0.70	0.10	$< 10^{-4}$	0.12
0.70	1.49	0.69	0.80	0.51	0.75	$< 10^{-3}$	$< 10^{-4}$	0.02
0.85	0.79	0.19	0.44	0.46				
0.88	0.26	$< 10^{-4}$	0.26	0.41				
0.90	$< 10^{-4}$			0.38				

From table 3 and figure 3 the following conclusions can be drawn:

a) Refinement of expressions for hydrodynamical forces carried out in this paper is essential at small values of $d (R < 20\ \mu)$ and it slightly changes the values of the collection officiency in comparison to these calculated by HOCKING if E_g is higher than 0.3 to 0.4.

b) The collection efficiency E_{tg} for turbulent gravitational coagulation is significantly higher than E_g. But values of critical parameters $a = R_2/R_1$ beyond the limits of which ($a > a_{max}$ and $a < a_{min}$) coagulation is impossible ($E = 0$) are not changed by turbulence. It means that critical sizes of cloud drops obtained taking turbulence into account are so that drop growth by coagulation must occur only for drops with the diameter $d > 40\ \mu$. Thus, the account of turbulent does not take off the problems which were put in the beginning of the paper.

c) Due regard for electrostatic forces does not change the situation. Electric charges mean in magnitude in fact do not effect[10]). Charges 3 to 10 times higher the

[9]) Several calculations made by us from HOCKING's formulas gave values of E_g which agree reasonably well with E_g values reported by HOCKING.

LANGMUIR's calculations are given by us as functions of and a due to the fact that the Stokes number $\kappa = I\, a^2(1 - a^2)$.

[10]) The case when a is very close to 1, demands additional consideration. But even now it is clear that it cannot change the given conclusion.

mean ones ($\alpha = 10\ \bar{\alpha}$ and $\alpha = 100\ \bar{\alpha}$) are necessary for significant increase of E to take place (E_{teg} is considerably larger than E_{tg}). However, the appearence of such charges in non-thunderstorm clouds is very unlikely[11]).

Summarizing all this the following can be said. In the considered model at the assumed boundary conditions turbulence provided approach of drops to each other at small distances with relatively high velocities.

Therefore results obtained with the help of computations based upon this model allow to conclude that turbulent diffusion even together with gravitational and electrostatic coagulation cannot provide growth with $R < 18 - 20\ \mu$ by coagulation.

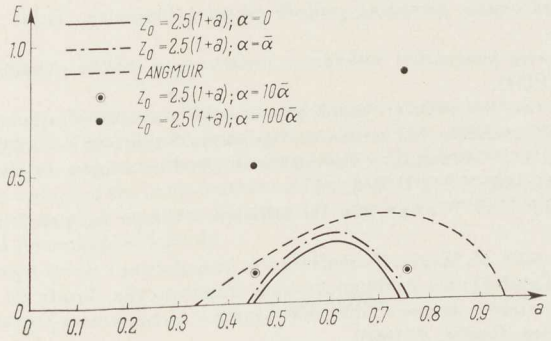

a) $R_1 = 20\ \mu$

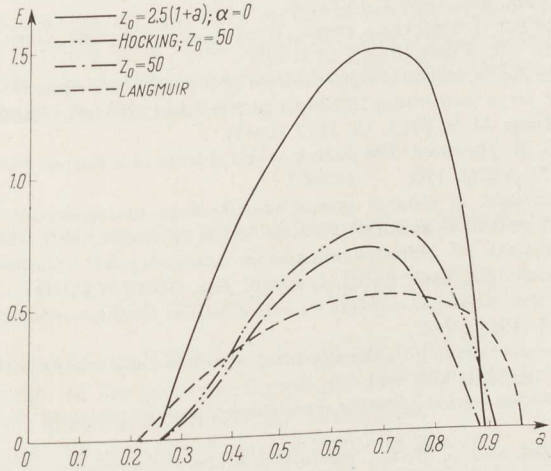

b) $R_1 = 25\ \mu$

Figure 4
Dependence of collection efficiency on the ratio a of drop radii

[11]) In thunderstorm cloud drops are so large that various kinds of coagulation and purely gravitational one among them are possible in them.

We think that formation of rather wide spectrum of cloud drops and appearance of large cloud drops (with $R > 25$ to 30 μ) are connected with condensation processes occurring under of fluctuation of main parameters: flow velocity, temperature and supersaturation. This demands special investigations.

References

[1] I. Langmuir, *The production of rain by a chain reaction in cumulus clouds of temperature above freezing*, J. Meteorol. *5*, N 5 (1948), 175.

[2] N. S. Shishkin, *Oblaka, osadky, atmosfernoie elektrichestvo*, Gostehizdat (1954).

[3] L. M. Hocking, *The theoretical collision efficiency of small drops*, Quart. J. Roy. Meteor. Soc. *85* (1959), 44.

[4] L. M. Levin, *Issledovaniie po fizike grubodispersnich aerosoley*, Izdat. Akademiia Nauk SSSR (1961).

[5] V. G. Levich, *Teoriia koagulatzii kolloidov v turbulentnom potoke*, Akademiia Nauk SSSR, Doklady *99*, N 5 (1954).

[6] V. G. Levich, *Teoriia koagulatzii i osazdeniia chastitz aerosolia v turbulentnom potoke gasa. O koeffitziente ulavlivaniia chastitz aerosolia*, Akademiia Nauk SSSR, Doklady *99*, N 6 (1954).

[7] T. W. A. East and I. S. Marshall, *Turbulence in cloud as a factor in precipitations*, Quart. J. Roy. Meteor. Soc. *86*, N 343 (1954), 26.

[8] P. G. Saffman and T. S. Turner, *On the collision of drops in turbulent clouds*, J. Fluid. Mech. *I* (1956), 16.

[9] A. I. Ivanovskii and I. P. Masin, *Turbulentnaiia koagulatziia i eie rol v protzesse ukrupneniia oblachnich kapel*, Tsentral'naia Aerologicheskaia Observatoriia, Trudy *35* (1960).

[10] Y. S. Sedunov, *Vzaimnoe dvizenie Stoksovih chastitz v turbulentnom potoke*, Akademiia Nauk SSSR, Izvestiia, Ser. Geofiz. *5* (1963).

[11] Y. S. Sedunov, *Raschet vzaimnyh skorostey Stoksovyh chastitz v turbulentnom potoke*, Akademiia Nauk SSSR, Izvestiia, Ser. Geofiz. *II* (1963).

[12] Y. S. Sedunov, *Nekotorie voprosy coagulatzii chastitz v turbulentnom potoke*, Akademiia Nauk SSSR, Izvestiia, Ser. Geofiz. *I* (1964).

[13] H. Faxen, *Gegenseitige Einwirkung zweier Kugeln, die in einer zähen Flüssigkeit fallen*, Arkiv för mat. Astr. och. Fysik *19* [A], 13 (1925).

[14] T. M. Burgers, *On the influence of concentration of a suspension upon the sedimentation velocity (in particular for a suspension of spherical particles)*, Nederl. Akademie, Van Wetenschappen, Proceedings *44*, 9, 1045, *10*, 1177 (1941).

[15] M. Stimson and G. B. Jeffery, *The motion of two spheres in a viscous fluid*, Proc. Roy. Soc., London [A], *V*, *III* (1926), 110.

[16] S. V. Pshenay-Severin, *O vliianii gidrodinamicheskogo vzaimodeyistviia malih oblachnyh kapel na skorost ih pedeniia*, Akademiia Nauk SSSR, Izvestiia, Ser. Geofiz. *8* (1957), 1045.

[17] S. V. Pshenay-Severin, *O gidrodynamicheskom vzaimodeystvii oblachnih kapel na malyh rasstoiyaniiah*, Akademiia Nauk SSSR, Izvestiia, Ser. Geofiz. *10* (1958), 1254.

[18] H. Brenner, *The slow motion of a sphere through a viscous fluid towards a plane surface*, Chem. Eng. Scien. *16*, 3/4 (1961), 242.

[19] A. D. Maude, *The movement of a sphere in front af a plane at a low Reynolds number*, British. J. of Appl. Phys. *14*, 12 (1963), 894.

[20] G. T. Kynch, *The slow motion of two or more spheres through a viscous fluid*, J. Fluid Mech. *5* (1959), 193.

[21] G. Eveson, E. Hall and S. Ward, *Interaction between two equal-sized equal-settling spheres moving through a viscous liquid*, Brit. J. Appl. Phys. *10* (January 1959), 43.

[22] L. M. Levin and Y. S. Sedunov, *O turbulentno-gravitatzionnoi koagulyatzii oblachnih kapel*, Akademiia Nauk SSSR, Doklady *164*, 3 (1965).

(Received 10th May 1966)

Measurements of the Coefficient of Combination of Small Ions with Aerosol Particles

By V. P. V. Flanagan[1])

Summary – The equilibrium small ion concentration (n) was measured in aerosols for various ionization rates (q) and particle concentrations (Z). The results agree with the formula $q = b\,Z\,n + \alpha\,n^2$. These experiments were carried out with different particle sizes and the results provided a series of values of the combination coefficient b. The size of the particles was determined by the diffusion box method and the diameter (d) ranged from 0.01 to 0.1 microns. The results fitted an empirical formula $b = 0.29\,d$.

1. Introduction

When air containing aerosol particles is ionized the small ions produced combine with the particles. The combination rate and hence the equilibrium ion concentration is a function of the concentration and size of the particles. Up to the present there have been no good experimental data on simultaneous measurements of combination coefficients and particle sizes. This paper describes some experiments on ionization equilibrium in aerosols and these experiments provided a series of values of the combination coefficient as a function of particle size.

2. Theory

The rate at which the number of small ions varies with time may be written as [1][2])

$$\frac{dn}{dt} = q - \alpha\,n^2 - \eta_0\,n\,N_0 - \eta\,n\,N\,, \tag{1}$$

where n = number of small ions of one sign per cm^3,
q = number of ion pairs produced per cm^3 per second,
α = recombination coefficient for small ions,
N_0 = number of uncharged aerosol particles per cm^3,
N = number of large ions, i.e. charged aerosol particles of one sign per cm^3,
η_0 = combination coefficient for small ions and uncharged aerosol particles,
η = combination coefficient for small ions and large ions fo opposite sign.

[1]) Cavendish Laboratory, Cambridge. Now at Berkeley Nuclear Laboratories, Berkeley, Glos., England.

[2]) Numbers in brackets refer to References, page 203.

A similar relationship may be written for large ions;

$$\frac{dN}{dt} = \eta_0 \, n \, N_0 - \eta \, n \, N \, . \tag{2}$$

In these equations the effect of multiple charging has been ignored as also has the difference between positive and negative ions. If large ion equilibrium exists i.e. $dN/dt = 0$ then:

$$\eta_0 \, N_0 = \eta \, N \, . \tag{3}$$

It is convenient to put $\eta/\eta_0 = l$ and in equilibrium $N_0/N = l$. The total concentration of particles is usually denoted by Z and $Z = N_0 + 2\,N$. In equilibrium the fraction uncharged $N_0/Z = l/(l + 2)$.

In the case of small ion equilibrium:

$$q = \alpha \, n^2 + \eta_0 \, n \, N_0 + \eta \, n \, N = \alpha \, n^2 + b \, Z \, n \, , \tag{4}$$

where

$$b = \frac{(\eta_0 \, N_0 + \eta \, N)}{Z} \, . \tag{5}$$

When Z is much larger than n an approximate form of equation (4) may be used $q = b \, Z \, n$. This is usually the case in the lower atmosphere over land areas and so there should be an inverse relationship between Z and n.

If large ion equilibrium exists then;

$$b = \frac{2 \, \eta_0 \, l}{(l + 2)} \, . \tag{6}$$

For the particle sizes usually encountered in atmospheric air, b is nearly independent of the degree of large ion equilibrium attained [2] and equation (6) can be applied even in non equilibrium conditions without serious error. However, in all the experiments described here the measurements were made under equilibrium conditions.

3. Experimental arrangements

3.1 Small ion measurements

The ions were produced in a 'Tetroon' i.e. a balloon in the shape of a tetrahedron consisting of aluminium foil bonded with plastic. A side of the Tetroon was 170 cm long and it could hold over seven hundred litres of air. The ionization rate in the balloon could be varied by placing various Co–60 sources in the vicinity. An Ebert type ion counter was used to count the positive small ions. It must be emphasised that all results refer to positive small ions only.

The ion counter was inserted through one of the faces of the Tetroon. Air was sucked through the ion tube by an electric pump and the air flow, which was monitored by a rotameter, was usually about one litre per second. With this arrangement the air was drawn from the centre of the balloon and calculations showed that any reduction in the ion count due to diffusion to the walls should be negligible. The ion current was measured by a vibrating reed electrometer and full scale deflection on the most sensitive range corresponded to an ion concentration of about two hundred ions per cm^3.

3.2 The measurement of ionization rates

The ionization rate (q) was calculated from measurements on the equilibrium ion concentration in aerosol free air by using the relationship $q = \alpha n^2$. The value of the recombination coefficient α was measured in a separate series of experiments which will be reported elsewhere. In these experiments the ionization rate in the Tetroon was suddenly altered and the variation in ion concentration with time was then observed. The recombination coefficient was determined from a relationship of the type $K - 1/n = \alpha t$ where t is the time in seconds and K is a constant for a particular

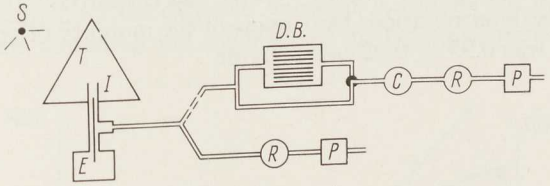

Figure 1
Diagram of apparatus
S radioactive source, T Tetroon, I small ion counter, E electrometer, DB diffusion box, C aerosol particle counter, R rotameter and P pump

experiment. The value of α is thus inversely proportional to the absolute value of n and hence the observed ionization rate ($q = \alpha n^2$) is directly proportional to the absolute value of n. As b is calculated from a relationship of the type $b = q/n\,Z$ any systematic error in the ion count would be eliminated. This is of importance as there is the possibility of some ions being turned back at the entrance to the ion counter because of charges on the apparatus. The errror in b caused by errors in ion concentration measurements was estimated to be about five per cent.

3.3 Aerosol measurements

The production and measurements of aerosols is similar to that described in a previous paper [3]. Particles were produced either by blowing filtered air over a glowing nichrome wire or by bubbling the air through water. The aerosol was then passed into the Tetroon via the small ion counter. For the aerosol measurements the small ion counter was connected to a photo electric nucleus counter [4]. The absolute accuracy of this counter is considered to be better than ten per cent. In all aerosol measurements the small ion counter was earthed even though calculations showed that the number of large ions captured would be negligible.

The diffusion box method [5] was used to measure the diffusion coefficient of the particles and the corresponding particle diameter was obtained from tables [6]. In most of the measurements the air flow through the diffusion box was adjusted so that the fraction of the aerosol penetrating the box was in the vicinity of 55%. The effects of any heterogeneity would then be minimised [7, 8]. In some experiments this was not possible but investigations of the size distributions of the aerosol showed that the resultant error would not be serious. The air flow through the diffusion box was measured by a rotameter and it varied from one to ten litres per minute.

Different particle sizes were produced by allowing the particles to coagulate and by careful selection of the initial concentrations and coagulation times any suitable size in the range could be obtained.

4. Experimental results

4.1 Mobility measurements

The mobility of the small ions was measured by the McClelland method in which the capture efficiency of the ion counter was determined for different collecting voltages. Knowing the dimensions of the ion counter and the air flow the mean mobility can be calculated. Six determinations were made of the mobility of positive small ions and the mean value was 0.93 ± 0.02 cm²/sec/volt.

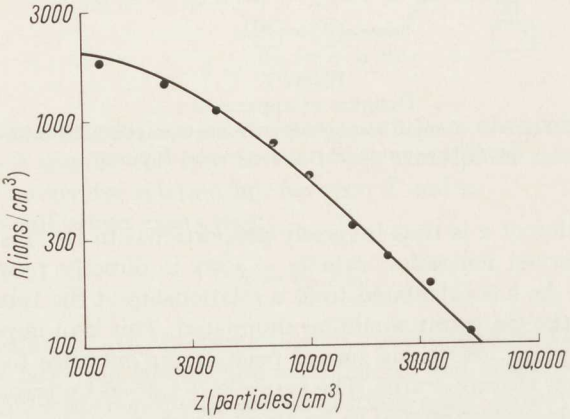

Figure 2
The relationship between small ion concentration and particle concentration. The points are the experimental results obtained on 3rd May 1964, and the curve is that calculated from equation (4)

4.2 The relationship between small ion concentration and particle concentration

In the first series of experiments the ion concentration was measured for different aerosol concentrations and the ionization rate kept constant. The Tetroon was filled with an aerosol and both Z and n were measured. Filtered air was then pumped into the Tetroon and the new values of Z and n determined. This process was continued until finally the Tetroon was aerosol free. The size of the particles was measured in the course of the run and the ionization rate determined by measuring the ion concentration in aerosol free air both before and after the run.

Figure 2 shows the result obtained from a run of this type on 3rd May 1964. The ion concentration n is plotted against particle concentration Z on a log-log scale. The curve is that calculated from the formula $q = b\,Z\,n + \alpha\,n^2$. The value of b was found by calculating $Z\,n/(q - \alpha\,n^2)$ for each point and then taking the average. On this occasion it was $2.26 \cdot 10^{-6}$ cm³/sec for a mean particle diameter of 0.070 microns. The ionization rate q was 12.6 ion pairs/cm³/sec both before and after the run. It is interest-

ing to note from figure 2 that the ion concentration is inversely proportional to particle concentration for n less than one thousand and so the approximate formula $q = b\,Z\,n$ is valid.

4.3 The variation in ion concentration with ionization rate

In another series of experiments the ionization rate was varied by placing radioactive sources near the Tetroon and the ion concentration was determined for each source. The ionization rate produced by each source had been measured in a separate series of experiments. The particle concentration and size were first measured and then n was determined for the different values of q. Finally the particle concentration and size were again measured and the mean of the two measurements assigned to that run.

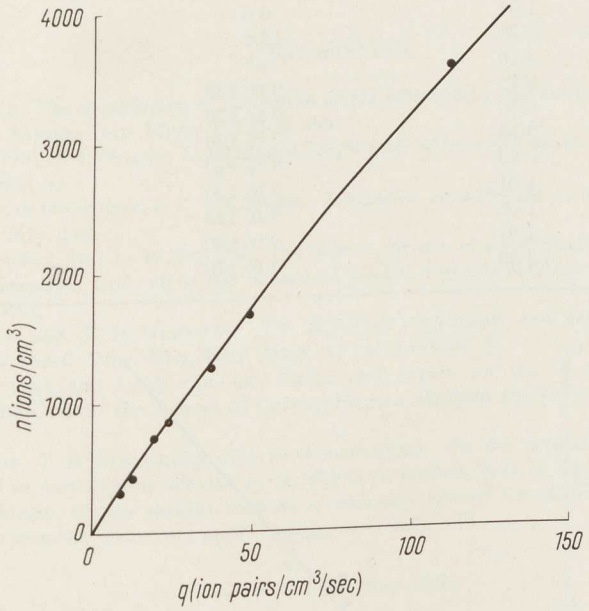

Figure 3
The variation in ion concentration with ionisation rate. The points are the experimental results obtained on 23rd April 1965, and the curve is that calculated from equation (4)

Figure 3 shows the results obtained from an experiment of this type made on the 23rd April 1965. The curve is that calculated from formula (4) and again the approximate relationship $q = b\,Z\,n$ holds for n less than one thousand. The value of b was $0.76 \cdot 10^{-6}$ cm³/sec for a mean particle diameter of 0.028 microns.

5. The combination coefficient b *as a function of particle diameter*

Table 1 summarises the results of eleven combination coefficient measurements. The values of b are given together with the mean particle diameter d. Also shown are the particle concentrations and ionization rates used in each experiment. In figure 4

these values of b are plotted against particle diameter d. The results fit an empirical line $b = A\,d$, where A is 0.287 ± 0.007 cm²/sec.

These results may be compared with the estimate of KEEFE and NOLAN [2]. They combined the results of measurements of b made on samples taken from Dublin City air with size determinations made several years later. They estimated that the value

Table 1

Summary of combination coefficient measurements

Particle Diameter (10^{-4} cm)	Combination Coefficient (10^{-6} cm³/sec)	Ionization Rate (ion pairs/cm³/sec)	Particle Concentration No/cm³
0.069	1.91	6.6	0 to 25 000
0.070	2.26	12.6	0 to 50 000
0.117	3.16	4.7	0 to 11 000
0.011	0.15	0 to 120	130 000
0.014	0.50	0 to 120	60 000
0.028	0.76	0 to 120	32 400
0.031	0.82	0 to 120	12 600
0.033	1.01	0 to 120	9 600
0.051	1 66	0 to 120	13 300
0.069	2.07	0 to 120	27 100
0.086	2.38	0 to 120	4 300

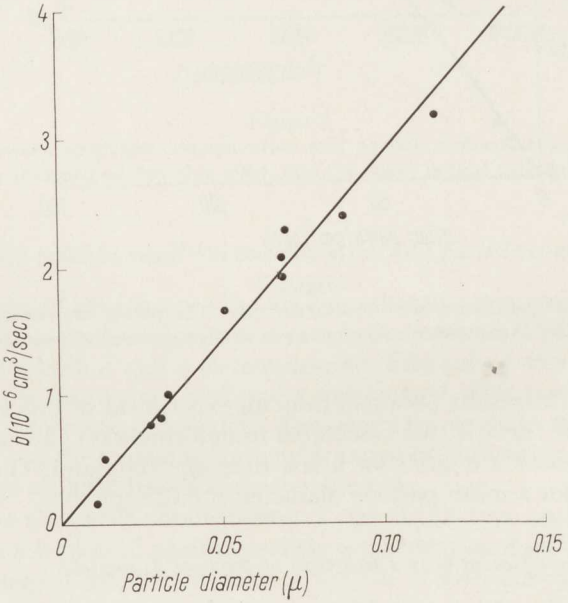

Figure 4

Graph showing the combination coefficient b as a function of particle diameter. The straight line is the empirical formula $b = A\,d$, where A is 0.29 ± 0.01 cm²/sec

of b for positive ions and Dublin atmospheric particles was of the order of $2 \cdot 10^{-6}$ cm³/sec and that the average diameter was 0.06 microns. The empirical formula given above predicts a combination coefficient of $1.7 \cdot 10^{-6}$ cm³/sec for particles of this diameter. In view of the assumptions made in arriving at this estimate the agreement is rather satisfactory.

6. *Acknowledgements*

I wish to thank Dr. T. W. WORMELL and Professor K. L. S. GUNN for their advice and encouragement during this work, the staff of the Cavendish Laboratory, Cambridge for help with the construction of apparatus, and Mr. W. J. MEGAW of AERE, Harwell for the loan of some apparatus and for helpful discussion of results. I am very grateful for financial support from the Institute for Industrial Research and Standards Dublin and the Napier Shaw Fund, University of Cambridge.

REFERENCES

[1] P. J. NOLAN, *The equilibrium of ionization in the atmosphere and the nuclear combination coefficients*, J. Atmos. Terr. Phys. *9* (1956), 295.

[2] D. KEEFE and P. J. NOLAN, *Combination coefficients of ions and nuclei*, Proc. Roy. Irish Acad. [A] *62* (1962), 43.

[3] V. P. V. FLANAGAN and T. C. O'CONNOR, *Ionization equilibrium in aerosols*, Geofis. pura e appl. *50* (1961), 148.

[4] A. L. METNIEKS and L. W. POLLAK, *Instruction for use of photo-electric condensation nucleus counters*, Geophys. Bull. *16* of the School of Cosmic Physics (Dublin Institute for Advanced Studies, 1959).

[5] J. J. NOLAN and V. H. GUERRINI, *The diffusion coefficients and velocities of fall in air of atmospheric nuclei*, Proc. Roy. Irish Acad. *43* [A 2] (1935), 5.

[6] A. L. METNIEKS and L. W. POLLAK, *Tables and graphs for use in aerosol physics*, part I, Geophys. Bull. *19* of the School of Cosmic Physics (Dublin Institute for Advanced Studies, 1961).

[7] N. A. FUCHS, I. B. STECHKINA and STAROSSELESKII, *On the determination of particle size distribution in polydisperse aerosols by the diffusion method*, Brit. J. App. Phys. *13* (1962), 280.

[8] A. L. METNIEKS, *On the various methods of deducing aerosol size distribution from diffusional decay measurements*, Pure and appl. Geoph. *61* (1965), 183.

(Received 5th May 1966)

The Inversion of Accurate Data on the Extinction Coefficient by the Transparency Method

By V. G. Bakhtiyarov[1]), Leonhard Foitzik[2]), A. Y. Perelman and K. S. Shifrin[1])

Summary – The problem of the particle distribution restoration by the dependence of the extinction coefficient computed from exact Mie formulae (when the absorption is absent) on wave length is considered. The transparency method is used. As an example the inversion of the polydisperse extinction coefficient for two models with the normal logarithmic distribution has been made. The agreement is quite satisfactory.

1. Introduction

The transparency, method developed in [1, 2, 3][3]), is based on a number of hypotheses of physical character on the properties of those particles whose spectrum is determined. One of these hypotheses consists in the fact that the refractive coefficient of particle substance m is close to unity, so that the extinction coefficient is described by the approximate formula of Van de Hulst [4]. At first sight this hypothesis is seem to be a very essential limitation of the method. It is known that the values of extinction coefficient computed from the approximate formula (4.2) differ considerably from exact values. For example, for $m = 1.50$ in the first maximum the exact value is by 36% large than that of the approximate one. It is important to make clear whether this divergence is essential from the viewpoint of the transparency method and generally for which m the inversion is possible.

The theoretical analysis of the question in general is a very complicated matter. In the present work this question is studied in a form of numerical experiment. We shall consider particles with $m = 1.50$. This value is apparently the largest of those which are discussed in literature [5] on the particles of atmospheric aerosol. Besides, for m there are detailed tables [6] of the exact values of extinction cross section $K(\varrho)$ for a great number of values ϱ

$$\varrho = 2\pi r v\,, \quad v = \lambda^{-1}\,, \tag{1.1}$$

where r is particle of radius, λ is wave length, v is wavenumber. As models we shall consider the systems with normal logarithmic particles distribution by radii. The choice of such a distribution depends on the atmospheric aerosol. It has been shown

1) Main Geophysical Observatory, Leningrad, K-18, Malaya Spasskaya 7, USSR.
2) Institut für Optik und Spektroskopie, Berlin-Adlershof, Rudower Chaussee (Germany).
3) Numbers in brackets refer to References, page 211.

in [7, 8] that this distribution (named in [7, 8] logarithmic Gaussian distribution) or a set of similar distributions describes very well new data on the structure of atmospheric aerosol [9].

2. *Initial data*

The system of spherical particles (models 1 and 2) with the normal logarithmic distribution by radii are considered. We shall call $f(r)$ the differential function and N_G the full number of particles

$$f(r) = \frac{dn}{dr} = n_{r_0} \exp\left[-A\left(\ln \frac{r}{r_0}\right)^2\right] \frac{1}{r}, \tag{2.1}$$

$$N_G = \int_0^\infty n_{r_0} \exp\left[-A\left(\ln \frac{r}{r_0}\right)^2\right] \frac{dr}{r} \simeq n_{r_0} \sqrt{\frac{\pi}{A}}. \tag{2.2}$$

For the first model $r_0 = 0.1$ μ, $A = 50$, $N_G = 500$, for the second one $r_0 = 0.25$ μ, $A = 100$, $N_G = 100$ [7]. All the values concerned with models 1 and 2 will be provided with a corresponding index below.

The initial data are: numbers of particles n_r at the radius r for intervals of Δr ($\Delta r = 0.01$ μ) and are given in tables 1 and 2 (column 1). Let us note the dependence between the values of n_r and of $f(r)$.

$$n_r = f(r)\, \Delta r \sum n_r. \tag{2.3}$$

Table 1

r μ	n_{1r} cm^{-3}	$m_1(r)$ μ^{-1}	$\tilde{m}_1(r)$ μ^{-1}	$\tilde{m}_{H_1}(r)$ μ^{-1}
	1	2	3	4
0.04	0.03	0.00	0.00	—
0.05	0.90	0.04	0.12	—
0.06	7.70	0.45	3.08	1.30
0.07	24.00	1.91	5.40	4.01
0.08	51.00	5.31	8.08	7.47
0.09	77.00	10.15	10.80	10.26
0.10	86.60	14.10	12.41	12.81
0.11	78.00	15.36	12.73	13.92
0.12	63.00	14.77	11.87	13.89
0.13	40.00	11.01	10.13	11.45
0.14	28.00	9.93	8.10	9.04
0.15	17.60	6.45	6.20	6.60
0.16	10.40	4.33	4.47	4.10
0.17	6.30	2.96	2.83	2.75
0.18	3.36	1.77	1.93	1.63
0.19	1.76	1.03	1.08	0.76
0.20	0.96	0.62	0.52	—
0.21	0.51	0.37	0.15	—
0.22	0.24	0.19	0.10	—
0.23	0.12	0.10	0.00	—
0.24	0.06	0.06	0.00	—
0.25	0.03	0.03	0.00	—

With the help of the extinction cross section $K(\varrho)$ computed in [5] we have found the polydisperse extinction coefficients (transparency) $g^*(\nu)$,

$$g^*(\nu) = \pi \sum r^2 f(r) K(\varrho) . \tag{2.4}$$

Values $g^*(\nu)$ computed from formula (2.4) are given in table 3 and illustrated by figures 2 and 3 (curve *1* corresponds to model 1, curve *2* to model 2).

The transparency method allows one to solve the indirect problem the computation of the particle distribution function by the dependence of the extinction coefficient on wavelength. When inverting it is convenient to operate with the spectrum of optical cross sections $m^*(r)$ and not with the particle spectrum $f(r)$

$$m^*(r) = \pi r^2 f(r) . \tag{2.5}$$

Table 2

$r\ \mu$	n_{2r} cm^{-3}	$m_2(r)\ \mu^{-1}$	$\tilde{m}_2(r)\ \mu^{-1}$	$\tilde{m}_{H_2}(r)\ \mu^{-1}$
	1	2	3	4
0.08	—	—	0.05	—
0.09	—	—	0.37	—
0.10	—	—	0.62	—
0.11	—	—	0.83	—
0.12	—	—	0.87	—
0.13	—	—	0.81	—
0.14	0.02	0.00	0.73	—
0.15	0.08	0.03	0.69	—
0.16	0.19	0.07	0.84	—
0.17	0.58	0.25	1.36	—
0.18	1.22	0.58	1.86	—
0.19	2.32	1.23	2.70	0.21
0.20	3.46	2.04	3.90	1.23
0.21	5.30	3.45	4.97	3.33
0.22	7.00	5.00	6.21	5.53
0.23	8.30	6.48	7.35	8.11
0.24	9.20	7.82	7.75	9.62
0.25	9.76	9.00	8.18	10.61
0.26	9.10	9.08	8.32	8.99
0.27	8.50	9.14	6.95	8.33
0.28	7.62	8.82	7.10	8.80
0.29	6.30	7.82	7.24	8.64
0.30	5.00	6.64	6.43	7.59
0.31	3.76	5.33	5.20	6.53
0.32	3.00	4.53	4.21	5.58
0.33	2.10	3.37	2.78	4.60
0.35	1.06	1.92	0.12	0.80
0.36	0.79	1.51	—	—
0.37	0.55	1.11	—	—
0.38	0.34	0.72	—	—
0.39	0.22	0.49	—	—
0.40	0.15	0.35	—	—
0.41	0.09	0.22	—	—
0.42	0.06	0.16	—	—
0.43	0.04	0.11	—	—
0.44	0.02	0.06	—	—

According to (2.3) and (2.5)

$$m^*(r) = C\, n_r\, r^2\,, \quad C = \frac{\pi}{\Delta r\, \Sigma\, n_r} = \text{const}\,. \tag{2.6}$$

We shall normalize the spectrum $m^*(r)$ with respect to area. We shall call $m(r)$ the normalized spectrum. We have

$$m(r) = \frac{m^*(r)}{\Delta r\, \Sigma\, m^*(r)} = \frac{n_r\, r^2}{\Delta r\, \Sigma\, n_r\, r^2}\,, \tag{2.7}$$

and

$$\sum m(r)\, \Delta r = 1\,. \tag{2.8}$$

Table 3

	Model 1		Model 2	
ν	$g_1^*(\nu)$	$g_{H_1}^*(\nu)$	$g_2^*(\nu)$	$g_{H_2}^*(\nu)$
0.63	0.00424	0.016	0.0556	0.108
0.72	0.00628	0.025	0.0842	0.147
0.83	0.0099	0.035	0.133	0.190
1.00	0.017	0.046	0.235	0.277
1.11	0.0233	0.056	0.303	0.334
1.25	0.033	0.072	0.387	0.433
1.33	0.0398	0.081	0.438	0.483
1.43	0.0488	0.094	0.495	0.514
1.54	0.0613	0.112	0.556	0.560
1.67	0.077	0.122	0.623	0.624
1.80	0.099	0.143	0.688	0.680
2.00	0.127	0.175	0.752	0.705
2.22	0.178	0.213	0.803	0.774
2.50	0.252	0.260	0.822	0.810
2.86	0.310	0.317	0.783	0.787
3.33	0.408	0.394	0.675	0.700
4.00	0.530	0.502	0.518	0.567
4.80	0.617	0.597	0.454	0.475
5.00	0.635	0.614	0.456	0.484
5.26	0.648	0.632	0.468	0.495
5.55	0.660	0.647	0.486	0.507
5.88	0.660	0.657	0.507	0.527
6.25	0.654	0.664	0.521	0.544
6.67	0.637	0.661	0.524	0.557
7.14	0.616	0.644	0.517	0.562
7.69	0.577	0.625	0.502	0.557
8.33	0.533	0.589	0.482	0.542
9.09	0.483	0.551	0.476	0.528
10.00	0.444	0.506	0.477	0.526
11.00	0.424*	0.468	0.473*	0.536
12.00	0.424*	0.450	0.474*	0.539
13.00	0.409*	0.443	—	0.534
14.00	0.406*	0.440	—	—
15.00	—	0.452	—	—

Extinction coefficients are given in 10^{-6} cm^{-1}, wavenumbers in μ^{-1}.
Values of extinction coefficients found with the help of extrapolation are provided with asterisk.

In tables 1 and 2 and figure 1 the normalized with respect to area spectra $m(r)$, which satisfy the equation (2.8) are given. In particular, the values of $m(r)$ obtained according to n_r (from column 1) with the help of normalization (2.7) are given in the second column of tables 1 and 2. In figure 1 these are curves *1* (model 1) and *2* (model 2).

All the further computations which are carried out by the transparency method are given accurate to the factor of proportionality (vertical scale) which is determined by the equation (2.8).

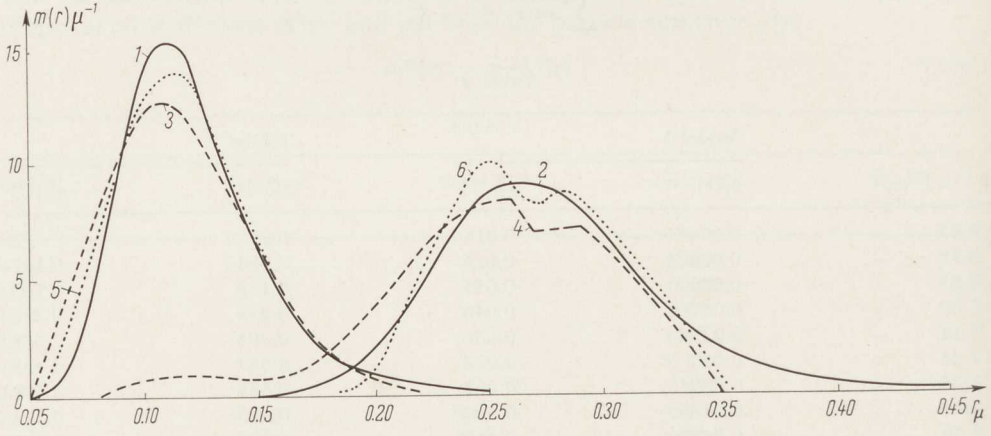

Figure 1
Particle distribution by radii
1 ≡ spectrum $m_1(r)$, *3* ≡ spectrum $\tilde{m}_1(r)$, *5* ≡ spectrum $\tilde{m}_{H_1}(r)$ (model 1)
2 ≡ spectrum $m_2(r)$, *4* ≡ spectrum $\tilde{m}_2(r)$, *6* ≡ spectrum $\tilde{m}_{H_2}(r)$ (model 2)

3. The determination of particle spectrum by the transparency method

The transparency method is developed in works [1a–e, 2]. The experimental check of the method is described in [3]. We shall recall the main results, necessary for further computations.

In the case of inversion of the tabulated information on the transparency $g^*(\nu)$ we have formula [1, 2]:

$$\tilde{m}^*(r) \sim -\left\{\frac{\tau}{n}\sum_{j=1}^{n} g\left(\frac{x_j}{2}\right)\omega(a\,x_j) + c_0\,\tau\,\omega_0(a\,\tau) + c_2\,\frac{\omega_2(a\,\tau)}{\tau}\right\}, \tag{3.1}$$

where $\tilde{m}^*(r)$ is the approximation to the exact spectrum $m^*(r)$ (determined by the transparency method). The sign $\sim$ denotes: accurate to the constant positive factor.

We have introduced the following symbols:

$$\left.\begin{aligned} \omega(y) &= y\sin y + \cos y - 1\,, \quad \omega_0(y) = \cos y - 2\,\frac{\sin y}{y} + 1\,, \\ \omega_2(y) &= \cos y - 1\,, \end{aligned}\right\} \tag{3.2}$$

$$r = a\,r_0\,, \quad x = 4\,\pi(m-1)\,\nu\,r_0\,, \quad x_j = (j-0.5)\,\frac{\tau}{n}\,, \quad g\left(\frac{x}{2}\right) = r_0\,g^*(\nu)\,, \tag{3.3}$$

where r_0 is the linear scale of the problem, m is the refractive index. Values τ and r_0 are connected by the relation

$$\tau = 4\,\pi(m-1)\,\tau^*\,r_0 \tag{3.4}$$

where τ^* is the wavenumber which satisfies the main requirement of the method: interval $(0, \tau^*)$ contains all the clear extrema of transparency $g^*(\nu)$, function $g^*(\nu)$ chainging more slowly at $\nu > \tau^*$ than at $\nu < \tau^*$ (usually $g^*(\nu)$ monotonically decreases at $\nu > \tau^*$)[4]).

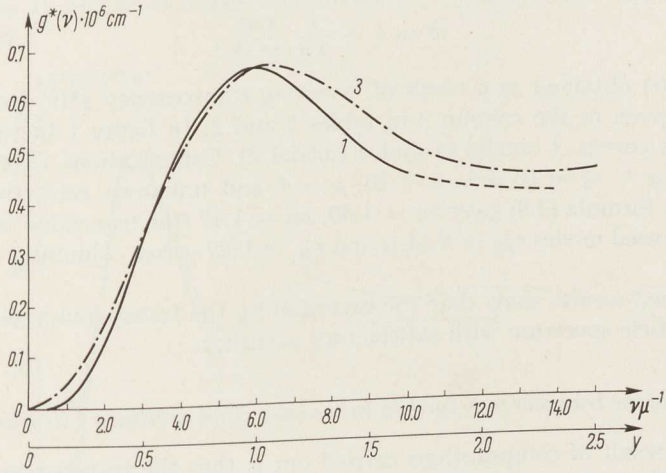

Figure 2
Extinction coefficients (model 1)
$1 \equiv$ transparency $g_1^*(\nu)$, $3 \equiv$ transparency $g_{H_1}^*(\nu)$

It results in the following: the information on the transparency in interval $(0, \tau^*)$ should secure the reliable estimation of value c_0

$$c_0 \lim_{x\to\infty} g\left(\frac{x}{2}\right). \tag{3.5}$$

Value c_2 is determined from the equation

$$\kappa\, c_0 + c_2 \sum_{i=1}^{\kappa} \frac{1}{x_i^2} = \sum_{i=1}^{\kappa} g\left(\frac{x_i}{2}\right), \quad x_i > \tau\,. \tag{3.6}$$

Integral values n and κ must be taken as large as possible. However, practically it is quite enough to take $n \simeq 20$ and $\kappa \simeq 3$.

The transparency method allows one to compute the particle spectrum when the refractive index m is known [1e]. But in this case the spectrum $m^*(r)$ is computed accurate to a horizontal scale [5]) as it is impossible to determine r_0. One could find the value of r_0 if the supplemental information on the disperse system is known. So, if we

[4]) In particular, if $g^*(\nu)$ has the only maximum $\nu = \nu_M$, it is necessary $\tau^* \gtrsim 2\,\nu_M$.

[5]) The vertical scale is arbitrary and after the calculation of the spectrum $m^*(r)$ it is determined by the equation (2.8).

know some characteristic value of r^* (for example, mode r_m) of spectrum $m^*(r)$ which is determined, then

$$r_0 = \frac{r^*}{a^*}, \tag{3.7}$$

where a^* is the corresponding characteristic value for the dimensionless function, which is placed in the right part of the equation (3.1). Let us note that value a^* is determined directly by the data on transparency.

Further on by r^* one can estimate the refractive index m,

$$m = 1 + \frac{1}{4\pi} \frac{\tau a^*}{\tau^* r^*}. \tag{3.8}$$

Spectra $\tilde{m}(r)$ obtained as a result of inverting transparency $g^*(\nu)$ from (2.4) (see table 3), are given in the column 3 of tables 1 and 2. In figure 1 these spectra are represented as curves *3* (model 1) and *4* (model 2). Computations were carried out with $\tau_1^* = 12\ \mu^{-1}$, $\tau_2^* = 10\ \mu^{-1}$, $n = 20$, $\kappa = 4$ and unknown refractive index m. Calculation by formula (3.8) gave $m_1 = 1.48$, $m_2 = 1.47$ (the true value of $m = 1.50$). Here we have used modes $r_{M_1} = 0.11\ \mu$ and $r_{M_2} = 0.27\ \mu$ (see columns 2 of the tables 1 and 2).

The obtained results show that the inversion by the transparency method determines the particle spectrum with satisfactory accuracy.

4. Utilization of the transparency method in the case of an arbitrary extinction coefficient

The main result of computations carried out is that the transparency method is quite applicable to $m = 1.50$. We shall understand better the reason of this, if we compare the results of computations of the direct problem, made with the help of tables for exact extinction cross sections $K(\varrho)$ [formula (2.4)] with computations made with the help of approximate formula

$$g_H^*(\nu) = \pi \sum r^2 f(r)\, K_H(\varrho), \tag{4.1}$$

where the extinction cross section $K_H(\varrho)$ is given by Van de Hulst formula

$$\frac{1}{2} K_H(\varrho) = 1 - \frac{\sin 2\delta}{\delta} + \frac{1 - \cos 2\delta}{2\delta^2}, \quad \delta = \varrho(m - 1). \tag{4.2}$$

The results of computations $g_H^*(\nu)$ are given in table 3 and illustrated by figures 2 and 3 (curve *3* corresponds to the first model, curve *4* to the second). The vertical scale is chosen in such a way that the ordinates of the first maximum for exact and approximate curves [$g^*(\nu)$ and $g_H^*(\nu)$ respectively] are equal.

The similarity of curves *1* and *3* and curves *2* and *4* shows that the use of Van de Hulst kernel in the transparency method instead of the exact kernel found from Mie formula for $m = 1.50$, is quite possible. It is explained by the fact that the forms of curves $g^*(\nu)$ and $g_H^*(\nu)$ (when absorption is absent) are similar, and the difference of vertical scales are not essential for the transparency method.

Spectra $\tilde{m}_H(r)$ obtained as a result of inverting transparency $g_H^*(\nu)$ from (4.1) (see table 3) are given in columns *4* of the tables 1 and 2. In figure 1 these spectra are shown as curves *5* (model 1) and *6* (model 2).

Computations were made with $\tau = 8$, $r_0 = 0.1\ \mu$, $n = 20$, $c_2 = 0$.

As it was to be expected spectra *5* and *6* approximate better the exact spectra *1* and *2* than spectra *3* and *4*. However, this more accurate definition has not changed essentially the result. It is of great importance that spectra *3* and *4* restore quite satisfactorily the exact size distribution. All this confirms the correctness of the transparency method utilization for particles with $m \leq 1.50$. Consequently, the transparency method can be used for atmospheric aerosol.

Let us add to the above that the computations made have shown that one can use the computation scheme developed earlier for the inversion of normal logarithmic distributions. In all the examples considered in [1] the systems with Γ-distributions were studied.

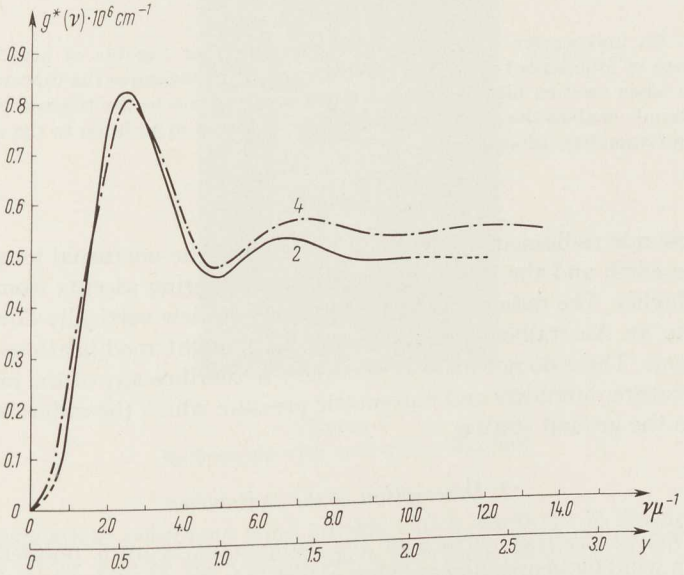

Figure 3
Extinction coefficients (model 2)
$2 \equiv$ tarnsparency $g_2^*(\nu)$, $4 \equiv$ transparency $g_{H_2}^*(\nu)$

References

[1] K. S. Shifrin and A. Y. Perelman, Optics and spectroscopy,
a) *15*, N 4 (1963); b) *15*, N 5 (1963); c) *15*, N 6 (1963); d) *16*, N 1 (1964); e) *20*, N 1 (1966).
[2] K. S. Shifrin and A. Y. Perelman, Pageoph *58* (1964/II).
[3] K. S. Shifrin, A. Y. Perelman and V. G. Bachtiarov, Optics and spectroscopy *20*, N 4 (1966).
[4] H. G. van de Hulst, *Light scattering by small particles* (New York-London 1957).
[5] F. Volz, *Optik des Dunstes*, Hdb. d. Geophysik *8* (Berlin 1956), 822.
[6] R. H. Giese, E. de Bary, K. Bullrich and C. D. Vinneman, *Tabellen der Streufunktionen und des Streuquerschnittes*, Abh. Dt. Akad. Wiss. Berlin *6* (1961).
[7] L. Foitzik, Gerlands Beiträge zur Geophysik *73*, N 3 (1965).
[8] L. Foitzik, G. Hebermehl and D. Spänkuch, Optik *23* (1966), 268.
[9] R. W. Fenn, Beitr. Phys. Atmosphäre *37* (1964), 69.

(Received 2nd May 1966)

A Radiosonde Radiometer

By J. P. Funk[1]), E. L. Deacon[2]) and B. G. Collins[2])

Summary – An inexpensive and simple form of radiometer capable of attachment to the American Bureau of Standards type radiosonde is described: it measures the upward flux of long-wave radiation when used on night ascents. A slight modification to the telemetry circuit of the standard radiosonde enables the radiation signals to be obtained in addition to the usual pressure, temperature and humidity information.

1. General

The radiosonde radiometer is designed to measure the nocturnal long-wave emission from the earth and the intervening atmosphere during ascents from the surface to 50 mb or higher. The radiometer has a 180° field of view vertically downwards and is attached to an Australian type radiosonde with slight modifications to the telemetering circuit. These do not make it necessary to sacrifice any of the measurements of air temperature, humidity and barometric pressure which the radiosonde normally telemeters to the ground station.

2. Description of the radiometer

The blackened receiver surface of the radiometer bears a temperature sensor shielded from wind by hemispheres of thin polythene, the whole being mounted on the bottom of the Australian radiosonde. The sensor used is a Philips miniature thermistor type B8 320 OP/15K. This has a resistance/temperature characteristic similar to that of the air temperature measuring thermistor of the radiosonde and hence is compatible with the existing telemetering circuits. The polythene wind shields are about 0.05 mm thick and have a transmissivity for long wave radiation which in the present application can be taken to be about 86% [1, 2][3]). The 14% of radiation not passed consists of about 5% absorbed by the polythene and 9% reflected at its surfaces. The radiosonde with radiometer attached is shown in figure 1.

3. Construction

The thermistors are initially aged with a small amount of d.c. for three or four weeks to ensure a stable resistance/temperature relationship. The small size (about

---

[1]) Deceased.

[2]) Division of Meteorological Physics, CSIRO, Station Street, Aspendale S. 13, Victoria, Australia.

[3]) Numbers in brackets refer to References, page 219.

0.05 mm diameter) facilitates mounting inside the polythene hemispheres, and this is carried out as follows: the thermistor is attached to the surface of a disc of black polythene by a spot of adhesive, and it is then covered by a disc of blackened tissue paper 2.5 cm in diameter which acts as the receiving surface for incoming radiation. The paint used was Parson's black. A similar sized disc of very thin aluminium foil is stuck to the back of the black polythene to minimise radiant heat loss from the thermistor in the upward direction.

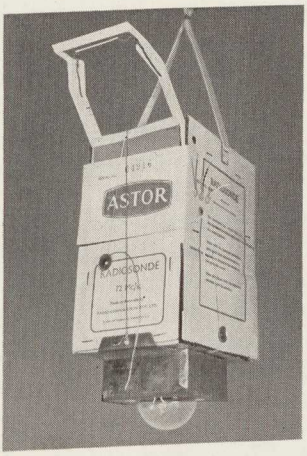

Figure 1
Radiosonde with radiometer attached

The hemispherical polythene wind shields which are 6 cm in diameter are heat sealed on to either side of the central black polythene diaphragm with cardboard stiffening rings on the outside. On the upper side a double polythene shield is used to prevent the formation of convection currents which would increase the rate of cooling of the thermistor (this point will be discussed in more detail in a subsequent section). A fine hypodermic needle is sealed between the edges of the upper and lower polythene shields and later withdrawn leaving a hole which provides a leak to relieve the internal pressure as the balloon ascends. The hypodermic needle also serves as an inlet for purging the hemispheres with dry nitrogen before release. This prevents condensation occurring on the inside of the polythene shields when the sonde rises into the cold layers of the atmosphere.

4. Telemetery

The Australian radiosonde is patterned on the American Bureau of Standards sonde. This has a transmitter which radiates a radio frequency carrier modulated by an audio signal, the frequency of which is determined by the resistance of the measuring elements. Normally two of these are used (temperature and humidity) and the change from one to the other is effected at known values of the atmospheric pressure by a barometric switch operated by an aneroid capsule. Also high and low reference signals

are provided and these are brought into circuit by the barometric switch in a similar way. The operation of this switch gives a record of pressure and hence altitude.

To obtain readings from the radiometer an extra channel is required. This is obtained by dispensing with the high reference signal and modifying the circuit to bring the radiometer in its place. The high reference serves normally to provide indentification in the switching sequence, and the radiation signal is equally satisfactory for this purpose. One miniature relay is the only additional component required to do this. A diagram of the transmitter circuit is given in figure 2. The changes required are:

a) Terminal 3 to be disconnected from junction of *R2* and *R3* and connected via coil of relay 2 to $+ A$.

b) Moving contact of relay 1 disconnected from earth and connected to break contact of relay 2.

c) Make contact of relay 2 to be connected to radiometer thermistor, the other lead to which is connected to the common lead to the temperature and humidity resistors.

d) Moving contact of relay 2 earthed.

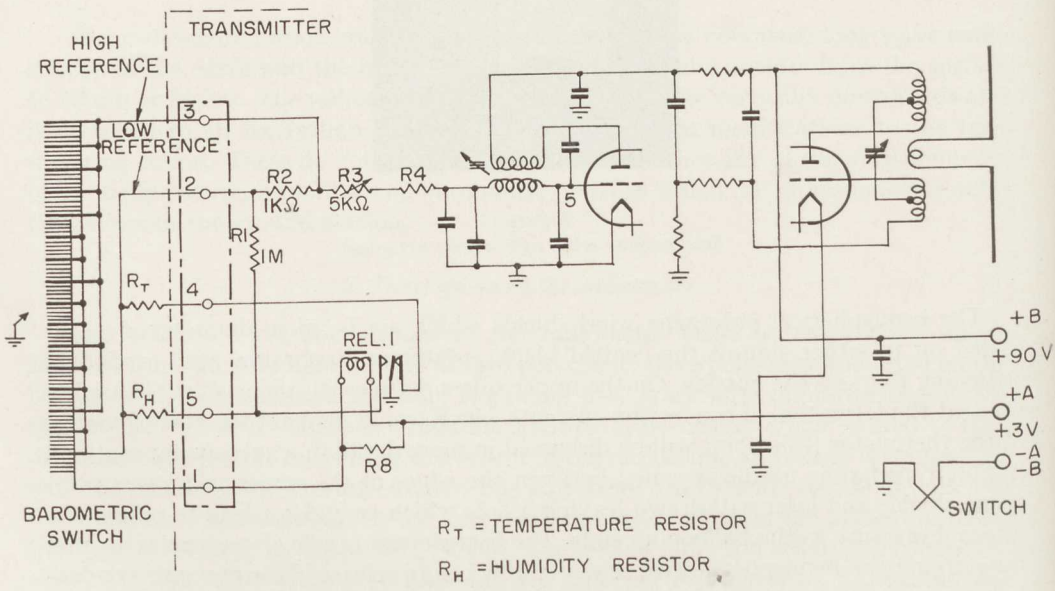

Figure 2
Radiosonde circuit

5. *Theory*

The following notation will be used:

T_D = temperature of receiver surface, deg. K,
T_A = air temperature,
a_1 = absorptivity of black receiver surface,
a_2 = absorptivity of bright aluminium upper surface,

r = reflectivity of polythene film,
k = thermal conductivity of air at a temperature T_{DA} intermediate between T_D and T_A,
l = effective thickness of air layer in radiometer hemispheres,
b = heat conduction along thermistor leads, per deg. C,
σ = Stefan-Boltzmann constant (5.67×10^{-9} milliwatt cm^{-2} deg^{-4}),
λ = heat capacity per unit area of receiver.

In writing the heat balance for the receiver the small absorption of radiation by the polythene hemisphere will be neglected and the polythene assumed to be at air temperature. The balance equation is then approximately:

$$\left.\begin{aligned} a_1 R\uparrow(1-r) = a_1(1-r)\,\sigma\, T_D^4 + \alpha\, a_2\, \sigma(T_D^4 - T_A^4) \\ + 2\left(\frac{k}{l}\right)(T_D - T_A) + b(T_D - T_A) + \lambda\left(\frac{dT_D}{dt}\right) \end{aligned}\right\} \quad (1)$$

On the RHS the first term is the downward radiation loss by the black receiver undersurface while the second allows for radiation loss upward from the aluminium backing to the bright aluminium base plate which is assumed to be approximately at air temperature. The factor α is between 0.5 and 1 depending on the geometry. The third term expresses the heat loss by molecular conduction through the air in the hemispheres while the fourth allows for losses along the leads to the thermistor. The last term involving the heat capacity of the disc is only important when T_D varies rapidly. The value of λ for the present design is about 25 mW cm^{-2} deg^{-1} sec.

The difference of fourth powers in the second term of equation (1) can be approximated to $4\, T_{DA}^3(T_D - T_A)$ and the equation rewritten then becomes:

$$R\uparrow = \sigma\, T_D^4 + B(T_D - T_A) + f\,\lambda\left(\frac{dT_D}{dt}\right) \quad (2)$$

with

$$B = f\left\{2\left(\frac{k}{l}\right) + b + 4\,\alpha\, a_2\, \sigma\, T_{DA}^3\right\}$$

and

$$f = \{a_1(1-r)\}^{-1}\,.$$

This relationship is similar to that derived by SUOMI, STALEY and KUHN [3] for their design of balloon radiometer. The main difference is that they eliminated the need to allow for radiative heat loss from the back of the receiver by using silvered mylar films to make it negligible. With the present instrument this was not adopted on the grounds of cost.

The error involved in assuming the polythene films to be at air temperature is examined in Appendix 1.

6. Calibration

The coefficient B in equation (2) can be estimated approximately using the following values:

k = 0.26 milliwatt cm^{-2} deg^{-1} at 25 °C
= 0.21 milliwatt cm^{-2} deg^{-1} at − 50 °C
$a_1 = 0.95$; $a_2 = 0.1$; $\alpha = 0.8$; $r = 0.09$.

The effective depth of air layer in the hemisphere is somewhat less than the radius (3 cm) so 2.5 cm is assumed. The conductive heat loss along the 0.005 cm diameter copper leads to the thermistor bead is small enough to be neglected ($b = 0$). The resulting estimates are:

T_{DA} (°C)	B (mW cm^{-2} deg^{-1})
25	0.31
− 50	0.22 .

With hemispherical wind shields the calculation of B can hardly be made precise enough to eliminate the need for calibration of typical specimens. However, the radiometers should be capable of manufacture in quantity with sufficient uniformity for an average calibration established for a few samples to be applicable to a whole production run.

In the absence of convective motions of the air in the radiometer hemispheres, the value of B should be independent of air pressure as the thermal conductivity of air is constant over a wide pressure range. In pressure chamber tests of the first pattern, with single polythene hemispheres, a 30 percent decrease of B was found as the pressure was reduced from 1000 mb to 100 mb; this was using a source of radiation such as to give a rise in black disc temperature of 8 to 10 °C—a value which is quite often exceeded in practice. To make this variation acceptably small—less than 10 percent—it was found effective to fit the upper side of the radiometer, in which a destabilising temperature gradient exists, with two polythene shields, the outer one hemispherical as before and the inner less convex one half way between this and the black disc. The residual variation of B with pressure is, at least in part, due to the effect considered in Appendix 1.

For calibration the radiometer was mounted in a copper box blackened inside. Radiation from a water-jacketted black-body cavity irradiated the instrument via an aperture 2.5 cm in diameter. The arrangement is that shown in figure 1 of FUNK [4]. This calibration at 1010 mb pressure gave

$$B(25\,^{\circ}\mathrm{C}) = 0.32$$

in satisfactory agreement with the estimate above. A short-wave calibration in which it was possible to use a higher intensity of radiation gave under the same conditions a value of 0.33.

As the observed and calculated values of B agree well, the theoretical variation of B with temperature is adopted and this in the linear approximation gives:

$$B(t) = B(0\,^{\circ}\mathrm{C})\,\{1 + 0.004\,t\}$$

in which t = temperature, deg. C.

Prior to making a balloon ascent the instrument is stood in a thermometer screen to give a base line check. The temperature indicated by the radiometer thermistor should coincide with those indicated by the air temperature thermistor and the dry-bulb thermometer.

7. *Specimen results*

Two specimen ascents on clear evenings are shown in figure 3 and for one of these the details are given below for a few levels to show the relative magnitude of terms contributing to $R\uparrow$.

Table 1

31 March 1964, 20.06 to 21.30 EST

Pressure (mb)	T_A (°C)	$T_D - T_A$ (°C)	$B(T_D - T_A)$ (mW cm^{-2})	σT_D^4 (mW cm^{-2})	$R\uparrow$ (mW cm^{-2})
800	10.8	1.8	0.5	38.1	38.6
600	− 2.9	6.0	1.7	33.2	34.9
400	− 25.2	13.8	3.7	26.8	30.5
200	− 55.0	23.2	5.5	19.4	24.9
100	− 66.4	28.1	6.4	17.3	23.7
50	− 59.8	25.7	6.0	18.6	24.6

For these occasions of clear sky values of $R\uparrow$ were also estimated using ELSASSER's radiation chart [5]. On these experimental ascents humidity elements were not fitted so the humidity distributions were taken from the radiosonde ascents at Laverton

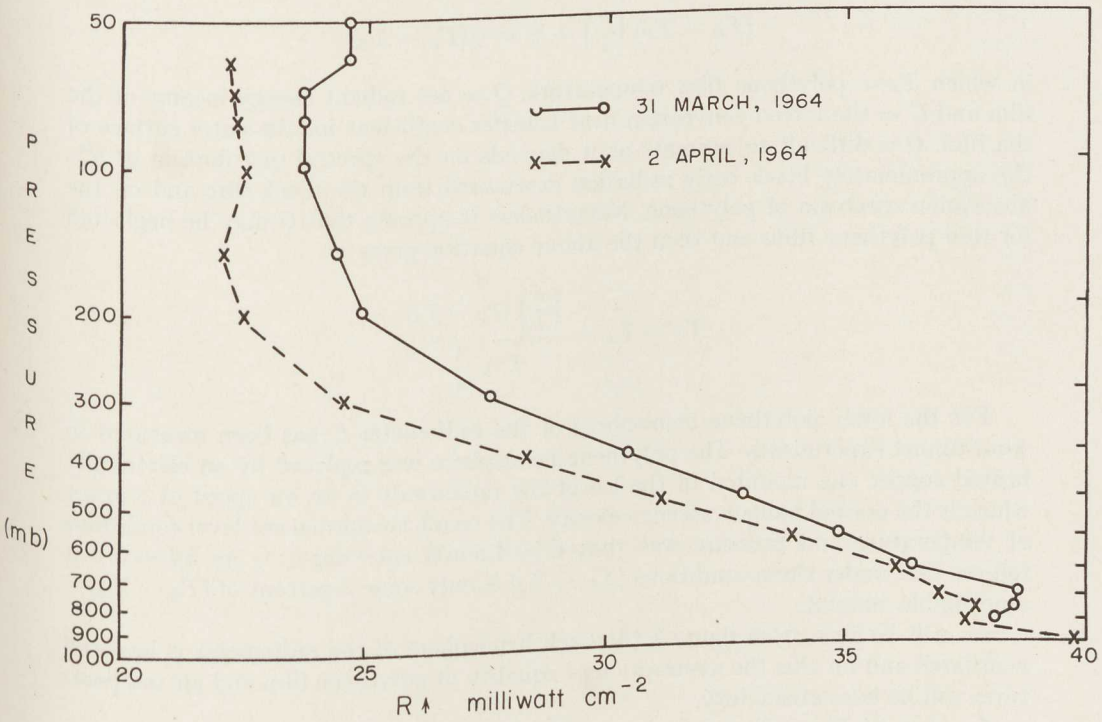

Figure 3

Specimen upward long-wave radiation soundings for two clear evenings at Aspendale, Victoria

30 km to westward. Surface temperatures were taken to be those given by the local grass-minimum thermometer. A first power pressure correction was used in calculating water paths as this is now recognised to be better than the square-root relationship originally proposed. The comparison resulting is:

Table 2

Level	Date	Observed $R\uparrow$ mW cm^{-2}	Calculated mW cm^{-2}
500 mb	31 March 1964	32.9	31.5
	2 April 1964	31.2	32
200 mb	31 March 1964	24.9	25
	2 April 1964	22.5	26

This shows satisfactory agreement at these levels as has generally been found in other such studies.

Appendix 1 – Effect of polythene film temperature

The error involved in assuming the polythene wind shield to be at air temperature can be examined as follows. The heat balance of the film is:

$$(T_D - T_P)\left(\frac{k}{l}\right) + Q = C(T_P - T_A)$$

in which T_P = polythene film temperature, Q = net radiant energy income of the film and C = the forced convection heat transfer coefficient for the outer surface of the film. Q is difficult to estimate as it depends on the spectral distribution of $R\uparrow$, the approximately black body radiation downward from the black disc and on the absorption spectrum of polythene. Nevertheless it appears that Q may be neglected for thin polythene films and then the above equation gives:

$$T_P - T_A = \frac{\left(\frac{k}{l}\right)(T_D - T_A)}{C + \frac{k}{l}}.$$

For the lower polythene hemisphere of the radiometer C has been measured in wind-tunnel experiments. The polythene hemisphere was replaced by an electrically heated copper one mounted in the lee of the radiosonde in an air speed of 5 m/sec which is the normal balloon ascent velocity. The result for normal sea level conditions of temperature and pressure was that $C = 4.5$ mW cm^{-2} deg C^{-1}. As $k/l \sim 0.1$ it follows that under these conditions $(T_P - T_A)$ is only some 2 percent of $(T_D - T_A)$ — a negligible amount.

As will be seen from figure 1 the back hemisphere of the radiometer is less well ventilated and for this the assumption of equality of polythene film and air temperatures will be less satisfactory.

In view of the radiometers having been calibrated the film temperature effect would not be of any importance were it not for the fact that it increases as the air

pressure decreases. This arises from the fact that C depends on the Reynolds number of the flow around the hemisphere and therefore on the kinematical viscosity of the air which is inversely proportional to pressure. To minimise the dependence of the coefficient B upon pressure it is necessary to design for good ventilation of both hemispheres.

References

[1] B. G. Collins and T. G. Kyle, *The spectral variation of the sensitivity of a polythene shielded net radiometer*, Pure and Appl. Geophys. *63* (1966), 82.

[2] L. Wartena, C. L. Palland and A. Koetsier, *Some experiences on the measuring of long-wave radiation fluxes*, Archiv. Met. Geophys. Biokl. *B 14* (1966), 189.

[3] V. E. Suomi, D. O. Staley and P. M. Kuhn, *A direct measurement of infra-red radiation divergence to 160 mb*, Quart. J. Roy. Met. Soc. *84* (1958), 134.

[4] J. P. Funk, *A note on the long-wave calibration of convectively shielded net radiometers*, Archiv. Met. Geophys. Biokl. *B 11* (1961), 70.

[5] W. M. Elsasser, *Heat transfer by infra-red radiation in the atmosphere*, Harvard Met. Studies *6* (1942).

(Received 13th June 1966)

Sky Radiation, Polarization and Twilight Radiation in Greenland[1])

By Kurt Bullrich, Reiner Eiden and Wolfram Nowak[2])

Summary – A) The measurements of the spectral radiances in the solar almucantar (scattering function) and the degree of polarization of the skylight in Greenland indicate the following: 1) The air near the surface of the ice cap of Northern Greenland is very pure. 2) The sky radiance however is different from the pure molecular (Rayleigh) atmosphere, the measured scattering function does not follow Rayleigh's law. 3) On the other hand the measured scattering functions cannot be explained satisfactoryly by scattering on the aerosols which have been measured near the surface. 4) Therefore the presence of a few particles per cm^3 with radii in the range $0.10 \leq r \leq 1\mu$ in heigher atmospheric layers has to be postulated.

B) The measured twilight radiances give information on the vertical distribution of the aerosol concentration. The results show a lack of particles near the ice cap surface. The vertical increase of the particle number has a maximum at heights between 4 and 8 km. The profile above these heights is the same as in mid-latitudes.

1. Introduction and scope of problem

Some basic investigations have been made during the last years in the field of atmospheric optical radiation transmission and scattering as well as of sky radiation and polarization. Some interesting results were obtained with regard to the dependence of the scattered radiation on the size distribution of natural aerosols. The main reason for measurements of sky radiation and its degree of polarization in Greenland was to obtain more information on sky radiation for extremely pure atmospheres. Such conditions can only be expected in the arctic regions or in the high atmosphere. By comparing the observational results with the theoretical values it could be shown that even in Greenland the atmosphere is not completely clean, and that the natural aerosol particles even exist in regions far from the anthropogenetic and other aerosol sources. This aerosol could not be found on the surface [2][3]).

Therefore it is probably located in heights of some hundreds or thousands of meters above the ground and has to be considered as a part of a world-wide aerosol distribution.

In order to support this assumption also some twilight measurements have been carried out to get information about the aerosol distribution with hight.

---

[1]) Detailed reports are given in [1].

[2]) Meteorologisch-Geophysikalisches Institut der Johannes-Gutenberg-Universität, Mainz (Germany).

[3]) Numbers in brackets refer to References, page 242.

In June 1961 and September 1962 measurements of

a) spatial distribution of radiance of the skylight and the degree of polarization in various narrow spectral ranges and of

b) the twilight radiance in various narrow spectral ranges

have been carried out near Camp Century in North Greenland. The observations were made at a distance of 1 mile east of Camp Century, which is situated 77° 11′ N and 60° 09′ W, about 2000 meters above sea level.

In order to interpret the measured radiance it seems useful to calculate the sky radiance using MIE's theory. Hereby we had to take into account the high purity of the air i.e. the small number of aerosol-particles near the ice surface in Greenland. It is reasonable to make one of the two following assumptions about the aerosols:

1. The aerosol size distributions based on the measurements performed by R. FENN [2] in Greenland as a first rough approximation.

2. A pure molecular (Rayleigh) atmosphere i.e. neglecting the aerosol particles. In that case we can apply the results of the theoretical investigations of COULSON, DAVE, SEKERA [3] which include the multiple Rayleigh scattering within the atmosphere and the Lambert albedo.

2. Equipment

The instruments used for the daylight and twilight measurements were sturdy and simple photometers being reliable also under polar conditions. They have been described in [1, 4]. Here we want to give some comments about the absolute calibration of the photometers only.

The calibration is valid for the photometer in connection with the photomultiplier, the power supply unit (both type MAURER) and a high sensitive galvanometer. The calibration was performed and controled by a light standard. The mean value of the spectral range of this standard light source was $\lambda = 0.771\ \mu$ with a half bandwidth of $\Delta\lambda = 0.023\ \mu$. The irradiance was known and given in absolut units by the 'Physikalisch Technische Bundesanstalt'. A good linear relation between the incident radiation flux and photomultiplier current was stated by several laboratory investigations. Furthermore, the relative spectral sensitivity of the photomultiplier was measured and the influence of low temperatures on the sensitivity has been checked in a cooling box. Taking into account the transmittance of the interference filters, the field of view and the effective lens area of the photometer objective the sensitivity of the complete measuring device could given in absolut units.

3. Results of the measurements

3.1 Results of the measurements of the relative spectral sky radiance in the solar almucantar – The spectral radiance in the solar almucantar, also called scattering function is a sensitive indicator for the size distribution of the aerosol in the atmosphere. The radiance near and very far from the sun is particularly well suited for the observation of the larger particles.

Figure 1 shows the examples of measured results of the spectral scattering functions carried out in 1962. φ is the scattering angle. Figure 2 presents results obtained in 1961 and for comparison a series from Mainz, (Germany). Generally, the results show

that in Greenland the radiances do not depend as strongly on the scattering angle as in Central Europe. Particularly the forward scattering is much smaller. This indicates that the concentration of large aerosol particles over Greenland is much smaller than the concentration over the European Continent. The drop of the relative function for the blue wavelength is smaller than for the red one. In any case here the decrease is less than a power of ten. However in spite of the purity of the air near the ice surface in Greenland the decrease is much stronger than in a Rayleigh atmosphere. The difference definitely indicates the presence of aerosol particles as mentioned above.

3.2 Results of measurements of the spectral radiance in the solar almucantar in the sky in absolute units – The absolute values of the radiance in the solar almucantar in the sky (absolute scattering functions) are given in figure 3. It is to be seen that mostly the scattered light in the blue wavelength range is the highest. If the sun approaches the horizon the radiance of the shorter wavelengths decrease. In this case at small scattering angles the values are smaller than in the red wavelength range. This effect is caused by the increasing thickness of the air mass near the horizon. The

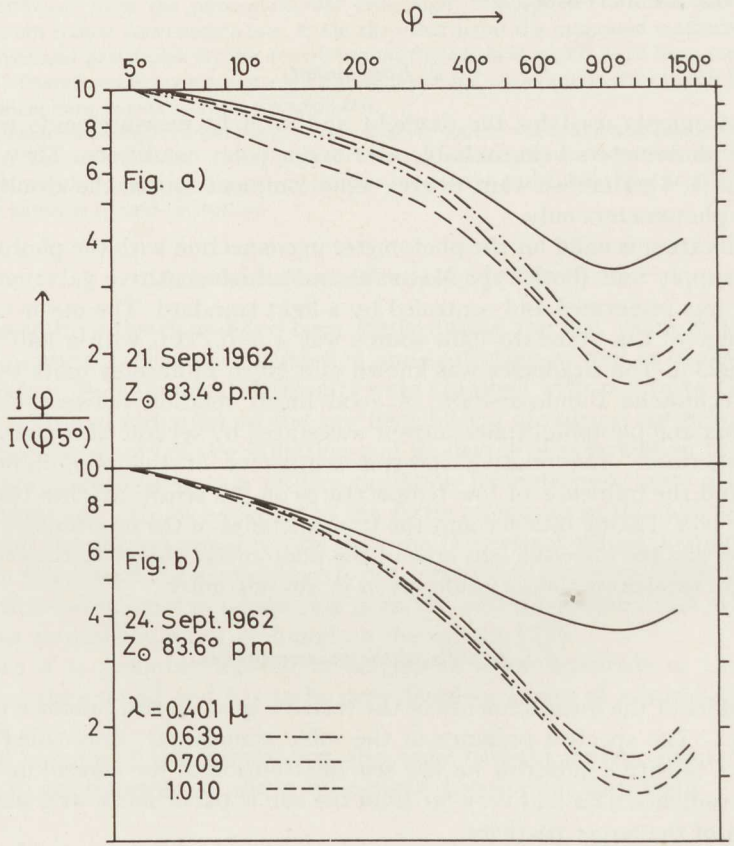

Figure 1
Spectral radiances in the solar almucantar in the sky (scattering functions) measured in Greenland 1962, relative units

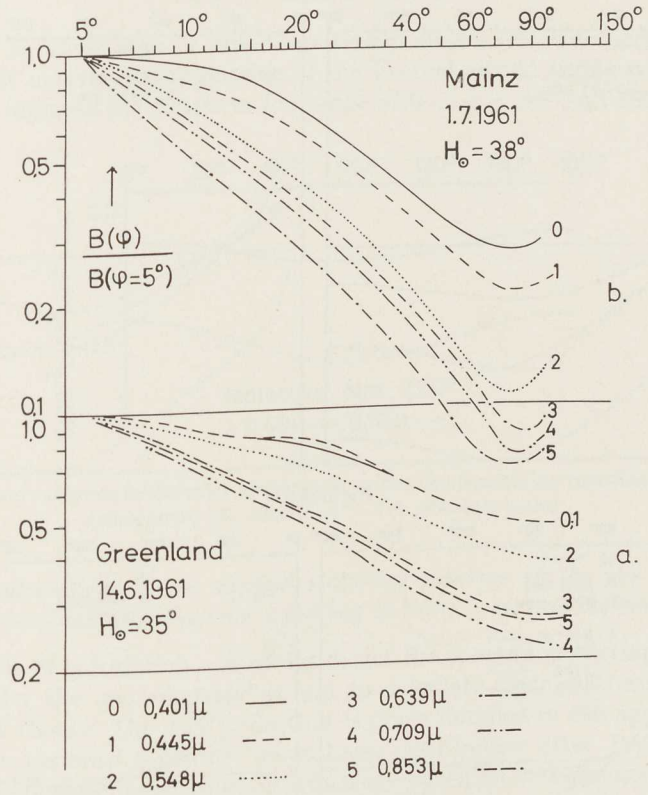

Figure 2
Same as figure 1, 1961

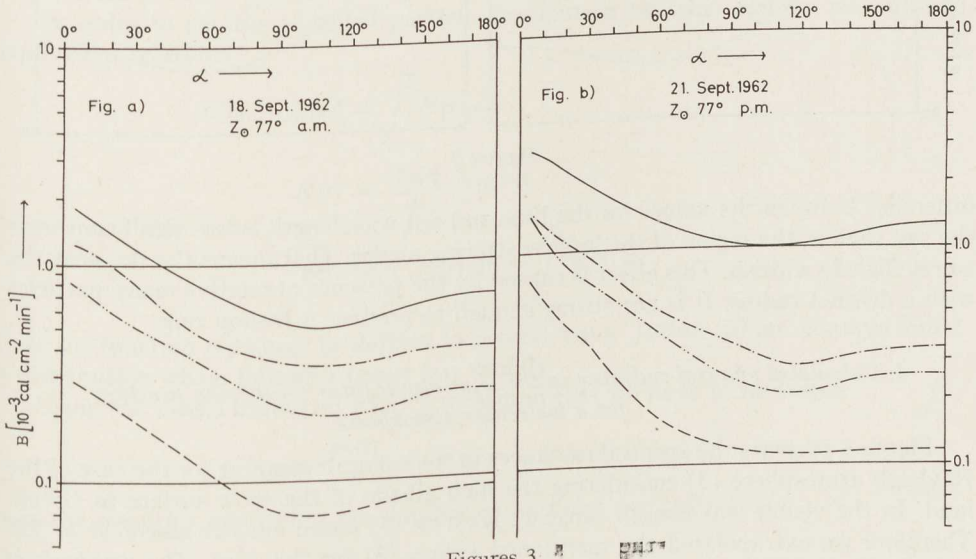

Figures 3
Same as figure 2, 1962, absolute units

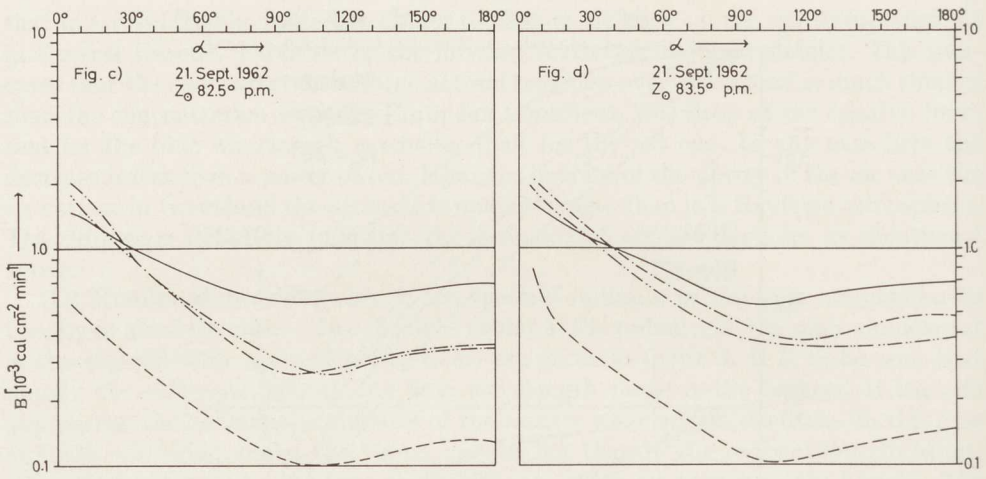

Figures 3

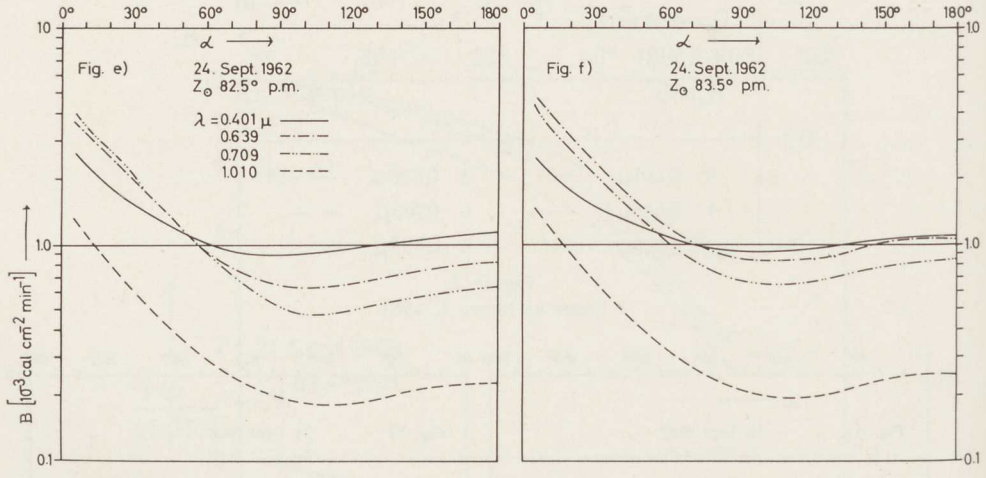

Figures 3

difference between the values for the blue and red wavelength is less significant near the sun than in the region of the large scattering angles. That means the sky near the sun is slightly whitish. This effect is caused by the presence of relative many particles with a distinct radius. It is not strong enough to produce a Bishop ring.

4. Calculated spectral radiance in the solar almucantar (scattering function) for a molecular atmosphere

Figure 4 presents the spectral radiances in the solar almucantar for the case of the Rayleigh atmosphere [3] considering the high albedo of the snow surface in Greenland. In the visible wavelength range F. KASTEN [5] found out the albedo $A = 1.0$. Therefore we extrapolated the mentioned values [3] for this case. The comparison between figures 3 and 4 shows the discrepancies between the measured and computed

data, mainly in the range of small scattering angles (foreward scattering). One reason for that may be the neglecting of the Fresnel albedo in [3] eventually. This albedo would increase the values in the range of $0 < \varphi < 30°$ and $150 < \varphi < 180°$.

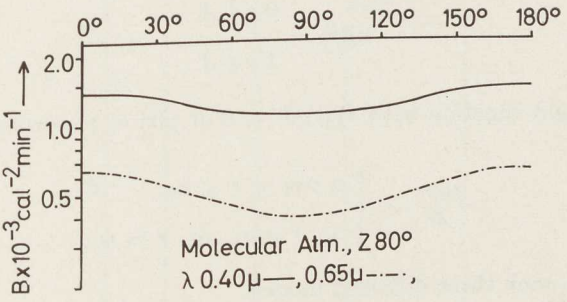

Figure 4
Calculated spectral radiance in the solar almucantar in the sky (scattering function) for a Rayleigh atmosphere [3], albedo $A = 1.0$, absolute units

5. Results of calculations of the spectral scattering function in the sky using special aerosol size distributions according to FENN*'s measurements*[4])

5.1 Principle of calculation – In order to get the spectral scattering function we have to consider the aerosol particles and to calculate their scattering properties based on MIE's theory. The way to do that is given detailed in the appendix of [4]. There has been assumed a distinct aerosol size distribution after JUNGE [6]. Here however we use models of distributions which are based on measurements performed by FENN [2] in Greenland 1961. They are a first rough approximation only.

A detailed derivation for this case is given in [1b] basing on [4].

In order to get the so-called particle distribution function $n(r)$ we use the two equivalent relations

$$n(r_2) - n(r_1) = \int_{r_1}^{r_2} N(r)\, dr$$

$$N(r) = \frac{dn(r)}{dr} \; [\mathrm{cm}^{-4}]$$

$$n(r) = \int_{0}^{r} N(r)\, dr = \int_{r_1}^{r_2} N(r)\, dr \,.$$

Now the function $N(r)$ may be defined in several ways. JUNGE [6] for example found a distribution which follows a power law usually.

Using the model basing on FENN's measurements we have to introduce

$$\frac{dn(r)}{dr} = N(r) = c_0\, \gamma\, \kappa_A(r) \,.$$

c_0 is the quantity expressing the number of particles per cm³.

[4]) Mr. B. BRAUN made the numerical calculations on the digital computer Siemens 2002 in the 'Institut für Angewandte Mathematik', Universität Mainz.

$\kappa_A(r)$ is the characteristic function of the intervall A

$$A = [r_1 , r_2]$$

and is defined as

$$\kappa_A(r) = \begin{matrix} 0 \; r \notin A \; , \\ 1 \; r \in A \; . \end{matrix}$$

$\gamma = \gamma(r)$ is a weight function with $d\gamma(r)/dr = 0$ or $\gamma(r) = \gamma = \text{const.}$

Then we get

$$\frac{dn(r)}{dr} = \begin{cases} c_0 \, \gamma \; r_1 \leq r \leq r_2 \; , \\ 0 \quad r < r_1 \quad \text{or} \quad r > r_2 \; . \end{cases}$$

Especially we took three different models

Model 1 $\qquad \gamma = 1.35 \quad A = [0.34 \, \mu \, , \quad 0.40 \, \mu]$

That is

$$\frac{dn(r)}{dr} = \begin{cases} 1.35 & 0.34 \, \mu \leq r \leq 0.40 \, \mu \\ 0 & 0.34 \, \mu > r \quad \text{or} \quad 0.40 \, \mu < r \; . \end{cases}$$

Model 2 $\qquad \gamma = 1.00 \quad A = [0.46 \, \mu \, , \quad 0.54 \, \mu]$

$$\frac{dn(r)}{dr} = \begin{matrix} 1.00 & 0.46 \, \mu \leq r \leq 0.54 \, \mu \\ 0 & 0.46 \, \mu > r \text{ or } 0.54 \, \mu < r \end{matrix}$$

Model 3 is the sum of Models 1 and 2.

Model 3

$$\frac{dn(r)}{dr} = \begin{cases} 1.35 & 0.34 \, \mu \leq r \leq 0.40 \, \mu \\ 1.00 & 0.46 \, \mu \leq r \leq 0.54 \, \mu \\ 0 & 0.34 \, \mu > r \quad \text{or} \quad 0.40 \, \mu < r < 0.46 \, \mu \quad \text{or} \quad 0.54 \, \mu < r \; . \end{cases}$$

For illustration see figure 5.

After evaluating formula for the turbidity factor T and the visual range V we obtain for the three models:

Total number of particles per cm³.

V [kms]	T	Mod. 1	Mod. 2	Mod. 3
300	1.054	1.4	1.1	1.2
250	1.096	2.5	1.9	2.1
200	1.159	4.2	3.1	3.6

The turbidity factor is defined $T = a_\lambda / a_{R\lambda}$; $a_\lambda = a_{D\lambda} + a_{R\lambda}$; $a_{D\lambda}$ extinction coefficient for an atmosphere containing aerosol particles only.

$a_{R\lambda}$ extinction coefficient for the molecular atmosphere (Rayleigh). The visual range is given by $V = 3.91/\sigma'$; $\sigma' = \sigma'_D + \sigma_R$ scattering coefficient of a unit air volume; the prime means the volume contains aerosol particles.

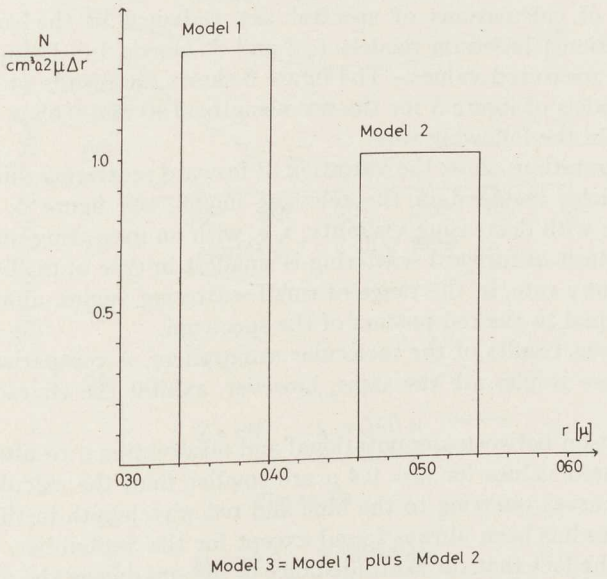

Figure 5
Aerosol size distribution models based on the measurements by FENN [2]

Finally we obtain the sky radiance and the degree of polarization for the following parameters.

1. $\lambda = 0.4, 0.45, 0.55, 0.65, 0.85, 1.00, 1.20\ \mu$.
2. Models 1 to 3.
3. $\varphi = 0°\ (1°)\ (10°)\ 180°$.
4. $Z = z = 60°, 70°, 80°$.
5. $V = 300, 250, 200$ kms.

(λ wavelength, φ scattering angle, Z zenith distance of the sun, z zenith distance of the point in the sky, V visual range).

5.2 Principle of calculation of the spectral sky radiance (scattering function considering the albedo $A = 1.0$ – Still now albedo and multiple scattering have been neglected. In order to consider the albedo $A = 1.0$ of the Greenland ice cap corrections must be applied. The number of aerosol particles have only a negligible influence on multiple scattering. Therefore it is a good approximation to use the radiance values B derived for a mere Rayleigh atmosphere and albedo. Such values have been calculated [3] for $A = 0.00$, 0.25 and 0.8. The visual albedo of the surface of Greenland is $A = 1.0$ [5]. Therefore the theoretical values [3] had to be extrapolated to $A = 1$. Increasing albedo causes an increasing of the intensities all over the sky. Calculations of $\Delta B(\lambda, \varphi, Z, z) = B(\lambda, \varphi, Z, z, A = 1.0) - B(\lambda, \varphi, Z, z, A = 0.0)$ show the remarkable fact that ΔB is independent of φ in the solar almucantar.

These ΔB values shall be characterized by the subscripts R (Rayleigh) and MS (multiple scattering). Thus the total intensities may be approximated by

$$B = B_{F+R} + \Delta B_{R+MS},$$

where F characterizes the results based on FENN's aerosol model of 5.1.

5.3 Results of calculations of spectral sky radiance in the solar almucantar (scattering functions) based on models 1, 2 and 3, albedo 1.0. Comparison between theoretical and measured values – The figure 6 shows the results of the calculations according to models of figure 5 for the wavelengths 0.40 and 0.65 μ. The results can be summarized in the following way.

All the computations show the variation of forward scattering due to the number of aerosol particles included in the relevant model, see figure 5. The intensities slightly increase with decreasing visibility, i. e. with an increasing number of aerosol particles. The effect of forward scattering is smallest in case of model 1 and greatest of model 2. At any rate, in the range of small scattering angles, almost the radiance in the blue is equal to the red portion of the spectrum.

Figure 4 shows results of the molecular atmosphere. A comparison with figure 6 proves that these results are the same, however, exhibit the characteristic forward scattering.

The comparison between computational and observational results (figure 3) show that the measured values for $\lambda = 0.4\ \mu$ are smaller than the calculated. The intersection of the curves referring to the blue and red wavelength in the range of small scattering angles has been always found except for the September, 21. The discrepancy is due to the fact that the zenithdistance of the sun during the measurement was different from that assumed for the computations. Furthermore the assumption that the reflected light is diffuse, on which the computations are based (LAMBERT's albedo) is not correct. Since the measured values are partly above and partly below the computed ones, it could be admitted that the shape as well as the values of the curves referring to the models 2 and 3 fit the measured values best. The general statement can be made that the measured curves show a steeper decrease than the computed ones.

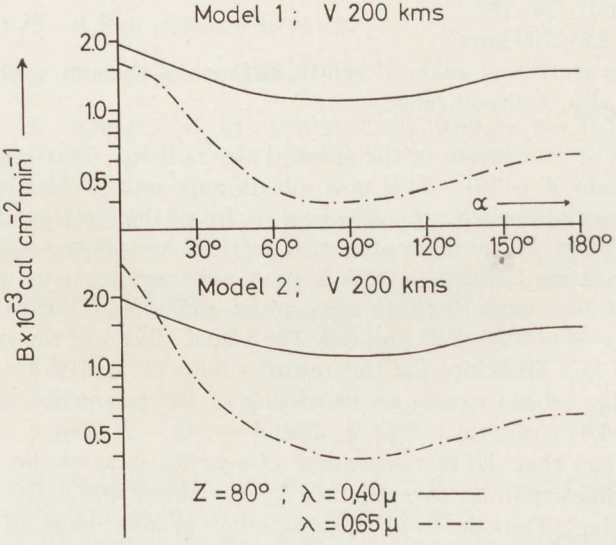

Figure 6a
Calculated spectral scattering functions in the sky using the models according to figure 5, $A = 1.0$

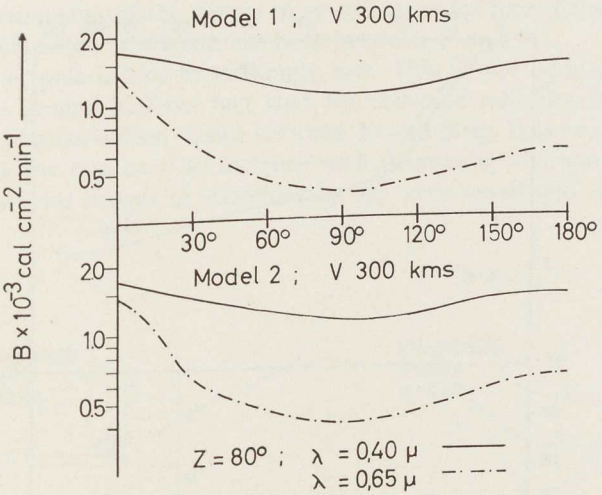

Figure 6b

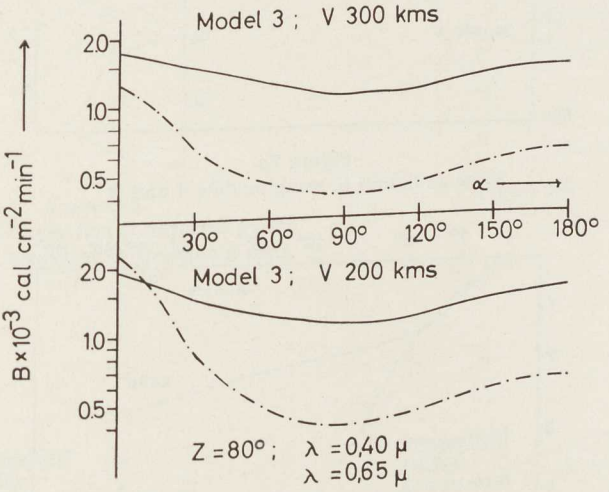

Figure 6c

5.4 Results of calculations of relative spectral sky radiance in the solar almucantar based on other models. – The interpretation of the measurements, which have been made in 1961, has been based upon a computational model similar to that described in part 4.3. A Gaussian distribution has been assumed, with a lower boundary radius $r_1 = 0.8\ \mu$, an upper boundary radius $r_2 = 1.2\ \mu$, the maximum has been related to $r_M = 1.0\ \mu$, and the half width of distribution curve being $\sigma_r = 0.2\ \mu$.

Only those models of visual range and particle number per cm³ are mentioned here which fit best the measured results. These are the model *A* with a visual range of 190 km and 1.0 particles per cm³ and the model *B* with a visual range of 253 km and 0.5 particles per cm³, see figure 7.

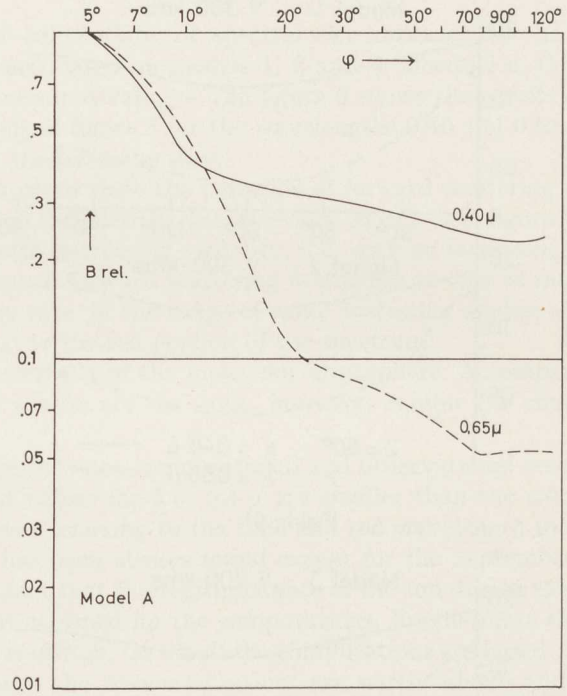

Figure 7a
Same as figures 6, using models *A* and *B*

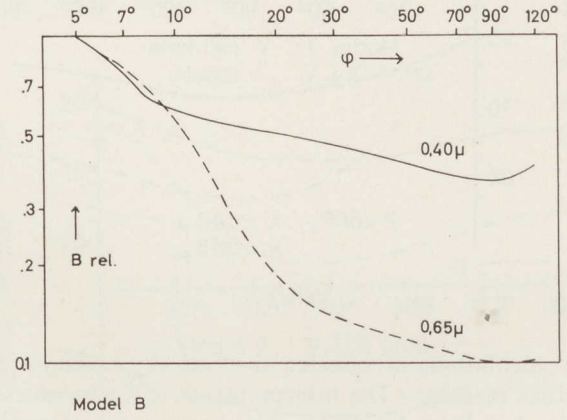

Figure 7b

6. Results of measurements of the spectral sky polarization at different points

6.1 Results from September 1962 – The degree of polarization of spectral radiation is a sensitive indicator for the turbidity and consequently for the aerosol content of the atmosphere. Therefore it arises some interest, to measure the spectral polarization as in a very clean atmosphere as over Greenland. In the figures 8 to 11 some

results of measurements of the degree of polarization for four different wavelengths are given. The elevation of the sun has been between 4° and 14°.

The degree of polarization is strikingly low. This is due mainly to the high reflectivity of the ground and the fact that the reflected radiation is nearly neutral. The maximum of polarization varies between 30 and 50%. It is remarkable that the polarization has the tendency to increase with decreasing altitude of the sun. The differences in several ranges of wavelengths are very small and do not show any tendency.

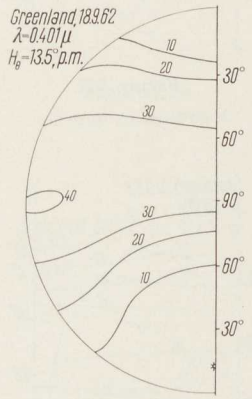

Figure 8a
Degree of polarization at different points in the sky, measured in Greenland 1962, $Z = 76° - 86°$

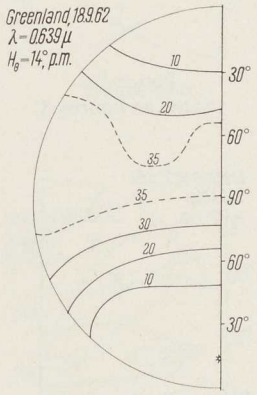

Figure 8b

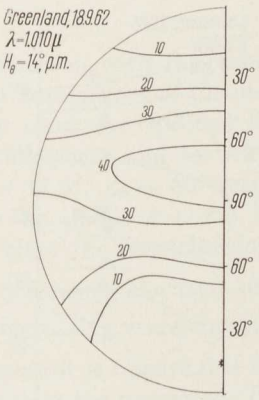

Figure 8c

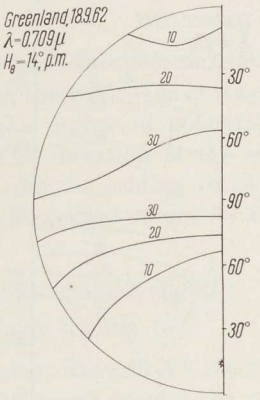

Figure 8d

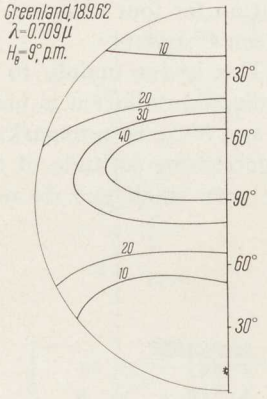

Figure 9a
Same as figures 8

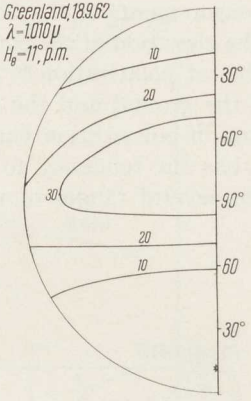

Figure 9b

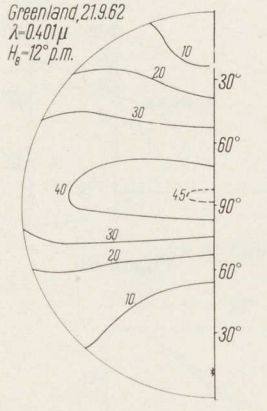

Figure 10a
Same as figures 8

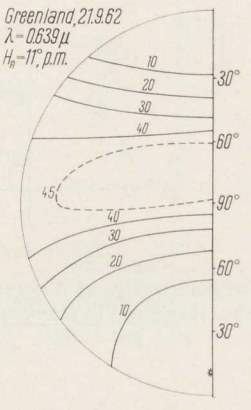

Figure 10b

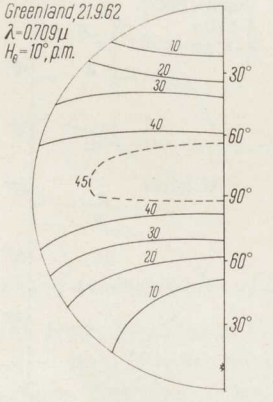

Figure 10c

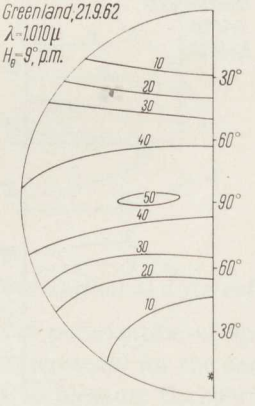

Figure 10d

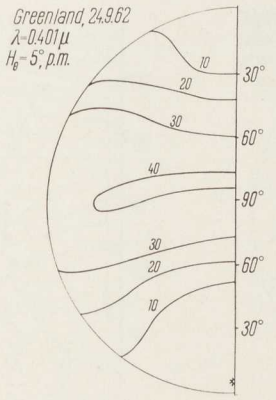

Figure 11a
Same as figures 8

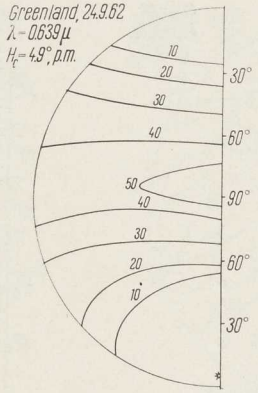

Figure 11b

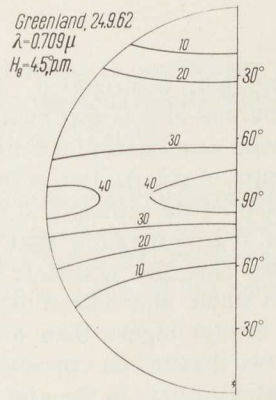

Figure 11c

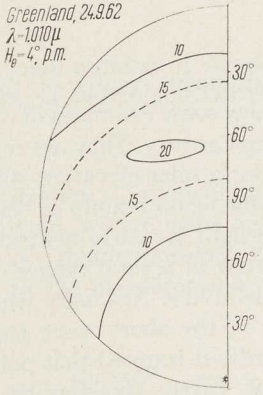

Figure 11d

6.2 Comparison with the values of the Rayleigh atmosphere – Figures 12 were prepared for comparison of the measurements with the values the at Rayleigh atmosphere. They show the spectral distribution of the degree of polarization for the Rayleigh atmosphere and for Albedo $A = 1.0$. The elevation of the sun has been chosen $H_0 = 11.5°$, $Z_0 \sim 80°$ respectively. The values according to [4] have been extended to the albedo $A = 1.0$. The mentioned theoretical values for the Rayleigh atmosphere show the two following facts:

1. With decreasing elevation of the sun the values increase slightly.
2. With increasing wavelengths the values increase slightly too.

Furthermore it is remarkable that the values after RAYLEIGH's theory are somewhat higher than the measured. The significant difference proofes the presence of a small number of aerosol particles.

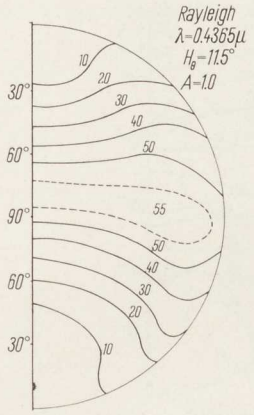

Figure 12a
Calculated degree of polarization for a Rayleigh atmosphere [3], $A = 1.0$, $Z = 80°$

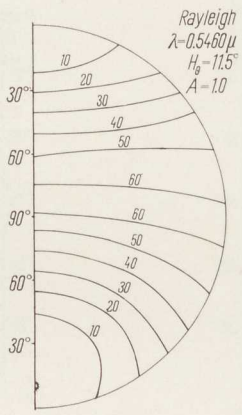

Figure 12b

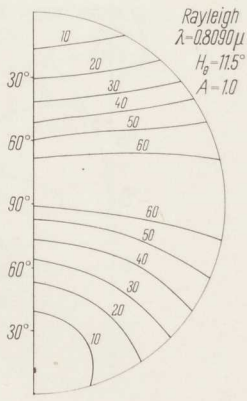

Figure 12c

6.3 Measurement results of the spectral sky light polarization, June 1961 – Figures 13 show some examples of observed distributions of polarization from June 14, 1961, in Camp Century. They are represented in polar coordinates for 3 different wave lengths and for a solar elevation 30°. Here the degree of polarization is strikingly low too. This is due again mainly to the high reflectivity of the ground and the fact that the reflected light is nearly neutral. Furthermore, it is remarkable that polarization differs but little in several ranges of wave lengths. This, also, is mainly the effect of the high reflectivity. Normally when turbidity is small, and reflectivity is low, the polarization in the short wave length range is always higher than for long wave lengths. Thirdly it is noted that polarization has two maxima on opposite sides of the sun's vertical. Partly, this may be caused by stratisfied haze in the atmosphere, and partly by multiple scattering.

The measurements of 1961 $Z \sim 60°$ and of 1962 $Z \sim 80°$ show slight increasing values with decreasing elevation of the sun. But they don't deliver the spectral slope we saw in the molecular atmosphere (6.1).

6.4 Comparison of the observations with the values of the Rayleigh atmosphere – Figure 14 was prepared for comparison of our measurements with the values of the Rayleigh atmosphere. They show the spectral distribution of the degrees of polarization for the Rayleigh atmosphere for $A = 1.0$. The solar elevations are 23.6° and 36.9°. The calculated values of [3] have been extended to the albedo of $A = 1.0$ here too. In order to compare the results of our measurements for 30° solar elevations with the theoretical values, we have to take the mean values of both figures. In doing so, it becomes obvious that the observed values are somewhat smaller than the theoretical ones of the Rayleigh atmosphere.

The maximum of the observed polarization is close to 35 per cent, the maximum of the theoretical results is about 40 per cent. The difference is not important, but

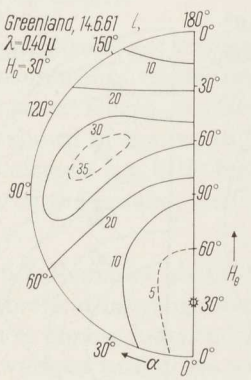

Figure 13a
Degree of polarization at different points in the sky, measured in Greenland 1961, $Z = 60°$

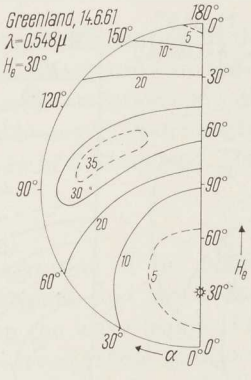

Figure 13b

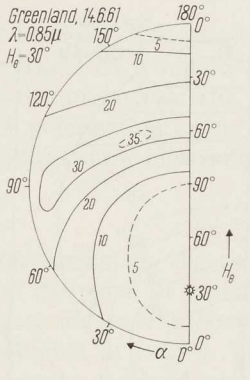

Figure 13c

significant, because it prooves the presence of a small number of aerosols, in agreement with the previous results. May be the difference can be explained by the CABANNES effect (anisotropy) partly.

6.5 Calculated distribution of the sky light polarization. – To calculate the distribution of polarization under the conditions in Greenland, we are using again the same model as described in 5.4. That means, we assume as a rough approximation some few particles with a radius of 1.0 micron according to the measurements of R. FENN.

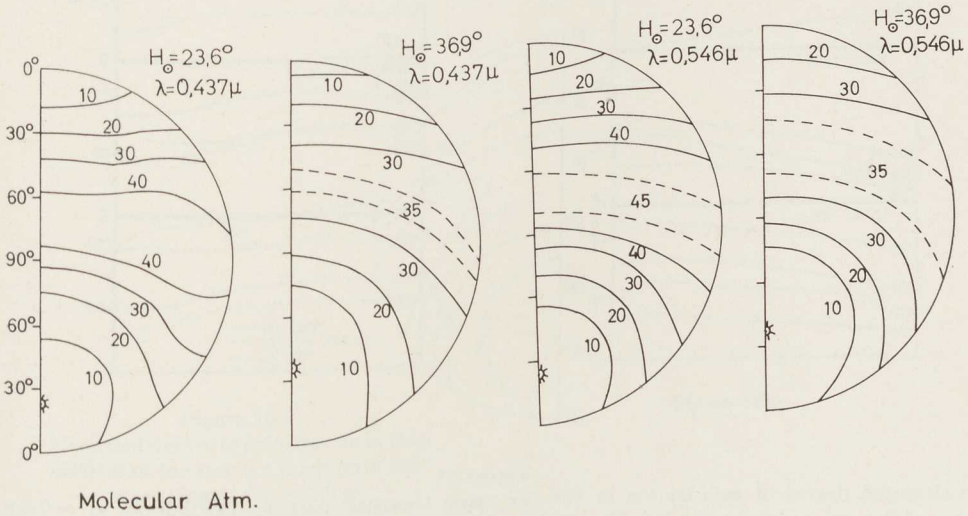

Figure 14a
Calculated degree of polarization for a Rayleigh atmosphere, $A = 1.0$, $Z = 66.4$ and 53.1°

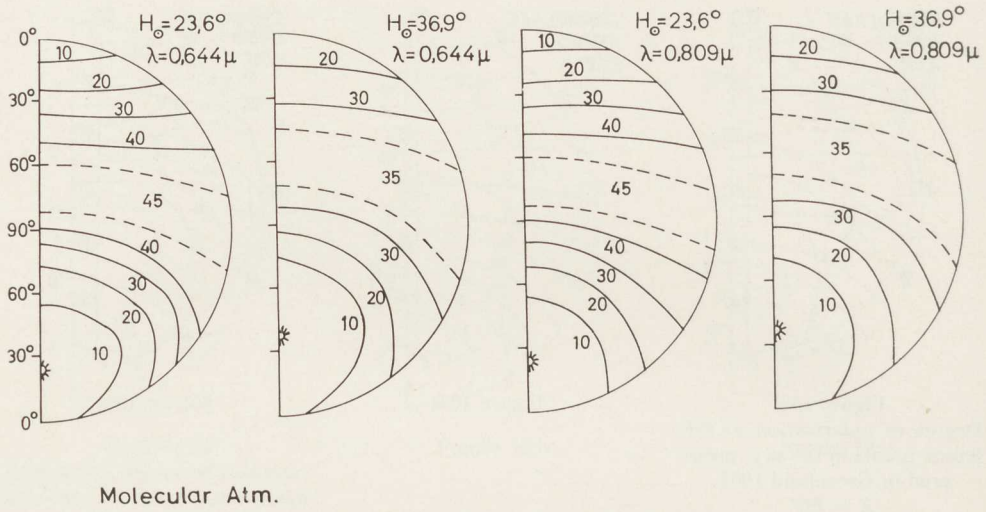

Figure 14 b

For these low aerosol concentrations it is permitted to neglect the multiple scattering.

Figure 15 shows the results of the calculations of the degrees of sky light polarization for $\lambda = 0.64\ \mu$ by using a Rayleigh atmosphere and a Gaussian particle size distribution, model A (visual range 190 kms, 1 particle per cm³). The multiple scattering for the Rayleigh atmosphere ($A = 0.8$) has been considered. Under these assumptions the degree of polarization becomes smaller than the observed values.

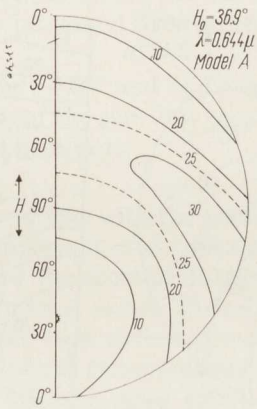

Figure 15

Calculated degree of polarization in the sky using Gaussian particle distribution: $r_1 = 0.8\ \mu$, $r_2 = 1.2\ \mu$, $r_M = 1.0\ \mu$, $\sigma = 0.2$, $V = 190$ km. 1 particle per cm³ Rayleigh multiple scattering included, $A = 1.0$

6.6 Results of measurements of polarization in the sun's vertical – The results of measurements of the degree of polarization in the sun's vertical as a function of the wave length at different solar elevations for different distances from the sun are shown in figures 16. It can be noted that sometimes the polarization in the red wavelength is a little higher than in the blue one. This is an effect of the high reflectivity of the ground, see 6.2.

6.7 Remarks about the orientation of the plane of polarization in the sky – Theoretical investigations [3, 7] show that the orientation of the plane of polarization is almost independent from the wave length. Furthermore no great differences for various turbidities were observed (these results were obtained in Italy[5]). That means the agreement with the tabulated theoretical results for the Rayleigh atmos-

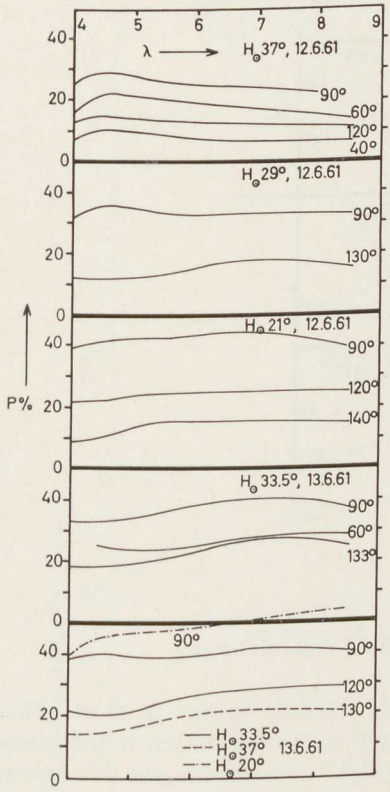

Figure 16a
Measured degree of polarization in the vertical of the sun as a function of the wave length, 0.4 – 0.9 μ

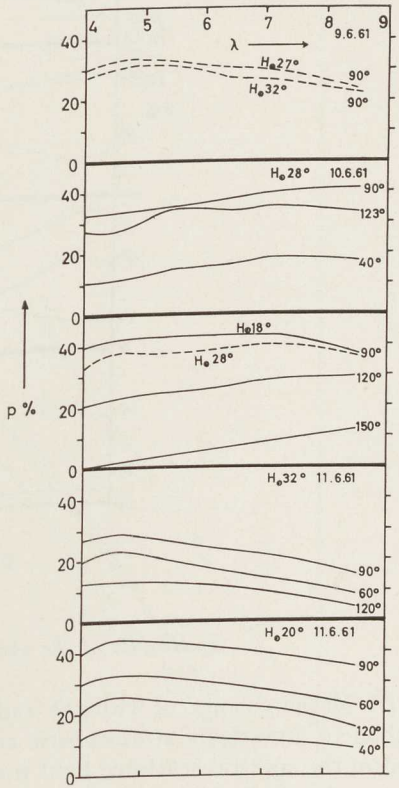

Figure 16b

[5]) K. Bullrich, E. de Bary and B. Braun (1962): Optical Radiation Transmission of the Atmosphere. Final Rep. February 1962. Contract AF (061)–52–325.

phere is relatively good. It follows that the orientation of the plane of polarization can be of great help an orientation in polar and other regions if fog covers the ground, but the blue sky radiation is yet detectable and polarized. For this case the known theoretical values can be used.

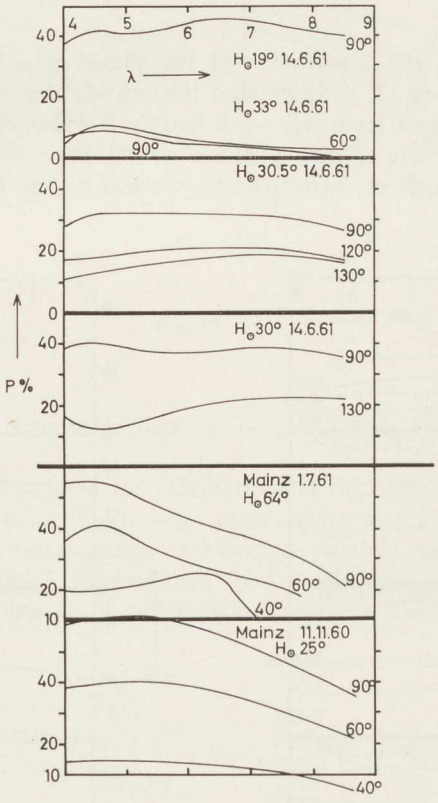

Figure 16c

7. Results of the spectral twilight measurements

7.1 Measurements of twilight radiances in absolute units – A most effective method to investigate stratospheric aerosols from a ground station is the measurement of the spectral scattered light from the twilight arch. As the sun sets below the horizon the earth shadow rises higher and the scattered light from each level of the atmosphere which depends on the number of aerosol particles and air molecules, yield some information about the aerosol distribution as function of height and the quantitative concentrations. The theory has been given detailed by VOLZ and GOODY [8]; for the conditions in Greenland see [1b].

The site of observation was also Camp Century, Greenland. The spectral radiances of the twilight were measured by a specially designed and calibrated photometer in

connection with a multiplier set (see [2]). Three series of measurements were carried out during sunset and sunrise on 26 and 27 September 1962. Some results are shown in figure 17. They are presented in Watt/cm² and refer to a band width of 23 mμ.

7.2 Turbidity profiles $\sigma'_D(\lambda)/\sigma_R(\lambda)$ – The ratio of the scattering coefficient for haze (σ'_D) of a unit volume to the molecular scattering coefficient (σ_R) in different heights is a measure for the aerosol concentration.

Using the observed data (7.1) the profiles of scattering coefficients for haze has been calculated according [8][6]). In order to calculate the turbidity profiles it was

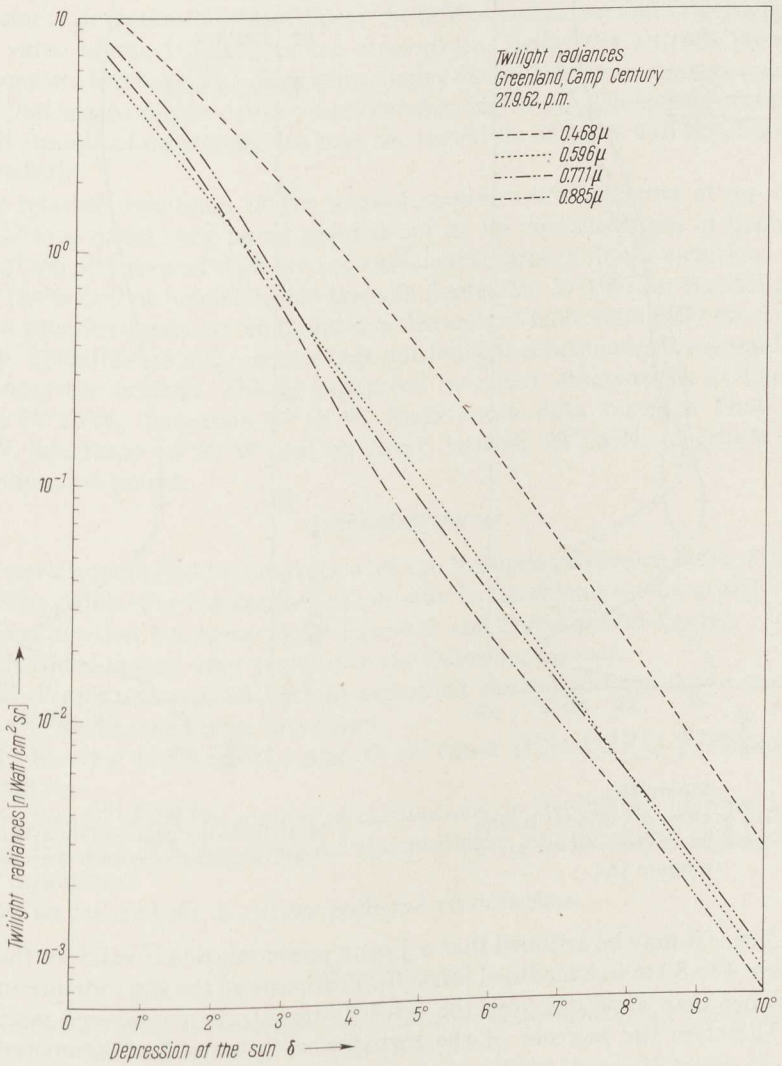

Figure 17
Measured twilight radiances, absolut units

necessary to evaluate the molecular scattering coefficient σ_R on the basis of the ICAO Standard Atmosphere.

The figure 18a shows some results for the turbidity profiles σ'_D/σ_R.

Above the ice cap the concentration increases from a very low value on the ice surface to a maximum between 4 and 8 km; from this the concentration takes the same course as the mid-latitude profile. FENN [2] found that the concentration of aerosol particles near the ground is of the order of only 1 particles per cm³ during summer and by a factor of 100 less during winter.

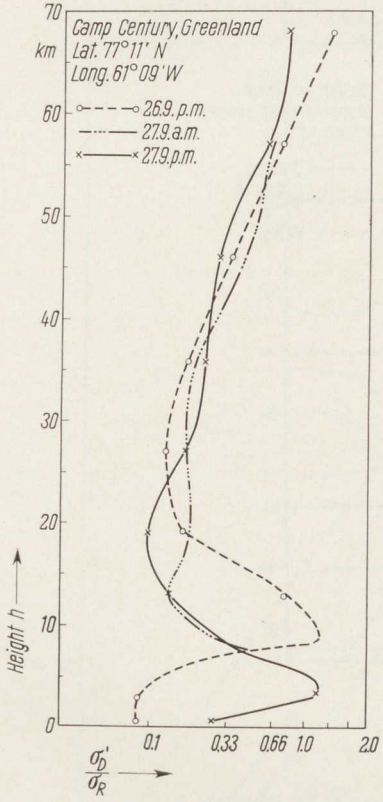

Figure 18a
Turbidity profiles $\sigma_D(\lambda)/\sigma_R(\lambda)$ basing on the twilight measurements given in figure 18a

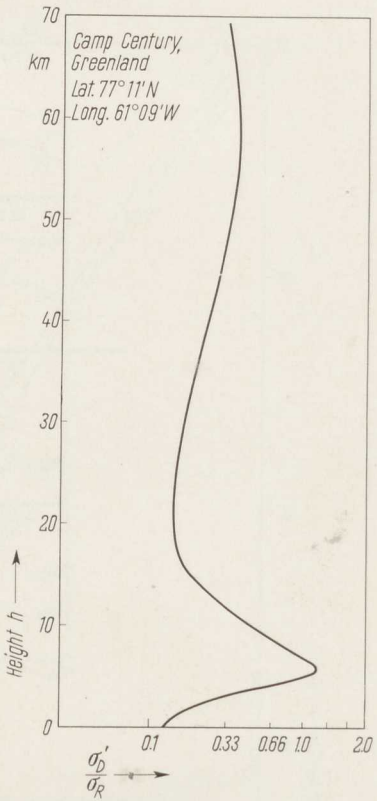

Figure 18b
Mean turbidity profile of three twilight sets of measurements in Greenland

From hence it may be assumed that a JUNGE power relation is valid for the atmosphere above 4 to 8 km in a modified form [9]. Furthermore the sky radiance in Greenland is higher than expected from the aerosol concentration measured near the ice surface. Therefore the increase of the turbidity within the first kilometers above

[6]) Dr. F. VOLZ was so kind to compute the profiles.

Greenland seems to be realistic. The lowest 8 or 10 km of the turbidity profile are obviously affected by the underlying surface, whereas above the troposphere we find the undisturbed profile caused by a world-wide intermixture.

The increase of aerosol concentration above 40 km seems to be unrealistic. Errors of measurements of such a magnitude can be excluded. The only interpretation of this phenomenon is a strong deviation from the ICAO standard atmosphere used to calculate the extinction $\sigma_R(\lambda)$. This opinion is supported by the investigations by QUIROZ [10]. His measurements of air density covering the period of 1947 to 1958 show seasonal and latitudenal variations in the mesosphere (30 to 80 km). The density deviations increase from midlatitudes to arctic regions. During the summer period they are positiv, exceeding the values of the ICAO standard atmosphere. The maximum of deviation is centered near the altitude of 65 km and can amount to 33% of the value of the ICAO standard atmosphere. Below the altitude of 30 km the deviations are less than 5%. Accepting similar deviations for the time of our measurements, that means higher density and therefore higher σ_R. The mean turbidity profile of the three sets of measurements have the curvature of figure 18b which seems to be more realistic.

The relative maximum of the aerosol concentration centered at an altitude of about 22 kms could only found pointed out at the measurements of September 27 a.m. But our few present data are not sufficient to draw a final conclusion.

For the period of September 26 through September 27 1962 on the daily weather map low pressure areas can be found in a distance of more than 1000 km from Camp Century. Therefore we may assume that our twilight measurements are uneffected by clouds near the horizon. This is supported by cloud observations at Camp Tuto, latitude 76°23′N, longitude 67°55′W. Radio sonde data taken at Thule, latitude 76°31′N, longitude 68°50′W and at Nord, latitude 81°36′N, longitude 16°40′W during the same period.

Acknowledgements

The work was funded by Contract with the European Research Office US Department of the Army. For the support of our stay in Greenland we are greatly indebted to the Organization US Army Polar Research and Development Center.

Furthermore we are very grateful to the following persons:

Dr. H. WEICKMANN (USA ERDL) organized the support and gave any help to perform the measurements in Greenland.

Dr. F. KASTEN (USA CRRL) and Dr. F. ODAR (USA CRRL) permitted to use their facilities.

Mr. B. BRAUN made the numerical calculations on the digital computer.

Dr. G. MAURER, Neuffen, prepared the multiplier and the power supply for arctic weather conditions.

Mr. K. DRÖLL and Mr. E. HIPPE built the photometers.

REFERENCES

[1a] K. BULLRICH, *Optical Transmission of the Atmosphere in Greenland.* Final Technical Report I. June 30, 1962. Contract DA-91-591-EUC-1718 (1962).

[1b] K. BULLRICH, B. BRAUN, R. EIDEN and W. NOWAK, Final Technical Report II, June 30, 1963. Contract DA-91-591-EUC-2310 (1963).

[2] R. Fenn, J. Geoph. Res. *65* (1961), 3371.
[3] K. Coulson, J. Dave and K. Sekera, *Tables related to radiation with Rayleigh scattering*, University of California Press (1960).
[4] K. Bullrich, *Advances in Geophysics 10* (1964), 99.
[5] F. Kasten, Beitr. z. Physik. d. Atm. *35* (1962), 18.
[6] Chr. Junge, Ber. d. D. W. D. *35* (1952), Bad Kissingen.
[7] E. de Bary and K. Bullrich, JOSA *54* (1964), 1413.
[8] F. Volz and R. Goody, J. Atm. Sciences *19* (1962), 385.
[9] E. de Bary and F. Rössler, J. Geoph. Res. *71* (1966), 1011.
[10] R. S. Quiroz, J. Geoph. Res. *66* (1961), 2129.
R. Giese, E. de Bary, K. Bullrich and C. Vinnemann, *Tabellen der Streufunktionen bis* $\alpha = 159$, Abh. d. Dtsch. Akademie d. Wiss., Berlin, Kl. f. Math., Physik u. Tech. Jahrg. 1961, Nr. 6 (1962).

(Received 5th April 1966)

A Remarkable Formation of Helmholtz Waves near Tropopause Level

By Dietrich Stranz[1])

Summary – A unique and very impressive wave cloud formation near tropopause level could be observed on 22 February 1966 over Southwestern Germany. This phenomenon may have been induced in a limited layer of rapid increase of wind speed by the updraught over the Schwarzwald mountains (Feldberg).

On 22nd February 1966, during the period from 14.30 until 17.00 GMT (dusk) an exceptionally persistent and impressive wave cloud formation could be observed first from Lake Constance south of Friedrichshafen and towards the end of the period from Ravensburg about 18 km northeast of Friedrichshafen.

Gravitational waves in the atmosphere occur in the boundary layer separating two air masses of different densities and with wind shear. They have been described by Helmholtz and Wien, and later A. Wegener gave an approximate formula for the wavelength λ being proportional to the square of the wind shear. A recent publication by E. R. Reiter and A. Burns describes the formation of gravitational waves in stable layers due to vertical wind shear [2].

Wave clouds of shorter wavelength at Sc or Ac level are phenomena observed relatively frequently when a marked inversion is separating two slightly different wind flows. The amplitude of the oscillation in an otherwise dry atmosphere and the lapse rate are responsible whether the movement of air appears as a visible cloud wave when reaching condensation.

A tropospheric single wave trace of 16 oscillations was described by Stranz [1] and referred to a local industrial heat source. A unique and very impressive feature occurring at tropopause level could be observed on 22nd February 1966, and will be discussed here.

1. Synoptic situation

A deep surface low was centred over the British Isles with its upper low south of Iceland and a very strong south to southwesterly flow over France and Germany at all levels. The jet stream situation was well established over the Alps with dense Cs along the presumably lifting southweaterly side and clear sky with subsidence at medium levels to the northwest. This is confirmed by the Stuttgart Temp in figure 1.

---

[1]) Dr. Dietrich Stranz, D 7980 Ravensburg, Karmeliterstrasse 63 (W-Germany).

[2]) Numbers in brackets refer to Reference, page 248.

This station was situated on the western side of the jet stream. There was subsidence between 670 and 500 mb and an almost dry-adiabatic lapse rate up to the tropopause at 280 mb at 12 Z.

Until 18 Z a considerable increase in wind speed had occurred in the tropopause region with no significant changes below and above. Thus a great wind shear was the consequence in the upper troposphere.

2. Cloud observations

Since the wave cloud first appeared at 14.30 Z fairly suddenly, it is assumed that at that time the zone of wind shear had reached the area of observation which can be

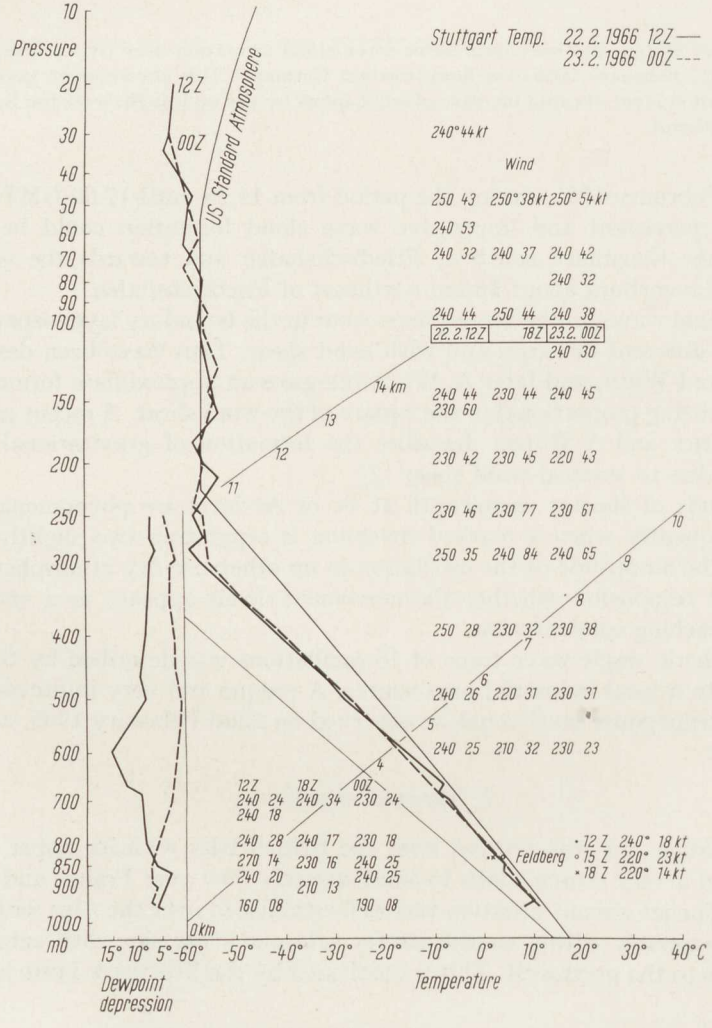

Figure 1
Stuttgart TEMPS

seen in figure 2. The distance of the wave trace was estimated to be about 90 km towards 320° from Lake Constance south of Friedrichshafen at the beginning. The wave formed at 8 to 9 km height, its wavelength was at first $\lambda = 7$ km, increasing later, and its amplitude $a = 1$ to 2 km. These dimensions were rather unusual, and so was the visibility of the wave cloud in the tropopause region which is otherwise known for 'clear air turbulence'.

Relatively high and, during the period of observation, increasing humidity in the upper troposphere can give the explanation for the visible appearance.

The wave cloud phenomenon was persevering during the whole afternoon and gradually expanding in length to 12 complete oscillations at times. This expansion happened upstream probably with the increase in moisture. Photos (figure 3) could be

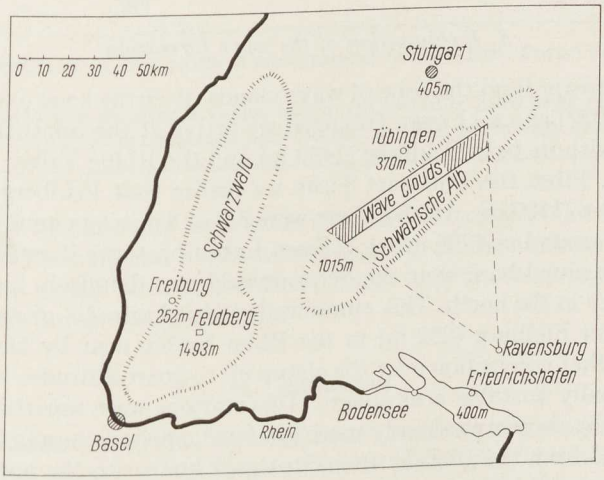

Figure 2
Area of observation

Figure 3
Wave clouds photoed at 16.55 GMT

taken from Ravensburg near sunset when the spectacularity had already declined somewhat. The wavelength had increased. The position was obviously still the same as in the afternoon and is shown in figure 2. The distance from Ravensburg was about 80 km and the range of azimuth angle from 305° to almost 360°. Two shots at 16.55 and 16.58 Z allow to estimate the speed of migration of the wave being 4 to 5 km in 3 minutes.

From the photo it is evident that the upper parts of some waves seem to be layered which could be referred to the structure of the lowest stratosphere on that day.

On top of these pronounced waves another few faint indications of condensation, however out of phase with the lower ones, may perhaps represent oscillations within the stratospheric layers around 200 mb (12 km) with an inverse wind shear just underneath. It is, however, possible too, that another wave trace had been forming closer to the observer.

3. Explanation of the wave formation

Looking upstream from the zone of wave clouds at cirrus level over the Schwäbische Alb (circa 1000 m a.s.l.) near Tübingen we arrive at the Southern Schwarzwald (Black Forest) with its peak Feldberg (1493 m) and the Rhine Valley to the west and south (figure 2). From the Stuttgart TEMP we realize that Feldberg was above the low level inversion (1300 m). At 15 Z there were 3/8 of towering cumulus with the base at 200 m above ground or 1700 m a.s.l. From Lake Constance it could well be distinguished that the cloud base over the Schwarzwald was definitely higher than along the Donau Valley in the north. This cumulus developed into 2/8 of cumulonimbus by 18 Z. The station Freiburg (252 m) in the Rhine Valley near by had $+17°$ surface temperature so that convection over the slopes up to great altitudes was well possible in the conditionally unstable atmosphere. Two stations were reporting 'past shower' at 18 Z. Obviously there was already more low level moisture supply in this area than could be inferred from the 12 Z TEMP in Stuttgart further to the northeast.

There was enough buoyancy also supported by orographic lifting of the southwesterly flow over the Feldberg area for an 'airparcel' to penetrate the second inversion near 680 mb (3000 m) and to bring a vertical movement with velocities surpassing 10 m/sec (when applying the 'parcel' method) up to the tropopause and somewhat into the lowest stratosphere. Depending on the amount of entrainment which could have been significant only through mid-tropospheric levels, the final velocities of the updraught entering the tropopause region can have reached 20 m/sec or more due to the almost dry-adiabatic lapse rate. Table 1 shows temperature differences and vertical velocities when the Stuttgart TEMP 12 Z is applied to the Freiburg surface temperature at 15 Z. No entrainment.

The pulse of updraught over the Southern Schwarzwald area had probably initiated the oscillation of the boundary layer in the tropopause region, and the wind of more than 80 kts starting at this level in the afternoon gave rise to the strong shear necessary to propagate the low frequency oscillations towards the northeast where they became visible as wave clouds due to condensation over the Schwäbische Alb (hatched area in figure 2).

The layered structure of the lowest stratosphere with a high humidity content would also allow for the explanation of the multiple wave clouds which appeared at times.—The dense cloud in the left half of the picture is due to the spreading of con-

Table 1

Height km	Pressure mb	Temperature Difference	Vertical Velocity m/s
11.5	200		< 0
10	250	+ 17 °C	25.5
9	300	+ 2 °C	27.4
7	400	− 2.5 °C	24.0
5.5	500	− 3 °C	20.0
4.2	600	− 3 °C	16.2
2.9	700	− 1 °C	14.8
1.9	800	− 2 °C	12.2
1.0	900	− 2 °C	9.2
0.3	960	− 5 °C	0

Temperature difference = Layer mean of environment temperature. Parcel temperature without entrainment.
The velocity figures mean maximum values which will certainly have to be reduced considerably from 800 mb upward due to entrainment between 800 and 500 mb of very dry environmental air.

vective clouds at medium and high levels over the Central parts of the Schwarzwald (Observations of Freiburg and Freudenstadt at 18 Z). At the moment when the photos were taken these clouds were in the shade whilst only the very high and thin cirrostratus in the northwest was still sunlit.

4. Conclusions

The rare occasion of a sudden big wind shear occurring at a moist tropopause level produced a narrow stretch of visible cloud waves presumably initiated by convection and/or orographic lifting in an atmosphere with almost dry-adiabatic lapse rate over the Schwarzwald mountains.

The extension of the oscillating clouds over the Schwäbische Alb was then more than 130 km from the source of the pulse. It lasted probably more than $2^1/_2$ hours with wavelengths between 7 and 10 km and amplitudes covering the whole upper troposphere and lowest stratosphere.

References

[1] D. Stranz, *Eine Studie über eine ausgeprägte Wellenbildung in der Atmosphäre*, Z. angew. Meteorologie *60* (1943), 359.
[2] E. R. Reiter und A. Burns, *The Structure of Clear-Air Turbulence derived from 'TOPCAT' Aircraft Measurements*, J. Atm. Sciences *23*, 2 (1966), 206.

(Received 30th April 1966)

Nuclear Technique in Tracing the Cumuli Clouds

By B. D. KYRIAZOPOULOS[1]), G. C. LIVADAS[1]) and P. N. DIMOTAKIS[2])

Summary – Within the scopes of Mount Olympus Cumulus Project (sponsored by NATO) which is currently in progress on the summit of Mount Olympus (Hellas), a new method has been applied, with non radioactive tracers, which would become radioactive afterwards by neutron irradiation at the 'Democritus' (Athens) nuclear reactor.

To this effect the solution of the tracers (various chemical compounds) was injected into the cumuli clouds by spraying it in the form of small droplets by means of an agricultural sprayer 'airblast nozzle type'. After tracing, samples of the cloud were taken by means of a filter paper connected with a high volume air sampler.

1. Introduction

The field of tracer technique in clouds research does not seem to be too rich. Although the problems of investigation of formation, motion, diffusion, identity, and other cloud characteristics demand a proper tool, no such methods of a proper elaboration are still available. As it is known, in certain cases it is not easy to judge by observation alone of the apparent motion of a cloud whether it is really a transitory motion towards a certain direction, or just an extension of the cloud mass, due to further water-vapour condensations in this same direction. Even more difficult is the investigation of the inside motions of a large cloud mass or a group of clouds.

The research works of the Mount Olympus Cumulus Project (sponsored by NATO, Grant 131, Director-Beneficiary Prof. B. D. KYRIAZOPOULOS) are being conducted at the Mount Olympus summit of Ayios Antonios ($\varphi = 40° 04'$ N, $\lambda = 22° 21'$ E, elevation 2817 m) where the installations of the alpine type meteorological station of the Institute of Meteorology of the University of Thessaloniki are located (LIVADAS [2], KYRIAZOPOULOS [4][3]).

Towards this peak, standing at a direct distance of 18.5 km from the sea, masses of cumuli clouds rise during the summer, coming either from the near-by sea-shore, or from the interior of the warm plain of Thessaly.

Within the scopes of the researches of the above mentioned Cumulus Project, we searched the possibility to elaborate a method to trace the cumulus clouds using radioisotopes. Such a method could rather have disadvantages like contamination of the atmosphere, the need of counting the samples in short time after sampling, espe-

---

[1]) Meteorological Institute, Aristotelian University, Thessaloniki.

[2]) Nuclear Chemistry Laboratory, 'Democritus' Nuclear Research Center, Athens.

[3]) Numbers in brackets refer to References, page 253.

cially for the short lived radioisotopes which are used as a rule, special precautions for the people etc. On the other hand tritium should not have the above disadvantages and in addition would be in the form of water which is the main constituent of the clouds — tritium is actually supplied in the form of tritiated water. Nevertheless the high cost of tritium and the need for special liquid scintillation apparatuses to count the samples obliged us to exclude this radioisotope.

Therefore the effort was focused in elaborating a method with non radioactive tracers which would become radioactive afterwards by neutron irradiation (W. S. LYON [3]) at the 'Democritus' nuclear reactor; that is a method similar to the one used by G. F. HAINES [1] but for different purposes.

In this work are presented the experimental results of a research in which various chemicals were used to trace the clouds and which constitue a new method in the field of cloud research. All experiments were run on the Olympus Mountain at the Ayios Antonios peak where the Meteorological Laboratory is located.

2. *Experimental*

Materials. The chemical compounds chosen were ammonium bromide NH_4Br, sodium nitrate $NaNO_3$, copper nitrate $Cu(NO_3)_2$, and magnesium nitrate $Mg(NO_3)_2$. All these were of analytical purity reagents and were used as 10% solution in water.

Method of injection. The solution of the tracer was injected into the cumuli clouds by spraying it in the form of small droplets (50 to 200 microns size) by means of an agricultural sprayer 'airblast nozzle type'.

Method of sampling. After tracing samples of the cloud were taken by means of a filter paper connected with a high volume air sampler.

Irradiation of the samples into the reactor. The fast pneumatic system of the Nuclear Chemistry Laboratory at the 'Democritus' NRC in Athens, was used to send the samples to the reactor for neutron irradiation. The irradiation time was 10 minutes and the thermal neutron flux 10^{12} n/cm^2 sec.

Radioactivity measurements. Five minutes after the neutron irradiation the samples were examined as far as their gamma-spectrum is concerned by means of a multichannel analyser connected with a $3'' \times 3''$ NaI(Tl) crystal. The analyser was a transistorized 400 channels instrument of the Intertechnique SA 40 type.

3. *Results*

The radioactivity and spectrum of neutron irradiated filter paper with and without cloud samples was found to be negligible. Nevertheless every sample was compared with this blank spectrum which was really subtracted from the spectrum of the tracer.

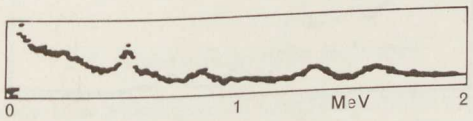

Figure 1
Gamma-rays spectrum of neutron activated filter paper

In figure 1 the gamma spectrum of neutron irradiated filter paper is shown which practically does not differ from a sample of a cloud.

In table 1 are included informations about the radioisotopes formed by neutron irradiation of the chemical tracers, the target isotopes with their neutron absorption cross section, the half-life of the radioisotopes produced and the energy of beta and gamma rays of them.

Table 1

Tracer	Target isotope	Absorption cross section in barns (10^{-24} cm)	Radio-isotopes formed	Half-life	Energy	
					β-part. MeV	γ-rays MeV
Ammonium bromide NH_4Br	Br^{79}	8.5	Br^{80}	18 m	2.04 1.42 EC	0.62 0.51
	Br^{81}	3.5	Br^{82}	35.9 h	0.465	0.554 etc.
Sodium nitrate $NaNO_3$	Na^{23}	0.54	Na^{24}	15.0 h	1.39	1.368 2.754
Copper nitrate $Cu(NO_3)_2$	Cu^{63}	4.3	Cu^{64}	12.8 h	0.571 EC	0.51
	Cu^{65}	2.1	Cu^{66}	5.1 m	2.63	—
Magnesium nitrate $Mg(NO_3)_2$	Mg^{26}	0.05	Mg^{27}	9.45 m	1.75 1.59	0.84 1.02

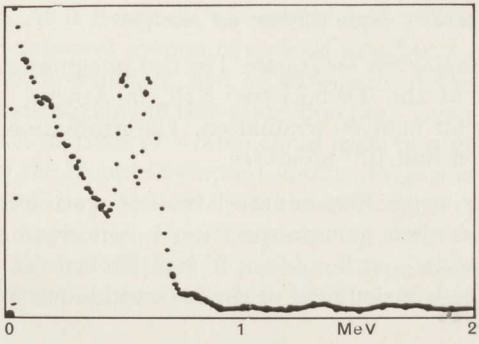

Figure 2
Gamma-rays spectrum of Br^{80} in a neutron activated sample containing as tracer NH_4Br

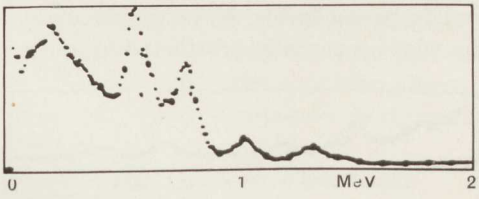

Figure 3
Gamma-rays spectrum of Br^{82} in a neutron activated sample containing as tracer NH_4Br

All tracers after neutron irradiadion showed a very characteristic gamma-ray spectrum which is different from any other one. Especially ammonium bromide is the most sensitive of all tracers used because of the formed short lived Br^{80}. Its spectrum is shown in figure 2. After the decay of Br^{80} the remaining Br^{82} which lasts longer is characterized by another spectrum (figure 3).

Sodium nitrate after neutron irradiation presented a very characteristic gamma-ray spectrum (figure 4) with a pronounced maximum at 1.37 MeV due to the decay of Na^{24}. The radioactivity of this isotope lasts for longer time because of the half-life of it which is 15 hours.

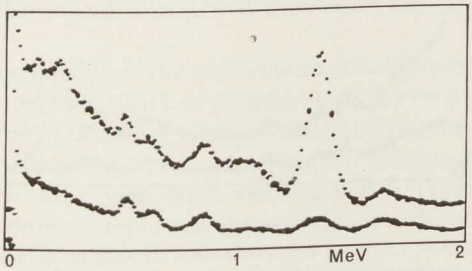

Figure 4
Gamma-rays spectrum of Na^{24} in a neutron activated sample containing as tracer $NaNO_3$ (upper curve) compared with the spectrum of a filter paper

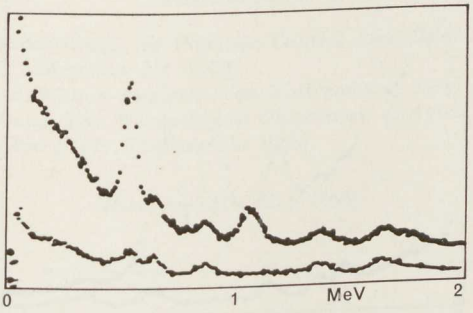

Figure 5
Gamma-rays spectrum of Cu^{64} in a neutron activated sample containing as tracer $Cu(NO_3)_2$ (upper curve) compared with the spectrum of a filter paper

Copper nitrate provided us with another useful tracer which by neutron irradiation shows another characteristic spectrum due to the formation of Cu^{64} (figure 5).

Magnesium nitrate which was also tested presented a characteristic spectrum of Mg^{27}.

In some cases where a foreign contamination of the cloud was present, this was also veryfied by a different spectrum of the neutron irradiated sample (figures 6, 7).

4. Application of the technique

In the application of this technique we sought to make experimental tracings:

1. On cumuli-form clouds, developing on the Olympus Mountain range, but coming from different areas, that is either coming from the closed warm plain of Thessaly or

from the near-by Aegean Sea. The path followed by these last mentioned, from the lowest levels up to the Ayios Antonios peak, was either through the Litohoron ravine, that is a short-cut of 18.5 km overland, or through the ravine of Xerolakki which is a somewhat longer course overland.

2. On cloud masses of different density, that is from passing patches of thin clouds to very thick ones. In one case i.e. the passing cloud was accompanied also by soft-hail. The opacity of the passing cloud mass was continuously followed and recorded by a Transmissographe TR 3, manufactured by the SAPE (Paris-France).

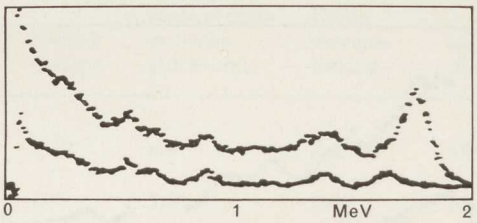

Figure 6
Gamma-rays spectrum of a foreign contamination of the sample activated by neutrons (upper curve) compared with the spectrum of a filter paper

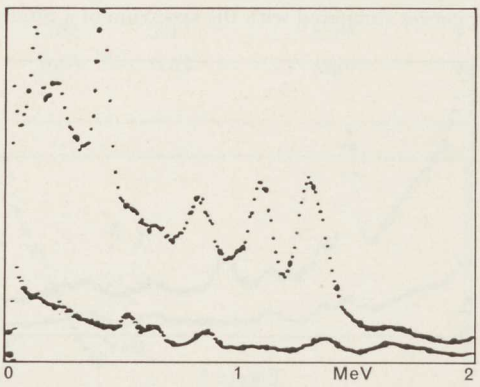

Figure 7
Gamma-rays spectrum of a foreign contamination of the sample activated by neutrons (upper curve) compared with the spectrum of a filter paper

3. The tracings were always effected on moving clouds with different velocities, from the slow-motion of 0.6 m/sec to the fast moving clouds of 24.0 m/sec. It should also be noted that the wind velocity usually changed at small intervals.

4. The distance between the point of injection of the tracer into the cloud and the sampling position, varied from 60 meters up to 1000 m.

From the elaboration of the data of the 10 tracings effectuated until now we draw the following conclusions:

In all the experimental tracings:

a) Although they were usually conducted under quite different weather conditions, in every case and in more than one filter, there has been definite evidence of the chemical reagent used as a tracer.

b) The peak of the concentration appears in the first filter of the sampler after the injection. When these injections are repeated at fixed intervals, these peaks are also succesisvely repeated. After the first peak there are still indications of the presence of tracers on the filters, but not in very high concentration.

The peaks recorded in the first filter after the injection of the tracer could be attributed to direct transport of the main mass of tracer by the wind, in a direction sensibly parallel to the ground, while the appearance of tracer from the same injection in the following filters are due to amounts of tracer left inside the cloud mass, and which arrive at the sampler with more or less delay, due to the longer trajectories they have to follow inside the cloud, because of the convective motions of cumuli-form clouds.

It can rather be concluded that the elaborated method presents certain advantages in cloud research. Through a network of samplers posted at various levels and various distances from the point of injection, and by exact timing of the time-lapse between the injection and the sampling, it is quite possible to obtain interesting data on kinetic characters of the cloud mass. Moreover this method requires low-cost material.

This paper is a preliminary report on the experimental research conducted during the summer of 1965 on this subject.

It should be noted that, as far as we know, this technique has never yet been applied in cloud research.

References

[1] George F. Haines, Proceedings, Air Pollution Control Association *50* (1957), paper No. 10.
[2] G. C. Livadas, Geofis. e Meteorol. *XI* (1963).
[3] W. S. Lyon, *Guide to Activation Analysis* (Van Nostrand Co., New York 1964).
[4] Basil D. Kyriazopoulos, *The Meteorological Observatory of Ayios Antonios Peak of Mount Olympus*, «Meteorologika» (Univ. Thessaloniki 1966).

(Received 21st May 1966)

ERRATA

The statement on the mechanism of the time marker generation made in page No. 35 and No. 39 of the paper entitled '*An Instrument for Seismic Velocity Measurements*', 1965, Vol. 62, pages 35 to 40 by Satyabrata Datta should be changed as follows:

The time marker signal at intervals of 2/3 microsecs are obtained from the output of the stable quartz crystal oscillator at a frequency of 1.5 Mc/s. The distorted sinsoids from the oscillator output through the cathode follower drive a co-axial cable (RG/58 U) of 3 meters length terminated at the other end by the capacitance (1200 Pf) of the receiving transducer. As a result the cable rings and produces time markers at intervals of 1/9th microsecs in groups of six damped oscillatory (9.0 Mc/s) cycles.

Book Reviews — Buchbesprechungen

SHEA L. VALLEY (Editor): *Handbook of Geophysics and Space Environments.* In–4°, 520 pp., with figures. McGraw-Hill Book Company, Inc., New York 1965 ($ 24.50).

This book, prepared by the Air Force Cambridge Research Laboratories, contains a comprehensive collection of geophysical data—formulas, definitions, theories, and hypotheses about the world's atmosphere, shape, gravity, and magnetic field, and the space environment—in so far as it is known or can be deduced. Whereas the usual handbooks are written for the reader with specialized knowledge of the particular subject matter of each handbook, this volume is written for the reader with some knowledge of general science or engineering who needs guidance in the discipline and language as well as data of a particular subject of specialization. The book's 22 fact-filled sections cover geodesy and gravity; model atmospheres; atmospheric temperature, density, pressure, and moisture; winds; precipitation, clouds, and aerosols; atmospheric composition; atmospheric optics; atmospheric electricity; aspects of electromagnetic wave propagation; transmission and detection of infrared radiation; the geomagnetic field; ionospheric physics; airglow and aurora; meteoritic phenomena; the sun; solar electromagnetic radiation; corpuscolar radiation; interplanetary space and the solar atmosphere; the lunar environment; planetary environments; astrophysics and astronomy; and radioastronomy. Here is comprehensive, authoritative, and unique coverage of geophysics and space environments—a book that will serve the need of the scientist, who will find the tables and figures a convenient, quick reference to data in his own field.

P. H. HURLEY (Editor): *Advances in Earth Science.* In–8°, 502 pp., with figures. M.I.T. Press, Cambridge, Mass., 1966 ($ 20.00).

The volume presents the papers of a conference held in connection with the dedication of the Cecil and Ida Green Building for the earth sciences at M.I.T. The Conference was divided into four broad groupings, i.e., the earth's environment, atmospheric motions, dynamics of the oceans, and the solid earth, and outstanding leaders in each field discussed their specialties. The publisher states that 'this is a major book on geophysics presented in a form that is understandable to the non-specialist. Yet, since theoretical treatments form the bases of this work, it should prove a valuable addition to every geophysical library of importance as well'. Effectively, this is far from a popular approach to the subject of advances in the earth sciences: it is a book by geophysicists for geophysicists, but not restricted on either and to a definite subdivisional branch of this growing multidiscipline.

WILMOT N. NESS (Editor): *Introduction to Space Science.* In–8°, 919 pp., with figures. Gordon and Breach Science Publishers, New York, 1965 ($ 10.00).

Written by the Staff of the Goddard Space Flight Center, the volume contains 23 papers on geophysics and space science, filling the need for cross-discipline communication, for communication between scientist and engineer, and for summaries useful to graduate students or to well educated technical audience that is not involved in space research. For his nature, the book is also a report on the present status of the space research program of the Goddard Space Flight Center. The topics of the chapters are the followings: The Earth's Magnetic Field; The Earth's Atmosphere; The Ionosphere; The Earth's Radiation Belt; The Aurora; Meteorology from Space; The Shape of the Earth; The Interplanetary Medium; The Boundary of the Magnetosphere; Cosmic Rays; Interplanetary Dust Particles; Cosmic Chemistry; Orbital Mechanics; Man in Space; Origin of the Solar System; The Sun; The Moon; Planetary Atmospheres; Planetary Structure; Space Astronomy; Stellar Evolution; Extragalactic Radio Sources; Nucleosynthesis. The bibliography for each chapter is not intended to be comprehensive; it has been confined to survey articles or major research papers on the topic of the individual article.

S. F. SINGER (Editor): *Interactions of Space Vehicles with an Ionized Atmosphere.* In–8°, 510 pp., with figures. Pergamon Press, Oxford, 1965 (£ 7 10s).

The book is based on material originally presented at a symposium of the American Astronomical Society in Washington, but an attempt has been made to cover the subject more completely by means of additional papers. In all there are fourteen contributions, divided in two parts. Part I deals principally with the interaction with a plasma of a charged boyd which may be moving; among the chapters of this part the longest single contribution is that by R. T. Bettinger dealing with probe methods of measurement in the ionosphere. Part II is devoted to the different radio-wave propagation effects, such as long-distance reception of the satellite transmitters, and particularly the effect observed by J. D. Kraus thought to be scattering of WWV transmissions from Sputnik I or its wake, the remarkable feature being the strength of the received signal which corresponded to a scattering cross-section of 10^4 to 10^6 m^2, several orders of magnitude greater than the geometrical area. However, radio signals are also reflected from ionized meteor trails, and the association of some signals with satellites has always been controversial. Three contributions have some general application in astronomy and plasma physics. The book will provide most informative and valuable reading for all concerned with scientific or research aspects of aeronautics and astronautics.

BILLY M. MCCORMAC (Editor): *Radiation Trapped in the Earth's Magnetic Field.* In–8°, 901 pp., with figures. D. Reidel Publishing Company, Dordrecht, Holland 1966 (F. 130).

The state of knowledge of the various facets of radiation trapped in the earth's magnetic field is rapidly changing. Here we dispose, as published in short time, the proceedings of the advanced study institute held on this subject in Bergen, Norway, August 13th to 3rd September, 1965. The 60 contributions are divided in nine sessions: B–L Space; Observed particle distribution in the natural belts I and II; Sources and sinks of natural trapped radiation; Physics of the outer magnetosphere; Artificial injected radiation; Synchrotron radiation; Effects of trapped radiation on sensors, electronic devices, etc.; Radiation doses received by manned flight in the trapped radiation belts. The Editor has presented at the end of the volume a summary from the point of view of future research requirements. The following areas will be important for the future: Experimental and theoretical research on outer magnetosphere, Injection of particles, Acceleration of particles, Life time above L of 1.25, Experimental observations in the belts, Secular variation, Solar wind, Artificial sources, New representation of the magnetic field, and Diffusion and precipitation of particles. The book is superbly printed and designed. It should be considered as fundamental for all geophysicists working from the space point of view, as it is now required in the study of the earth's magnetic field.

WILLIAM H. K. LEE (Editor): *Terrestrial Heat Flow.* In–8°, 276 pp., with figures. American Geophysical Union, Washington, 1965 ($ 10.00).

Terrestrial heat flow is the study of the outflow of heat from the earth's interior, but in a broader sense it embraces all geothermal problems. This monograph is the first attempt to present an up-to-date review of the fundamentals of terrestrial heat flow: theories and techniques of measuring heat flow, results of heat flow observations, and geophysical deductions. It also includes reviews of physical processes in geothermal areas and of geothermal resources, together with an historical introduction to terrestrial heat flow by Sir Edward C. Bullard. A fair amount of the materials in the monograph have not been published before. Each of the nine chapters has been written to be as self-sufficient as possible; all chapters have an abstract and most of them also have a summary. The volume will provide a good guidance for geophysicists beginning this field of research and serve as a reference for both specialists and nonspecialists.

THOMAS F. IRVINE, JR. and JAMES P. HARTNETT (Editors): *Advances in Heat Transfer,* Vol. 3. In–8°, Academic Press, New York–London, 1966 ($ 12.00).

This serial publication presents the continuing results of wide-spread research in the field of heat transfer. Volume 3 contains the following sections: The effect of free-stream turbulence on heat transfer rates; Heat and mass transfer in turbulence boundary layers; Liquid metal heat transfer; Radiation transfer and interaction of convection with radiation heat transfer; A critical survey of the major methods for measuring and calculating dilute gas transport properties. As well as serving as a broad review for experts, these articles will also be of great interest to nonspecialists with only a general knowledge of the field, who need to know the results of the latest research.

H. TAKEUCHI: *Theory of the Earth's Interior*. In–8°, 131 pp., with figures. Blaisdell Publishing Company, Waltham, Mass., 1966 ($ 6.50).

We cannot get into the interior of the earth, as the deepest hole we have made into its crust is only 1/500 of the planet's radius. By subjecting observational data to mathematical analysis, however, we try to discover what is going on within the earth, and this mathematical tool is the subject of the present book. Theory of elasticity, viscous fluid, and electromagnetics are developed as systematically as possible. And the similarities among these three fields of study, form the mathematical basis of this book, having an introductory character. The text is clearly written from a well reckoned specialist, as the Author received in 1964 the Lagrange Prize from Belgium's Academy of Science for his work in the study of earth tides and free oscillations of the earth.

O. A. SCHAEFFER and J. ZÄHRINGER (Editors): *Potassium Argon Dating*. In–8°, 234 pp., with figures. Springer Verlag, Berlin–Heidelberg–New York, 1966 (DM 42.40).

This book, dedicated to Wolfgang Gentner on his sixtieth birthday, contains 10 papers on the potassium argon method: History of the method, Determination of radiogenic argon, Potassium analysis, The diffusion of argon in potassium bearing solids, K-Ar dating in precambrium rocks, K-Ar dating of plutonic and vulcanic rocks in orogenic belts, K-Ar dating of sediments, The problem of contamination in obtaining accurate dates of young geologic rocks, Tektites, K-Ar ages of meteorites. At the end a very extensive bibliography (31 pages) is a nearly complete coverage of the literature of the potassium argon dating, also with regard to his wide range of applicability. The book is indispensable to anyone who should use the potassium argon dating method or working out their results.

K. S. SPIEGLER (Editor): *Principles of Desalination*. In–8°, 566 pp., with figures. Academic Press, New York–London, 1966 ($ 21.00).

The volume covers in detail the scientific, engineering, and economic aspects of the various desalting methods. The eleven authoritative contributions included are organized to make this volume a comprehensive treatment of the entire field, rather than a loose collection of specialized papers on diverse aspects of desalination. Among the subjects presented there are many of geophysical and meteorological nature, as those on distillation and particularly on Solar distillation, freezing methods, etc. Specific chapters contain detailed descriptions and flow sheets of the desalting methods now practiced, the first major review of the new process of hyperfiltration (reverse osmosis) and an economic analysis of the cost conventional water supplies. The book is to be considered as fundamental in the field of salt water purification.

Proceedings of the International Conference on Magnetism; Nottingham, September 1964. In–4°, 878 pp., with figures. The Institute of Physics and the Physical Society, London SW 1, 1965 (£ 8 8s).

The volume includes over 200 papers presented at the International Conference on Magnetism held at Nottingham, in September 1964. The contributions are presented in 39 chapters, devoted to the following headings: Theory, Transition metals, Critical phenomena, Fermi surface, Metals and alloys (5 chapters), Rare earth metals, Neutron diffraction, Spin waves, Covalency and exchange effects, Nuclear magnetic resonance, Resonance and relaxation, Non-metallic ferro and antiferromagnetics, Oxides and compounds, Miscellaneous oxides, Hematite, Ferrites, Garnets, Magnetization processes, Anysotropy, Hard magnetic materials, Thin films, Electron microscopy. A part of the papers are followed by the discussion. These proceedings give therefore a nearly complete representation of the present knowledge on magnetism, indispensable for the specialist. Also the geophysicists interested in rock-magnetism will find suitable data and interesting results.

PURE AND APPLIED GEOPHYSICS

(PAGEOPH)

Continuation of *Geofisica pura e applicata*

Birkhäuser Verlag, Basel and Stuttgart

Pageoph Vol. 64 Pag. 1-256 (1966/II)

PURE AND APPLIED GEOPHYSICS

(PAGEOPH)

Continuation of *Geofisica pura e applicata*
Editor: Prof. Mario Bossolasco, Istituto Geofisico Italiano, Piazza L. da Vinci 12,
P.O. Box 3689, Milano, Italy

RULES FOR CONTRIBUTORS

Pure and Applied Geophysics publishes only original papers.
Manuscripts should be submitted directly from the author or presented through one of the members of the Advisory Board. Manuscripts sent indirectly are not accepted Manuscripts and figures cannot be returned.
Each manuscript must be complete and legibly typed on one side only with line double spaced; the submission of two copies of the text and small photocopies of large drawings will speed the process of reviewing.
A summary (abstract) in English is required at the beginning of each article.
It is recommended to use, for guidance in the preparation of papers for journals, the 'Style Rules' available from Birkhäuser Verlag.
All figures will be reduced to the smallest size compatible with legibility. Original drawings should preferably be made about 2–4 times the final size and lettering should therefore be large enough so that after reduction the smallest character will be at least $^3/_4$ mm. Each figure must be provided with an adequate legend, and all legends should be typed together on one sheet of the paper.
Authors will receive galley proof but no page proof. When returning the proof, the number of the requested reprints (beside the 50 free copies) should be indicated. A price list for reprints is available from Birkhäuser Verlag.

Annual subscription rate: (3 volumes), postage incl., sFr. (DM) 190.–
Single volumes: sFr. (DM) 80.– and postages

Subscriptions should be sent to your bookseller, news agent or directly to the publisher

Additional costs for copies by air mail available on request

Mathematische Werke aus dem Birkhäuser Verlag

Lehrbücher und Monographien aus dem Gebiete der exakten Wissenschaften

Mathematische Reihe

1 *Versicherungsmathematik.* Von E. Zwinggi. 2. Auflage (1958). Fr./DM 36.—.

2 *Analytische Geometrie der Ebene und des Raumes.* Von R. Fueter (1945). Fr./DM 24.–.

3 *Statistische Methoden für Naturwissenschafter Mediziner und Ingenieure.* Von A. Linder. 4., unveränderte Auflage (1964). Fr/DM 56.—.

4/5/7 *Vorlesungen über Differential- und Integralrechnung.* Von A. Ostrowski. Band I: Funktionen einer Variablen. 2., neubearbeitet Funktionen einer Variablen. 2., neubearbeitete Auflage (1964). Fr./DM 35.—. Band II: Differentialrechnung auf dem Gebiete mehrerer Variablen. 2., neubearbeitete Auflage (1961). Fr./DM 38.50. Band III (1962): Integralrechnung auf dem Gebiete mehrerer Variablen. Fr./DM 48.—.

6 *Lehrbuch der darstellenden Geometrie.* Von E. Stiefel (1947). Fr./DM 28.50.

8/9 *Funktionentheorie.* In zwei Bänden. Von C. Carathéodory. Band I. 2., revidierte Auflage (1960). Fr./DM 27.50. Band II: 2., revidierte Auflage (1961). Fr./DM 22.50.

10 *Mass und Integral und ihre Algebraisierung.* Von C. Carathéodory (1956). Fr./DM 39.—.

11 *Über Kurven und Flächen in allgemeinen Räumen.* Von P. Finsler (1951). Fr./DM 16.—.

12 *Die zweidimensionale Laplace-Transformation.* Von D. Voelker und G. Doetsch (1950). Fr./DM 48.—.

13 *Theorie der geometrischen Konstruktionen.* Von L. Bieberbach (1953). Fr./DM 19.—.

14/15/19 *Handbuch der Laplace-Transformation.* Von G. Doetsch. Band I (1950): Fr./DM 84.—. Band II (1955): Fr./DM 57.—. Band III: Fr./DM 42.—.

16 *Analytische Geometrie.* Von W. Blaschke (1954). Fr./DM 19.—.

17 *Projektive Geometrie.* Von W. Blaschke (1954). Fr./DM 19.—.

18 *Übungen zur projektiven Geometrie.* Von H. Herrmann. Fr./DM 17.—.

20 *Elementare Differentialgeometrie.* Von W. Haack. Fr./DM 22.—.

22 *Theorie der Gruppen von endlicher Ordnung.* Von A. Speiser (1956). 4. Auflage. Fr./DM 26.—.

23 *Les problèmes aux limites de la physique mathématique.* Par H. R. Garnir (1958). Fr./DM 29.—.

24 *Einführung in Theorie und Anwendung der Laplace-Transformation.* Von G. Doetsch (1958). Fr./39.40.

25 *Vorlesungen über Funktionalgleichungen und ihre Anwendungen.* Von J. Aczél (1961). Fr./DM 37.50.

26 *Topologische Räume.* Von H.-J. Kowalsky (1961). Fr./DM 40.—.

27 *Einführung in die Theorie der algebraischen Zahlen und Funktionen.* Von M. Eichler (1963). Fr./DM 59.—.

28 *Aufgabensammlung zur Infinitesimalrechnung.* Band I: Funktionen einer Variablen, Von A. Ostrowski (1964). Fr./DM 38.50.

29 *Einführung in die Algebra und die Theorie der algebraischen Gleichungen.* Von F. Nevanlinna (1965). Fr./DM 34.50.

30 *Einführung in die Funktionentheorie.* Von R. Nevanlinna und V. Paatero (1965). Fr./DM 64.—.

31 *Lehrbuch der linearen Algebra.* Von W. Nef 276 (1966). Fr./DM 48.50.

32 *Zahlentheorie.* Von S. J. Borewicz und I. R. Safarevic. 467 Seiten. (1966). Fr./DM 56.—.

Mathematische Einzelwerke

Introduction to the Constructive Theory of Functions. By J. Todd (1963). Fr./DM 27.50.

Die Bewegungsgruppen der Kristallographie. Von J.J. Burckhardt (1947). Leinenband Fr./DM 34.—.

Differential- und Integralrechnung. Von L. Locher-Ernst (1948). Fr./DM 38.40.

Einführung in die freie Geometrie ebener Kurven. Von L. Locher-Ernst (1952). Fr./DM 13.—.

Primzahlen. Von E. Trost (1953). Fr./DM 14.—.

Adolf Hurwitz: *Mathematische Werke.* Band I, 2. Auflage (1963). Fr./DM 78.—; Band II, 2. Auflage (1963), Fr./DM 78.—.

Ludwig Schäfli: *Mathematische Abhandlungen.* Band I (1950), Fr./DM 54.—; Band II (1953), Fr./DM 54.—.; Band III (1956), Fr./DM 57.—.

Der Briefwechsel von Johann Bernoulli. Band I (1955). Fr./DM 60.—.

Altes und Neues über konvexe Körper. Von H. Hadwiger (1955). Fr./DM 14.—.

Einführung in die Geometrie der Waben. Von W. Blaschke (1955). Fr./DM 16.—.

Selecta Hermann Weyl (1956). Fr./DM 48.—.

Colloquium über Schaltkreis- und Schaltwerk-Theorie vom 26. bis 28. 10. 1960 in Bonn (1961). Fr./DM 20.—.

2. Colloquium über Schaltkreis- und Schaltwerk-Theorie vom 18. bis 20.10 1961 in Saarbrükken (1963). Fr./DM 14.—.

3. Colloquium über Automatentheorie vom 19. bis 22. Oktober 1965 in Hannover (1966). Ca. Fr./DM 40.—.

Zu beziehen durch Ihre Buchhandlung
Obtainable from your bookseller
Commandes à votre libraire